UNIVERSITAT JAUME I

Departament de Química Inorgànica i Orgànica

Àrea de Química Inorgànica

UNIVERSITAT POLITÈCNICA DE VALÈNCIA

Instituto de Tecnología Química

(UPV-CSIC)

Design of new nanomaterials for their use in catalysis and photochemistry

PhD Thesis
Francisco Gonell Gómez
PhD. supervisors: Beatriz Julián López and Avelino Corma Canós
Castelló de la Plana, March 2017

Dra. Beatriz Julián López Professora Titular de l'àrea de Química Inorgànica de la Universitat Jaume I i Prof. Dr. Avelino Corma Canós Professor d'Investigació del Consell Superior d'Investigacions Científiques

Certifiquen: Que la Tesi Doctoral amb títol "Design of new nanomaterials for their use in catalysis and photochemistry" ha sigut desenvolupada sota la seua direcció, en l'àrea de Química Inorgànica del Departament de Química Inorgànica i Orgànica de la Universitat Jaume I i l'Institut de Tecnologia Química centre mixt del Consell Superior d'Investigacions Científiques i la Universitat Politècnica de València, per Francisco Gonell Gómez.

Castelló de la Plana, a

Sign. Dra. Beatriz Julián López Sign. Prof. Avelino Corma Canós

Aknowledgements/Agraïments

En primer lloc m'agradaria donar les gràcies a Puri, que va ser qui em va iniciar en el camp de la investigació i en la química de l'estat sòlid. Les seues ensenyances, els seus valors i el compromís social sempre estaran en el meu record. Te'n vas anar massa prompte.

També m'agradaria donar les gràcies als meus directors de tesi Bea i Avelino, per totes aquelles coses que he m'han ensenyat. A Bea per la seua paciència, la seua alegria i comprensió i els seus consells i ensenyances en el sol-gel, en la síntesi de materials i en la luminescència. A Avelino per transmetrem la passió per la química, el valor de l'esforç i la constància i les seues ensenyances en el camp de la catàlisi i reacció.

La sort d'haver realitzat la tesi doctoral en dos llocs és que m'ha permès conèixer a moltíssima gent extraordinària. Així m'agradaria donar les gràcies als meus companys de màster Ricardo i Thales amb qui vaig compartir llargues classes i estones inoblidables preparant treballs. També a Fabrizio, l'altre membre del grup de Materials Multifuncionals, amb qui he compartit tantes estones al laboratori. A tots els companys i companyes que han passat pel grup de Química Organometàl·lica i Catàlisi Homogènia, en especial a Eduardo, Maca, Jose, Sara, Candela i Carmen, sempre és un plaer discutir amb vosaltres i aprendre sobre el vostre punt de vista de la química tot i ser *"del lado oscuro(hahahaha!!!"* i a la gent del grup de Dispositius Optoelectrònics i Fotovoltaics en especial a Sixto i Rafa, grans mestres de de les cel·les solars i de l'òptica.

A tota la gent del departament de Química Inorgànica i Orgànica de la UJI perquè sempre es trobava ajuda quan es necessitava i als tècnics de Serveis Centrals pels seus consells i ajuda a l'hora de la caracterització.

També m'agradaria donar les gràcies als meus companys de la carrera, Pedro, Neus, Ana, Roberto, Carlos, sempre va bé posar-se al dia i veure com es treballa en altres camps de la química i com funcionen en altres llocs.

Gràcies també a tota la gent que vaig conèixer durant les meues estades en França i Portugal en especial a Clèment, David, Irma, Rute, Luis, Vânia, Patricia, Carlos, Sangeehta, Mengestie, amb vosaltres el temps fora de casa em va passar volant.

A tota la gent amb qui he treballat en l'ITQ, Alex, Aroa, Sara, Mer, Michael, Patricia i José Miguel, ha sigut un plaer aprendre i treballar amb vosaltres. A tota la gent de

caracterització de l'institut, per la seua eficiència i rapidesa a l'hora de caracteritzar les mostres. A tota la gent d'administració i taller, per fer que les coses siguen fàcils i ràpides. I com no, a la gent dels Serveis de Microscopia de la Universitat Politècnica de València, Merche, Ximo, Alicia, Jose Luis i molt especialment a Manolo, pels seus grans consells i ensenyances sobre microscòpia i les bones estones passades en el microscopi.

A tots els companys de laboratori que han passat per fotoquímica de materials, Fran, Marco, Raquel, Canijo, Abde (un altre del *"lado oscuro "* xD), Ivan (el mestre del grafé), Jinbao, Sonia, als companys de Nanotecnologia, Pedro, Josep, Amparo, Ester, Teresa, Diego (algun dia acabaràs amb el CO_2), Alejandra, Rocío i Cristina i a tota la gent del departament de química. Al companys de dinar en l'ITQ, a Diego, Raquel, Vicent (pobrets si ens furten el lloc!), Amparo, Lidia, Marta, Edi i Ximo. A Jorge, Dani i Jaime (cavallers de la química i la cervesa) Marvin, Javi Navas, Víctor, Sergio, Javi (Ceuta), Ferran, Lina, Karen, Andrea, Borja, Carmen, Pablo, Ivàn S., Ángel, Manolo, Pascual, Alberto, Alejandro, Chema, Sebas, Ale, Miguel, Yannick, Jose Gaona, Tirso, Paula, Judit, Nacho, Saray, Victoria, Tere P., Belén, Chelo, Amada, Elena i a totes aquelles persones importants que se m'obliden.

A tots els meus amics de Somarruscos i Emboirats per els grans moments que hem viscut junts i per les festetes que ens hem pegat. A Maria per ser tant gran amiga i per aguantar-me les xapes que t'he pegat, aquesta tesi també és gràcies a tu.

A la meua família a Sergio, Mireia, Àngel, Albert, a mon tio, a ma mare i mon pare per fer que siga com sóc i per recolzar-me en el moments difícils.

Dit tot açò, ha arribat el moment, que comence la festa.

Index

Chapter 1

General introduction and objectives

1.1 General introduction

1.1.1 Nanomaterials: Fundamentals and basic apects

Nanomaterials are referred to those materials whose size is below one micron, more specifically, this term is usually employed for materials with size between 1 to 100 nm[1] (nanoscale). These concepts were first introduced in 1959 by Richard Feynman in his lecture *"There's Plenty of Room at the Bottom"* and further developed in the subsequent years.

The revolution of nanomaterials has been done in the late 90s with the development of controlled synthetic approaches and characterization technologies. The control of matter at nanoscale level is now possible in the laboratory, however nanoscaled materials are found in nature. Thus, it is possible to observe nanostructures in leaves, butterfly wings and bones or beaks developing amazing properties such as super hydrophobicity (Figure 1. 1), impressive colors and large size and low density properties, respectively.

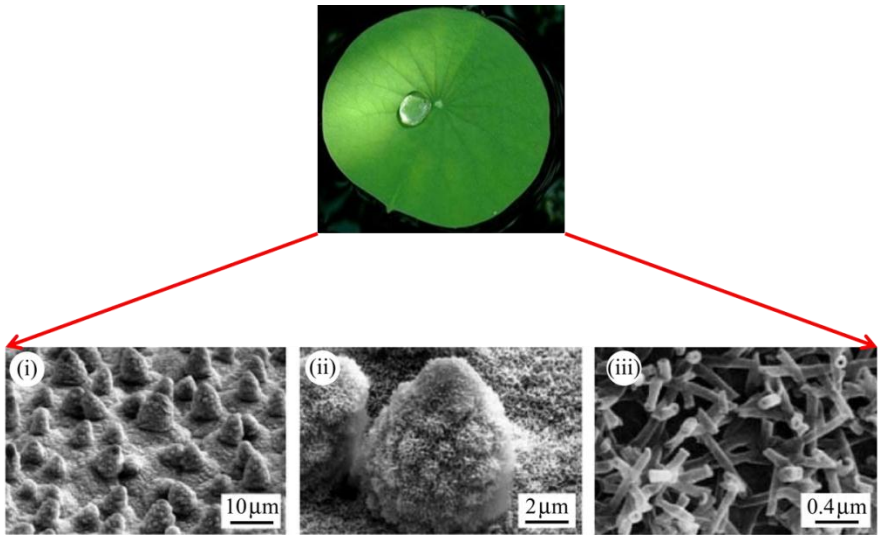

Figure 1. 1. Lotus leave and SEM micrographs of the leave at different magnifications showing the microstructure responsible of the superhydrophobic properties.[2]

Humans have also used nanomaterials from ancient times, for example in Lycurgus cup glass (4th century A.C.), where the gold and silver nanoparticles dispersed in the colloidal form provides a dichroic effect (Figure 1. 2).

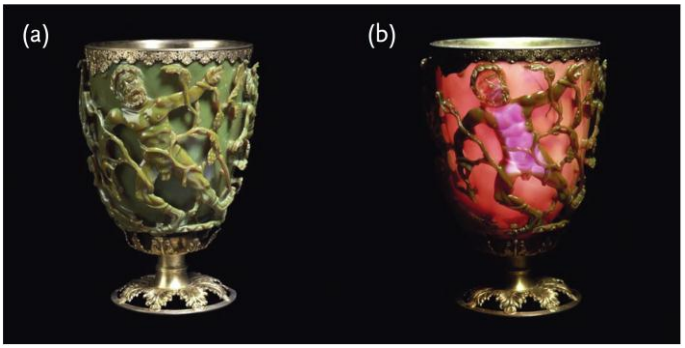

Figure 1. 2. Lycurgus cup glass and its dichroic effect (green/red color).[3]

The nanomaterials exhibit new properties compared to materials in the bulk size. Some of the reasons of this behavior are listed here:[4–6]

- The surface/bulk atoms ratio drastically increases in nanomaterials, providing more coordinative non-saturated atoms.
- Surface/volume ratio is inversely proportional to diameter of the particle, thus obtaining high surface materials.
- Diffusion at nanoscale is more homogeneous and faster compared to macroscopic materials as consequence of the small size.
- Surface stress and tension are bigger in nanomaterials, and a local lattice contraction can occur.
- The electrostatic forces become highly important at the nanoscale.
- The electrons are confined and have higher energy than its bulk counterpart, inducing a shift towards higher energies in the optical absorption and fluorescent emission spectra.
- Interaction with light also changes because the particle size is in the same range as the radiation wavelength.

The new synthetic approaches have allowed designing nanomaterials with different sizes, from nano to micro, and with different morphologies and shapes. Accordingly, they can be classified as a function of their aspect ratio as zero-dimensional (i.e., isolated small nanoparticles), one-dimensional (1D), two-dimensional (2D) and three-dimensional (3D) nanostructures. 1D nanoparticles (NPs) are those where the major growth occurs in one direction like rods, wires, tubes, etc. In 2D structures, the mayor growth takes place in two directions. Some examples of this kind of NPs are planar nanoparticles as hexagons, plates, disks, and thin films or stacks of layers. In 3D structures the growth occurs in the three directions, such as in tetrahedral and octahedral particles, cubes, prisms, etc (Figure 1. 3).[4,7]

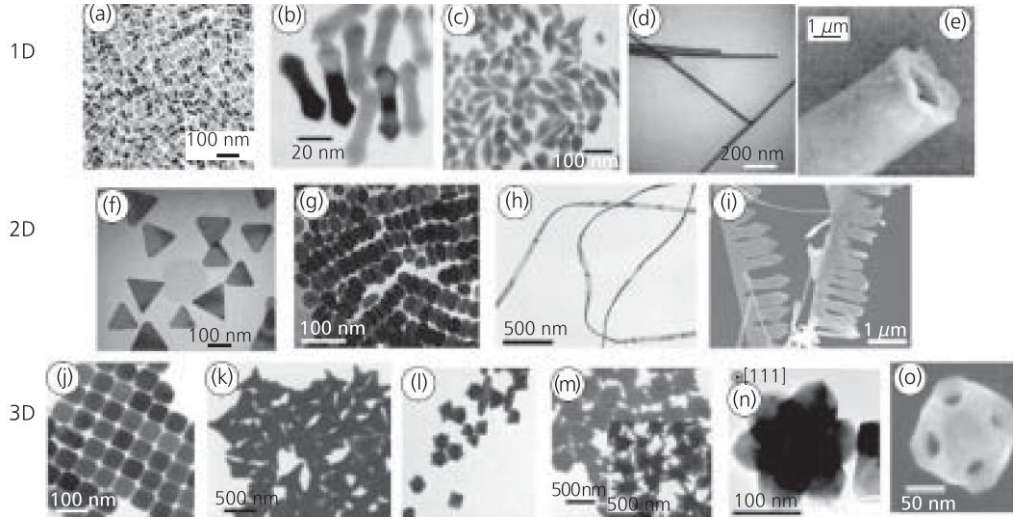

Figure 1. 3. TEM and SEM images of one- two and three-dimensional nanoparticles: a) nanorods, b) nanoshuttles, c) nanobipyramids, d) nanowires, e) nanotubes, f) triangular nanoplates, g) nanodiscs, h) nanoribbons, i) nanobelts, j) nanocubes, k) nanotetrapods, l) and m) star-shaped nanoparticles, n) a nanohexapod and o) nanocage.[7]

Size effects constitute a fascinating aspect of nanomaterials since they pertain to the evolution of structural, thermodynamic, electronic, spectroscopic, electromagnetic and chemical features of these finite systems. Some of the most important consequences in the physico-chemical properties of the materials related to the nanometric size are briefly explained below.[1,8,9]

In metal oxide nanoparticles, the growing importance of surface free energy and stress with decreasing particle size, induces changes in cell parameters and in the thermodynamic stability of some crystalline phases, facilitating unusual structural transformations.

Another important effect is related to the electronic properties of the materials. The nanostructuration produces the so-called quantum-size or confinement effects, which essentially arise from the presence of discrete atom-like electronic states. Additionally, the quantum confinement is responsible for energy shift of exciton levels and optical band gap. In nanooxides, a decrease in the average size changes the magnitude of the band gap with strong influence in the conductivity and also chemical reactivity. Therefore, surface properties are drastically affected by size, and nanostructures exhibit unprecedented sorption or acid/base characteristics.

The presence of undercoordinated atoms (like corners or edges) or atom vacancies produces specific geometrical arrangements as well as occupied electronic states located above the valence band of the corresponding bulk material, enhancing the chemical activity of the system.

In magnetic materials, as the particle size decreases, the number of magnetic domains per particle decreases, and below a critical size, the particle behaves as a single domain. Then, new magnetic phenomena appear, such as superparamagnetism. For these superparamagnetic NPs, thermal fluctuations overcome anisotropy forces and hence magnetization of the particles gets reversed easily from one direction to another, even in the absence of a magnetic field.

Regarding semiconductors such as CdSe, CdS and ZnS, the quantum confinement effect in particles with diameter lower than the Bohr exciton radius provides materials whereby the NP absorption onsets and emission energies are size-tunable.

This variation of properties with size is also observed in metals like gold, silver or copper exhibiting surface plasmon resonance. At the surface of these metallic nanoparticles, light with frequencies below the frequency of the surface plasmons (quantized waves of the free electrons in the incompletely filled conduction band) is reflected. Very few metals have plasmon frequencies in the visible range but that leads to their typical colors. The oscillation modes and frequency of the plasmon vibration depend heavily on the shape and size of the particles, thus changing the absorption of the material. Furthermore, in the case of resonance interaction, the electrical field of the light moves the free electrons at the particle surface and causes oscillations with the frequency of the light, that are highly dependent on the anisotropy of the nanoparticle.

In conclusion, nanostructured materials exhibit improved or even unique physical, chemical, and other properties, and open a land of possibilities for new and smart applications.

1.1.2 Top-down and bottom-up approaches

Different methodologies can be employed in order to obtain nanomaterials, but they are included in the top-down and bottom-up approaches. Figure 1. 4 shows a classification of the synthetic methods included in both approaches.

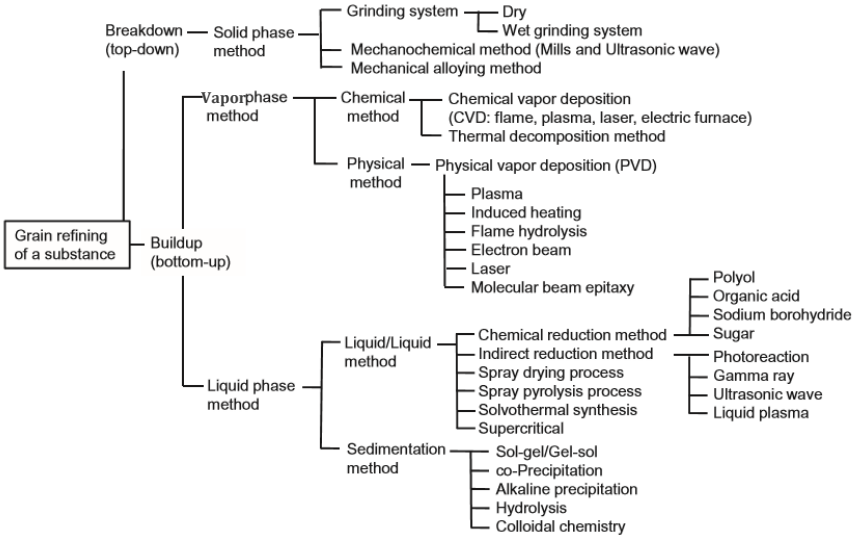

Figure 1. 4. Typical synthetic methods for nanoparticles for the top-down and bottom-up approaches.[3]

Top-down approach is based on microtechnology methods, which employs physical methods such as crushing or milling techniques for the preparation of nanomaterials.[4,10]

One example of the top-down approach is found in the production of ceramic nanopigments which have emerged as an important field for academia and ceramic industry. In the last years, the development of ink-jet printers has completely changed the ceramic tails industry since this technology allows producing more sophisticated and complicated designs compared to traditional methods. For this application, pigments based on metal oxide nanoparticles require to be produced with a controlled polydispersion, via nanogrinding, avoiding in this way obstructions in the expensive piezoelectric nozzles of the printing technologies.

The advantages of this approach relate with the low cost and ease to be implemented in the conventional industrial technologies, but the main problem lies in the broad particle size distribution obtained by this method.

On the other hand, bottom-up approach is based on chemical synthesis which uses atoms or molecules as building blocks to produce nanomaterials.[4,10] This approach is usually preferred in nanotechnology since it provides nanomaterials with more controlled size, morphologies compared to analogous materials obtained by top-down approaches.

The bottom-up approach is roughly divided into *gaseous phase* methods and *liquid phase* methods. For the former, the chemical vapor deposition method (CVD) involves a chemical reaction, whereas the physical vapor deposition method (PVD) uses cooling of the evaporated material. Although the gaseous phase methods minimize the occurrence of organic impurities in the particles, they necessitate the use of complicated vacuum equipment whose disadvantages are the high costs involved and low productivity.

Therefore, liquid phase methods have been the major preparation methods of nanoparticles. Among them, the most widely used are:

- Sol-gel route: this synthetic procedure starts from metal alkoxides or chlorides in solution (sol) which upon different processes of polycondensation evolves a gel-like diphasic system containing both liquid and solid phase whose morphologies range from discrete particles to continuous polymer network. The materials obtained by this approach usually are amorphous and need to be fired to make them crystalline. This fact leads to agglomeration and sintering of the nanoparticles. Even so, the temperatures required to obtain crystalline materials are much lower than the required in the ceramic approach. Moreover this chemical route is largely employed to produce films of different thickness and textures (Figure 1. 5).[11]

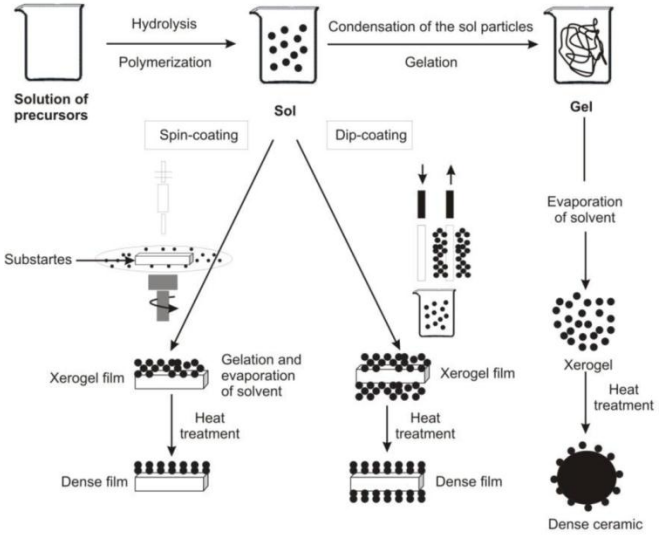

Figure 1. 5. Overview showing different sol-gel methods for obtaining films and powders from a colloidal sol.[12]

- Hydrothermal and solvothermal methods: these alternative approaches use solvents in a sealed container reactor (called "autoclave or bomb", Figure 1. 6 a) which is treated at a temperature above their boiling point. The autogenous pressure promotes the reaction of the precursor solution. The reaction can be performed on aqueous medium (hydrothermal) or with organic solvents like ethanol or benzyl alcohol (solvothermal).[13]
  Other parameters such as the nature of the molecular precursors and the percentage of fill of the vessel have an influence in the autogenous pressure (Figure 1. 6 b). Under these conditions, the dielectric constant of the solvent and ion and molecules mobility can drastically change, thus providing reaction conditions that would be difficult to obtain in other synthetic approaches.[13] This methodology has extensively used to produce inorganic solids, especially zeolites, but the main drawback is that the outcome of the reaction is difficult to predict.[14]

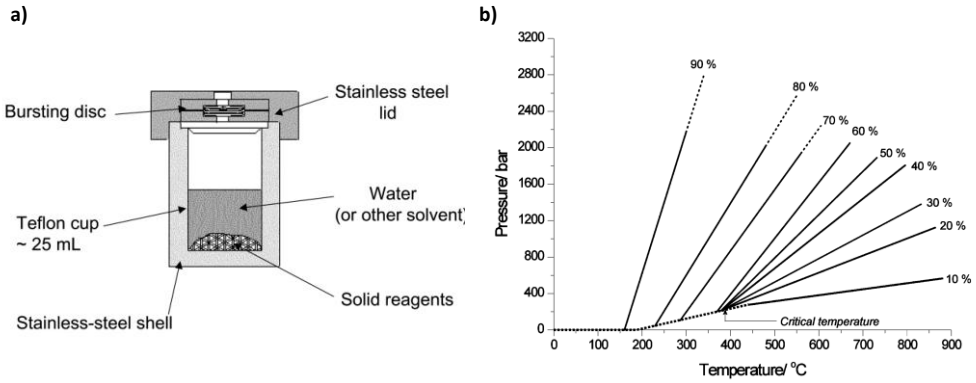

Figure 1. 6. a) Schematic representation of a typical Teflon stainless autoclave typically used for solvothermal or hydrothermal synthesis[13] and b) pressure as a function of temperature and percentage of fill of water in a sealed vessel. [13,15]

- Microwave synthesis: in this method the precursor solution is heated via microwave irradiation, avoiding in such a way thermal gradients in the reaction vessel and obtaining uniform reaction conditions and high reaction rates compared with conventional heating methods.[3]

- Thermal decomposition method: It is based on the decomposition of organometallic compounds and/or metal-surfactant complexes in hot surfactant solutions.[16] This approach can be carried out by two techniques:

- Hot-injection method: The precursor is rapidly injected in a hot surfactant solution (Figure 1. 7).
- Heating-up method: the mixture of the precursors is slowly heated to high temperature in order to initiate the crystallization reaction.

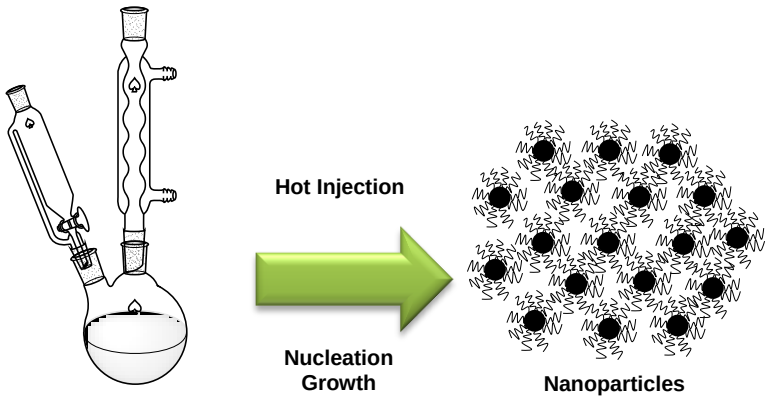

Figure 1. 7. Hot injection method for the synthesis of monodisperse NPs.[16]

Thermal decomposition provides very small and homogeneous crystalline NPs that can be dispersible in apolar organic solvents.

- Chemical reduction of metal nanoparticles: In this route, a metal salt in solution or supported in a carrier is reduced using a reductant such as H_2, sodium borohydride, phenylethanol, alcohols, dimethylformamide, etc. The addition of surfactants avoids the uncontrolled growth of the NPs. This methodology is widely employed for preparing metal NPs in suspension, as well as to support them on a substrate or carrier. The latter option is preferred in heterogeneous catalysis to get recyclable catalysts.

In the bottom-up approaches, organic components participate in the physico-chemical mechanisms directly involved in the nucleation and limited growth of the nanomaterials. However, for the preparation of inorganic solids, these organic moieties must be removed by calcination, ozonolysis, washing, etc. In other cases, the combination of both organic and inorganic components in a single material may be of interest. The development of hybrid organic-inorganic materials which combine in a synergistic way the properties of organic materials (hydrophobic/hydrophilic balance, chemical stability, bio-compatibility, optical and/or electronic properties and chemical functionalities) and the inorganic solids (mechanical and thermal stability, electronic, magnetic and redox properties, density refraction index, etc.) provides

hybrid materials with new functionalities. Furthermore, the interface between inorganic and organic does influence strongly their properties. Hybrid materials can be thus broadly classified in two main classes, depending on the nature of bonds and interactions existing at the hybrid interface: *Class I hybrids*, including systems with weak interactions such as hydrogen bonding, van der Waals or electrostatic forces between the constituents, and *Class II hybrids*, where at least parts of the organic and inorganic components are linked by one strong chemical bond (covalent, iono-covalent, or Lewis acid-base bonds).[17,18] They exhibit outstanding properties that can find application in such a different areas as photonics, electronics, catalysis, luminescence, biomaterials, biosensors, bioreactors, etc.[17]

1.1.3 Application of nanomaterials

The current applications and the possibilities of future markets for nanoparticles are schematically summarized in Figure 1. 8. Indeed, most of the current applications exploit the effect of the interaction of light governed by the size of the particles, such as inks, dyes or UV-filters for cosmetics, paintings, pigments or catalysis. However, the intense research on nanomaterials from the late nineteens has fostered the development of emerging applications that involve more sophisticated properties of the nanostructured materials. Thus, new technologies in the fields of solar cells and photofuels, color lighting systems and displays, lasers and telecommunications, chemical (bio-)sensors, biological probes and so on are envisaged to find industrial opportunities at short or medium-term.

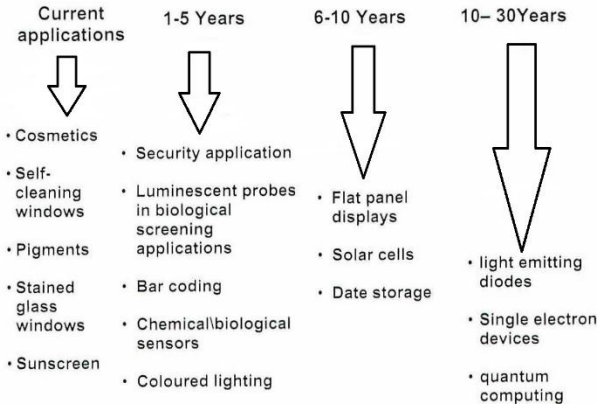

Figure 1. 8. Applications and future markets for nanoparticles.[1]

Recently, W. J. Stark *et al*. published a tutorial review providing the state of the art of nanomaterials in the industry.[19] In this report, they distinguish in the established industrial applications between the chemically inert nanoparticles or additives such as carbon, titania and silica polymer fillers, pigments, dyes and UV protection, functional surfaces, etc. and the chemically active particle as catalysts, biomaterials and antimicrobial additives. In Figure 1. 9, key examples of the outstanding properties and functionalities of inorganic nanoparticles are given. It is clear that diminution of the size affords an enormous change in surface area and provides a huge interface between the constituents. For catalytic, antimicrobial and many electronic properties, these interface properties add significant value to the final product.

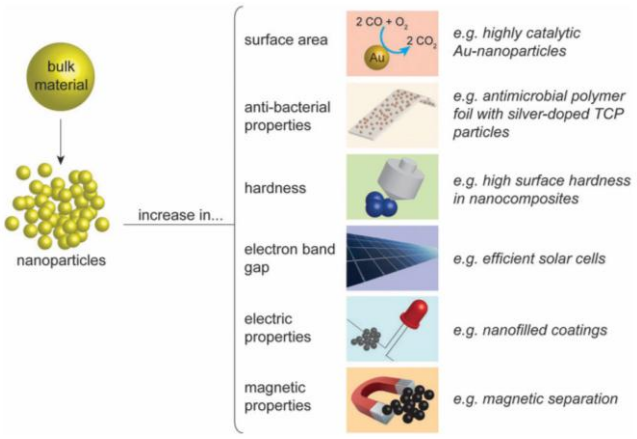

Figure 1. 9. Key examples of the properties of nanoparticles with potential industrial applications.[19]

In the following sections, the relevance of nanomaterials the fields of Catalysis, Photocatalysis and Photonics will be discussed in detail.

1.1.3.1 Catalysis for greener processes

In the eighties a social concern about all chemical risks regarding the industrial processes was developed. This leads to the need of designing and developing more environmentally friendly and sustainable processes. The Green Chemistry concept was introduced in the beginning of the 1990s by Anastas and Warner and was defined as the "design of chemical products and processes to reduce or eliminate the use and

generation of hazardous substances".[20] The same authors also introduce twelve principles in order to guide the practice of green chemistry, pointing out the importance of designing including novelty, planning and systematic conception. Moreover, to achieve a sustainability at the molecular level is also important.[21]

From the different principles of Green Chemistry one of the most important is the ninth one which enunciates the use of catalysts instead of stoichiometric reagents. This would led to deployment of more sustainable processes, lowering the energy required to carry out a process, avoiding the production of waste and directing the reaction towards the desired product.

A catalyst is able to increase the rate of a chemical reaction lowering the free energy required to reach the transition state while the free energy from reagents to products does not change. Moreover, a catalyst is not consumed into the reaction but may be inhibited, deactivated or destroyed by secondary processes.

Catalysis has been applied in many industrial processes including the production of fuels, energy, plastics, paints, fibers, removal of contaminants, etc., thus over 90% of all industrial chemicals are produced with the aid of catalysts.[22] Its use is quite important from the industrial point of view. They provide more environmentally friendly processes and led to a decrease in costs, because the amount of energy required and waste are reduced, and the natural resources are better employed.

The catalytic processes can be classified according to the media where the catalyst is located:

- Homogeneous: Same phase as the reagents.
- Heterogeneous: Different phase to the reaction medium.

The homogeneous catalysts are usually more active, selective and better characterized at molecular level than their counterparts. Nevertheless, heterogeneous catalysts present some advantages as easy separation, reusability and higher catalyst stability.

One of the areas where catalysis is of great importance is Fine Chemistry. Fine chemicals are defined as complex, single, pure chemicals substances that are produced in limited quantities (<1000 tons per year) in multistep batch chemical processes and they are usually sold for more than $10 per kilogram.[23] Even producing low volume of production, Fine Chemistry present high versatility and it is an interesting field for the research of new environmentally friendly processes.

In this context, the development of new heterogeneous catalysts with enhanced catalytic properties would be desirable. Nanotechnology offers new opportunities to get more active catalysts by increasing surface area and by exposing new faces of

crystals to the reagents. The enhanced activity of nanocatalysts is explained geometrically since when a nanoparticle became smaller, bigger the number of edges and corners is, what produce changes in the adsorption force or oxidation state due to modifications in its electronic structure.

One example of how nanotechnology can help to develop new active and selective catalysts is gold catalyst. Classically gold was considered as poor active metal when used as catalyst. The reason for that assumption resides in the traditional method employed to prepare NPs (deposition techniques). The materials exhibited large particle size distribution which hamper the appearance of quantum size-effects.[24] In recent years, with new methodologies and accurate preparation conditions, small and homogenous gold NPs have been prepared, being highly active and selective catalysts in CO oxidation, propylene epoxidation,[24] alcohol oxidation,[25] nitro compounds hydrogenation,[26] etc.

On the other side, the atomic distribution in the exposed surfaces of a catalyst has a great influence in the catalytic processes because each family of planes exhibit different distance between the active atoms, which strongly affects its catalytic activity. The development of new synthetic approaches has allowed designing new catalysts with preferentially exposed facets leading to more efficient catalysts. Selective carbamoylation of 2-4 diaminotoluene with dimethylcarbonate (Scheme 1. 1) is a reaction of industrial interest because the product is necessary for the production of polyurethanes, which are currently prepared using toxic fosgene.

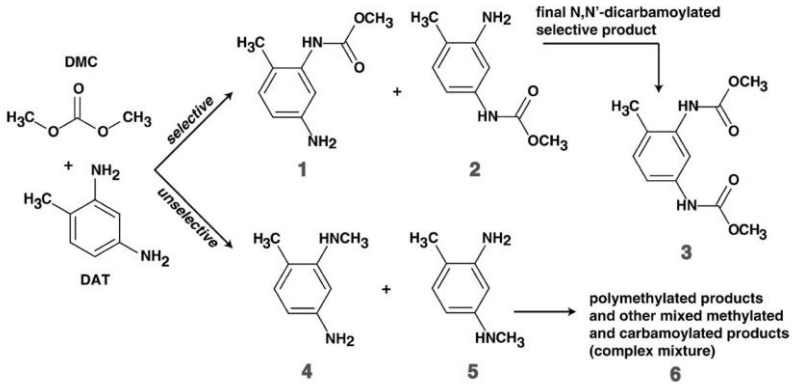

Scheme 1. 1. Reaction of dimethylcarbonate (DMC) with diaminotoluene (DAT).[27]

It has been recently reported that different exposed faces of CeO_2 has remarkable influence in the product distribution of this reaction. Thus, nanoparticles that expose preferentially (110) and (111) planes show high selectivity toward the carbamoylated product while NPs with preferentially (100) exposed facet show higher selectivity toward the methylated products.[27]

Gold NPs 111 oriented has been synthesized on layered N-doped graphene. This catalyst has been tested on Ullmann-like homocoupling, C-N cross coupling and in the oxidative coupling of benzene to benzoic acid, showing six orders of magnitude enhancement compared to non-oriented gold NPs.

Due to the outstanding properties of nanomaterials in the field of catalysis, Chapter 2 and 3 of this PhD defense will focus on the development of nanocatalysts with accurate control of morphology, phase, shape and size by using diverse synthetic methodologies. Their implications in different catalytic reactions will be further studied.

1.1.3.2 Photocatalysis

In the last years, an increase in the global temperature around the world, known as global warming, has been detected, which is caused by the increasing concentration of greenhouse gases such as methane or CO_2. These gases usually come from the combustion of fossil fuels used as energy source. In this sense, there is an urgent need of developing new environmentally friendly technologies in order to avoid the aforementioned problems.

Sunlight is an abundant and cheap energy source that has been used since ancient times by plants to obtain energy. In the last years a growing interest into development materials and devices able to take profit of this light to convert CO_2 into fuels, to split H_2O into H_2 and O_2, or to create electrical current has emerged. As a consequence of this interest, a new discipline was born known as photocatalysis, which refers to the action of a substance whose function is activated by the absorption of photons.[28]

In heterogeneous photocatalysis depending where the initial excitation occurs the photoreaction can be classified as.[29]

- Catalyzed system: when a molecule adsorbed on the catalyst surface is excited and interacts with the ground state of the catalyst.

- Sensitized system: when the catalyst is excited by the electromagnetic radiation and then transfers an electron or energy into a ground state of a molecule.

Semiconductors are those class of materials that present no electronic states between the top of the filled valence band (VB) to the bottom of the vacant conduction band (CB), this energy interval void is called band gap.[29,30] When a photon with higher energy than the band gap excites one electron from the CB to the VB, an electron-hole pair is created. If its lifetime is long enough they migrate to the surface of the semiconductor to carry out the reduction or oxidation reaction on previously adsorbed acceptor molecules (Figure 1. 10, pathways 1 and 2). Moreover, electron-hole recombination can occur in the surface (pathway 3) or in the volume of the semiconductor (pathway 4). Both processes are detrimental for the photocatalytic reaction.

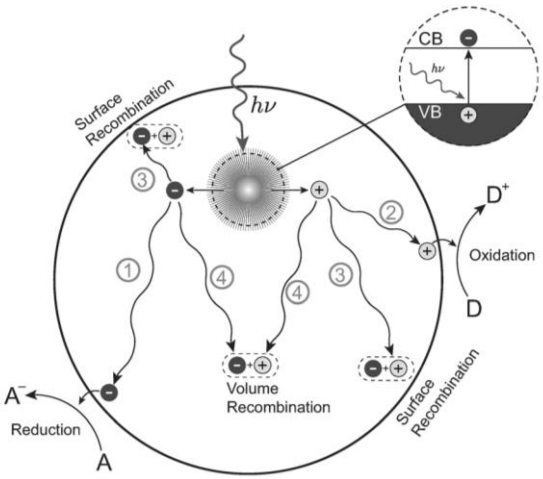

Figure 1. 10. Schematic photoexcitation in solid and possible relaxation paths. A= electron acceptor, D= electron donor.[29,30]

Since the first work of Fujishima and Honda who discovered the photocatalytic splitting of water on TiO_2 electrodes,[31] several semiconductors have been applied as photocatalysts, including oxides (WO_3, ZnO, α-Fe_2O_3, SnO_2, etc), metal chalcogenides (CdS, CdSe, MoS_2, WS_2, etc), oxynitrides, oxysulfides, oxyhalides, etc. [32]

In order to carry out a photocatalytic reaction, it is necessary a correct alignment of the band gap energy positions of the semiconductor and the redox potentials of the adsorbed molecules. Thus, for a reduction process, the conduction band edge must lie above the lowest unoccupied molecular orbital (LUMO) of the acceptor molecule

while, on the other side, for a transfer of an electron to the adsorbed molecule to the valence band of the semiconductor (hole transfer between VB and the oxidized molecule) the energy level of the highest occupied molecular orbital (HOMO) of the adsorbed molecule must lie above the valence band.[29,33] In this way, a good photocatalyst for a specific reaction should be able to have a band gap matching the potentials required to carry out the photocatalyzed reaction. Furthermore, for more sustainable catalysts, it would be desirable to be activated with visible light instead of ultraviolet radiation. Figure 1. 11 shows the band gap energies and the conduction and valence band potentials of various semiconductors.

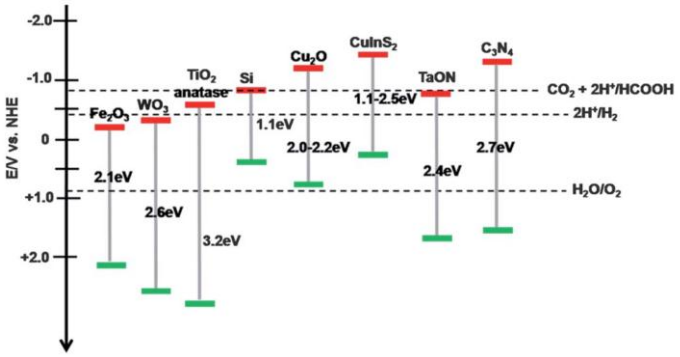

Figure 1. 11. Conduction (red line) and valence band (red line) potentials and band gap of selected semiconductors relative to the redox potentials at pH 7.[34]

Taking all this into account, the introduction of nanomaterials in this field has some advantages compared with its bulk counterpart:[35]

- Avoids back transfer from absorbed molecules to the semiconductor: the diffusion length is the average distance that a carrier can migrate without recombining. In nanoparticles, the carriers have higher probability of reaching the surface and to react with an adsorbed molecule.
- Shortened carrier collection pathway.
- Improved light distribution: nanoparticles offer higher light scattering than direct reflection from flat surfaces of the macroscopic particles, this produces better absorption of the incident light which otherwise would be lost.
- Surface area-enhanced charge transfer: as nanomaterials have high surface volume ratio, they offer higher sites and reactive surfaces to produces charge transfer between the semiconductor and the absorbed molecule.

Bottom-up methodologies provide nanoparticles with tunable band-gaps and electronic properties. Consequently, the design of nanostructures and their incorporation in complex architectures allows better light harvesting, avoiding electron-hole recombination, thus affording more efficient materials for photocatalysis. In recent years, several examples of highly efficient nanocatalysts have been reported. Complete photoreduction of CO_2 to methane by H_2 has been recently reported using Ni supported on silica-alumina,[36] where the nickel NPs size is of utmost importance, thus when its size grows up, its photocatalytic activity dramatically decreases.

In the chapter 4 of this PhD Tesis, the synthesis of nanomaterials using different methodologies and their application in CO_2 reduction and production of solar H_2 will be disclosed showing how the control over the size and the composition of the NPs is of central importance for the photocatalytic results.

1.1.3.3 Photonics

Photonics is the science of light generation, detection and manipulation through emission, transmission, modulation, signal processing, switching, amplification, and detection/sensing.[37,38] This field has emerged, in the last 40 years, as a really important science thanks to new discoveries and developments of new materials that have applications in fast communications, aerospace, sensing, lighting, computing and medical areas.[39]

The main advantage that nanomaterials exhibit in contrast to classical photonic materials relies on the possibility to modulate their dimensionality and the anisotropy of their optical properties. Today a huge amount of optical materials shaped as quantum dots (0D), nanowires (1D), nanosheets (2D) and tridimensional materials (3D) can be easily prepared. Furthermore the chemical nature of the photonic crystals ranges from oxides, chalcogenides, halides, fluorides, metal nanoparticles, etc.

In photonics, luminescent lanthanide-doped nanomaterials have become very important in the last decades. Lanthanide elements (also known as rare earths) have 4f orbitals gradually filled, from $4f^0$ (La^{3+}) to $4f^{14}$ (Lu^{3+}). The word lanthanide has its origin from Greek word lanthano (λανθάνω) which means “lying hidden”. Despite being naturally abundant elements they were considered rare because its separation from the minerals is not an easy task.

One of the most important feature of lanthanides is their photoluminescence. Upon irradiation in the UV region, luminescence in the visible and near-infrared region is

observed depending of the lanthanide ion. For example, Eu^{3+} emits red light, Tb^{3+} green, Sm^{3+} orange, and Tm^{3+} blue light (Figure 1. 12). Other elements such as Yb^{3+}, Nd^{3+} or Er^{3+} show luminescence in the near-infrared region.

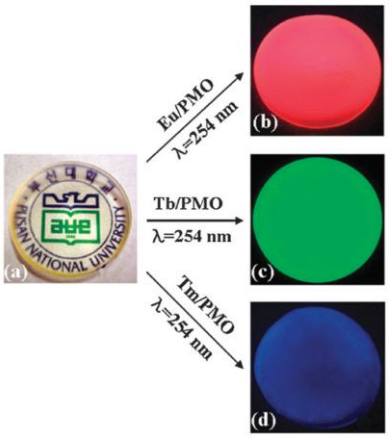

Figure 1. 12. Photographs of Eu^{3+}, Tb^{3+} and Tm^{3+} doped periodic mesoporous organosilica monoliths, a) day light illumination and b), c) and d) 245 nm.[40]

The emission comes from intraconfigurational *f-f* transitions. As these orbitals are well shielded from the environment by $5s^2$ and $5p^6$ orbitals, the ligands in the first and second coordination sphere don not perturb the electronic configuration of these elements. This fact leads to narrow band emissions and long lifetimes of the excited states, characteristic of the lanthanide elements.

Classically, luminescence of lanthanide ions is obtained through excitation using radiation with shorter wavelength than the emission generated. Nevertheless, it is also possible to obtain photoluminescence by exciting at longer wavelength (infrared or near infrared) than the emission, usually in the visible range. This process is called upconversion (UC) and it is a nonlinear optical process, in which two or more low energy photons are successively absorbed, and converted into one of higher energy (Figure 1. 13).

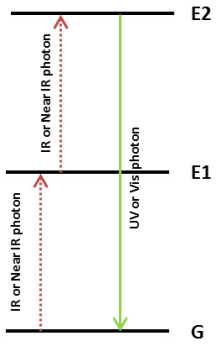

Figure 1. 13. Schematic representation of the UC process

This phenomenon is widely known for over 50 years[41] with high impact in the development of optical devices such as infrared quantum counter detectors, temperature sensors and compact solid state lasers that were developed in the past 30 years using bulk glass or crystalline materials.[42] In the last decade there is a growing interest in the UC materials as a consequence of the availability of low cost infrared laser diodes and the improvement of different synthetic approaches at the nanoscale level. They become interesting for new technologies such as photonics[43], photocatalysis[44,45] photovoltaics[46], sensors[47], biotechnology[48], etc. Regarding all these issues, in Chapter 5 of this PhD work, the synthesis of up-converting nanoparticles will be discussed as well as their introduction in different organic-inorganic hybrids. The structural and optical evaluation of the systems will be detailed.

1.2 Objectives

The general objective of this PhD Thesis is the study of new nanomaterials and hybrid nanocomposites using simple and low cost synthetic approaches based on Soft Chemistry routes, with improved activity in the field of catalysis, photocatalysis and photonics.

This general objective can be broken down to five more specific objectives that would together achieve the overall goal of the Thesis as follows:

- CATALYSIS #1: A study of the synthesis and characterization of ZrO_2 nanoparticles as nanocatalysts. The work includes the stabilization of the different crystalline phases as well as their chemical modification with WO_x species, and the evaluation of their catalytic activity in some interesting reactions.
- CATALYSIS #2: The synthesis of new nanomaterials for the selective hydrogenation of organic compounds with industrial interest.*
- PHOTOCATALYSIS #1: The development of new photocatalysts based on nanocrystalline Cu-doped TiO_2 materials. The main structural parameters including crystalline phase, size and morphology, distribution of cupper ions and superficial properties will be analyzed, and related with their photocatalytic activity in reactions with environmental implications such as CO_2 reduction and water treatment.
- PHOTOCATALYSIS #2: The preparation of upconverting Y_2O_3 NPs by an easy precipitation method and the evaluation of their photocatalytic properties in a photovoltaic device for hydrogen generation from water. The photovoltaic device will be sensitized with Y_2O_3 nanoparticles and quantum dots in order to absorb infrared radiation to enhance the photocatalytic efficiency.
- PHOTONICS #1: The development of two different hybrid nanocomposites prepared by sol-gel processes which both exhibit upconverting properties. The structural and optical features of these materials will be analyzed in detail and their potential application in photonics will be examined.

* The content of this chapter is classified as CONFIDENTIAL, thus its content will not be shown.

1.3 References

(1) *The Chemistry of Nanomaterials: Synthesis, Properties and Applications*; Rao, C. N. R., Müller, A., Cheetham, A. K., Eds.; WILEY-VCH: Weinheim, 2004.

(2) Bhushan, B. *Phil. Trans. R. Soc. A* **2009**, *367* (1893), 1445–1486.

(3) *Microwaves in Nanoparticle Synthesis Fundamentals and Applications*; Horikoshi, S., Serpone, N., Eds.; WILEY-VCH: Weinheim, 2013.

(4) Vollath, D. *Nanoparticles-Nanocomposites-Nanomaterials An introduction for beginners*; WILEY-VCH: Weinheim, 2013.

(5) Wilson, M.; Kannangara, K.; Smith, G.; Simmons, M.; Raguse, B. *NANOTECHNOLOGY Basic Science and Emerging Technologies*; CHAMPAN & HALL/CRC: New York, 2002.

(6) Ramsden, J. *Nanotechnology*; Ventus Publishing ApS, 2009.

(7) Sau, T. K.; Rogach, A. L. *Complex-Shaped Metal Nanoparticles: Bottom-Up Synthesis and Applications*; WILEY-VCH: Weinheim, 2012.

(8) Vollath, D. *Nanomaterials: An introduction to synthesis properties and applications*; WILEY-VCH: Weinheim, 2008.

(9) *Nanomaterials Inorganic and bioinorganic perspectives*; Lukerhart, C. M., Scott, R. A., Eds.; WILEY-VCH: Chichester (UK), 2008.

(10) Ko, M. *Nanotechnology*; 2007.

(11) Brinker, C. J.; Scherer, G. W. *Sol–Gel Science: The Physics and Chemistry of Sol–Gel Processing*; Academic Press: London, 1990.

(12) Znaidi, L. *Mater. Sci. Eng. B* **2010**, *174* (1–3), 18–30.

(13) Walton, R. I. *Chem. Soc. Rev.* **2002**, *31*, 230–238.

(14) Modeshia, D. R.; Walton, R. I. *Chem. Soc. Rev.* **2010**, *39* (11), 4303–4325.

(15) Rabenau, A. *Angew. Chemie Int. Ed. English* **1985**, *24*, 1026–1040.

(16) Park, J.; Joo, J.; Soon, G. K.; Jang, Y.; Hyeon, T. *Angew. Chemie - Int. Ed.* **2007**, *46* (25), 4630–4660.

(17) Sanchez, C.; Julián, B.; Belleville, P.; Popall, M. *J. Mater. Chem.* **2005**, *15* (35–36), 3559–3592.

(18) Sanchez, C.; Soler-Illia, G. J. de A. A.; Ribot, F.; Lalot, T.; Mayer, C. R.; Cabuil, V. *Chem. Mater.* **2001**, *13* (10), 3061–3083.

(19) Stark, W. J.; Stoessel, P. R.; Wohlleben, W.; Hafner, A. *Chem. Soc. Rev.* **2015**, *44*, 5793–5805.

(20) Anastas, P. T.; Warner, J. C. *Green Chemistry: Theory and Practice*; Oxford University Press: New York, 1998.

(21) Anastas, P.; Eghbali, N. *Chem. Soc. Rev.* **2010**, *39* (1), 301–312.

(22) Armor, J. N. *Catal. Today* **2011**, *163* (1), 3–9.

(23) Pollak, P. *Fine Chemicals The Industry and the Business*; WILEY-VCH: New Jersey, 2007; Vol. 1.

(24) Haruta, M. *CATTECH* **2002**, *6* (3), 102–115.

(25) Abad, A.; Concepción, P.; Corma, A.; García, H. *Angew. Chem. Int. Ed. Engl.* **2005**, *44* (26), 4066–4069.

(26) Corma, A.; Serna, P. *Science (80-.).* **2006**, *313*, 332–334.

(27) Laursen, S.; Combita, D.; Hungría, A. B.; Boronat, M.; Corma, A. *Angew. Chemie - Int. Ed.* **2012**, *51* (17), 4190–4193.

(28) Ohama, Y.; Van Gemert, D. *Application of Titanium Dioxide Photocatalysis to Construction Materials*; Springer, 2011.

(29) Linsebigler, A. L.; Lu, G.; Yates, J. T. *Chem. Rev.* **1995**, *95* (3), 735–758.

(30) Habisreutinger, S. N.; Schmidt-Mende, L.; Stolarczyk, J. K. *Angew. Chemie - Int. Ed.* **2013**, *52* (29), 7372–7408.

(31) Fujishima, A.; Honda, K. *Nature* **1972**, *238*, 37–38.

(32) Hernaández-Ramírez, A.; Medina-Ramírez, I. *Photocatalytic Semiconductors Synthesis, Characterization, and Environmental Applications*; Springer: London, 2015.

(33) Habisreutinger, S. N.; Schmidt-Mende, L.; Stolarczyk, J. K. *Angew. Chem. Int. Ed. Engl.* **2013**, *52* (29), 7372–7408.

(34) Tran, P. D.; Wong, L. H.; Barber, J.; Loo, J. S. C. *Energy Environ. Sci.* **2012**, *5* (3), 5902–5918.

(35) Pawar, R. C.; Lee, C. S. *Heterogeneous Nanocomposite-Photocatalysis for Water Purification*; Elsevier: Amsterdam, 2015.

(36) Sastre, F.; Puga, A. V; Liu, L.; Corma, A.; García, H. *J. Am. Chem. Soc.* **2014**, *136* (19), 6798–67801.

(37) Quimby, R. S. *Photonics and Lasers An Introduction*; WILEY-INTERSCIENCE: New Jersey, 2006.

(38) Yeh, C. *Applied Photonics*; Academic Press, Inc: San Diego, 1990.

(39) Escribano, P.; Julián-López, B.; Planelles-Aragó, J.; Cordoncillo, E.; Viana, B.; Sanchez, C. *J. Mater. Chem.* **2008**, *18* (1), 23–40.

(40) Park, S. S.; An, B.; Ha, C. S. *Microporous Mesoporous Mater.* **2008**, *111* (1–3), 367–378.

(41) Auzel, F. *Chem. Rev.* **2004**, *104* (1), 139–173.

(42) Wang, F.; Liu, X. *Chem. Soc. Rev.* **2009**, *38* (4), 976–989.

(43) Huang, X.; Han, S.; Huang, W.; Liu, X. *Chem. Soc. Rev.* **2013**, *42* (1), 173–201.

(44) Qin, W.; Zhang, D.; Zhao, D.; Wang, L.; Zheng, K. *Chem. Commun.* **2010**, *46* (13), 2304–2306.

(45) Wang, W.; Ding, M.; Lu, C.; Ni, Y.; Xu, Z. *Appl. Catal. B Environ.* **2014**, *144*, 379–

385.

(46) Zhang, M.; Lin, Y.; Mullen, T. J.; Lin, W.; Sun, L.; Yan, C.; Patten, T. E.; Wang, D.; Liu, G. *J. Phys. Chem. Lett.* **2012**, No. 3, 3188–3192.

(47) de Camargo, A. S. S.; Possatto, J. F.; Nunes, L. A. D. O.; Botero, É. R.; Andreeta, É. R. M.; Garcia, D.; Eiras, J. A. *Solid State Commun.* **2006**, *137* (1–2), 1–5.

(48) Wang, F.; Liu, X. *Chem. Soc. Rev.* **2009**, *38* (4), 976–989.

Chapter 2

ZrO_2-based nanoparticles as nanocatalysts: synthesis, characterization and evaluation of their catalytic properties

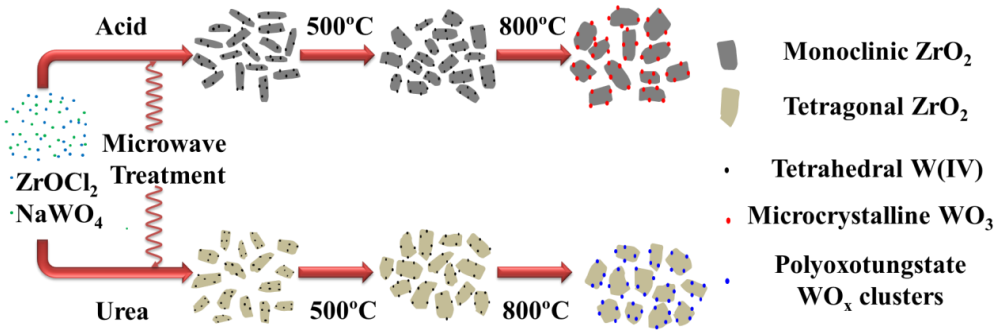

2.1 Introduction

A large number of acid-catalyzed industrial processes are requiring the substitution of the aggressive and ecologically harmful mineral acids by solid acid catalysts that are stable, regenerable and active at moderate temperatures. Zirconia based catalysts are promising candidates due to their thermal stability, structural versatility and surface properties.

The acid-base properties of zirconia depend on the crystalline phase. It is well known that ZrO_2 exhibits different polymorphs that can be obtained at different temperatures and pressures[1]. The thermodynamically most stable phase at room temperature is the monoclinic, but depending on the synthetic methodology or doping the material with different cations (Ce^{4+},[2] Ca^{2+},[34] La^{3+},[5] Y^{3+},[6] …), other metastable phases, like tetragonal and cubic ones can be isolated as single phases.

The acid-base properties of the ZrO_2 polymorphs are not well understood. It has been shown that the acid properties of zirconia can be enhanced by the addition of sulfate[7], Mo(VI)[8] or W(VI)[9] ions. Among them, the tungsten deposited zirconia is preferred because the sulfated zirconia undergoes partial deactivation due to sulfate loss during thermal treatment [10] and the molybdenum-doped zirconia is a less active catalyst. Since the first work of Hino and Arata[11,12] demonstrating the use of tungsten deposited on zirconia as a solid acid for isomerization of light alkanes, several reactions such as oxidative desulfurization,[13] alkylation of phenols,[14] o-xylene isomerization,[15] production of aromatics from alkylfurans,[16] 2-butanol dehydration,[17] among others, have been catalyzed by these materials.

Several synthetic pathways have been proposed to synthetize W/ZrO_2 materials, such as deposition of tungsten salts over hydrous zirconia,[11,18] anion exchange,[19,20] coprecipitation,[21,22] hydrothermal synthesis[23], sol-gel,[24] etc. In the three last methods mentioned, treatments at relatively high temperatures are required in order to activate the materials, probably because the tungsten is located inside the zirconia and it has to migrate to the surface in order to be catalytically active. Moreover, several authors have pointed out that the activity of the materials prepared impregnating tungsten salts over crystalline zirconia is much lower than the impregnated in the hydrous support.[12,25]

Microwave-assisted synthesis of solid materials presents several advantages compared to the previous synthetic pathways. Some of those advantages are: short reaction times (just few minutes to obtain crystalline materials), homogenous temperature inside the synthesis media, avoiding temperature gradient and

heterogeneities, and the possibility to control morphology and particle size by an accurate tuning of the synthetic conditions. Thus, microwave-assisted methodologies offer new opportunities to develop low cost and easy-to-prepare heterogeneous catalysts such as ZrO_2 or W-doped ZrO_2 that can be of interest for different reactions. Here we have used these materials in three catalytic reaction of industrial interest: aldoxime dehydratation, alkyne hydration and Meerwein-Pondorf-Verley reduction.

Nitriles are a family of organic compounds which are used as intermediates for the production of pharmaceuticals, agricultural chemicals dyes and materials.[26,27] Several synthetic pathways have been reported to obtain these compounds[27] but the most efficient is the catalytic dehydration of aldoximes. This reaction has been classically catalyzed by homogeneous catalysts[28–30] including H_2SO_4 among them[31,32]. However the use of a heterogeneous catalyst is desirable. In this sense, some heterogeneous catalysts have been reported[33] but they are too expensive (Ru)[34] or toxic (Sn)[35] elements.

Alkyne hydration is known since 1860[36] and is an important reaction from the industrial point of view to produce carbonyl compounds. Traditionally, this reaction has been carried out in the presence of Brønsted or Lewis acids as catalysts. Among them, Hg[37,38] salts are the most efficient but they are highly toxic. Other metals such as Au[39], Ru[40] or Fe[41] also present high efficiency, but it is difficult or very tedious to recycle them. In the last years, some reports on the use of alternative heterogeneous catalysts for alkyne hydration have been presented, but their usefulness is limited due to the necessity of using homogeneous cocatalysts[42,43] or expensive precious metals (Au[43] or Ag[44]) and toxic elements (Sn[45]).

The reduction of an aldehyde or a ketone via hydrogen transfer from an alcohol is called Merwein-Pondorf-Verley (MPV) and it is of particular interest because it is a very selective reaction, in which other reducible groups such as double bonds and carbon-halogen bond are not reduced.[46] This reaction is known since 1925[47–49] and it has been classically catalyzed in homogeneous phase by aluminum or zirconium alkoxides requiring an excess of the alkoxide between 100 and 200%.[50] The use of a homogeneous non-recoverable catalyst with a high excess have been overcome in the last years by the use of heterogeneous recyclable catalysts. In this sense, several solid catalysts have been successfully employed in this reaction such as, MgO[51], ZrO_2[50], grafted alkoxides[52] and mesoporous materials[53,54], etc.

Sn[53,54] and Zr-beta[55,56] shows very good activity in the MPV reduction as a consequence of its high Lewis acidity. The main drawback or these materials is the use of expensive organic synthetic directing agents, and the use of fluorinated media

for their synthesis. One of the most effective materials in MPV reduction is zirconium oxide, which presents amphoteric character, high thermal and chemical stability and low costs synthetic pathways[57]. Several works have tested ZrO_2[50,52], and promoted modified zirconias[58–60] in MPV reduction with different substrates.

In this thesis chapter a fast and environmentally friendly microwave-assisted synthesis of ZrO_2 and WO_x-ZrO_2 nanoparticles is presented. The crystal phase of zirconia and the distribution of W species will be tuned through an accurate control of the synthetic conditions. These materials are tested in the aldoxime dehydration and alkyne hydration, and their catalytic activity and reaction mechanisms have been discussed in terms of the zirconia crystal phase and the nature of the W species present in the final materials. In addition, their activity in the MPV reduction is studied. In this case the combination of the experimental catalytic results with quantum chemical calculations, provide new insights in the MPV reduction reaction mechanism over oxides.

2.2 Results and discussion

2.2.1 Synthesis and characterization

2.2.1.1 Microwave assisted ZrO_2 and WO_x-ZrO_2 materials

For this study, pure ZrO_2 and W-Zr mixed oxide (with 5 and 10% W molar percentage to Zr ions) were prepared. The materials were synthesized through microwave synthetic route. Since the pH of the medium has a great influence on the stability of the zirconium species, two synthetic pathways were used:

- In the first synthetic route (or acid route) the proper amount of $ZrOCl_2 \cdot 8H_2O$ and $Na_2WO_4 \cdot 2H_2O$ were dissolved in miliQ water. The solution was treated under microwave radiation increasing the temperature at 20^oC/min until 220^oC for 10 minutes (See Experimental Section for further details). The precipitated products were washed, centrifuged and dialyzed until no chlorides were detected. Finally, the suspension was dried under air flow and further annealed at 500 and 800^OC for 2 hours in a muffle furnace. These samples were denoted as ZA-x for the pure zirconia and y-WZA-x for the tungsten-doped samples in acid media (A), where x denotes the annealing temperature of the sample and y the molar percentage of tungsten.

- The second synthetic route (or basic route) is similar to the previously described acid synthesis with the only difference that urea was added to the initial zirconium and tungsten aqueous solution. The samples obtained in this basic medium were denoted as ZU-x for the pure zirconia and y-WZU-x for the tungsten-doped samples in basic medium, where x denotes the annealing temperature and y the molar percentage of tungsten.

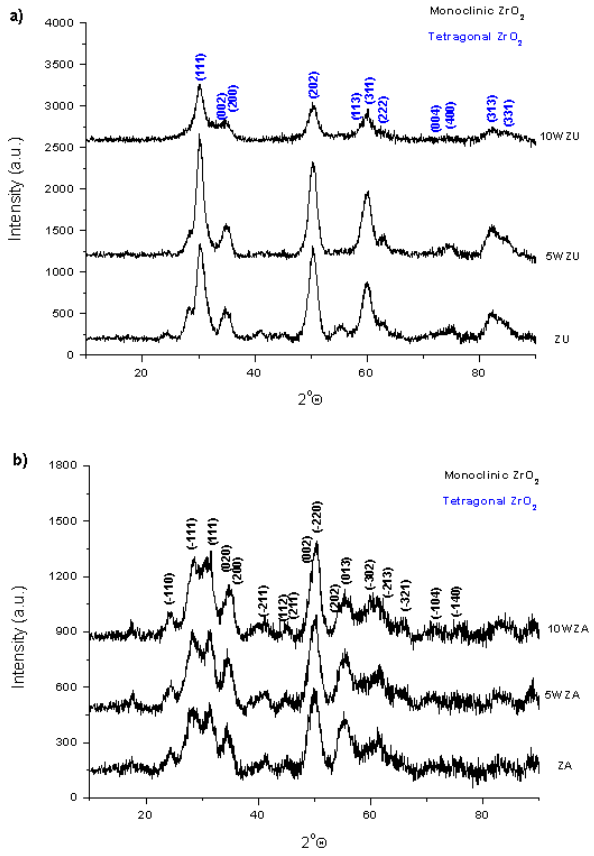

Figure 2. 1. XRD patterns of as-synthetized zirconia prepared by a) the urea and b) acid syntheses.

The evolution of the crystalline phase of ZrO_2 NPs with the synthesis conditions (acid/basic media) and the content of W have been firstly studied. As shown in Figure 2. 1. For the as-synthesized sampled, the non-doped zirconia obtained under acid conditions exhibit the monoclinic phase (JCPDS card no. 37-1484) (ZA) while the sample synthesized with urea is mostly (89%) in the tetragonal phase (JCPDS card

no. 17-0923) (ZU). Upon the addition of 5 to 10% molar tungsten (5ZWU and 10WZU) in the urea synthesis the tetragonal phase is stabilized (95% tetragonal phase in 5%W and 100% at 10%W loading) while in the acid conditions (5ZA and 10WZA for 5 and 10% W) the monoclinic phase is preserved for the entire W contents (Figure 2. 1).

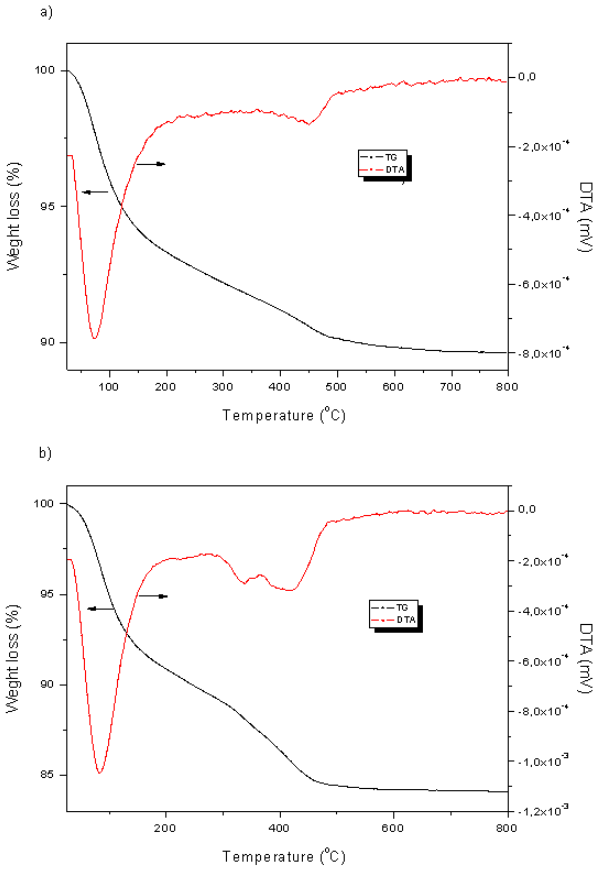

Figure 2. 2. TG (in black) and DTA (in red) curves of (a) 10WZA and (b) 10WZU samples.

The thermal stability of these materials was studied by differential thermal analysis (DTA) and thermogravimetry (TG) techniques (Figure 2. 2). In the 10WZA sample, a mass loss of around 7% below 250ºC associated to the removal of water molecules adsorbed at the surface is detected, and another mass loss of around 3% weight at around 450ºC occurs, which is probably due to the loss of structural hydroxyl species. 10WZU sample shows larger weight loses, around 10% weight for the first process, and 5% loss in the second process.

FT-IR spectra of pure materials activated at 220°C under vacuum were performed in order to confirm the presence of structural hydroxyl. As Figure 2. 3 shows, vibrational bands corresponding to structural hydroxyls appear at ca. 3550 and 3700 cm^{-1} and decrease their intensity upon heating until complete removal at 800°C.

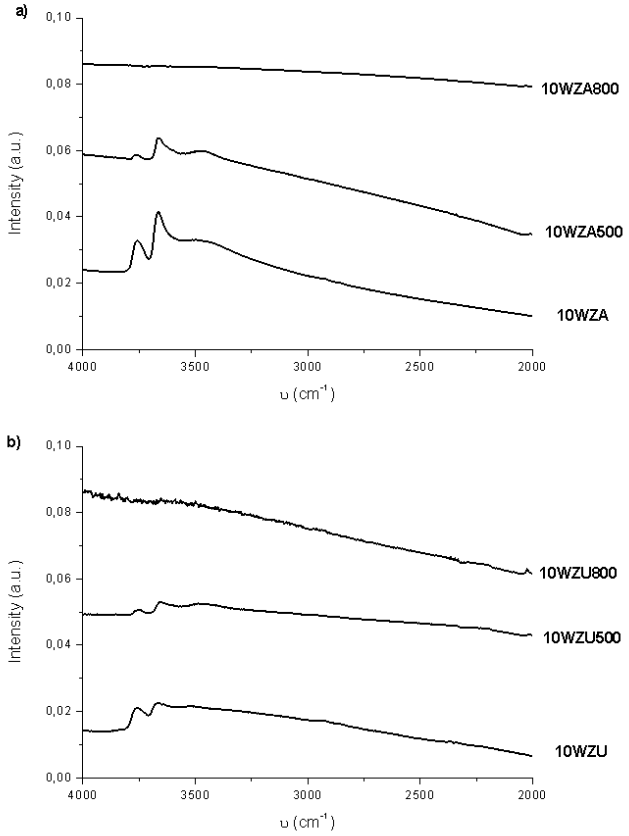

Figure 2. 3. FT-IR spectra of a) 10WZA, 10WZA500, 10WZA800 and b) 10WZU, 10WZU500 and 10WZU800.

The phase evolution with the annealing temperature was studied by XRD. In the case of the materials obtained by the acid procedure, the tungsten free and 5% W doped samples present, in all range of calcination temperatures, the monoclinic as the main phase, with sharper and narrower peaks when the sample was treated at higher temperatures (Figure 2. 4 a and b). No peaks associated to WO_3 were observed,

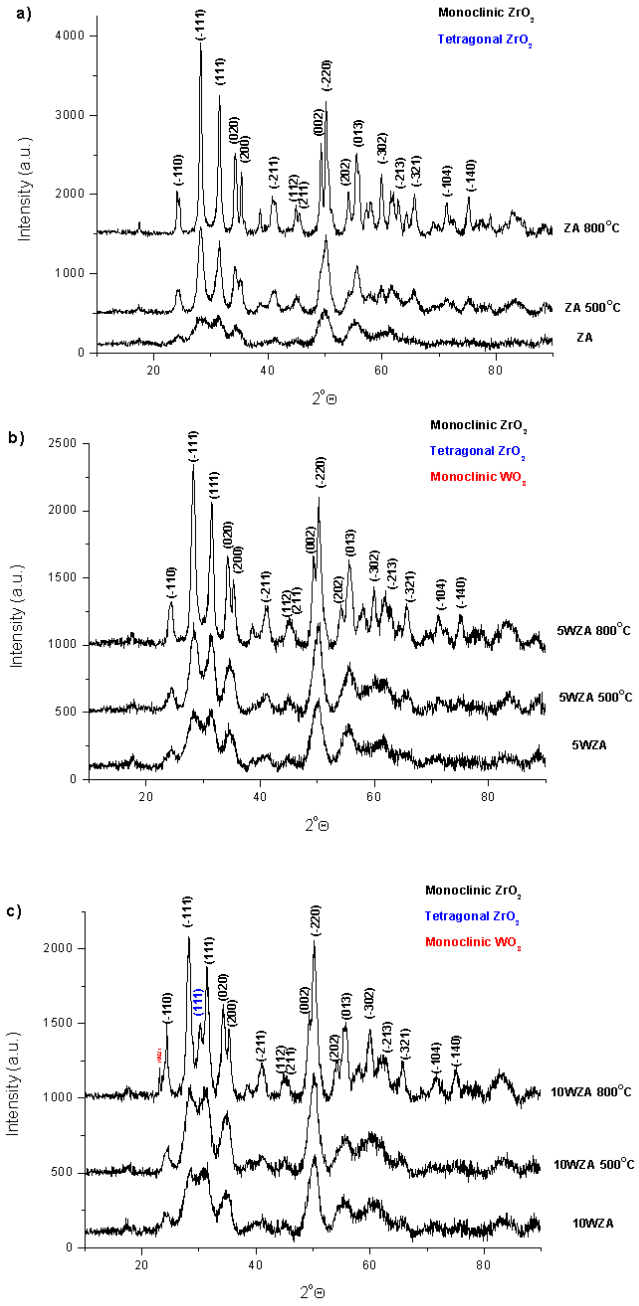

Figure 2. 4. XRD of a) ZA, b) 5WZA and c) 10WZA as prepared and annealed at 500ºC and 800ºC.

suggesting that the tungsten is highly dispersed and/or incorporated into the ZrO_2 matrix. For 10%W molar sample (Figure 2. 4c), the monoclinic phase remains as the main phase until 500ºC, but at 800ºC peaks associated to crystalline WO_3 and tetragonal ZrO_2 phase (around 13%, see Table 2. 1) appear together with m-ZrO_2 peaks.

Table 2. 1. Percentage of tetragonal phase, crystal size calculated by the Scherrer equation, BET surface areas and W/Zr atomic ratio determined by ICP-AES of materials obtained by acid synthesis.

Sample	% Tetragonal	Crystal Size (nm)	S_{BET} (m^2/g)	W/Zr
ZA	0	2.5	210.0	-
ZA 500ºC	0	8.1	64.7	-
ZA 800ºC	0	17.8	22.0	-
5WZA	0	3.2	213.2	0.047
5WZA500ºC	0	5.0	109.2	0.047
5WZA800ºC	0	10.5	50.5	0.046
10WZA	0	3.5	221.5	0.102
10WZA500ºC	0	4.4	137.2	0.102
10WZA800ºC	13.4	9.8	56.5	0.098

In Table 2. 1, the percentage of the tetragonal phase, the crystal size calculated by the Scherrer equation, BET surface area of the materials prepared under acidic conditions and W/Zr atomic ratio determined by inductively coupled plasma atomic emission spectroscopy (ICP-AES) are compiled (see Experimental Section for further details). Concerning BET surface area, the non-annealed materials present similar surface area values (around 220 m^2/g) but this area is better preserved at higher temperatures when higher is the W content in the material. If we observe the crystal size of the materials reported, the higher the W content the smaller the crystal size is and as consequence the larger is the surface area. This fact can be explained due to the presence of WO_x which inhibits the surface mobility of zirconia, avoiding in this way the sintering process and keeping high surface area values[9] of the final material, or to the stabilizing effect of W which substitute OH and the defects in the material.[19] Regarding the molar W/Zr ratio determined by ICP-AES, the nominal value determined by this technique is quite near to the theoretical value introduced in the synthesis, supporting the idea that all tungsten and zirconium is precipitated during

the microwave assisted synthesis. In addition, this molar ratio is constant upon heating indicating that tungsten is not lost during the calcination step.

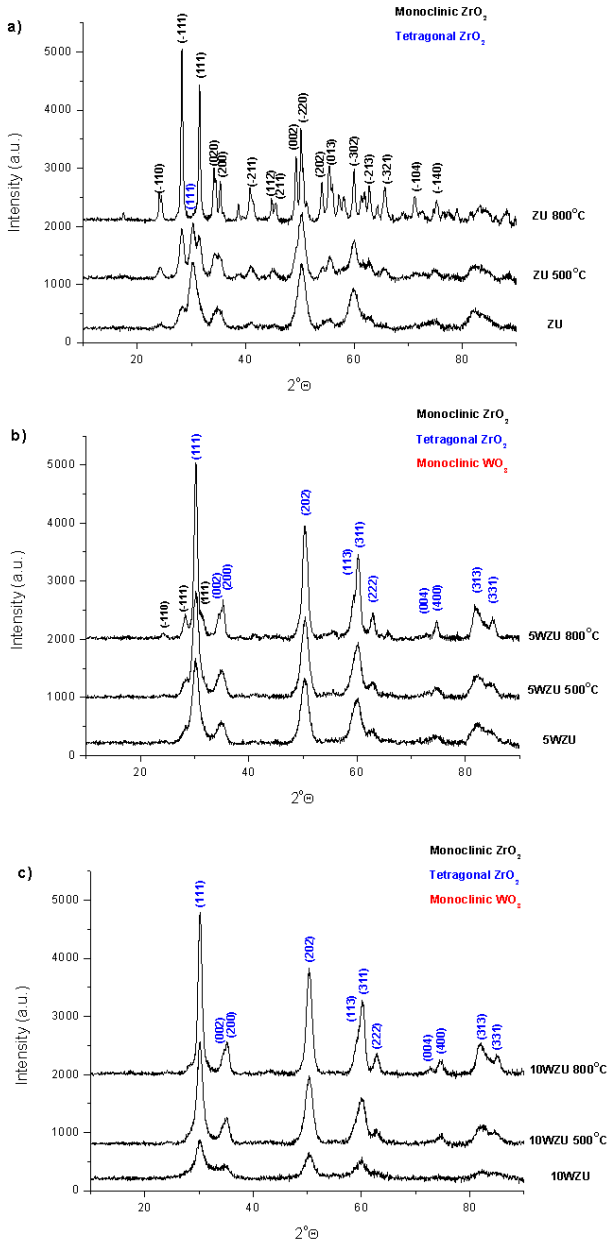

Figure 2. 5. XRD of a) ZU, b) 5WZU and c) 10WZU as prepared and annealed at 500ºC and 800ºC.

The thermal evolution of the materials synthetized under basic conditions is quite different. The as-synthetized non-doped sample mostly occurs in tetragonal phase (89 %). However when this material is annealed, the monoclinic phase becomes the most important one. So, at 500ºC there is 36% of tetragonal phase while at 800ºC the material is completely monoclinic (Figure 2. 5 and Table 2. 2). A significant stabilization of the tetragonal phase is observed in the materials after doping with W species. Thus, the percentages of tetragonal phase in 5WZU are 99.9, 96.3 and 84.5% for the as-synthesized and annealed at 500ºC and 800ºC samples respectively. The materials doped with 10% W molar present pure tetragonal phase at all temperatures (Figure 2. 5 and Table 2. 2).

As in the acid synthesis, the addition of W in the sample decreases the crystal size, and the BET surface area increases (Table 2. 2). Atomic W/Zr molar ratio agrees well with the theoretical value and is kept upon heating as the same way as in the materials obtained by the acid protocol.

Table 2. 2. Percentage of tetragonal phase, crystal size calculated by Scherrer equation, BET surface areas and W/Zr atomic ratio determined by ICP-AES of materials obtained by urea synthesis.

Sample	% Tetragonal	Crystal Size (nm)	S_{BET} (m^2/g)	W/Zr
ZU	88.5	4.9	136.6	-
ZU 500ºC	35.9	8.2	53.3	-
ZU 800ºC	0.0	22.7	7.6	-
5WZU	99.9	5.3	172.3	0.047
5WZU 500ºC	96.3	8.8	106.9	0.048
5WZU 800ºC	84.5	12.5	44.0	0.048
10WZU	99.9	3.8	297.9	0.096
10WZU500ºC	99.9	6.5	139.5	0.100
10WZU800ºC	99.9	10.4	67.4	0.099

Regarding the type of N_2 physisorption isotherms, these materials show type IV isotherm with a hysteresis loop, associated with capillary condensation in mesopores (Figure 2. 6).

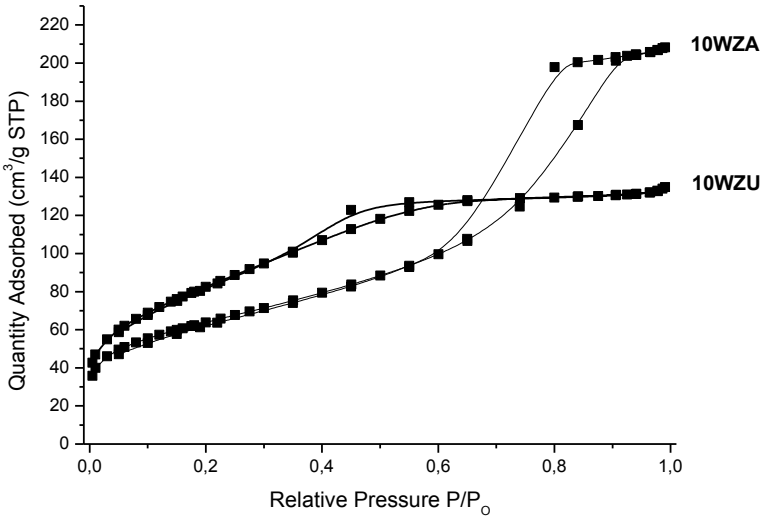

Figure 2. 6. N_2 adsorption-desorption isotherms of 10WZA and 10WZU.

XRD provided information about the crystalline phase of zirconia but nothing is said about tungsten species. Thus, the samples were characterized by Raman spectroscopy since this spectroscopy technique is a powerful tool to elucidate the nature of the W species.

The Raman spectra of ZA and ZU calcined at different temperatures are given in Figure 2. 7. The spectra of ZA shows the typical bands corresponding to monoclinic ZrO_2 (637 (s), 618 (s), 558, 537 (w),504, 477 (s), 381, 343, 335, 305, 221 (w), 187 (s), and 177)[61] at all temperatures. The spectra of ZU exhibit the typical bands from tetragonal ZrO_2 (639 (s), 604 (sh), 462 (s), 313 (s), 271 (s), and 149 (s) cm^{-1})[61] but when temperature increases the bands associated to the monoclinic phase appear, in good agreement with the XRD analysis.

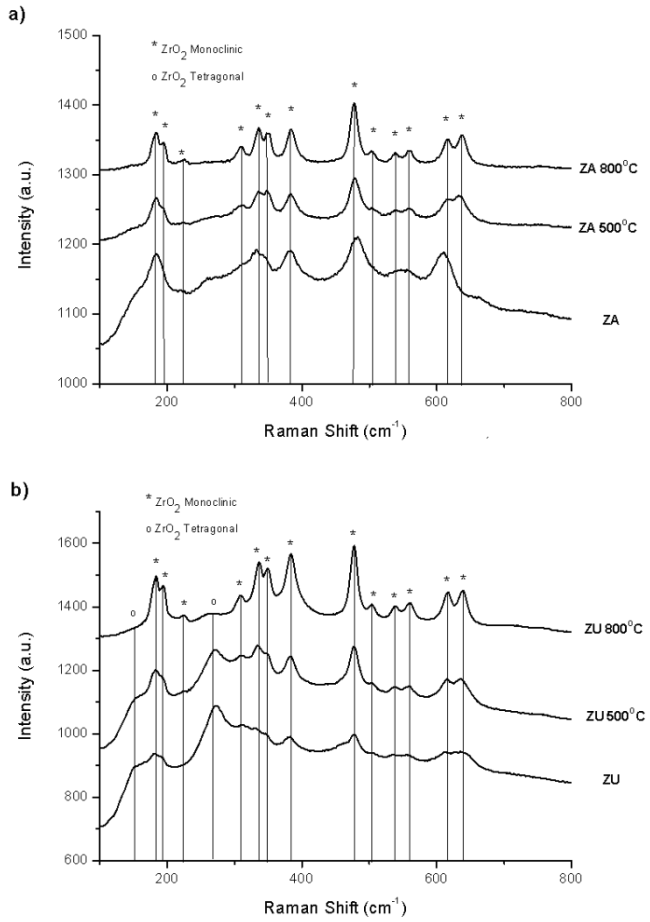

Figure 2. 7. Raman spectra of a) ZA as prepared, calcined at 500 and 800ºC and b) ZU as prepared calcined at 500 and 800ºC.

In the W-doped samples, the zirconia bands follow the tendency observed in the XRD analysis. Interestingly, in the range where usually appear the bands associated to W species (from 700 to 1100 cm^{-1}), significant differences are found.

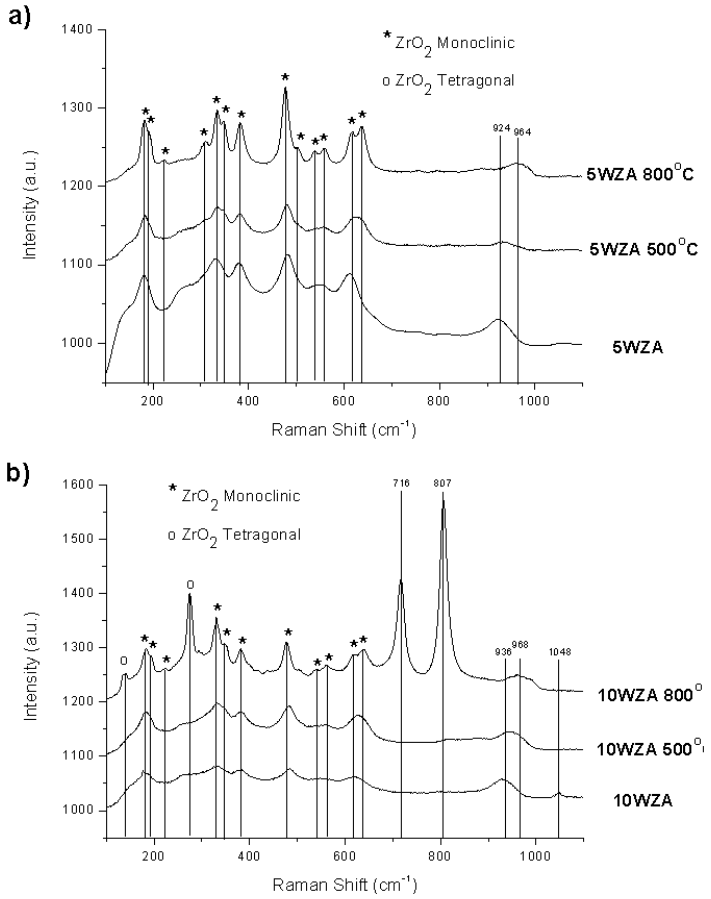

Figure 2. 8. Raman spectra of a) 5WZA and b) 10WZA as-prepared and annealed at 500ºC and 800ºC.

Concerning the samples prepared under acidic conditions, the spectra for the W-doped samples (Figure 2. 8) show a band around 930 cm^{-1} attributed to the A_1 mode (ν_1 symmetric stretching vibration) of tetrahedral W(VI) cations[19,23], which shifts towards larger wavenumbers (945 cm^{-1}) when the material is annealed at 500ºC, probably due to the lowering of the symmetry resulting from the aggregation of the tungsten species[23]. At 800ºC, different bands depending on the W content are detected. In this way, both samples (5WZA and 10WZA) present a band around 965 cm^{-1} corresponding to W=O stretching modes, while 10WZA exhibits two intense

bands at 716 and 807 cm^{-1} associated to W-O-W and W=O stretching modes of microcrystalline WO_3 species.[13,16]

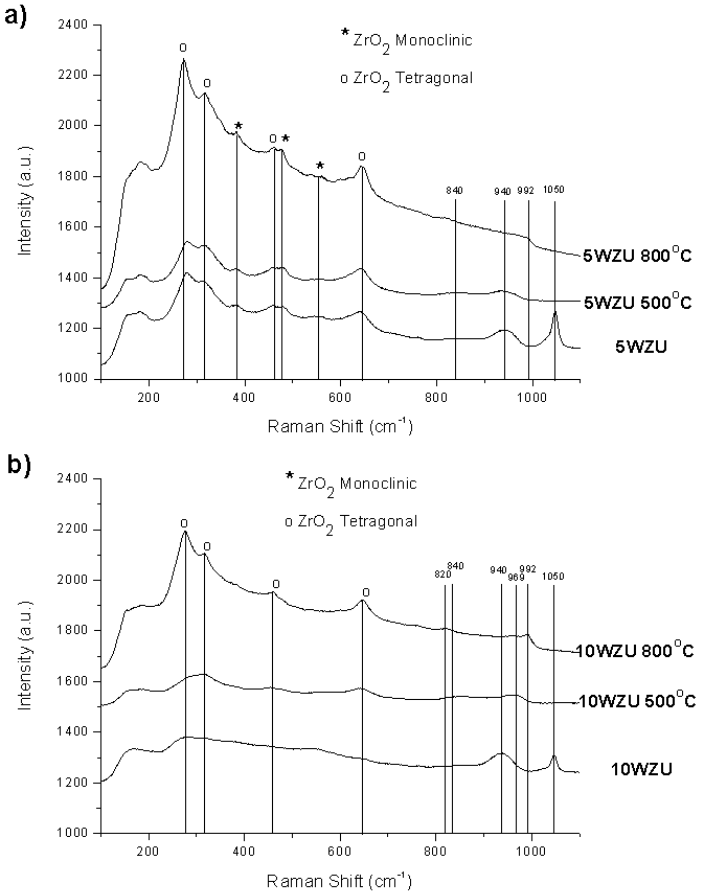

Figure 2. 9. Raman spectra of a) 5WZU and b) 10WZU as prepared and, calcined at 500 and 800ºC.

In basic conditions (Figure 2. 9), the as-prepared materials show the previous band at 940 cm^{-1} and a new one at 840 cm^{-1} which corresponds to the A_1 and F_2 (ν_3 antisymmetric stretching vibration) of tetrahedral W(VI) cations, respectively. In these samples, we also find at 1050 cm^{-1} a band attributed to carbonates neutralizing the basic sites unoccupied by tungstates for low W contents[19]. At 500ºC, the band at 1050 cm^{-1} disappears, while the others remain almost constant. At 800ºC, two bands located at 820 and 992 cm^{-1} assigned to W-O-W and W=O stretching modes of hydrated interconnecting polyoxotungstate clusters are visible. From the data reported above we can conclude that tungsten is better dispersed on the tetragonal phase

compared to the monoclinic when the materials are treated at high temperature. This behavior is quite different from Mo species supported on different zirconia polymorphs in which a better dispersion of Mo species is obtained on the monoclinic phase, mainly due to the presence of 2D polymolibdate species. Meanwhile in the tetragonal phase, crystalline MoO_3 is observed. This fact also affects the catalytic activity in which the higher catalytic rates, in front of methanol oxidation, are observed for the higher dispersed sample.[61]

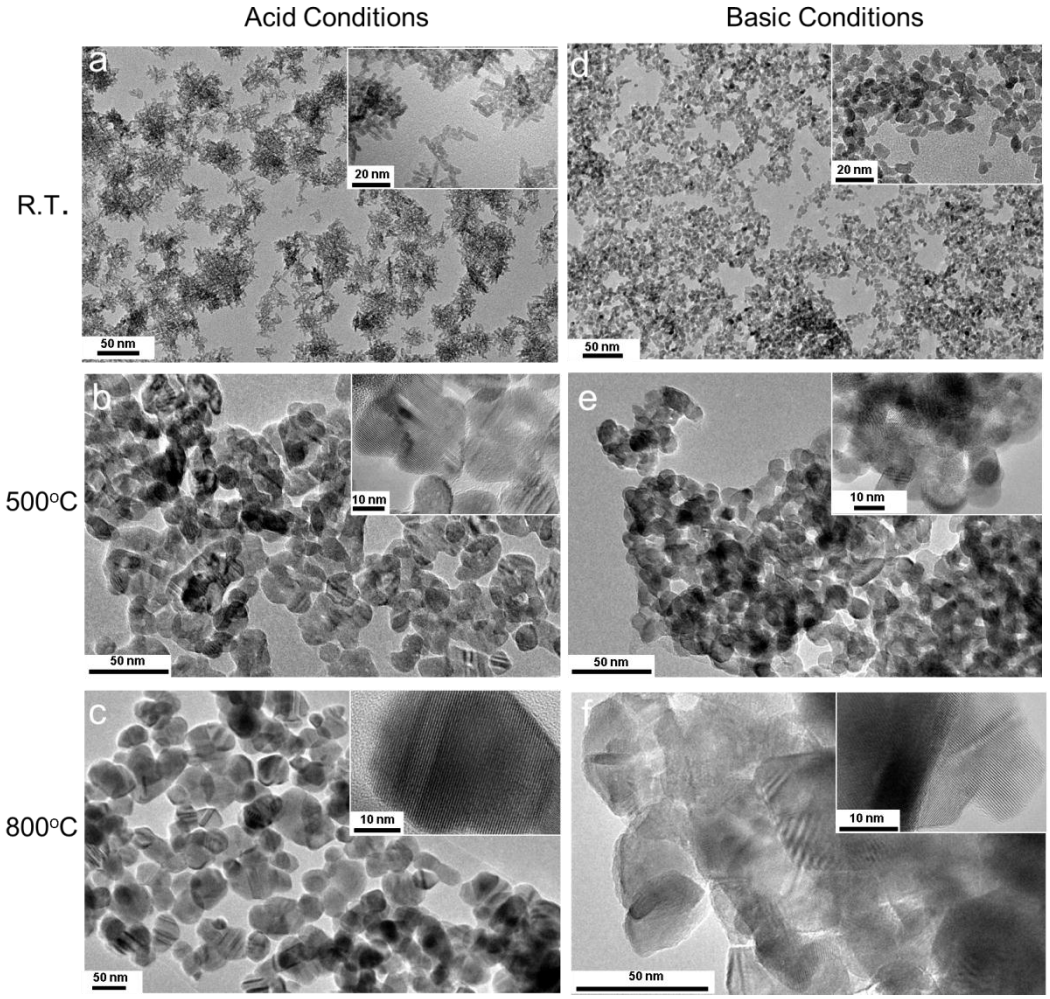

Figure 2. 10. HRTEM micrographs of ZA a) as prepared, b) annealed at 500°C, c) 800°C and ZU d) as prepared, e) annealed at 500°C, f) 800°C.

The morphology of the different samples was studied by transmission electron microscopy (TEM). Figure 2. 10 shows the images for pure zirconia samples. Under

acid conditions, ZA sample, rod-like crystals (10 x 3 nm) agglomerated into 40 nm particles are formed, meanwhile well dispersed 5 nm nanoparticles are found in the ZU sample. Upon heating, the materials grow providing nanoparticles with crystals sizes near from the calculated by the Scherrer equation (Figure 2. 10).

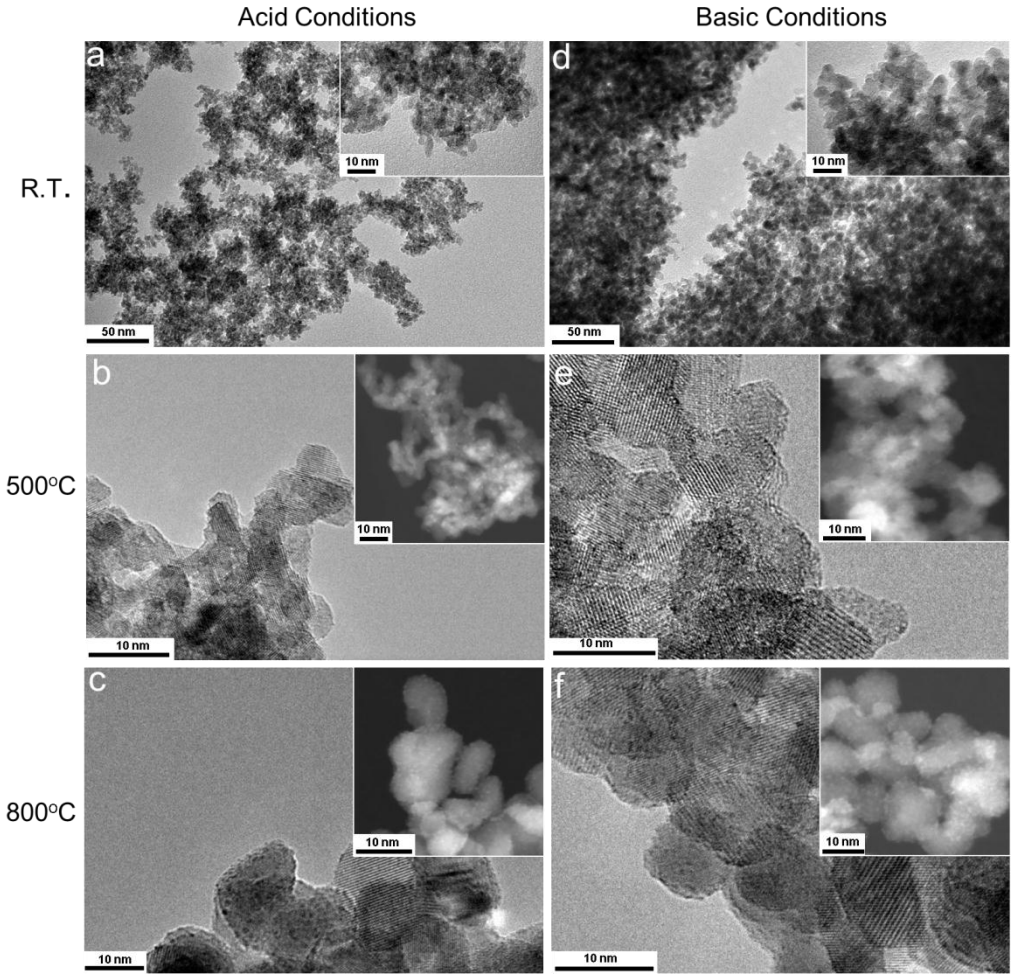

Figure 2. 11. HRTEM micrographs of 10WZA a) as-prepared, b) annealed at 500ºC, c) 800ºC and 10WZU d) as prepared, e) annealed at 500°C and f) 800°C. Insets show HAADF-STEM micrographs of the corresponding material.

The addition of W in the system induces morphological changes. In acid conditions, small "quasi-spherical" particles of 4 nm instead of rods are detected; these particles agglomerate into larger aggregates than in the case of non-doped samples (Figure 2. 11a). Under basic conditions, larger (6 nm) and more agglomerated particles are

obtained (Figure 2. 11 d). Thus, the presence of W species in the synthesis affects the nucleation and growth mechanisms during the microwave process, in both synthetic approaches (acid and basic).

With the thermal treatment, surface tungsten species become visible in HRTEM (High Resolution Electron Microscopy) in form of dark spots and in HAADF-STEM (High-Angle Annular Dark Field Scanning Electron Microscopy) in form of bright spots. Indeed, 10WZA sample exhibits small spots at the surface of the 5 nm zirconia particles after annealing at 500ºC (Figure 2. 11b). The phenomenon is more visible after annealing at 800ºC (Figure 2. 11c). These spots of less than 1 nm correspond to the crystalline WO_3[62] species detected by XRD and Raman spectroscopy for 10WZA annealed at 800°C.

In 10WZU sample calcined at 500°C (Figure 2. 11e), the small spots are also visible but, as discussed with Raman data, they are attributed to W(VI) species in tetrahedral coordination. At 800ºC, the images show very small nanoparticles (few angstroms) that can be associated to polyoxotungstate clusters,[21,63,64] in agreement with Raman analysis.

The surface composition and tungsten oxidation state were studied by X-ray photoelectron spectroscopy. Figure 2. 12 shows the XPS spectra of 10WZA and 10WZU as prepared and calcined at 500 and 800ºC. The peaks corresponding to tungsten appears a bit overlapped with Zr(4p) orbitals (ca. 30.5 eV), moreover two doublets in the tungsten region are observed which can be assigned to W^{5+} (Binding Energies (BE) ca. 34.8 eV) and W^{6+} (BE ca. 35.6 eV).[21] The W^{6+}/W^{5+} ratio increases from 1, for as prepared samples, up to 6-7 for samples annealed at 800ºC (Table 2. 3). In the as prepared samples a strong interaction of tungsten atoms with zirconia matrix (forming Zr-O-W bonds) leads higher amount of W^{5+}.[21] Increasing calcination temperature tungsten-zirconia interaction decreases increasing the amount of oxidized state. The high W/Zr ratio (Table 2. 3) for non-annealed samples is caused by the high tungsten dispersion and small particle size. Increasing the calcination temperature to 500ºC this ratio decreases which means that tungsten dispersion decreases forming patches in tetrahedral coordination and doing zirconium more accessible to this technique. Finally the W/Zr ratio at 800ºC is the highest because of the growth of NPs to 10 nm making some zirconium atoms not detectable (analysis depth 6.5nm), in agreement with previous works.[65]

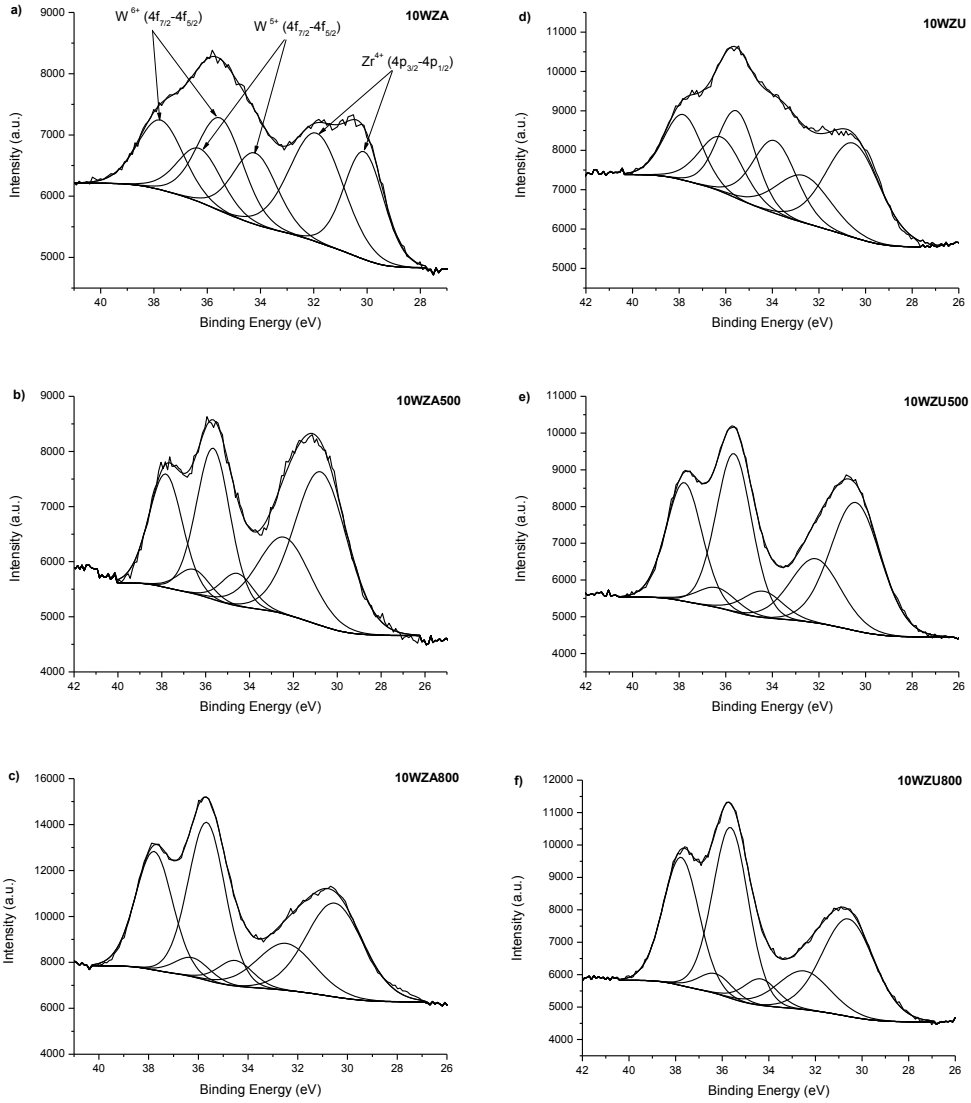

Figure 2. 12. XPS spectra of a) 10WZA, b) 10WZA500, c) 10WZA800, d) 10WZU, e) 10WZU500 and f) 10WZU800.

Table 2. 3. XPS parameters of W (4f) region in 10WZA and 10WZU as prepared and calcined at 500 and 800°C.

Sample	W/Zr	W^{6+}/W^{5+}
10WZA	0.151	1.3
10WZA500	0.098	4.9
10WZA800	0.161	6.6
10WZU	0.174	1.0
10WZU500	0.115	5.4
10WZU800	0.184	6.8

The type of acid sites, their strength and density were evaluated by adsorption of pyridine and desorption at different temperatures (Figure 2. 13 and Table 2. 4). The materials calcined at 500°C show only Lewis acidity with comparable density and

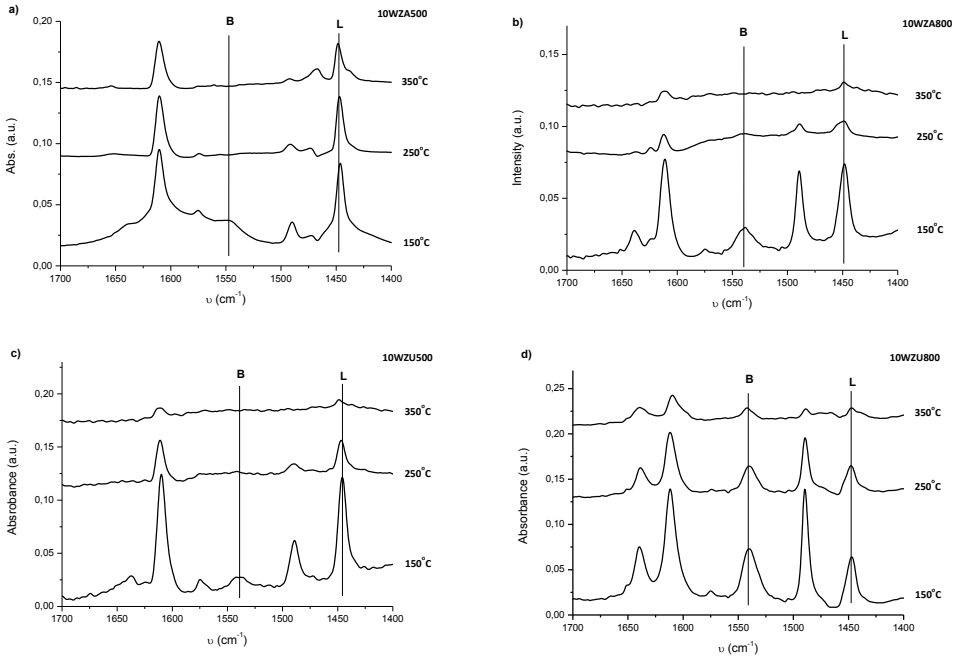

Figure 2. 13. FT-IR spectra in the region of adsorbed pyridine evacuated at 150, 250 and 350°C of a) 10WZA500, b) 10WZA800, c) 10WZU500 and d) 10WZU800. The vibrational bands marked as B and L can be associated to Brønsted and Lewis acid sites.

strength, which can be assigned to tungsten in tetrahedral coordination. For samples annealed at 800°C the number of Lewis acid sites is the same at the lower desorption

temperature, while the strength is higher for 10WZU800. On the other side, both materials present Brønsted acidity but the density and strength is higher for 10WZU800, the difference in acidity may rely on the different tungsten species discussed above.

Table 2. 4. Acidity of 10WZA500, 10WZA800, 10WZU500 and 10WZU800 determined by adsorption of pyridine.

Sample	Brønsted sites			Lewis Sites		
	150°C	**250°C**	**350°C**	**150°C**	**250°C**	**350°C**
10WZA500	0.006	0.000	0.000	0.064	0.048	0.026
10WZA800	0.015	0.002	0.000	0.052	0.009	0.000
10WZU500	0.008	0.002	0.000	0.090	0.029	0.007
10WZU800	0.055	0.053	0.029	0.054	0.030	0.030

2.2.1.2 Reference materials

Different reference materials from literature were also synthetized in order to compare their structural and catalytic properties with our materials. Amorphous (A) pure monoclinic (M) and tetragonal (T) pure zirconia and their tungsten impregnated counterparts (10WZDep, 10WZM and 10WZT respectively) were synthesized following procedures reported in the literature (see Experimental Section (Chapter 6) for further details). 10WZDis was prepared by coprecipitation of a tungsten and zirconium salts and further annealed at 500 and 800°C. Finally Sn-W (in a molar ratio 2Sn:1W) was prepared following the procedure described by Mizuno e. al[35,45,66] in order to compare their catalytic activity with the microwave-based materials.

Figure 2. 14a shows the XRD patterns of the amorphous and pure *m* and *t*-ZrO_2 polymorphs obtained by coprecipitation, hydrothermal and solvothermal methodology, respectively. 10%wt tungsten deposited on the pure crystalline polymorphs and calcined at 800°C are also shown, keeping in both cases the original phase and not showing any peak corresponding to crystalline WO_3.

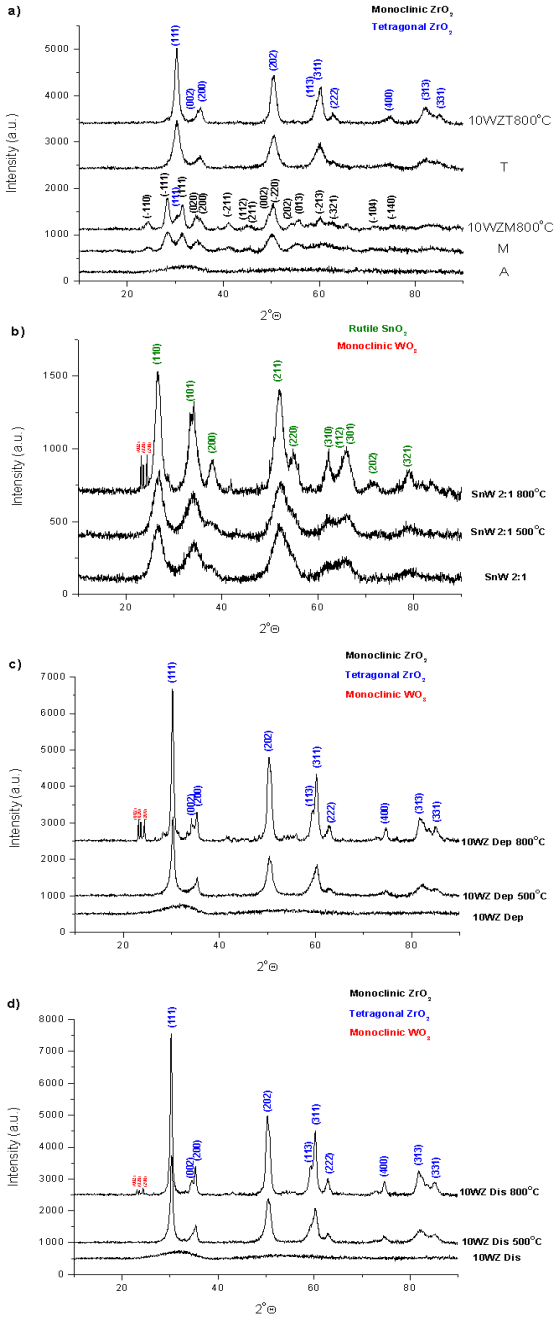

Figure 2. 14. XRD of a) amorphous and pure monoclinic and tetragonal zirconia and tungsten deposited over these pure polymorphs and calcined at 800°C b) SnW 2:1, c) 10WZ Dep and d) 10WZ Dis as prepared and annealed at different temperatures..

Table 2. 5. Percentage of the tetragonal phase, crystal size calculated by the Scherrer equation and the BET surface areas of reference materials.

Sample	% Tetragonal	Crystal Size (nm)	S_{BET} (m^2/g)
A	-	-	297.0
M	0.0	5.0	152.1
10WZM	3.1	9.8	47.1
T	99.9	5.3	120.7
10WZT	99.9	9.9	42.7
SnW 2:1	-	3.8	172.7
SnW 2:1 500ºC	-	4.1	142.8
SnW 2:1 800ºC	-	5.7	83.8
10 WZ Dep	Amorphous	-	273.6
10 WZ Dep 500ºC	99.9	10.6	139.9
10 WZ Dep 800ºC	95.4	16.8	57.8
10 WZ Dis	Amorphous	-	263.7
10 WZ Dis 500ºC	99.9	13.3	98.5
10 WZ Dis 800ºC	99.9	19.2	48.6

For SnW 2:1, XRD (Figure 2. 14b) shows pure rutile structure (casiterite, SnO_2). Therefore, the W remains amorphous as highly dispersed or incorporated into the SnO_2 matrix as solid solution, in good agreement with Mizuno et al.[67] Similarly to our samples, at 800ºC, XRD peaks of microcrystalline WO_3 appear in the pattern. For the other reference samples (coprecipitate and impregnation methods), the as-prepared samples are amorphous (Figure 2. 14b and c). After annealing, the main zirconia phase is the tetragonal in both cases. Again, at 800ºC, microcrystalline WO_3 is detected.

Other parameters such as crystal size calculated by Scherrer equation, percentage of tetragonal phase and BET surface area are compiled in Table 2. 5. The values are not far from our materials, what is of importance for comparing the catalytic activities.

As conclusions from the microwave-assisted synthesis work presented here we can say that zirconia crystalline phase can be tuned from monoclinic to tetragonal by changing the pH conditions (acid to basic, respectively). Also, the higher W doping level induces a phase transformation towards the tetragonal phase (Scheme 2. 1). The annealing temperature favors the monoclinic stabilization. The morphology can be changed from rod-like to more spherical, and from aggregated to more disperse systems by changing the pH of the synthesis from acid to basic conditions. Also, different W species have been detected by HRTEM and identified by Raman spectroscopy and those depend on the thermal treatment and synthesis conditions.

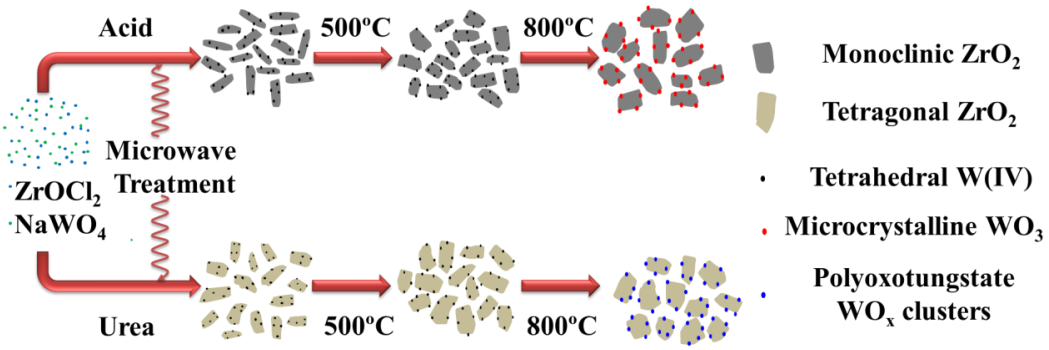

Scheme 2. 1. Microwave assisted WO_x-ZrO_2 synthesis. ZrO_2 phase and W species tuning upon acid or urea synthesis.

Comparing our materials 10WZA and 10WZU with the reported references materials 10 WZ Dep and 10WZ Dis prepared by impregnation or coprecipitation respectively, our microwave-assisted synthetic approach allows to easily obtain as-prepared nanocrystalline materials of few nanometers and controlled morphology, which are more resistant to sintering at higher temperatures (as shown in Table 1, 2 and 3). Furthermore, different species of tungsten with potential activity can be obtained depending on the pH of the synthesis.

2.2.1.3 Study of the formation mechanism of *m* and *t*-ZrO_2 under microwave synthesis

The formation mechanism of the nanoparticles was further studied carrying out the microwave synthesis in the same reaction conditions, but quenching the reaction at different temperatures and times.

The XRD patterns of the different materials are compiled in Figure 2. 15a and b. The materials synthetized in acid conditions at 120ºC are amorphous. After 1 min at 170ºC, very weak peaks of *m*-ZrO_2 are superimposed to the amorphous background. If the reaction time is prolonged at this temperature, the monoclinic polymorph is developed, as revealed by the appearance of the corresponding XRD peaks, which become narrower at higher temperature and reaction time (220ºC for 1min and 220ºC for 10 min), indicating an increase in crystallinity. Under basic conditions, the crystallization takes places at higher reaction times and temperatures. Is not until 220ºC/1min when diffraction peaks more defined are observed, whose intensity increases with longer reaction time. The crystalline phase obtained with this method is mainly *t*-ZrO_2 as previously discussed.

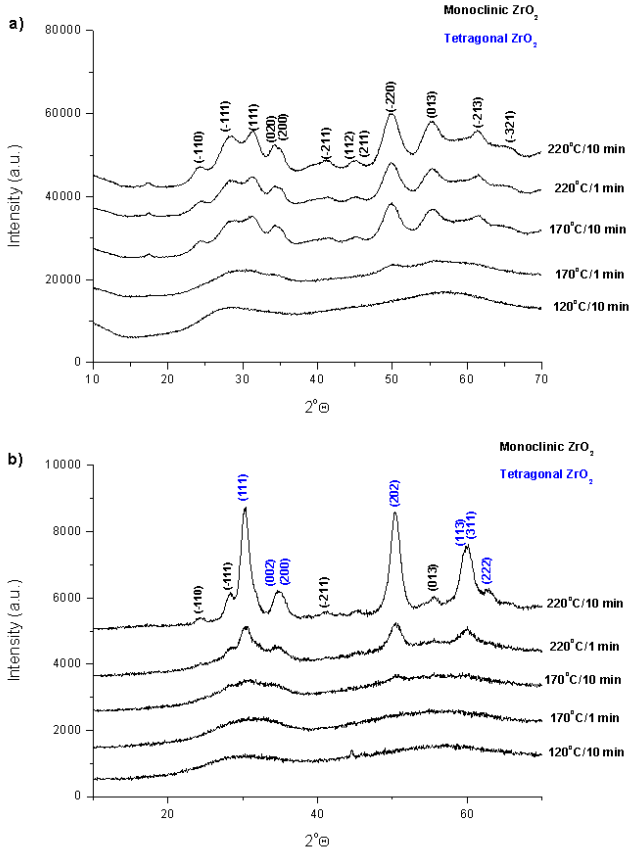

Figure 2. 15. XRD of ZrO_2 synthetized with a) acid and b) urea method at different temperatures and times.

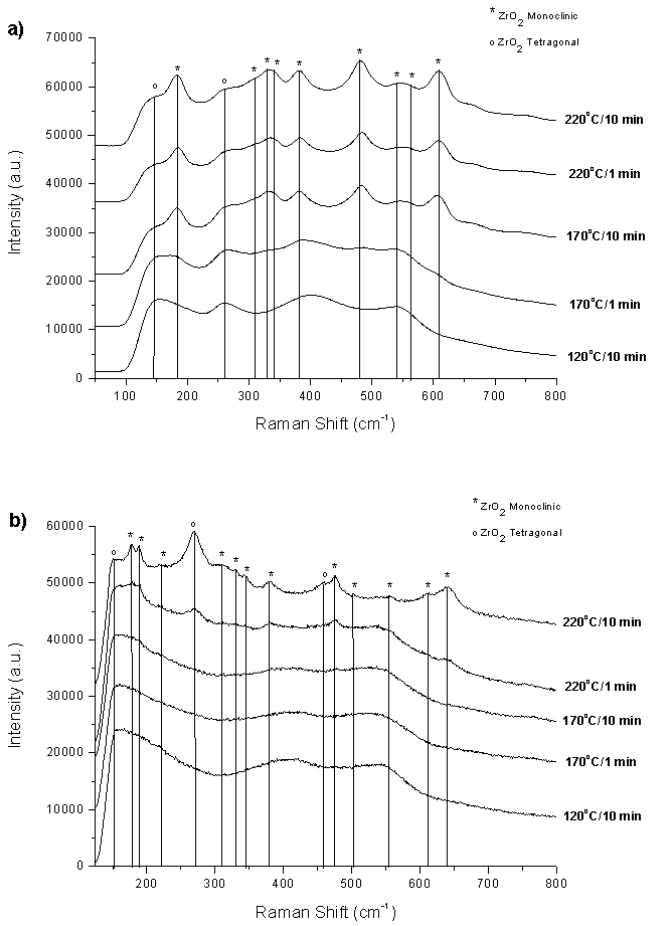

Figure 2. 16. Raman spectra of ZrO_2 synthetized with a) acid and b) urea method at different temperatures and times.

The different materials were also characterized by Raman spectroscopy (Figure 2. 16). The sample treated at lower temperature obtained by acid route shows broad peaks at 151, 260, 405 and 546 cm^{-1}, the two first signals can be assigned to the tetragonal ZrO_2 polymorph[68] while the two others correspond to hydrolyzed polymeric zirconium species.[69–72] At higher synthesis temperatures, bands corresponding to monoclinic ZrO_2 appear, becoming narrower as the temperature increases while the peak of *t*-ZrO_2 is observed too. This fact indicates that a small amount *t*-ZrO_2 still remains in the *m*-ZrO_2. With reference to the samples obtained by the urea method, in the lower temperature synthetized sample we can observe the same bands as the observed for the same sample obtained with the acid method

except the signal around 260 cm^{-1} which correspond to the *t*-ZrO_2. Increasing the synthesis temperature and time, this peak clearly appears and the other characteristic of the *m*-and *t*-ZrO_2, in good agreement with the XRD analysis.

The evolution of the morphology of ZrO_2 was studied by TEM. For the acid synthesis (Figure 2. 17), at 120°C an amorphous dendritic sol is observed which still remains at 170°C with more dense aggregates (in black) not showing any clear morphology. These aggregates could be assigned as incipient monoclinic nuclei, according to XRD and Raman analysis. At this temperature, if the reaction time is prolonged, rod- like

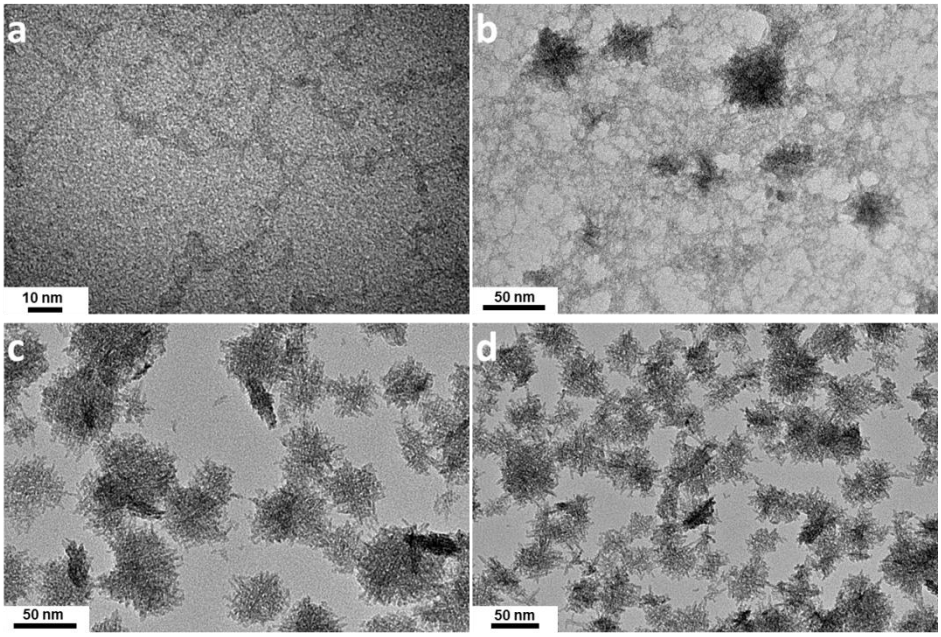

Figure 2. 17. TEM micrograph of ZrO_2 synthetized under acid conditions at a) 120°C/10 minutes, b) 170°C/1 minute, c) 170°C/10 minutes and d) 220°C/10 minutes.

nanoparticles (10 x 3 nm) agglomerated into 40 nm particles appear, this morphology is preserved when the reaction temperature is increased to 220ºC at different reaction time. On the other side, the materials obtained with the urea method (Figure 2. 18) remain amorphous until 170ºC/10 min where we can observe some crystalline fringes immersed in the amorphous particles. Increasing the temperature to 220ºC/1min the crystallinity of the sample increases and the nanoparticles begin to be more defined. Finally, at 220ºC/10min well defined crystalline nanoparticles are obtained.

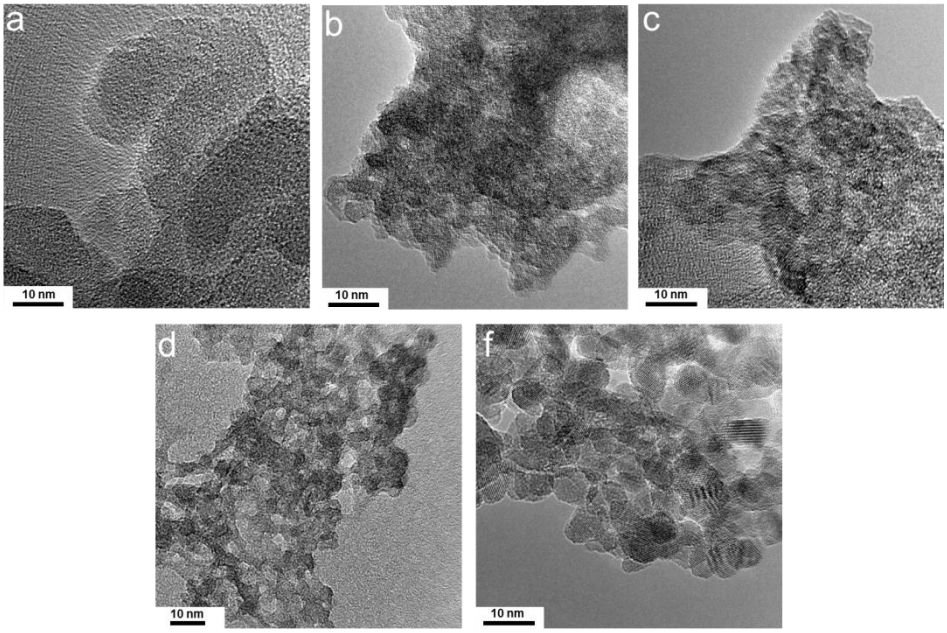

Figure 2. 18. TEM micrographs of ZrO_2 synthetized under urea conditions at a) 120°C for 10 minutes, b) 170°C for 1 minute, c) 170°C for 10 minutes and d) 220°C for 10 minutes.

From the experimental results, we can propose the following mechanism concerning the acid/basic synthesis by microwave heating. When $ZrOCl_2 \cdot 8H_2O$ is dissolved in water, cyclic $[Zr(OH)_2 \cdot 4H_2O]_4^{8+}$ tetramers (which consist in four Zr^{4+} atoms forming a square linked by two OH groups, and four molecules of water filling out the coordination sphere of the zirconium atoms) are the major species in solution.[73,74] For the acid synthesis, upon heating, the tetramers polymerize via hydroxyl binding and olation[75,76] forming amorphous hydrous zirconia sol $[ZrO_x(OH)_{4-2x} \cdot yH_2O]_n$. Some works have shown that this amorphous zirconia has the same structure as *t*-ZrO_2 at short order[77] in good agreement with our Raman analysis. Increasing the temperature and time, monoclinic zirconia begins to crystallize (170°C/1min). At this point, a coordination change is occurring, in which the eightfold coordinated Zr^{4+} (hydrous zirconia with tetragonal local order) change to seven coordination characteristic of the monoclinic polymorph. Upon increasing the temperature *m*-ZrO_2 becomes the main phase. This process, is facilitated by a dissolution-crystallization mechanism..[78,79] Thus the zirconium species in acid media are soluble and this fact has a direct influence on the initial dendritic morphology.

For the urea synthesis, upon heating, urea hydrolyses to CO_2 and NH_3 increasing the pH solution and leading an increase in OH^- concentration, which replace some

coordinated water in the zirconium tetramers. These hydroxyls condense via olation, in several directions. In the tetramers exists several olation sites leaving amorphous hydrous zirconia with tetragonal local order, that upon increasing the temperature synthesis leads mainly *t*-ZrO_2. Thus, in this pH conditions the zirconia species solubility is low leading to minimal ion displacements and as consequence zirconia crystallizes in tetragonal polymorph. The presence of minor monoclinic phase can be explained by the non-negligible solubility of zirconium species at this pH.

2.2.2 Catalytic results

2.2.2.1 Synthesis of aldoximes from nitriles

The catalytic activity of all the materials was tested in three different reactions such as aldoxime dehydration, alkyne hydration and Merwein-Pondorf-Verley (MPV) reduction.

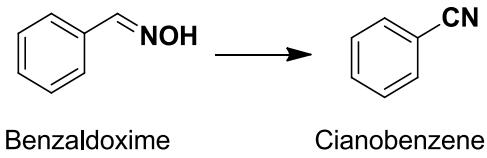

Scheme 2. 2. Benzaldoxime dehydration reaction

In the aldoxime dehydration (Scheme 2. 2), pure zirconia (ZU and ZA) show very poor catalytic activity, with a maximum conversion of ~38% for the as-synthesized ZA sample. The activity diminishes for the annealed catalysts until 10% conversion (for ZU-800). In all cases, the materials synthetized by the acid route exhibited slightly higher activity (~ 5% conversion higher) than those synthetized by the basic route. Anyway, the selectivity toward the ciano product were not higher than 60%, obtaining benzamide or benzaldehyde as by-products (Table 2. 6).

Table 2. 6. Conversion and Selectivity of ZA and ZU. Reaction Conditions: Catalyst 50 mg, 0.50 mmol Benzaldoxime, nitrobencene as standard, 1.5 mL o-xylene, 150ºC, 5h.

Catalyst	X Oxime (%)	Y Ciano(%)	Sel Ciano(%)
ZA	39.8	24.6	61.8
ZA500	29.6	17.7	59.8
ZA800	14.9	7.6	50.6
ZU	34.5	17.1	49.6
ZU500	26.1	15.6	59.6
ZU800	10.7	4.1	38.5

Table 2. 7 and Table 2. 8 show the catalytic activity of the W-doped samples prepared in acid and basic conditions. For 5WZA the conversion of the oxime is higher as the annealing temperature of the catalyst increases, but the highest selectivity is obtained for 5WZA-500 (90%). On the other hand, for 10WZA, the highest conversion and better selectivity towards the ciano product (98% and 92% respectively) is obtained for 10WZA500.

Table 2. 7. Conversion and Selectivity of X-WZA-Y obtained by microwave-assisted synthesis in acid media. Reaction Conditions: Catalyst 50 mg, 0.50 mmol Benzaldoxime, nitrobencene as standard, 1.5 mL o-xylene, 150ºC, 5h

Catalysts	X Oxime (%)	Y Ciano (%)	Sel. Ciano (%)	Initial rate/ S_{BET} ($g/h \cdot m^2$)
5WZA	53.6	43.7	81.5	0.05
5WZA500	71.0	64.1	90.3	0.14
5WZA800	94.1	78.9	83.8	0.54
10WZA	85.4	76.5	89.6	0.10
10WZA500	**97.8**	**89.7**	**91.7**	**0.25**
10WZA800	85.0	72.6	85.3	0.39

In the samples prepared under basic conditions (Table 2. 8), the highest activity and selectivity is detected for the catalysts annealed at 500ºC, independently of the W content. A general tendency in the samples WZA and WZU is that increasing the

amount of W, the conversion and also the selectivity towards the desired product increase.

Table 2. 8. Conversion and Selectivity of X-WZA-Y obtained by microwave-assisted synthesis in basic media. Reaction Conditions: Catalyst 50 mg, 0.50 mmol Benzaldoxime, nitrobencene as standard, 1.5 mL o-xylene, 150ºC, 5h

Catalysts	X Oxime (%)	Y Ciano (%)	Sel. Ciano (%)	Initial rate/ S_{BET} ($g/h \cdot m^2$)
5WZU	62.8	49.8	79.2	0.08
5WZU500	80.8	69.9	86.5	0.14
5WZU800	49.4	39.1	79.1	0.20
10WZU	69.2	58.5	84.6	0.05
10WZU500	**98.2**	**87.6**	**89.3**	**0.25**
10WZU800	72.0	60.6	84.2	0.21

Notice that by the microwave-assisted synthesis conversion and selectivity of 98% and 90% respectively have been obtained while the reference catalysts, prepared by impregnation or coprecipitation, showed lower activity and selectivity than our best materials, 10WZA500 and 10WZU500 (see Table 2. 9).

Table 2. 9. Reaction Conditions: Catalyst 50 mg, 0.50 mmol Benzaldoxime, nitrobencene as standard, 1.5 mL o-xylene, 150ºC, 5h.

Catalyst	X Oxime (%)	Y Ciano(%)	Sel Ciano(%)
SnW 2:1 raw	88.5	54.9	62.0
SnW 2:1 500ºC	82.7	51.3	62.0
SnW 2:1 800ºC	83.7	57.4	68.6
10%W/ZrO_2 Dep raw	80.0	64.2	80.2
10%W/ZrO_2 Dep 500ºC	88.3	73.4	83.1
10%W/ZrO_2 Dep 800ºC	89.7	76.6	85.4
10%W/ZrO_2 Dis raw	63.5	46.7	73.7
10%W/ZrO_2 Dis 500ºC	72.9	60.1	82.5
10%W/ZrO_2 Dis 800ºC	80.7	66.9	82.9

A large amount of hydroxyls covering the surface of the as-prepared catalysts are detrimental for this reaction. Once part of these hydroxyls are removed (500ºC),

catalytic results improve being the most active catalysts at 10%W loading. Further annealing at 800ºC is also detrimental for the activity and the selectivity towards the desired product.

If we calculate the initial rate as a function of the BET surface area (Table 2. 7 and Table 2. 8) we can observe that the specific activity of the materials increase as the thermal treatment increases, despite that the materials calcined at 500ºC are the most active and selective. This is because not all W is on the surface in raw and calcined at 500ºC materials, being some in the bulk of the material. Meanwhile with the annealing, W is expelled out of the bulk of the material, having higher concentration of W per surface area in these materials.[21]

Since the crystalline phase of zirconia is very different in the materials prepared under acid (monoclinic) and basic conditions (tetragonal), the matrix seems not to play a direct role on the catalytic activity. Taking into account the previous structural analysis, we can conclude that the most active species for this reaction are the W(VI) species in tetrahedral coordination, present in the samples annealed at 500ºC, with the right Lewis acidity for this reaction. The as-synthesized samples, which also contains the W(VI) tetrahedral species, the presence of hydroxyls and other adsorbed species (carbonates) at the surface are detrimental. Furthermore, it is concluded that both, the microcrystalline WO_3 nanoparticles on monoclinic ZrO_2 and the interconnecting polyoxotungstate clusters on tetragonal ZrO_2 detected at 800ºC, are less active than the tetrahedral species.

The reference samples (Table 2. 9) show lower activity than our microwave-synthesized materials. In the case of SnW, we cannot do comparisons, but in the case of W/ZrO_2 samples prepared by coprecipitation and impregnation methods, they exhibited similar tetragonal phase and S_{BET} area but the crystallite sizes were larger than in WZU materials. It may then very well occur that crystalline size of ZrO_2 influences W dispersion with the corresponding effect in the catalytic activity.

2.2.2.2 Hydration of alkynes

The catalytic activity of all the materials was also tested for the hydration of alkynes, and more specifically for the phenyl acetylene (Scheme 2. 3).

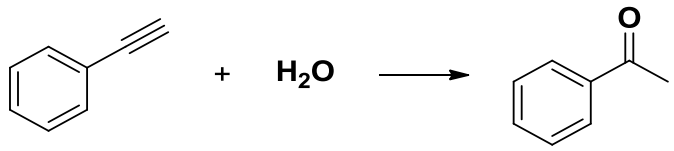

Scheme 2. 3. Hydration of phenylacetylene.

In this reaction, only W-doped zirconias annealed at 800ºC showed good results (Table 2. 10), and the best activity (98%) and selectivity (89%) was presented by the 10WZU-800 sample (100% *t*-ZrO_2). The sample 10WZA800 (87% *m*-ZrO_2) exhibit quite lower activity, what means that the tetragonal phase is more favorable for the catalysis of this reaction. The reference materials also showed good activity, around

Table 2. 10. Reaction conditions: Catalyst 50 mg, 0.50 mmol Phenylacetylene, 2.5 mmol water, dodecane as standard, 1.5 mL cyclooctane, 95°C, 5 hours.

Catalyst	X Phenylacetylene (%)	Y Acetophenone (%)	Sel. Acetophenone (%)
5WZA800	16.9	11.7	68.9
10WZA500	6.2	0.2	2.5
10WZA800	65.5	55.7	85.0
5WZU800	43.6	37.4	85.8
10WZU500	10.4	0.7	7.1
10WZU800	97.7	87.4	89.4

98% conversion (Table 2. 11). SnW 2:1 800ºC sample presents less selectivity towards the desired product (84%), even having 3 times larger amount of W than ZrO_2 materials. The good results of the 10WZDep800 and 10WZDis800 samples point out that the tetragonal phase has a clear role on this catalysis.

Table 2. 11. Reaction conditions: Catalyst 50 mg, 0.50 mmol Phenylacetylene, 2.5 mmol water, dodecane as standard, 1.5 mL cyclooctane, 95°C, 5 hours.

Catalyst	X Phenylacetylene (%)	Y Acetophenone (%)	Sel. Acetophenone (%)
SnW 2:1 800	99.3	84.6	85.3
10WZDep800	97.8	86.3	88.7
10WZDis800	97.6	86.5	88.7

Pure zirconias and W(VI) species in tetrahedral coordination, with only Lewis acidity, appears not to be active in alkyne hydration, probably due to the highly acidic character of the catalyst required to activate this reaction. Even at 800ºC, where 10WZA800 and 10WZU800 samples exhibit strong acidity, their activity is not similar. The material with tetragonal phase (10WZU800) is very active, so the active species are the interconnecting polyoxotungstate clusters and also microcrystalline WO_3 on *t*-ZrO_2. This behavior is in good agreement with previous works reporting that the activity of materials prepared by impregnating tungsten salts over crystalline monoclinic zirconia is much lower than those impregnated in the hydrous support[12,25,64] which develop tetragonal phase upon annealing.

In order to gain insight about this fact the pure monoclinic and tetragonal ZrO_2 impregnated with tungsten and annealed at 800ºC (10WZM800 and 10WZT800 respectively) were tested in this reaction.

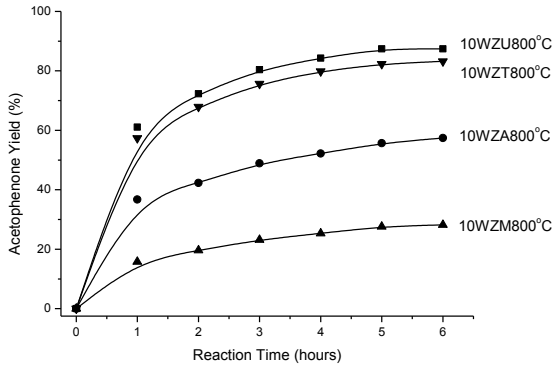

Figure 2. 19. Kinetics plots for the hydration of phenylacetylene. Reaction Conditions: 0.5 mmol of phenylacetylene, 2.5 mmol of water, 1.5 Ml of cyclooctane, dodecane as standard and 95ºC.

Figure 2. 19 shows that, the most active material in this reaction was 10WZU800, followed by 10WZT800, 10WZA800 and 10WZM800. If we plot the tetragonal phase percentage in the materials in front of the yield of acetophenone obtained, we can observe that the catalytic activity increases with increasing the content of tetragonal ZrO_2 (Figure 2. 20).

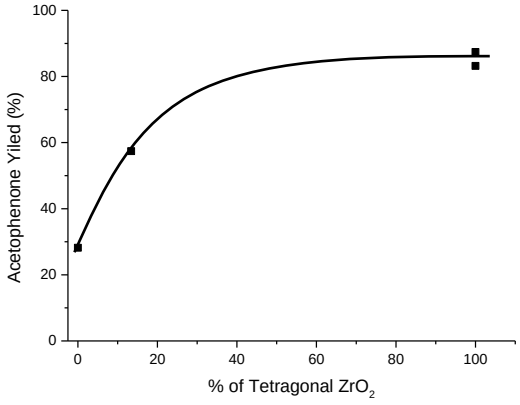

Figure 2. 20. Acetophenone Yield (reaction time 5 hours) as a function of tetragonal ZrO_2 content.

Several authors have studied the influence of the of the zirconia polymorphs in supported Cu[80–82], Au[83], Ag[84], Rh[85], Mo[68] catalysts. According to those studies, we conclude that the species isolated in the tetragonal polymorph tend to exhibit a more cationic character than those isolated in the monoclinic phase (more metallic character). The reason of that relies on the presence of anion vacancies originated in the metastable tetragonal polymorph with the introduction of trivalent or divalent ions.[86] As a consequence, the more ionic character of the tetragonal polymorph induces a higher Lewis and Brönsted acidity[80] than in the more covalent monoclinic structure, in good agreement with pyridine adsorption/desorption experiments. As a consequence, the most acid species stabilized over the tetragonal zirconia would explain the higher activity in the hydration of alkynes.

The better activity of 10WZU800 compared to 10WZT800 reference (both pure *t*-ZrO_2) reveals differences in the active W-based clusters. According to the previous work, Kiely and co-workers[64] demonstrated that the catalytic active species in the alkane isomerization reaction are 0.8-1 nm WO_x clusters incorporating some Zr(IV) cations, we suggest that the microwave-assisted technique allows partial incorporation of zirconium cations within the small polyoxotungstate clusters, as a consequence of its high heating efficiency which levers the different reactivities of zirconium and tungsten precursors. Thus, both contributions, the tetragonal crystalline phase and the presence of Zr-W oxoclusters, would be responsible for the good catalytic results of our 10WZU800 catalyst in the hydration of alkynes.

2.2.2.3 Meerwein-Pondorf-Verley reduction

The different materials synthesized by the microwave-assisted pathway were tested in the MPV reduction of cyclohexanone to cyclohexanol (Scheme 2. 4).

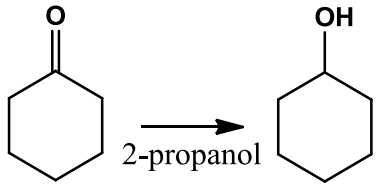

Scheme 2. 4. MPV reduction of cyclohexanone to cyclohexanol.

The tungsten doped materials show quite good activity, which decreases as the calcination temperature increases (Table 2. 12). Checking the results we can observe that in all cases the materials synthesized by the acidic route presents a slight higher activity (yield and initial reaction rate) than its counterparts.

Table 2. 12. Reaction conditions: Catalyst 25mg, 0.50 mmol cyclohexanone, 1 mL isopropanol, docecane as standard, 85°C, 3 hours.

Catalyst	Conversion (%)	Yield (%)	Initial rate (h^{-1})
10WZA	85,7	85,0	45,9
10WZA500	68,3	64,7	23,1
10WZA800	8,7	7,9	2,5
10WZU	78,9	76,7	33,5
10WZU500	62,3	59,0	21,5
10WZU800	1,9	2,9	0,8

For the non-doped samples, a decrease in the catalytic activity upon heating the materials is also observed (Table 2. 13). In all cases, as before, the materials synthesized by the acid route present much higher activity than the obtained by the urea method. The non-annealed sample obtained by the acidic route shows excellent catalytic results, more than twice than the materials obtained by the urea pathway.

Table 2. 13. Reaction conditions: Catalyst 25mg, 0.50 mmol cyclohexanone, 1 mL isopropanol, dodecane as standard, 85°C, 3 hours.

Cat	Conversion (%)	Yield (%)	Initial Rate (h^{-1})
ZA	**91,0**	**90,0**	**46.8**
ZA500	77,6	77,5	29,7
ZA800	7,3	6,4	2,0
ZU	41,5	38,8	12,6
ZU500	12,0	10,4	3,5
ZU800	1,9	1,5	0,0
A	31.9	31.0	25.2
M	85.3	85.0	39.8
T	7.1	6.6	5.6

None of three, tungsten in tetrahedral coordination, polyoxotungstates over *t*-ZrO_2 or microcrystalline WO_3 over *m*-ZrO_2 seem to be the most active species for the MPV reduction. As the most active catalysts are those non-annealed, it seems that the hydroxyls which were detrimental in the aldoxime dehydration, now in MPV reduction have a critical role.

Several works have tuned the amount of this surface hydroxyl groups among annealing the hydrous zirconia at different temperatures without changing the zirconia structure. It has been observed that the higher is the concentration of surface hydroxyl groups the higher is the activity of the zirconia catalyst in the MPV reduction of cinnamaldehyde[52]and citral[87]. These authors proposed that the hydroxyl groups act as sites for ligand exchange with the alcohol to form the corresponding alkoxide on the catalyst which will transfer the hydride to the aldehyde or ketone (coordinated to a zirconium metal center) via six-membered ring intermediate, classically proposed in the homogeneous mechanism (Scheme 2. 5 (O-Zr-OH)).

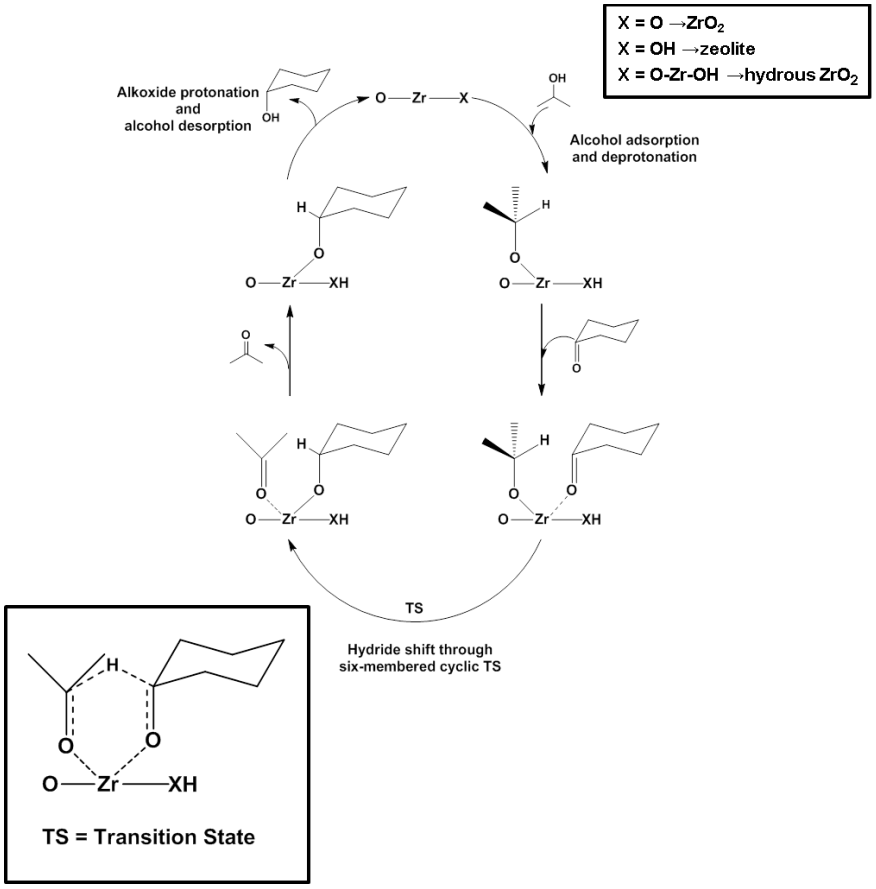

Scheme 2. 5. General mechanism over ZrO_2, zeolite and hydrous ZrO_2 for the MPV reduction:

Reference amorphous zirconia material (A), which is expected to contain a great number of surface hydroxyls groups, was also tested in this reaction. However, its catalytic activity is not higher than the non-calcined samples (Figure 2. 21 and Table 2. 13); thus, other parameters, in addition to surface hydroxyl groups, must influence the catalytic activity.

By other hand, the presence of tungsten in the materials synthesized through the acid route is detrimental for the MPV reaction. Indeed, all non-doped samples show higher catalytic activity even having lower surface area than the doped materials. Moreover, comparing the catalytic activity of the non-doped and non-annealed samples, a great difference in the catalytic activity is observed, the explanation of this fact may rely on the main crystallographic polymorph developed in each material. In order to check this hypothesis, pure *t*- and *m*-ZrO_2 reference materials[61] were tested in the MPV

reaction (Table 2. 13). Figure 2. 21 shows the kinetic plots for the non-doped reference and non-calcined materials where is possible to see that the most active are those which present the monoclinic crystallographic polymorph. On the other side, ZU (which present 89% vol. of tetragonal phase) and T with only tetragonal ZrO_2 polymorph show much lower activity.

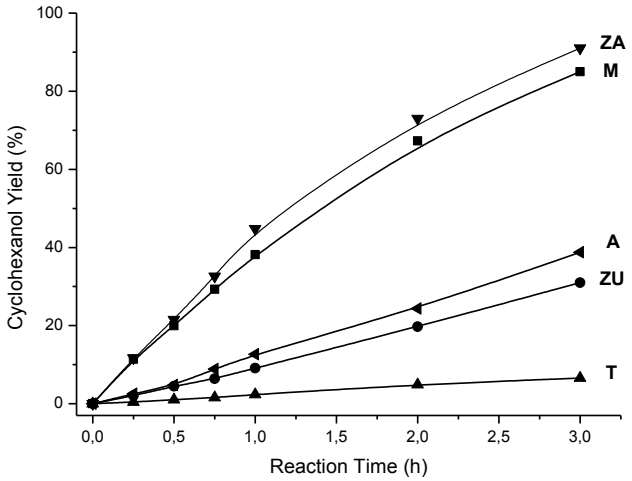

Figure 2. 21. Kinetic plots for MPV reduction. Reaction conditions: Catalyst 50mg, 0.50 mmol cyclohexanone, 1 mL isopropanol, dodecane as standard, 85^{o}C, 3 hours.

If we plot the initial rate versus the monoclinic percentage of zirconia (Figure 2. 22) it is possible to see a correlation between the catalytic activity and this polymorph concentration. Moreover, ZA shows higher activity than M even having the same crystallographic phase. This difference in the catalytic activity may be caused by the higher surface area that ZA presents, thus the other materials (ZU, M and T) show similar BET surface areas(120-150 $m^2 \cdot g^{-1}$).

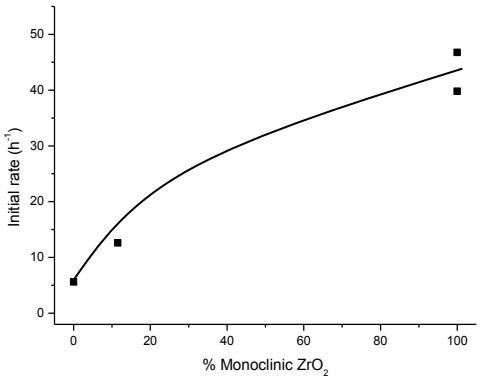

Figure 2. 22. Initial rate versus % monoclinic ZrO_2.

Classically, in homogeneous phase, the proposed reaction mechanism for the MPV reduction occurs via direct hydrogen transfer involving six-membered ring transition state[88] in which both, ketone and alcohol, are coordinated to the metal center (Scheme 2. 5).

Sn[53 54] and Zr-beta[55 56] shows very good activity in the MPV reduction. The tetragonal metal coordination, which provides high Lewis acidity, is responsible of the high activity in this reaction. These isolated metal centers are able to polarize the carbonyl groups, thus activating the CO group forming a six-member cyclic transition state with the alcohol, previously deprotonated by a hydroxyl group. In such a way, as in the homogeneous mechanism, ketone and alcohol are coordinated to the same metal center (Scheme 2. 5).

So the metal center also plays a key role in the MPV reduction. Zirconium oxide has been deposited on different support such as silica, titania, ceria, Zr-beta zeolite, Zr-MCM41[89] and MgO and ɤ-Al_2O_3[90] for its use in the MPV reduction. The zirconia deposited on the oxides (CeO_2, TiO_2, MgO and ɤ -Al_2O_3) showed poor catalytic activity because when zirconia is supported in these materials loses its Zr^{4+} Lewis acidity. While the most acid ones present better activity, being the Zr-beta zeolite the most active.

Taking all these precedents into account the reaction mechanism for the MPV reduction over oxides always have been assumed the same as for isolated metal species (alkoxides or metal containing molecular sieves) but is not yet clear. In better understand this aspect combined kinetic and theoretical study was performed.

As 2-propanol is in high excess, the reaction can be considered as a pseudo-first order reaction, and the kinetic constant *k*, was calculated obtaining the initial rate (r_0) at different cyclohexanone concentrations ($r_0=k\cdot$[cyclohexanone]). The apparent activation energies E_{act} were calculated from the measured kinetic constants at different temperatures (*T*) according to equations 1 and 2, where *A* is the frequency factor and *R* is the gas constant.

$$k = Ae^{\frac{-E_{act}}{RT}} \quad (1)$$

$$\ln k = \ln A - \frac{E_{act}}{R}\left(\frac{1}{T}\right) \quad (2)$$

Figure 2. 23 shows the Arrhenius plots for the five materials characterized above in which no appreciable difference is observed in the calculated apparent activation energy (43-52 KJ/mol). For comparison, the same tests were carried out for Zr-beta zeolite. In order to have measurable initial rates, the amount of catalyst had to be decreased to 10 mg, which indicates that this catalyst is much more active than the other zirconia polymorphs. The apparent activation energy calculated for this material is 41 KJ/mol, which is in the same range as the other materials (Figure 2. 23). These energy activation values are quite similar to those obtained by Michikazu and coworkers for ZrO_2, TiO_2 and Nb_2O_3.[91]

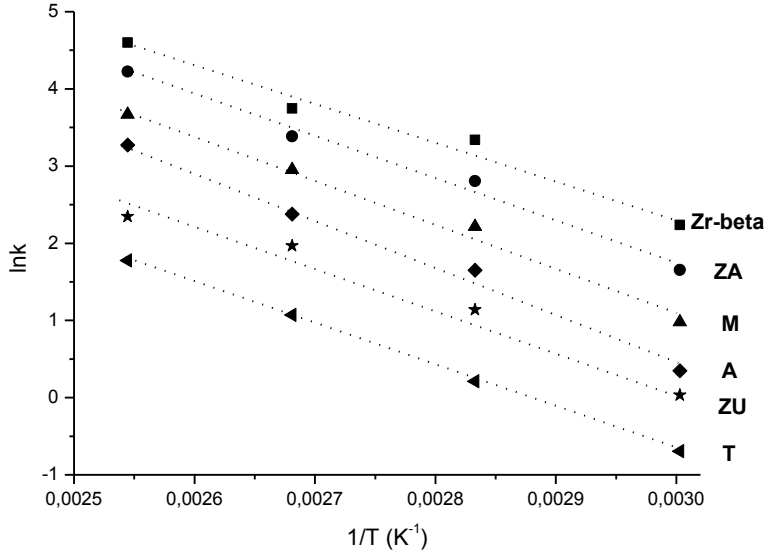

Figure 2. 23. Arrhenius plots for MPV reduction of cyclohexanone with 2-propanol.

In contrast to the similar apparent activation energies obtained, the pre-exponential frequency factor (*A*) obtained from the intersection with the ordinate of the Arrhenius plots is quite different (Figure 2. 23). This frequency factor is related to the entropy effects (*S*) (equation 3, where k_B is the Boltzmann constant and *h* is the Plank constant)

$$A = \frac{\left(\frac{k_B T}{h}\right) e^{\Delta S^{\ddagger}}}{R} (3)$$

From all these results we can conclude that the great difference in the catalytic activity of zirconia polymorphs cannot be attributed to different activation energies, but it is consequence of the difference in the frequency factor *A*, associated to the correct orientation of reagents on the catalyst surface (entropy effects)

In order to gain insight about this fact, the mechanism of MPV reduction of cyclohexanone with 2-propanol over the most stable crystallographic facets of *m*-ZrO_2 (-111 facet) and *t*-ZrO_2 (101 facet)[92–95] were studied by means of DFT calculations and compared with that previously reported for Zr-beta zeolite.[96] The mechanism is composed by three steps (Scheme 2. 5): (i) alcohol absorption and deprotonation, (ii) ketone co-absorption and hydride shift through a six-membered ring transition state, and (iii) protonation and desorption of alcohol.

The optimized geometries in the first elementary steps over *m*-ZrO_2 and *t*-ZrO_2 surface models with the relative energy of each structure with respect to separated ZrO_2 surface model and reactant molecules are shown in Figure 2. 24.

Absorption of the alcohol occurs through absorption complex R1 which is more exothermic on *m*-ZrO_2 than on *t*-ZrO_2. In this complex, the O atom of the hydroxyl group of the alcohol interacts with a Zr Lewis acid center and a hydrogen bond is also formed between proton of the hydroxyl group and a basic surface O atom. Deprotonation occurs via transition state TS1 structure which evolves to intermediate I1 that shifts to a more stable position on the catalyst surface, intermediate species I2. The different steps over two ZrO_2 phases are equivalents but the energies are not equal. Thus the activation barrier required to deprotonate 2-propanol on *t*-ZrO_2 is almost cero, and the relative stability of the two intermediates I1 and I2 is quite similar. On the other hand, deprotonation step over *m*-ZrO_2 has an activation energy of 14.2 KJ/mol and the second structure I2 is 16.6 KJ/mol more stable than intermediate I1.

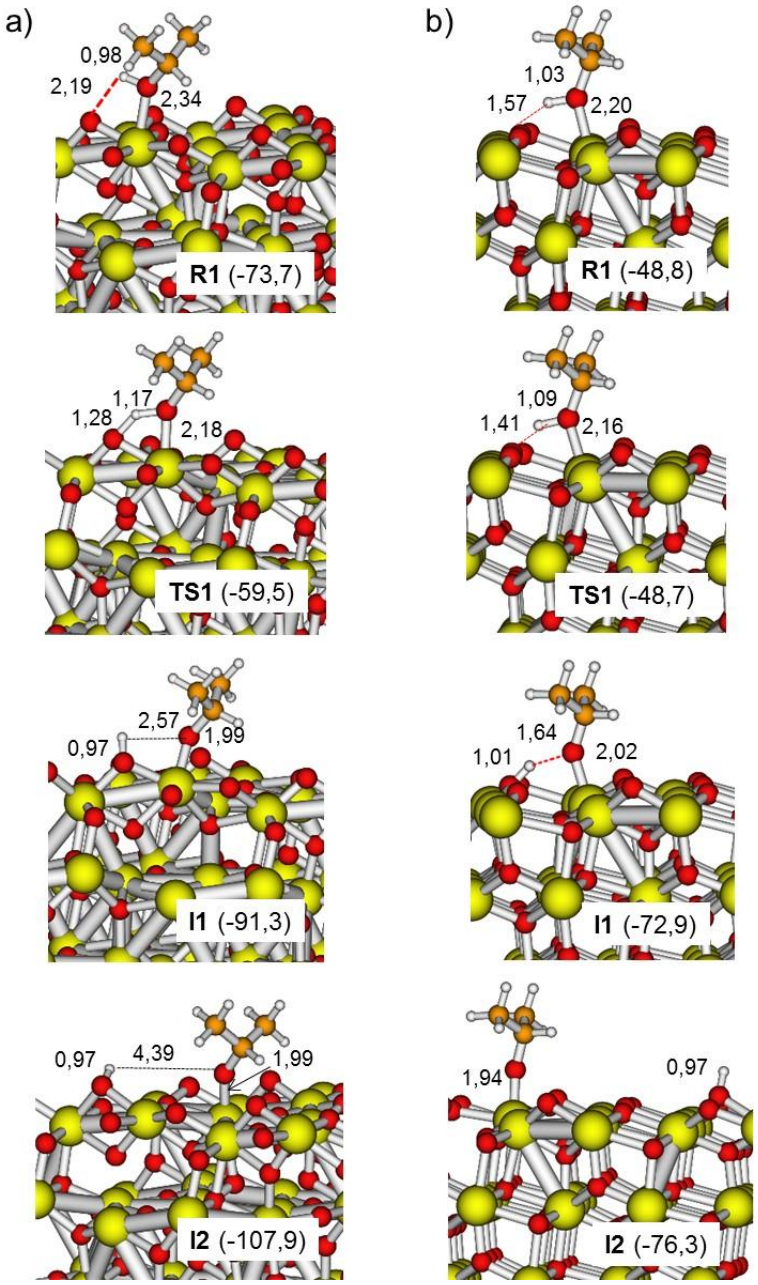

Figure 2. 24. Optimized geometry reactant R1, transition state TS1 and intermediate I1 and I2 structures involved in the deprotonation of 2-propanol over a) *m*-ZrO_2 and b) *t*-ZrO_2. Distances in Å. Relative energies E_{rel} with respect to isolated ZrO_2 surface and 2-propanol in KJ/mol are given in parenthesis. Zr, O, C, and H atoms are despicted in yellow, red, orange and wihte respectively

The next step is the co-absorption of cyclohexanone at the Zr center and hydride shift from the previously formed propoxy specie. The optimized geometries and the relative energies are shown is Figure 2. 25. The first difference that we observe is that instead of forming a six-membered ring transition state observed in Zr-alkoxides and Zr-containing zeolites, over zirconium oxides cyclohexanone and propoxy fragment do not absorb to the same Zr center, but on two close surface Zr atoms separated by an O atom (structure R2 Figure 2. 25). Once the reagents are in this position, the hydride shift occurs through a seven-membered ring transition state (TS2 in Figure 2. 25). Finally, in intermediate I3, 2-propanone and cyclohexyl fragment is formed.

The energetic profile is also different depending of the crystallographic zirconia phase. For *m*-ZrO_2, co-adsorption of cyclohexanone from structure I2 forming R2 is exothermic (49.4 KJ/mol) and the activation energy for the hydride shift is 54.4KJ/mol, and the process is endothermic by 23.0 KJ/mol (Figure 2. 25a). On the other hand, on *t*-ZrO_2 cyclohexanone co-absorption from I2 to R2-A (Figure 2. 25b) is nearly thermoneutral, the activation energy for the hydride shift is 60KJ/mol, and the process is exothermic, leading 32.4 KJ/mol. Another important finding regarding the mechanism over this zirconia polymorph is that intermediate I1 (Figure 2. 24b) is energetically preferred and produces a highly stable intermediate R2-B in which the propoxy fragment is stabilized by a hydrogen bond with the proton generated in the first deprotonation step. From this structure (Figure 2. 25c), the activation energy for the hydride shift through TS2-B is 133.5 KJ/mol and the process is endothermic (84.4KJ/mol). Moreover, a third pathway also exists in *t*-ZrO_2 (Figure 2. 25d) in which intermediate reactant R2-C has an intermediate stability between the two shown before and the activation energy is 75.7 KJ/mol and the process is slightly endothermic. Thus, even existing a less energetic pathway on *t*-ZrO_2 with an activation energy of 60 KJ/mol, which is comparable with the calculated for *m*-ZrO_2 and with the values obtained experimentally (43-51KJ/mol), the starting structure of this pathway is significantly less stable than others arrangements of reactant fragments on the catalyst surface which leads high activation barriers and therefore to a lesser reactivity.

In this way, the different activity observed experimentally on *m*-ZrO_2 and *t*-ZrO_2 is caused by entropy effects associated to different frequency factors *A* which is caused by the different distribution of reactant fragments on both surfaces. Thus, for *m*-ZrO_2 the most stable reactant fragments arrangements involves an activation energy of 54.4 KJ/mol for the hydride shift in good agreement with the experimental data. While for *t*-ZrO_2 several reactant fragments distributions on its surface are possible, leading to

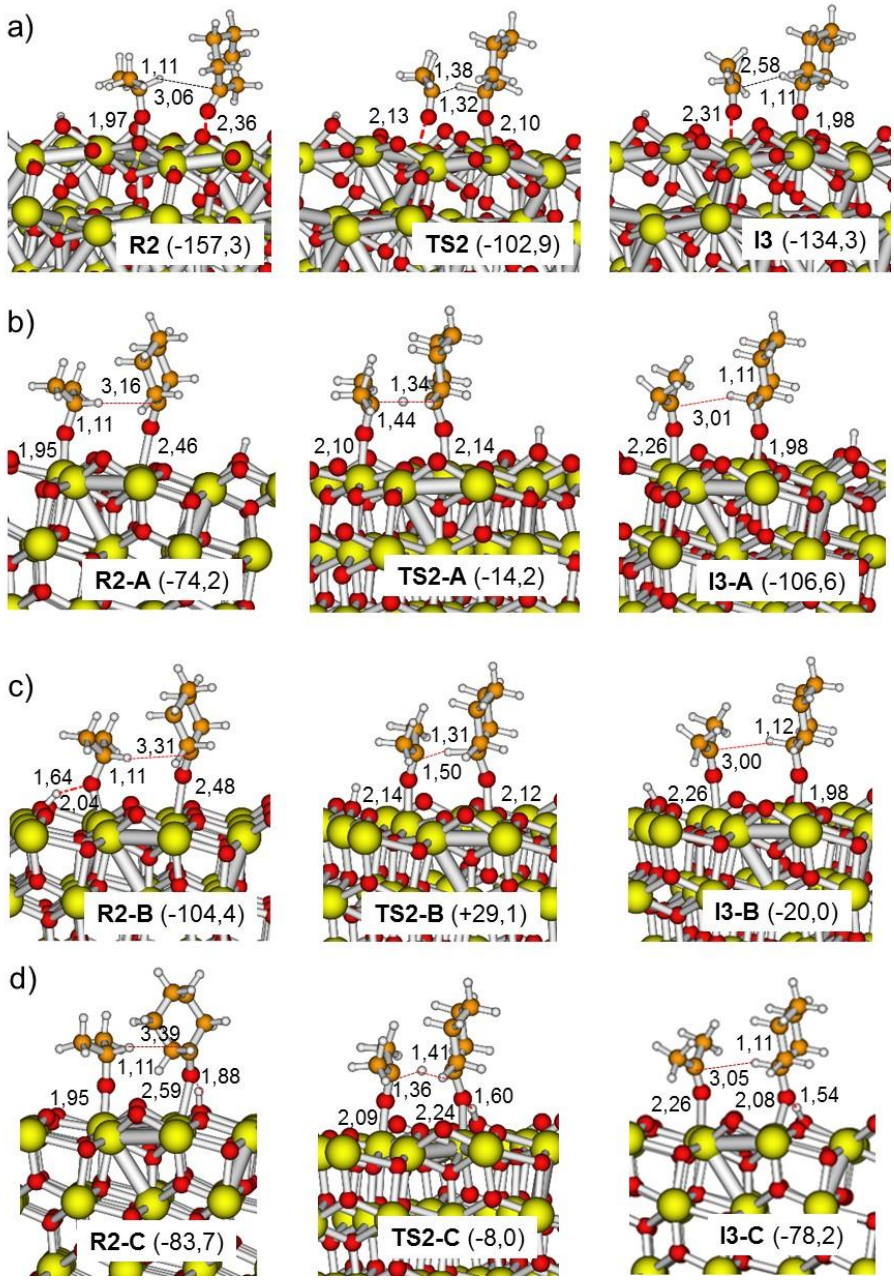

Figure 2. 25. Optimized geometry or reactant R2 transition state TS2 and intermediate I3 structures involved in the hydride shift step over a) *m*-ZrO_2, b) *t*-ZrO_2 route A, c) *t*-ZrO_2 route B, d) *t*-ZrO_2 route C. Distances in Å. Relative energies E_{rel} with respect to isolated ZrO_2 surface, 2-propanol and cyclohexanone in KJ/mol are given in parenthesis. Zr, O, C and H are despicted in yellow, red, orange and white respectively.

high activation energies for the hydride shift and the less energetically demanding pathway, with an activation barrier of 60 KJ/mol, is not the most stable and therefore neither the most probable one.

The last step in the mechanism is protonation of cyclohexoxide and desorption of the two products propanone and cyclohexanol, from the catalyst surface. The calculated energy profiles for the MPV reduction over *m*-ZrO_2 and *t*-ZrO_2 compared to that reported for Zr-beta zeolite[96] are depicted in Figure 2. 26. For Zr-beta zeolite (gray line) the reaction occurs through a six-membered transition state and the calculated activation energy for the rate determining step is 64.6 KJ/mol, in good agreement with the experimental value.

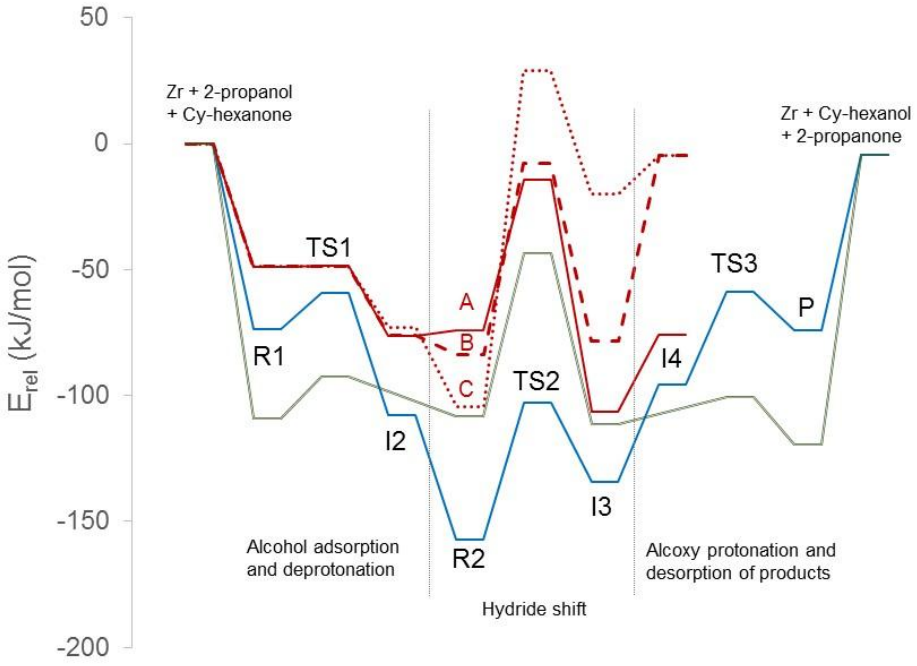

Figure 2. 26. Calculated energy profile of MPV reduction over Zr-beta zeolite (doble gray line), *m*-ZrO_2 (blue line), *t*-ZrO_2 (red line).

On zirconium oxides the hydride shift occurs via seven-membered transition state. On *m*-ZrO_2 the most stable arrangement of cyclohexanone and propoxy fragment is structure R2, in which the hydride shift has an activation energy of 54.4 KJ/mol, also in good agreement with the experimental value. On the other hand, on *t*-ZrO_2 the pathway which shows less activation energy for the hydride shift step (60 KJ/mol) comes from less stable fragment arrangements, and another reagent distribution more

stable but with higher activation energy competes with this one. This explains the lower reactivity of *t*-ZrO_2 associated not to higher activation energy but to entropy effects related with the probability of finding reactant molecules in the proper way.

2.3 Conclusions

Different ZrO_2 and W-ZrO_2 materials were synthetized by a microwave-assisted route for the first time. The variation of different synthetic parameters (pH of the reaction medium, the W- doping level, further thermal treatment…) allows to obtain zirconia in its tetragonal or monoclinic polymorphs, and also stabilize different tungsten species.

The performance of these materials as catalysts were tested for the aldoxime dehydration, alkyne hydration and MPV reduction and compared with reference materials. For the aldoxime dehydration, the most active materials were those having W(VI) species in tetrahedral coordination, mainly found in samples annealed at 500ºC, and the polymorph of zirconia resulted not being relevant on the activity.

In the alkyne hydration, the active species seem to be the interconnected polyoxotungstate clusters and microcrystalline WO_3 supported on the tetragonal polymorph, which is more acid than those species supported on monoclinic zirconia. This fact may be due to the more ionic character of the tetragonal phase compared to the monoclinic one. Furthermore, the microwave-assisted methodology seems to easily incorporate of Zr^{4+} ions in the WO_x clusters located in the tetragonal polymorph.

For the MPV reduction, the most active materials are those which present monoclinic zirconia polymorph, compared with amorphous, tetragonal or modified tungsten zirconias. The different polymorphs show the same apparent activation energy, but differerent pre-exponential frequency factor, which is related with entropy effects. The reaction mechanism over ZrO_2 was theoretically investigated by means DFT calculations and showed that the hydride shift occurs via seven-membered transition state. Moreover *t*-ZrO_2 shows several reactive arrangement with different stabilities that lead hydride shift transition states with different activation energies, while for *m*-ZrO_2 only one pathway is possible. This explains the lower reactivity of *t*-ZrO_2 related to entropy effects that come from the probability of finding the reactant molecules adsorbed in the proper way.

2.4 References

(1) Shukla, S.; Seal, S. *Int. Mater. Rev.* **2005**, *50* (1), 1–20.

(2) Postole, G.; Chowdhury, B.; Karmakar, B.; Pinki, K.; Banerji, J.; Auroux, A. *J. Catal.* **2010**, *269*, 110–121.

(3) García, J.; Quintana, P.; Aguilar, D. H.; López, T.; Gómez, R. *J. Sol-Gel Sci. Technol.* **2006**, *37*, 185–188.

(4) Liu, S.; Ma, J.; Guan, L.; Li, J.; Wei, W.; Sun, Y. *Microporous Mesoporous Mater.* **2009**, *117* (1–2), 466–471.

(5) Thangadurai, P.; Chandra Bose, A.; Ramasamy, S. *J. Mater. Sci.* **2005**, *40*, 3963–3968.

(6) Ghosh, A.; Suri, A. K.; Pandey, M.; Thomas, S.; Rama Mohan, T. R.; Rao, B. T. *Mater. Lett.* **2006**, *60*, 1170–1173.

(7) Reddy, B. M.; Patil, M. K. *Chem. Rev.* **2009**, *109* (6), 2185–2208.

(8) Chen, K.; Xie, S.; Iglesia, E.; Bell, A. T. *J. Catal.* **2000**, *189* (2), 421–430.

(9) Scheithauer, M.; Grasselli, R. K.; Knözinger, H. *Langmuir* **1998**, No. 14, 3019–3029.

(10) Larsen, G.; Lotero, E.; Parra, R. D.; Petkovic, L. M.; Silva, H. S.; Raghavan, S. *Appl. Catal. A Gen.* **1995**, *130*, 213–226.

(11) Hino, M.; Arata, K. *J. Chem. Soc., Chem. Commun* **1988**, 1259.

(12) Arata, K.; Hino, M. *Proc. 9th Int. Congr. Catal. Calgary, Canada, 1988; Philips, M. J., Ternan, M., Eds.; Chem. Inst. Canada, Ottawa, Canada* **1988**, 1727.

(13) Hasan, Z.; Jeon, J.; Jhung, S. H. *J. Hazard. Mater.* **2012**, *205–206*, 216–221.

(14) Sarish, S.; Devassy, B. M.; Böhringer, W.; Fletcher, J.; Halligudi, S. B. *J. Mol. Catal. A Chem.* **2005**, *240*, 123–131.

(15) Barton, D. G.; Soled, S. L.; Meitzner, G. D.; Fuentes, G. A.; Iglesia, E. *J. Catal.* **1999**, *181*, 57–72.

(16) Wang, D.; Osmundsen, C. M.; Taarning, E.; Dumesic, J. a. *ChemCatChem* **2013**, *5*, 2044–2050.

(17) Baertsch, C. D.; Komala, K. T.; Chua, Y.; Iglesia, E. *J. Catal.* **2002**, *205*, 44–57.

(18) Corma, A. *Chem. Rev.* **1995**, *95* (3), 559–614.

(19) Figueras, F.; Palomeque, J.; Loridant, S.; Fèche, C.; Essayem, N.; Gelbard, G. *J. Catal.* **2004**, *226*, 25–31.

(20) Loridant, S.; Feche, C.; Essayem, N.; Figueras, F. *J. Phys. Chem. B* **2005**, *109*, 5631–5637.

(21) Cortés-Jácome, M. A.; Angeles-Chavez, C.; López-Salinas, E.; Navarrete, J.; Toribio, P.; Toledo, J. A. *Appl. Catal. A Gen.* **2007**, *318*, 178–189.

(22) Santiesteban, J. G.; Vartuli, J. C.; Han, S.; Bastian, R. D.; Chang, C. D. *J. Catal.* **1997**, *441*, 431–441.

(23) Cortés-Jácome, M. A.; Toledo, J. A.; Angeles-Chavez, C.; Aguilar, M.; Wang, J. A. *J. Phys. Chem. B* **2005**, *109*, 22730–22739.

(24) Boyse, R. A.; Ko, E. I. *J. Catal.* **1997**, *171*, 191–207.

(25) Lebarbier, V.; Clet, G.; Houalla, M. *J. Phys. Chem. B* **2006**, *110*, 13905–13911.

(26) Friedrich, K.; Wallenfels, K. *The Chemistry of the Cyano Group*, Wiley-Inte.; Rappaport, Z., Ed.; New York, 1970.

(27) Fatiadi, A. *Preparation and synthetic applications of cyano compounds*, Wiley.; Patai, S., Rappaport, Z., Ed.; New York, 1983.

(28) Yan, P.; Batamack, G. K.; Prakash, S.; Olah, G. A. *Catal. Letters* **2005**, *101* (June), 141–143.

(29) Yang, S. H.; Chang, S. *Org. Lett.* **2001**, *3* (7), 4209–4211.

(30) Ishihara, K.; Furuya, Y.; Yamamoto, H. *Angew. Chemie Int. Ed.* **2002**, *41* (16), 2983–2986.

(31) Li, D.; Shi, F.; Guo, S.; Deng, Y. *Tetrahedron Lett.* **2005**, *46* (4), 671–674.

(32) Rezaei, R.; Karami, M. *Chinese Chem. Lett.* **2011**, *22* (7), 815–818.

(33) Thomas, B.; Prathapan, S.; Sugunan, S. *Microporous Mesoporous Mater.* **2005**, *79*, 21–27.

(34) Choi, E.; Lee, C.; Na, Y.; Chang, S. *Org. Lett.* **2002**, *4*, 2369–2371.

(35) Yamaguchi, K.; Fujiwara, H.; Ogasawara, Y.; Kotani, M.; Mizuno, N. *Angew. Chem. Int. Ed. Engl.* **2007**, *46*, 3922–3925.

(36) Berthelot, M. *Acad. Sci. C. R.* **1860**, No. 50, 805–808.

(37) Kutscheroof, M. *Ber. Dtsch. Chem. Ges* **1884**, *17*, 13.

(38) Hennion, G. F.; Killian, D. B.; Vaughn, T. H.; Nieuwland, J. A. *J. Am. Chem. Soc.* **1934**, *56*, 1786.

(39) Marion, N.; Ramo, R. S.; Nolan, S. P. *J. Am. Chem. Soc.* **2009**, *131*, 448–449.

(40) Suzuki, T.; Tokunaga, M.; Wakatsuki, Y. *Org. Lett.* **2001**, *3* (5), 735–737.

(41) Cabrero-Antonino, J. R.; Leyva-Pérez, A.; Corma, A. *Chem. Eur. J.* **2012**, *18* (35), 11107–11114.

(42) Iimura, S.; Manabe, K.; Kobayashi, S. *Org. Biomol. Chem.* **2003**, *1*, 2416–2418.

(43) Huang, J.; Zhu, F.; He, W.; Zhang, F.; Wang, W.; Li, H. *J. Am. Chem. Soc.* **2010**, *132* (100), 1492–1493.

(44) Rao, K. T. V.; Prasad, P. S. S.; Lingaiah, N. *Green Chem.* **2012**, *14*, 1507–1514.

(45) Jin, X.; Oishi, T.; Yamaguchi, K.; Mizuno, N. *Chem. Eur. J.* **2011**, *17* (4), 1261–1267.

(46) Graauw, C. F. de; Peters, J. A.; Van, B. H.; J., H. *Synthesis (Stuttg).* **1994**, *10*, 1007–1017.

(47) Verley, A. *Bull. Soc. Chem. Fr.* **1925**, *37*, 537.

(48) Meerwein, H.; Schmidt, R. *Liebigs Ann. Chem.* **1925**, *444*, 221–238.

(49) Ponndorf, W. *Angew. Chem.* **1926**, *39*, 138–143.

(50) Makoto, S.; Takahashi, K.; Matsushita, H. *Bull. Chem. Soc. Jpn.* **1988**, *61*, 3283–3288.

(51) Aramend, A. M.; Borau, V.; Jiménez, C.; Marinas, J. M.; Ruiz, J. R.; Urbano, F. J. *Appl. Catal. A Gen.* **2003**, *244*, 207–215.

(52) Liu, S. H.; Jaenicke, S.; Chuah, G. K. *J. Catal.* **2002**, *206* (2), 321–330.

(53) Corma, A.; Domine, M. E.; Nemeth, L.; Valencia, S. *J. Am. Chem. Soc.* **2002**, No. 124, 3194–3195.

(54) Corma, A.; E, D. M.; Valencia, S. *J. Catal.* **2003**, *215* (2), 294–304.

(55) Zhu, Y.; Chuah, G.; Jaenicke, S. *J. Catal.* **2004**, *227* (1), 1–10.

(56) Zhu, Y.; Chuah, G. K.; Jaenicke, S. *J. Catal.* **2006**, *241* (1), 25–33.

(57) Tanabe, K.; Yamaguchi, T. *Catal. Today* **1994**, *20*, 185–198.

(58) Miñambres, J. F.; Aramendía, M. a.; Marinas, A.; Marinas, J. M.; Urbano, F. J. *J. Mol. Catal. A Chem.* **2011**, *338*, 121–129.

(59) Urbano, F. J.; Aramendía, M. a.; Marinas, A.; Marinas, J. M. *J. Catal.* **2009**, *268* (1), 79–88.

(60) Miñambres, J. F.; Marinas, A.; Marinas, J. M.; Urbano, F. J. *Appl. Catal. B Environ.* **2013**, *140–141*, 386–395.

(61) Li, W.; Huang, H.; Li, H.; Zhang, W.; Liu, H. *Langmuir* **2008**, *24* (15), 8358–8366.

(62) Cortés-Jácome, M. a.; Angeles-Chavez, C.; Bokhimi, X.; Toledo-Antonio, J. a. *J. Solid State Chem.* **2006**, *179* (8), 2663–2673.

(63) Soultanidis, N.; Zhou, W.; Psarras, A. C.; Gonzalez, A. J.; Iliopoulou, E. F.; Kiely, C. J.; Wachs, I. E.; Wong, M. S. *J. Am. Chem. Soc.* **2010**, *132* (38), 13462–13471.

(64) Zhou, W.; Ross-Medgaarden, E. I.; Knowles, W. V; Wong, M. S.; Wachs, I. E.; Kiely, C. J. *Nat. Chem.* **2009**, *1* (9), 722–728.

(65) Martinez, A.; Prieto, G.; Arribas, M.; Concepcion, P.; Sanchezroyo, J. *J. Catal.* **2007**, *248* (2), 288–302.

(66) Ogasawara, Y.; Uchida, S.; Yamaguchi, K.; Mizuno, N. *Chem. - A Eur. J.* **2009**, *15*, 4343–4349.

(67) Ogasawara, Y.; Uchida, S.; Yamaguchi, K.; Mizuno, N. *Chem. Eur. J.* **2009**, *15*, 4343–4349.

(68) Li, W.; Huang, H.; Li, H.; Zhang, W.; Liu, H. *Langmuir* **2008**, *24* (15), 8358–8366.

(69) Tosan, J.-L.; Durand, B.; Roubin, M.; Chassagneux, F.; Mosoni, L.; Bertin, F.; Moraweck, B. *J. Non. Cryst. Solids* **1993**, *160* (1–2), 167–176.

(70) Tosan, J.-L.; Durand, B.; Roubin, M.; Chassagneux, F.; Bertin, F. *J. Non. Cryst. Solids* **1994**, *168* (1–2), 23–32.

(71) Southon, P. D.; Bartlett, J. R.; Woolfrey, J. L.; Ben-Nissan, B. *Chem. Mater.* **2002**, *14* (10), 4313–4319.

(72) Ambrosi, M.; Fratini, E.; Canton, P.; Dankesreiter, S.; Baglioni, P. *J. Mater. Chem.* **2012**, *22* (44), 23497.

(73) Thot, L. M.; Lin, J. S.; Felker, L. K. *J. Phys Chem* **1991**, *95* (3), 3106–3108.

(74) Clearfield, A.; Vaughan, P. A. *Acta Crystallogr.* **1956**, *9* (7), 555–558.

(75) Jung, K. T.; Bell, A. T. *J. Mol. Catal. A Chem.* **2000**, *163* (1–2), 27–42.

(76) Clearfield, A.; Serrette, G. P. D.; Khazi-Syed, A. H. *Catal. Today* **1994**, *20* (2), 295–312.

(77) Livage, J.; Doi, K.; Mazières, C. *J. Am. Ceram. Soc.* **1968**, *51* (6), 349–353.

(78) Denkewicz, R. P.; TenHuisen, K. S.; Adair, J. H. *J. Mater. Res.* **1990**, *5* (11), 2698–2705.

(79) Jolivet, J.-P. *De la solution à l'oxyde*; EP Sciences-CNRS Editions: Paris, 2015.

(80) Samson, K.; Sliwa, M.; Socha, R. P.; Góra-Marek, K.; Mucha, D.; Rutkowska-Zbik, D.; Paul, J.-F.; Ruggiero-Mikolajczyk, M.; Grabowski, R.; Sloczynski, J. *ACS Catal.* **2014**, *4*, 3730–3741.

(81) Rhodes, M. D.; Bell, A. T. *J. Catal.* **2005**, *233* (1), 198–209.

(82) Rhodes, M. D.; Pokrovski, K. A.; Bell, A. T. *J. Catal.* **2005**, *233* (1), 210–220.

(83) Li, J.; Chen, J.; Song, W.; Liu, J.; Shen, W. *Appl. Catal. A Gen.* **2008**, *334* (1–2), 321–329.

(84) Grabowski, R.; Sloczynski, J.; Sliwa, M.; Mucha, D.; Socha, R. P. *ACS Catal.* **2011**, *1*, 266–278.

(85) Campa, M. C.; Ferraris, G.; Gazzoli, D.; Pettiti, I.; Pietrogiacomi, D. *Appl. Catal. B Environ.* **2013**, *142–143*, 423–431.

(86) Julián-López, B.; De La Luz, V.; Gonell, F.; Cordoncillo, E.; López-Haro, M.; Calvino, J. J.; Escribano, P. *J. Alloys Compd.* **2012**, *519*, 29–36.

(87) Zhu, Y.; Liu, S.; Jaenicke, S.; Chuah, G. *Catal. Today* **2004**, *97* (4), 249–255.

(88) Cohen, R.; Graves, C. R.; Nguyen, S. T.; Martin, J. M. L.; Ratner, M. A. *J. Am. Chem. Soc.* **2004**, *126* (6), 14796–14803.

(89) Sushkevich, V. L.; Ivanova, I. I.; Tolborg, S.; Taarning, E. *J. Catal.* **2014**, *316*, 121–129.

(90) Zhang, B.; Tang, M.; Yuan, J.; Wu, L. *Chinese J. Catal.* **2012**, *33* (4–6), 914–922.

(91) Komanoya, T.; Nakajima, K.; Kitano, M.; Hara, M. *J. Phys. Chem. C* **2015**, *119*, 26540–26546.

(92) Christensen, A.; Carter, E. A. *Phys. Rev. B* **1998**, *58* (12), 8050–8064.

(93) Ricca, C.; Ringuedé, A.; Cassir, M.; Adamo, C.; Labat, F. *J. Comput. Chem.* **2015**, *36*, 9–21.

(94) Morterra, C.; Cerrato, G.; Ferroni, L.; Montanaro, L. *Mater. Chem. Phys.* **1994**, *37*, 243–251.

(95) Cerrato, G.; Bordiga, S.; Barbera, S.; Morterra, C. *Appl. Surf. Sci.* **1997**, *115*, 53–65.

(96) Boronat, M.; Corma, A.; Renz, M. *J. Phys. Chem. B* **2006**, *110* (42), 21168–21174.

Chapter 3

Nanomaterials for selective hydrogenations

The content of this chapter is classified as CONFIDENTIAL, thus its content will not be shown.

Chapter 4

Nanomaterials for photocatalysis

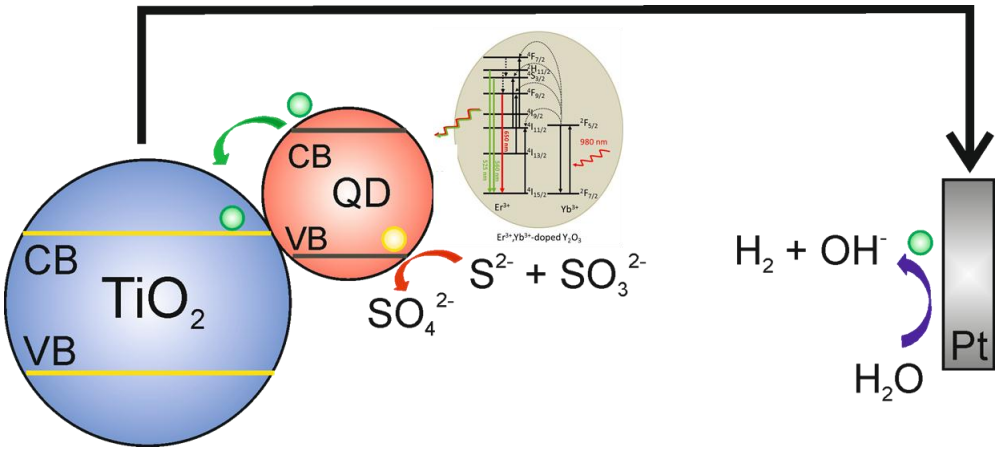

4.1 Introduction

Photocatalysis can be defined as the acceleration of a photoreaction by the presence of a catalyst. Extensive research in understanding the fundamental processes and in enhancing the efficiency of photocatalytic materials have been performed by chemists, physicists, and chemical engineers. In recent years, applications to energy production as well as environmental cleanup have been two of the most active areas in heterogeneous photocatalysis. Hence, this chapter deals with the implementation of different nanomaterials in photocatalytic processes related with energy and environmental issues, in particular, for hydrogen production, CO_2 removal and water purification. The aim is to provide more sustainable and less impacting photocatalytic nanotechnologies.

4.1.1 Photocatalysis for environmental issues: CO_2 conversion and water purification

The human race has been living in the planet earth since 195000 years. During most of this time the interaction between the humanity and the nature has arrived to equilibrium in which human took from the nature what they need to live and this one produces again the resources, due to its high capacity to grow up. The humanity began to control the nature with the appearance of the agriculture and the animal domestication thus the number of human beings increased. But no was until the industrial revolution and the application of fertilizers, for the intensive agriculture, when the demography increased to high levels. As a consequence of all these, there was an increasing demand of energy and goods which were satisfied with the use of non-renewable energies sources.

Since the fossil fuels reserves will not last forever, in the last years environmental conscience has emerged regarding the need to keep the natural resources and to minimize the human footprint. Thus, several technologies and renewable energy sources, as hydraulic, wind power, biomass, etc. have emerged. Among them the most abundant and available is the solar energy which plants have been using since ancient times.

An important issue from the environmental point of view is the CO_2 conversion to other useful molecules. With the use of fossil fuels as energy source in the last years, a worrying increase of the CO_2 concentration in the atmosphere has emerged, producing a temperature rise around the world known as global warming. The use of

CO_2 as raw material has two advantages: its high availability and the decrease of its concentration in the atmosphere leading to more environmentally friendly processes.

Since CO_2 is a highly stable molecule, its transformation requires a high amount of energy. Then, the use of catalysts is highly desirable in the CO_2 conversion in order to increase the efficiency for the production of methanol, carboxylic acids, polycarbonates, polylactones or hydrocarbons[1–5] One possible strategy to activate the C-O bonds is by using metallic catalysts and a renewable energy source such as solar light. In this sense, several works have been carried out using nanomaterials composed of Ni[6] or Ru[7] for the CO_2 reduction with H_2, despite being more desirable to use H_2O as reducing agent, which is a big challenge. Another approach involves the use of semiconductors, such as TiO_2, and co-catalysts for improving the efficiency of the processes[8–11].

In the last years several authors have reported the ability of Cu-TiO_2 system for the photocatalytic reduction of CO_2. Different synthetic methodologies have been developed in order to afford these materials, such as impregnation[12], sol-gel[13], etc., and very different catalytic results for the aforementioned reaction have been reported.

To illustrate the controversial results found in the literature, let us focus on the Cu-TiO_2 system prepared by deposition of cupper species onto titania surface by impregnation techniques. Salmet *et al.* showed high production rates of methanol (443 μmol $g_{cat}^{-1}h^{-1}$)[12] irradiating an aqueous CO_2 solution with black light. Other studies of similar Cu-impregnated TiO_2 materials reported the production of methanol but in lower yields under different irradiating condition (10-23 μmol $g_{cat}^{-1}h^{-1}$)[13,14]. Conversely, Richardson *et al.* demonstrated the production of CO, methane, ethane, ethylene and high amounts of H_2 with the same catalyst[15]. Taking all these precedents into account, it is quite clear that the results obtained in this reaction using Cu/TiO_2 as catalyst are quite heterogeneous. Thus, small variations in the synthetic protocols and irradiation conditions entail important modifications on the activity and mechanisms of the photoreaction. Moreover, special attention has to be paid with the carbonaceous residues or contaminations in the catalyst that can lead to wrong CO_2 reduction quantifications.[16]

Novel synthetic pathways and accurate photoreaction conditions need to be developed in order to provide not only highly efficient Cu/TiO_2 nanomaterials but also reliable photocatalytic results. Hence, in the first part of this chapter, the synthesis of Cu doped titania through a solvothermal procedure is disclosed. This methodology allows the dispersion of Cu species within the titania framework in such a good way that

very efficient catalysts are obtained. The materials were tested for the photocatalytic CO_2 reduction in aqueous media in the presence of different solutes, acting as sacrificial electron donating agents.

Among the different solutes tested, the use of sulfide anions is particularly interesting for its environmental implication. This anion is a common water pollutant usually found in sewage effluents.[17] Sulfide and its conjugated acid, hydrogen sulfide, is a common by-product in the petrochemical processing[18 19], which is converted to sulfur, so there is an intense research looking for new practical applications of this by-product. In this thesis chapter, we propose to use the sulfides present in residual water as sacrificial electron donor in the photocatalytic production of fuels. .

Thus, this section is focused to the development of new Cu-TiO_2 catalysts for combined action in the CO_2 photoreduction and the sulfide removal from water.

4.1.2 Photocatalysis for energy production: solar hydrogen generation

The solar spectra which arrives to the sea level consists in 5% of ultraviolet (UV) light, 40% visible (VIS) light and 55% of infrared (IR) light,[20] as Figure 4. 1 shows. Classically, the solar energy devices only takes profit of the most energetic part of the solar spectra (UV-VIS), being the IR part wasted, despite being the most abundant. Several strategies have emerged in order to take profit of this energy. Among them, one of the most exciting and promising is the introduction of up-conversion materials in solar cells devices.

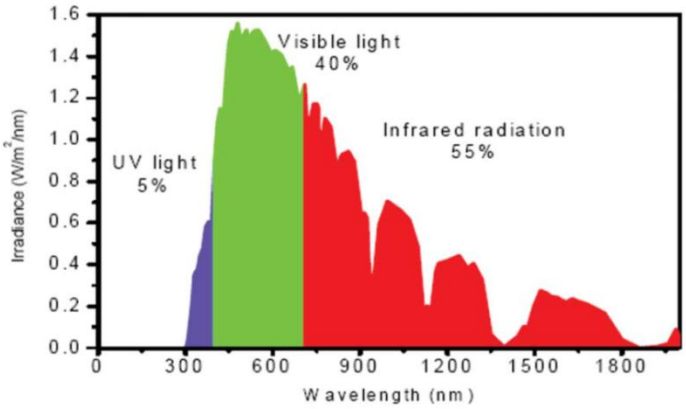

Figure 4. 1. Solar spectrum at sea level, after the absorption of the different atmosphere layers.[20]

The photon up-conversion (UC) is a physical process in which the sequential absorption of two or more photons leads to the emission of light, energetically higher than the incident radiation (Figure 4. 2). This phenomenon is widely known for over 50 years[21] but only in recent years with the control of different synthetic approaches at the nanoscale level, they become interesting for new technologies such as photonics[22], photocatalysis[23, 24], photovoltaics[25], sensors[26], biotechnology[27], etc.

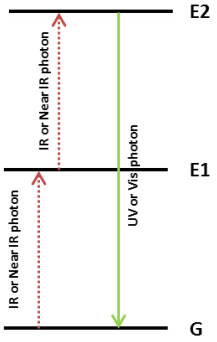

Figure 4. 2. Scheme of an UC process.

The most studied UC systems are inorganic matrices doped with lanthanide ions (e.g. Er^{3+}, Tm^{3+}, Yb^{3+}). Among them, hexagonal phase of $NaYF_4$ is the most studied because is by far the most efficient up-converter due to a wide energy bandgap (~8eV) and its low phonon energy (~360 cm^{-1})[27], as compared to oxide nanocrystals[28]. Even so, it presents several disadvantages such as limited thermal and chemical

stability, complex synthetic pathways and the use of highly toxic and expensive fluoride reagents.

An alternative to fluoride compounds, even being less efficient, are metal oxides which present low toxicity and its optical, structural and morphological properties can be easily tuned through controlled synthetic pathways. Yttrium Oxide, Y_2O_3, is one of the most studied material due to its low phonon energy (300-380cm^{-1})[29], ease to be doped with rare earths ions, broad transparency range (0.2-8 µm), large band gap (5.8 eV) and excellent physical, chemical and thermal stability.[30]

The second section of this thesis chapter is devoted to the synthesis of submicrometric up-converting Y_2O_3 nanoparticles codoped with Er^{3+} and Yb^{3+} ions and their incorporation into heterostructured TiO_2/CdSe photoanodes for H_2 generation. The results of the structural and optical characterization of the nanomaterials as well as the photocurrent generation of the final device under near infrared irradiation will be shown.

4.2 Results and discussion

4.2.1 Photocatalysis for environmental issues: CO_2 conversion and water purification.

In this section, the synthesis of Cu-TiO_2 samples and their photocatalytic activity in reactions with environmental implications are evaluated.

4.2.1.1 Cu-doped Titania synthesis and characterization

The synthesis of Cu-TiO_2 was carried out following a solvothermal methodology previously reported by our group[31] with some modifications. Briefly, the proper amounts of $Cu(Ac)_2$ and $Ti(iOPr)_4$ for obtaining 1g of the material were dissolved in 50mL of EtOH. Once dissolved, acetylacetonate (acac) was added in a molar ratio metal (Cu+Ti):acac 1:2 in order to afford the corresponding complex and to avoid the un-controlled hydrolysis and condensation[32] of the reagents. The mixture was stirred for 0.5 hours and transferred into a 125 teflon-lined autoclave and heated to 180ºC for

24h. The solid products were washed with EtOH, isolated by centrifugation several times and dried at 100ºC overnight.

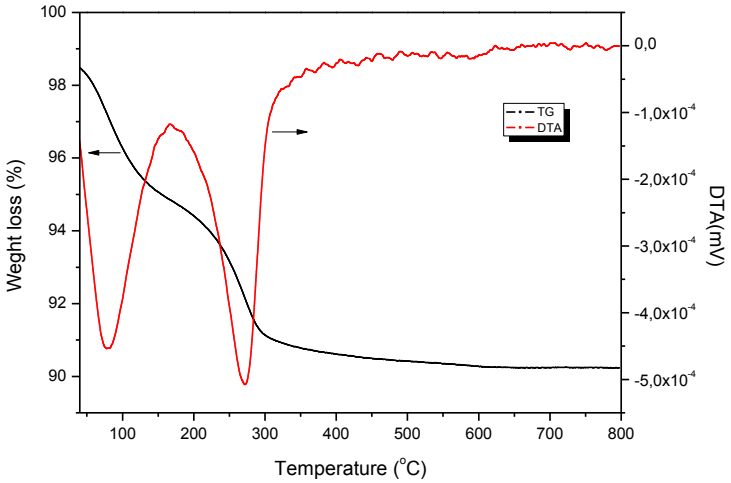

Figure 4. 3. TG (black line) and DTA (red line) of 3CT.

These materials are designated as XCT (X=0, 0.5, 1.0, 1.5, 2.0 and 3.0 where X is the molar percentage of Cu relative to the sum of Cu and Ti atoms in the structure). The thermal behavior of 3CT was studied by DTA-TG as a representative sample (Figure 4. 3). The thermal curves of the as-prepared material exhibit two steps: a first weight loss was recorded at around 80ºC (most likely due to desorption of both water and residual solvents), and a second one at around 275ºC (probably related to the combustion of organic moieties from acetate and acetylacetone derivatives, and corresponding to ca. 10% organic matter by weight). According to the TGA results, the XCT materials were calcined in air at 500ºC for 2 hours in order to remove any possible organic moiety, thus yielding the final XCT500 samples (X= 0.0, 0.5, 1.0, 1.5, 2.0 and 3.0).

The XRD patterns of the as-prepared materials (Figure 4. 4a) show an incipient crystallization of the system, while after the heat treatment at 500ºC much more intense diffraction peaks are observed, indicating that the crystal size increased (Figure 4. 4b). In both cases, the single crystalline phase detected was anatase TiO_2 (JCPDS 21-1272). This is the first indication that a successful solid solution has been obtained. The average crystallite size of the Cu-doped anatase materials was calculated by Scherrer equation. In the annealed samples, a similar crystal size of around 20 nm was estimated.

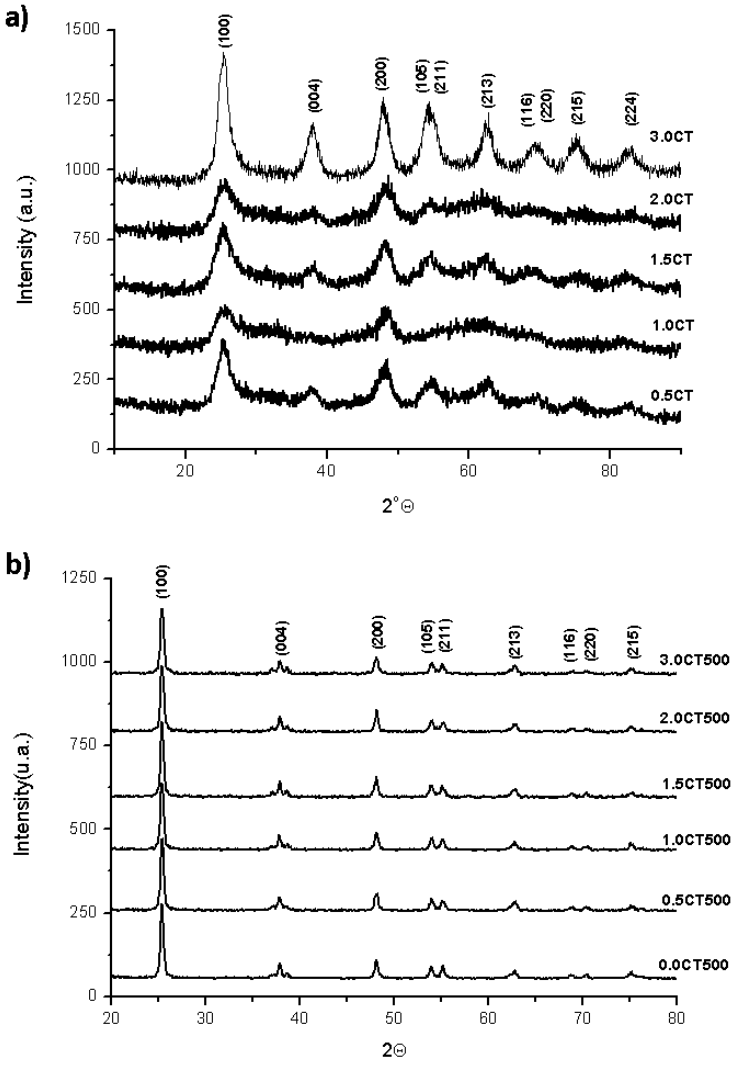

Figure 4. 4. XRD patterns of a) XCT and b) XCT500 samples.

Since these materials will be tested as photocatalysts, it is important to know their specific surface area. Thus, nitrogen adsorption and desorption experiments were conducted. The BET surfaces areas of these materials were calculated, obtaining poor

values; lower than 3 m^2/g (Table 4. 1). These values are much lower than expected, so we decided to revise the synthetic procedure.

Table 4. 1. Crystal sizes and BET surface area of XCT500 samples

Sample	Crystal Size (nm)	$S_{BET}(m^2/g)$
3.0CTH500	19.9	2.69
2.0CTH500	22.6	1.53
1.5CTH500	20.9	1.09
1.0CTH500	20.4	0.14
0.5CTH500	20.4	0.35
0.0CTH500	22.0	0.75

An important remark about this synthesis was that the clear supernatant isolated by centrifugation after the synthesis, in the presence of the humidity from air, became turbid. The solid originating this turbidity was isolated by solvent evaporation and further calcined at 500ºC leading to anatase TiO_2. This fact indicates that the reaction was uncomplete. Therefore, the synthesis protocol was modified by adding a small amount of water in order to complete the hydrolysis and condensation of the Ti alkoxide.

A new set of samples (named XCTH) were prepared following the same procedure but adding small amounts of water (0.9mL) before the solvothermal treatment.

The XRD patterns of this new samples (Figure 4. 5) present the same crystal phase (anatase) but higher degree of crystallinity than those synthetized in the absence of water. The average crystallite size estimated from Scherrer equation was found to be around 6.5 nm.

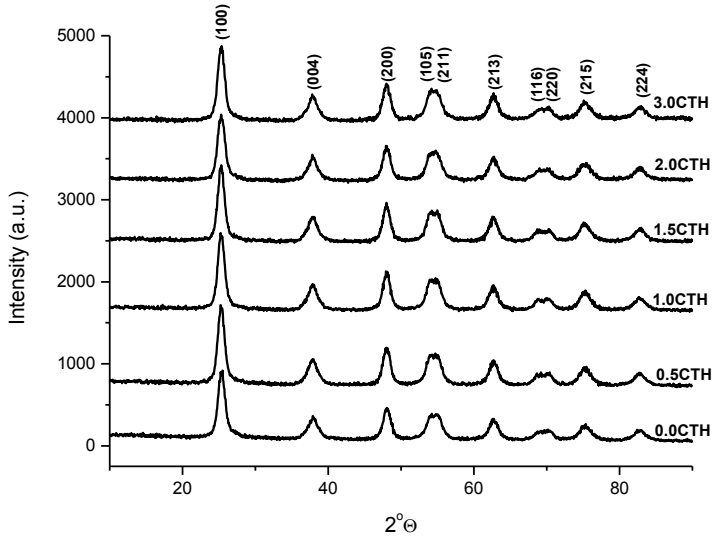

Figure 4. 5. XRD patterns of the as synthetized XCTH.

The thermal behavior was similar to the previous materials prepared in the absence of water, so in order to remove all the organic moieties, they were treated at 500ºC. After this treatment, the anatase phase is preserved, but the XRD peaks become sharper as a consequence of the crystallization of any remaining amorphous domains, diminution of lattice defects and crystal growth. The Scherrer calculations indicate larger, but still nanometric, crystallite sizes of around 13 nm (Table 4. 2). In contrast to the as-synthetized materials, the peaks of the annealed Cu-doped samples show a shift towards lower 2θ values in comparison to the TiO_2 reference (Figure 4. 6). The figure shows this effect for the signal associated with the (101) planes at ca. 25.3. Taking into account the ionic radii of the copper and titanium ions in octahedral coordination (Cu^{2+}: 73 pm and Ti^{4+}: 60.5 pm)[33], the shift agrees with a substitutional solid solution in which Cu ions would occupy the Ti sites in the TiO_2 lattice. No

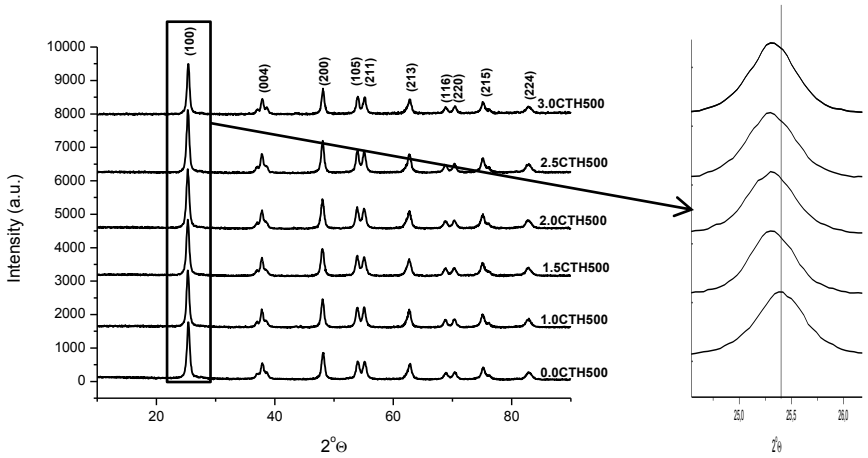

Figure 4. 6. XRD patterns of XCTH500, inset right side shows the shift of the (101) plane.

peaks from CuO or Cu_2O phases were observed. These results point out the importance of the presence of a small amount of water in this synthetic procedure. This addition produces higher reaction yields and smaller crystal sizes of the annealed materials than the anhydrous procedure. Therefore, all the study was continued with this new set of samples.

Table 4. 2. Crystallite size, BET surface area and band gap of X-CTH samples.

Sample	Crystallite size (nm) as-prepared	Crystallite size (nm) after calcination	S_{BET} (m^2/g)	band gap (eV)
3.0Cu-TiO_2	6.6	13.1	37.2	2.98
2.0Cu-TiO_2	6.6	13.5	38.3	3.06
1.5Cu-TiO_2	6.4	12.9	49.2	3.10
1.0Cu-TiO_2	6.8	12.9	46.1	3.12
0.5Cu-TiO_2	6.9	14.1	30.2	3.14
TiO_2	6.6	12.9	45.7	3.17

Figure 4. 7 shows the Raman spectra of the X-CTH-500 samples. All the signals recorded correspond to the anatase phase, in good agreement with the XRD analysis. The spectra are characterized by an intense band at 144 cm^{-1}, three less intense bands at 396, 517, 639 cm^{-1} and a shoulder at 196 cm^{-1}, which correspond to the TiO_2 vibrational modes of E_g, B_{1g}, A_{1g}, B_{1g}, and E_g, symmetries, respectively[34]. As in the case of XRD, the presence of CuO or Cu_2O could not be detected by Raman,[35] although that possibility cannot be completely discarded due to the low copper contents.

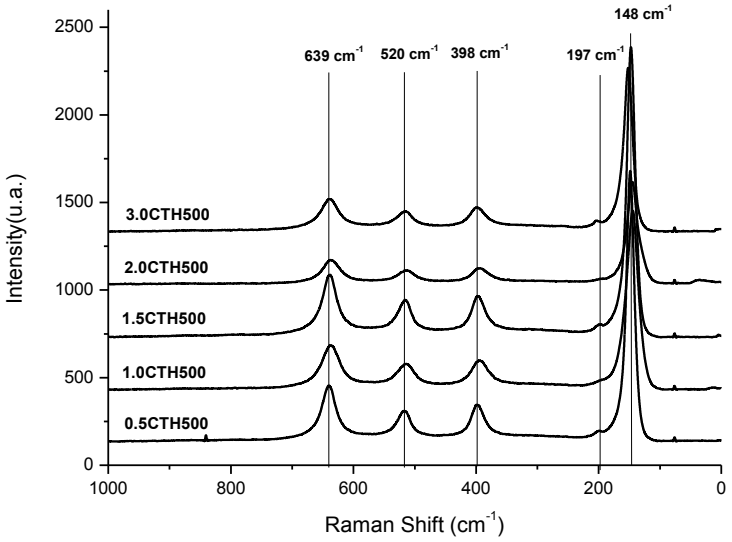

Figure 4. 7. Raman spectra of X-CTH samples.

The field emission gun scanning electron microscopy (FEG-SEM) images of the annealed samples (Figure 4. 8) reveal that the Cu-TiO_2 materials were composed by aggregates of small nanoparticles. Therefore, a more detailed analysis by transmission electron microscopy (TEM) was also performed.

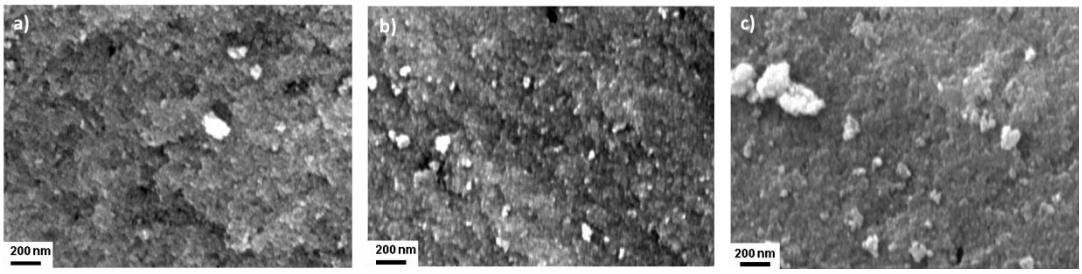

Figure 4. 8.FEG-SEM micrographs of a) 1%Cu-TiO_2, b) 2%Cu-TiO_2 and c) 3%Cu-TiO_2.

Characterization of the morphology and structure of 3.0CTH (selected as representative sample) by high-resolution transmission electron microscopy (HR-TEM, (see Figure 4. 9) confirmed that the non-calcined material consists of agglomerates of quasi-spherical nanocrystalline particles with a size of 7 nm, which fits well with the crystal size calculated by the Scherrer equation (see above).

After annealing, the morphology was mostly preserved. The material is composed of small particles (10-15 nm) agglomerated into bigger aggregates, confirming the crystal growth previously pointed out in the XRD analysis (Figure 4. 10)

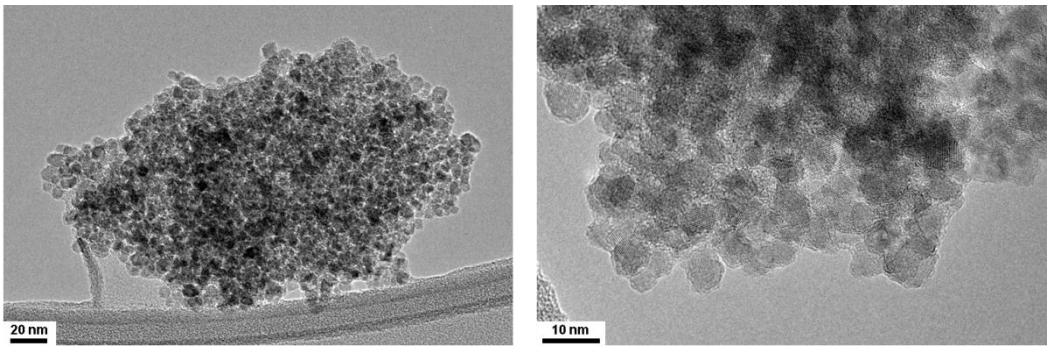

Figure 4. 9. HR-TEM micrographs of 3.0CTH.

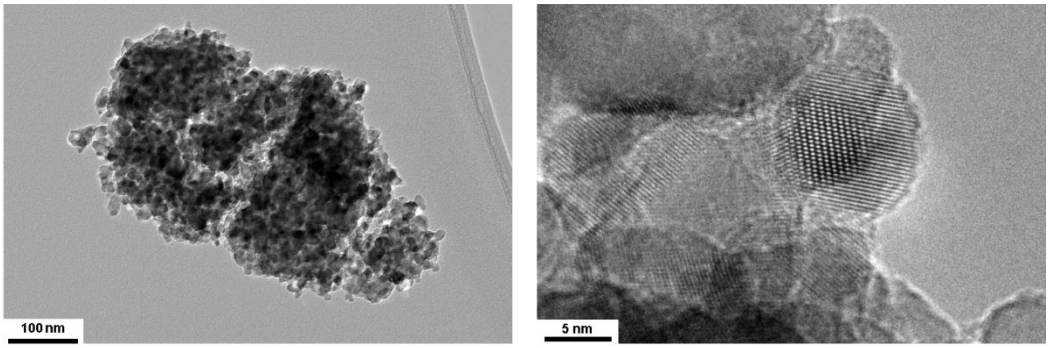

Figure 4. 10. HR-TEM micrographs of 3.0Cu-TiO_2-500.

The planar distances of the crystalline particles measured from the HR-TEM images fit well with the distance of anatase planes (3.5 Å for 101 plane). No segregated copper species or particles were detected for any copper-doped samples. Furthermore, elemental mapping analysis performed by energy dispersive X-ray (EDX) spectroscopy under scanning transmission mode, indicates a good dispersion of copper throughout the solid (Figure 4. 11). These observations suggest that an effective solid solution is obtained, in good agreement with XRD and Raman data.

Textural properties were studied by N_2 adsorption-desorption showing a BET surface area around 30–50 m^2/g with no dependence on the Cu content. As expected, when crystal sizes estimated by the Scherrer equation decrease, BET surface areas increase (Table 4. 2). These results point out the importance of the water addition in the synthetic protocol, going from very low BET surface areas for the water-free synthesis to 30-50 m^2/g after water addition.

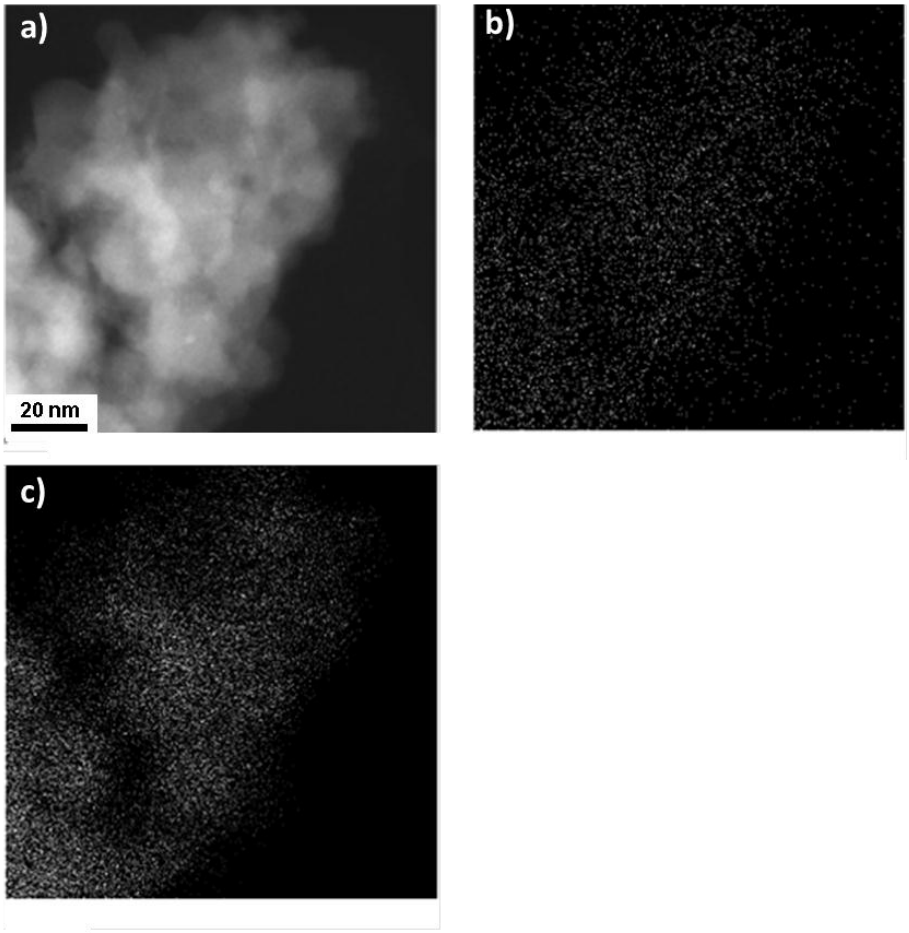

Figure 4. 11. a) Scanning transmission electron microscopy (STEM) image recorded by a high-angle annular dark field (HAADF) detector of 3.0Cu-TiO_2 sample, and b) copper and c) titanium elemental mapping of the same region performed by energy dispersive X-ray (EDX) spectroscopy.

Regarding the optical characterization, Figure 4. 12 shows the diffuse reflectance UV-VIS (DRUV-VIS) spectra of the different Cu-doped samples. As previously mentioned, TiO_2 is a semiconductor exhibiting a wide band gap (Eg) of around 3.17 eV (value estimated from the 0.0CTH500 spectrum using the relation proposed by Tauc, David and Mott), thus only light below 400 nm is absorbed and capable of forming the e^-/h^+ pair. Upon addition of Cu, the absorption edge shifts towards the visible region, and the band gap decreases from 3.17 to 2.98 eV when the doping level goes from 0 to 3% (Figure 4. 12). The band gap shift can be attributed to the incorporation of Cu species within the TiO_2 lattice, what introduces new energy levels

to the intra-band space. The broad band between 600 and 800 nm could be ascribed to d-d transitions of Cu^{2+} in O_h symmetry with a tetragonal distortion. Anyway, the presence of metallic copper was discarded since no bands at 580-590 nm were observed [36 37 38].

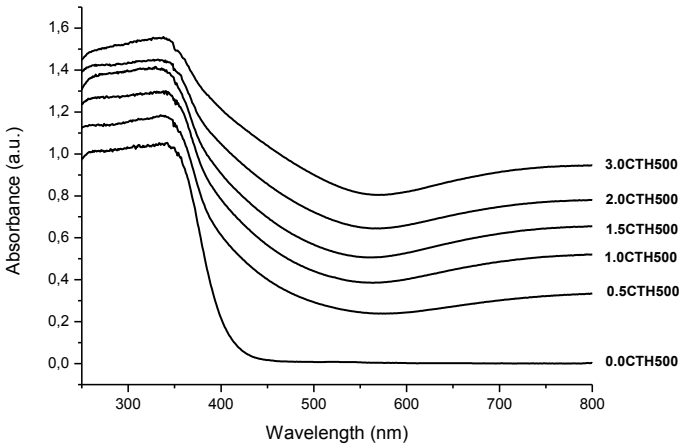

Figure 4. 12. DRUV-VIS spectra of *X*CTH500.

The different samples were studied by X-ray photoelectron spectroscopy (XPS) in order to gain insight about the oxidation state of cupper. A reference catalyst was prepared by impregnation of commercial titania P25 (from Degussa) with 3%wt of Cu ions and annealed at 500ºC (3CTimp500) for comparison purposes.

The low Cu content in the samples and the Cu reduction under the X-ray beam made difficult the registration of XPS spectra with a good quality. The experimental conditions were optimized but short accumulation times were required, thus some uncertainties in the binding energies must be considered.

Despite that, the position of Cu 2p3/2 photoelectron energies are listed in Table 4. 3 for comparison. In all cases, the bands were deconvoluted in one component, indicating that cupper was present in only one oxidation state. The reference material shows higher binding energy than the doped samples. This fact suggests that in the reference material the cupper species (probably CuO) are more positively charged than in the *X*CTH500 samples. Moreover, in the doped samples a slight but steady decrease in the binding energy was observed when the Cu content decreases, which implies a lower positive charge density of Cu ions.

Table 4. 3. XPS data for 3.0CTimp500 and *X*CTH500 samples.

Photocatalyst	Cu 2p3/2 binding energy/eV
3.0Ctimp500	935.3
3.CTH500	934.5
2.0CTH500	933.6
1.5CTH500	934.1
1.0CTH500	932.3
0.5CTH500	932.7

4.2.1.2 Photocatalytic CO_2 reduction

The different Cu-TiO_2 materials were tested for the photocatalytic reduction of CO_2 in aqueous media under UV-rich mercury lamp under different reaction conditions. The liquid and gas phases obtained after reactions were further analyzed.

First, 3.0CTH500 sample was selected to optimize the photocatalytic reaction conditions. This composition was expected to be the most efficient catalyst due to the higher amount of cupper and its low band gap. After that, the effect of the cupper content on the photoreaction was investigated.

A blank experiment was also carried out irradiating the catalyst suspended in water in Ar atmosphere. The existence of any photocatalytic product was not observed (Table 4. 4, entry 1). This fact precludes the presence of residual organic moieties adsorbed at the surface of the catalysts which could afford non-desired byproducts. This is in good agreement with the DTA-TG analysis. In this way, all the products detected after the photocatalytic reactions with CO_2 can be attributed to the reduction of this gas. Moreover, no H_2 was generated under these reaction conditions, discarding any influence of water splitting in the study.

Different sacrificial electron donors (*solute* in Table 4. 4) were used in order to promote the photoreduction of the unreactive CO_2. The reaction with CO_2 atmosphere

but without the presence of any electron donor gives small amount of products (Table 4. 4, entry 2).

The use of NaOH as solute was tested in order to increase pH and solubility of CO_2 in the aqueous media, forming carbonate and bicarbonate species. No liquid products were detected and only small amounts of CO were produced (Table 4. 4, entry 3).

Sodium halides (Cl^- and Br^-) were also employed, but no liquid products were afforded. Only small amounts of CO and H_2 were produced (Table 4. 4, entry 4 and 5 respectively).

At this point, the use of a more easily reducible sacrificial electron donor as sulfur-based anions was tried. Sodium sulfide (Na_2S) was found to produce high amount of H_2 and formic acid (HCOOH) and small amounts of CO (Table 4. 4, entry 6). The production of H_2 is caused by the competitive reduction of water, because it is much easier to reduce water than the high stable CO_2 molecule. These results become significant when comparing these values with the best results reported in the literature for the same kind of materials.[13,14,39] Additionally, in our work, the amount of sulfide is very low and no additional reducing agents are required, as usually happens with ZnS photocatalysis.[40]

Regarding the catalytic activity of the samples synthetized by the solvothermal method and the one prepared by impregnation, we can conclude that the first one is much more active. The reference sample (3.0Ctimp) in the presence of sulfide led to the formation of lower amounts of H_2 and CO (175.9 and 0.5 μmol $g_{cat}^{-1}h^{-1}$, respectively) and no formation of formic acid was detected (Table 4. 4 entry 7). Moreover, it was also inactive without the presence of any sacrificial electron donor (Table 4. 4 entry 8).

Table 4. 4. Product yields for the photocatalytic reduction under UV-rich light on 3.0CTH500[a)]

			Production rate/μmol g_{cat}^{-1} h^{-1}			
			Gas phase			Liquid phase
Entry	**Solute**	**Photocatalyst**	**CH_4**	**CO**	**H_2**	**HCOOH**
1	-[b)]	3.0CTH500	-	-	-	-
2	-	3.0CTH500	0.3	0.3	0.6	-
3	NaOH (100 mM)	3.0CTH500	-	0.3	-	-
4	NaCl (500 mM)	3.0CTH500	-	0.8	1.8	-
5	NaBr (500 mM)	3.0CTH500	-	0.5	0.7	-
6	Na_2S (13 mM)	3.0CTH500	-	2.8	209.4	25.7
7	Na_2S (13 mM)	3.0CTimp	-	0.5	175.9	-
8	-	3.0CTimp	-	-	-	-

[a)] Reaction conditions: catalyst (25mg) in water (25mL) containing the specified sacrificial electron donor (solute) in CO_2 atmosphere (1.4bar) at 25ºC for 15 hours under Hg lamp irradiance (125W). Hyphens denote values lower than the corresponding detection limits. [b)] Performed under Ar atmosphere (1.4bar) without CO_2.

In order to check if the formic acid product (entry 6, Table 4. 4) comes from CO_2 or any carbonaceous residue present in the catalyst, the same experiment was performed with ^{13}C labeled carbon dioxide, $^{13}CO_2$. The formic acid produced in this reaction was analyzed by ^{13}C nuclear magnetic resonance (^{13}C NMR) confirming the formation of $[H^{13}COO]^-$ (δ= 170ppm) together with $[H^{13}CO_3]^-$ and $^{13}CO_2$, while in the experiment with regular CO_2 no ^{13}C NMR signal was observed.

These results suggest that doping titania with copper led to a much more homogeneous distribution of copper in the host matrix than in the impregnated sample, leading to isolated cupper atoms which promotes an efficient transfer of the photogenerated charges from titania. Moreover, the presence of these isolated atoms

would result in more accessible catalytic active sites, compared to the impregnated samples where copper is presented as particles or aggregates.

The influence of cupper content of the catalyst was also studied performing the photoreduction of CO_2 under the best reaction conditions. Figure 4. 13 shows the production of H_2, CO and HCO_2H vs cupper loading. The main product for all catalysts was H_2 (Figure 4. 13, white bars) whose production increases until a maximum at 2.0CTH500 (313.2 μmol $g_{cat}^{-1}h^{-1}$) and then decreases again. The second product obtained was formic acid, which presents a minimum at 1.5CTH500 (3.0 μmol $g_{cat}^{-1}h^{-1}$) and after that the production increases up to 25.7 μmol $g_{cat}^{-1}h^{-1}$ for 3.0CTH500 (Figure 4. 13, grey bars). Finally, the minor product was CO whose production increased as the cupper loading increased up to 2.8 μmol $g_{cat}^{-1}h^{-1}$ for 3.0CTH500 (Figure 4. 13, black bars).

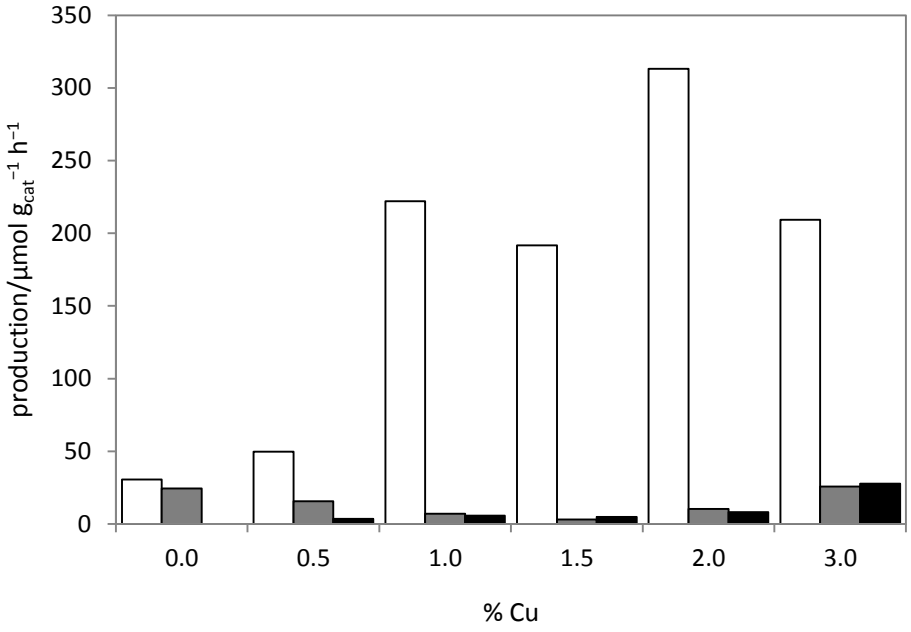

Figure 4. 13. Influence of copper content in the catalyst on product formation for photocatalytic reduction of CO_2. Experimental conditions: catalyst (25mg) in water (25mL) containing Na_2S under CO_2 atmosphere (1.4bar) at 25ºC for 15 hours; Hg lamp irradiance ≈ 1.5 kW m^{-2}. White bars: H_2; grey bars: HCO_2H; black bars: CO (due to low CO amounts, these values are magnified ten-fold for clarity)

A kinetic study was also performed in order to see the evolution of the H_2 and formic acid over time (the formation of sulfur and CO was unable to be followed due to the low amounts formed during the reaction). Figure 4. 14 shows that in the first hours of the photocatalytic reaction high amounts of formic acid were produced (1247 μmol $g_{cat}^{-1}h^{-1}$ after 2 hours of reaction), after that formic acid is consumed. On the other hand, the production of H_2 increases as the reaction time increases. This finding is quite interesting because at short reaction times the selectivity for CO_2 reduction is higher than at longer reaction times.

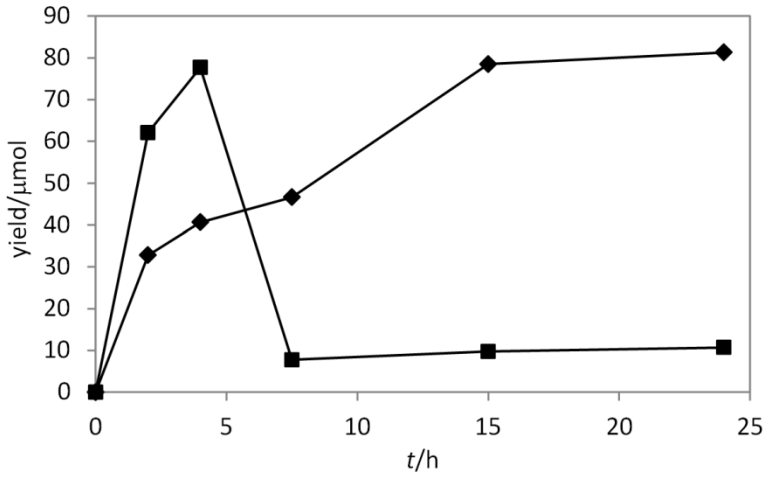

Figure 4. 14. Kinetics plot for CO_2 reduction. Reaction conditions: CO_2 (1.4 bar), Hg lamp (irradiance ≈ 1.5 kW m^{-2}), 25 mg of 3.0CTH500, 25 mL of water and Na_2S (13 mM). Squares: HCO_2H;diamonds: H_2.

A last point important to be mentioned is that after finishing the photocatalytic reactions an off-white insoluble solid was observed on top of the solution. This solid was isolated by decantation after sedimentation of the catalyst and it was further characterized. It was elemental sulfur (S_n). Thus, for quantification purposes, sulfur was extracted with tetrachloroethylene, obtaining 324.4 μmol $g_{cat}^{-1}h^{-1}$ for 2.0CTH500, which is consistent with the total amount of photocatalytic products (324.4 μmol $g_{cat}^{-1}h^{-1}$), taking into account the following stoichiometries in which the equations 1-3 correspond to the reduction processes and the equation 4 corresponds to the oxidation.

$$2\ H^{+}(ac) + 2\ e^{-}(Cu\text{-}TiO_2)(s) \rightarrow H_2(g) \quad (1)$$

$$CO_2(g) + 2\ e^{-}(Cu\text{-}TiO_2)(s) + 2\ H^{+}(aq) \rightarrow HCO_2H(aq) \quad (2)$$

$$CO_2(aq) + 2\ e^{-}(Cu\text{-}TiO_2)(s) + 2\ H^{+}(aq) \rightarrow CO(g) + H_2O(aq) \quad (3)$$

$$S^{2-}(aq) + 2\ h^{+}(Cu\text{-}TiO_2)(s) \rightarrow {}^{1}/_{n}\ S_n(s) \quad (4)$$

From these results, we can say that cupper doped TiO_2 prepared by solvothermal route has proved to be an efficient photocatalyst for environmental issues. The materials exhibit significant rates for the photoreduction of CO_2 affording formiate products and H_2. Moreover, sodium sulfide is oxidized to elemental sulfur which can be easily isolated by physical methods. The combined use of sulfur ions as sacrificial agents for the CO_2 photoreduction, and the ability to remove sulfide species from water, open new opportunities for novel applications in wastewater treatment plants. This procedure presents advantages compared to other strategies in which sulfides are transformed into water soluble sulfates and/or thiosulphates.[18]

Taking all these data into account, the materials presented herein combine both, the sulfide abatement and the reduction of water and CO_2 for the production of fuels. Thus, providing a new strategy to eliminate sulfides, which are noxious pollutants, from the wastewater, converting them into easily isolable and valuable elemental sulfur besides the generation of fuels (H_2).

4.2.2 Photocatalytic materials for solar hydrogen generation

In this section, the preparation of up-converting Er,Yb-Y_2O_3 nanoparticles (NPs) and their integration in a photovoltaic device for hydrogen generation is presented. First, the synthesis and characterization of the nanostructured material is detailed. After that, their incorporation in the final device and the evaluation of the photocurrent generation will be discussed.

4.2.2.1 ErYb-Y_2O_3 NPs: synthesis and characterization

Up-converting nanoparticles (UCNPs) with $Er_{0.04}Yb_{0.1}Y_{1.86}O_3$ stoichiometry (this concentration of Er^{3+} and Yb^{3+} was chosen from literature in order to obtain red and green emissions[41]) were synthetized by homogeneous precipitation method. In a typical synthesis, the proper amount of Y, Er and Yb nitrates were dissolved in water and the temperature of this solution was increased to 80ºC, after that, urea was added. At this temperature urea is slowly hydrolyzed to CO_2 and NH_3 and it induces the precipitation of Yttrium hydroxycarbonate ($Y(OH)CO_3$) [42] because of the basicity of the yttrium ion. Finally, the precipitates were thoroughly filtered and washed, dried and calcined at 800ºC.

Figure 4. 15 shows the XRD pattern of the annealed sample, where peaks can be assigned to highly crystalline yttrium oxide (JCPDS 71-0049) as single phase. The average crystal size calculated by Scherrer equation from the most intense peak was around 35 nm. Moreover, according to the Bragg equation, the diffraction peaks were slightly shifted towards higher $2\theta^o$ values in good agreement with the incorporation of the lanthanides in the Y_2O_3 framework. This fact indicates that a solid solution where the Y^{3+} ions are replaced by smaller Yb^{3+} and Er^{3+} ions is obtained (effective radii in a sixfold coordination: Y^{3+} 104 pm, Yb^{3+} 101 pm, and Er^{3+} 103 pm).

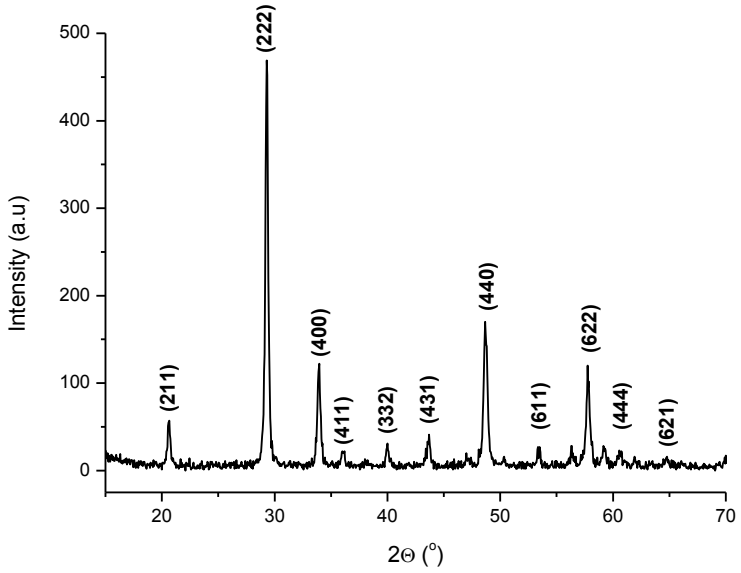

Figure 4. 15. XRD of $Er_{0.04}Yb_{0.1}Y_{1.86}O_3$ sample annealed at 800ºC.

The scanning electron microscopy (SEM) revealed that this material presents a very homogeneous spherical morphology of around 300 nm in diameter, and these submicrospheres are composed of aggregates of ~ 40 nm NPs (inset of Figure 4. 16). A narrow particle size distribution centered at 292 ± 30 nm was confirmed by Dynamic Light Scattering (DLS) (Figure 4. 16). The atomic percentage of yttrium and lanthanide atoms was estimated by Energy-dispersive X-ray spectroscopy (EDS), giving values in good agreement with the theoretical stoichiometry (Y: 92.74%, Er: 1.87% and Yb: 5.38%).

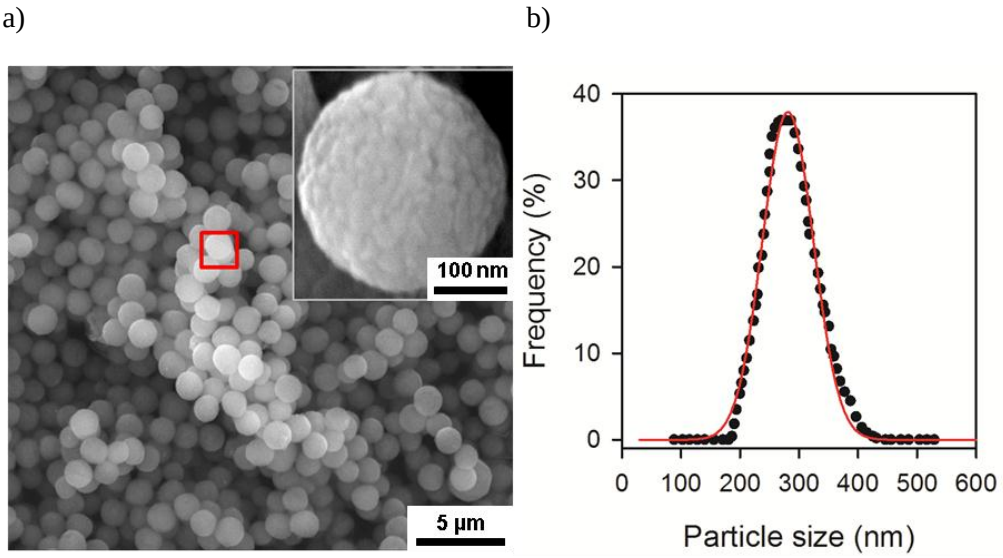

Figure 4. 16. a) SEM micrograph and b) DSL diagram of the $Er_{0.04}Yb_{0.1}Y_{1.86}O_3$ sample.

The UV-VIS-NIR absorbance spectrum of this material shows the bands which correspond to the *f-f* electronic transitions characteristic of Er^{3+} (Figure 4. 17a red line). The broad band at 980 nm is caused by the overlap of the energy levels from Er^{3+} ($^4I_{11/2}$) and Yb^3+ ($^2F_{5/2}$) ions. Thus, when $Er_{0.04}Yb_{0.1}Y_{1.86}O_3$ is excited at 980nm, the emission spectrum (black line) displays two inhomogeneous bands at around 560 nm ($^2H_{11/2}\rightarrow{}^4I_{15/2}$ and $^2S_{3/2}\rightarrow{}^4I_{15/2}$, in the green region) and 660 nm ($^4F_{9/2}\rightarrow{}^4I_{15/2}$, in the red region) from erbium ions. For a better understanding of these spectra, the energy levels of the Er and Yb ions are depicted in Figure 4. 17b.

The relative intensity between green and red emissions depends on the concentration of the two lanthanides as well as the nature of the matrix.[43] The higher intensity of the red emission compared to the green one is characteristic of Yb^{3+} rich systems (around

5%) and it is caused by a cross relaxation between $^2H_{11/2} \rightarrow {}^4I_{9/2}$ and $^4I_{15/2} \rightarrow {}^4I_{13/2}$ transitions.[29]

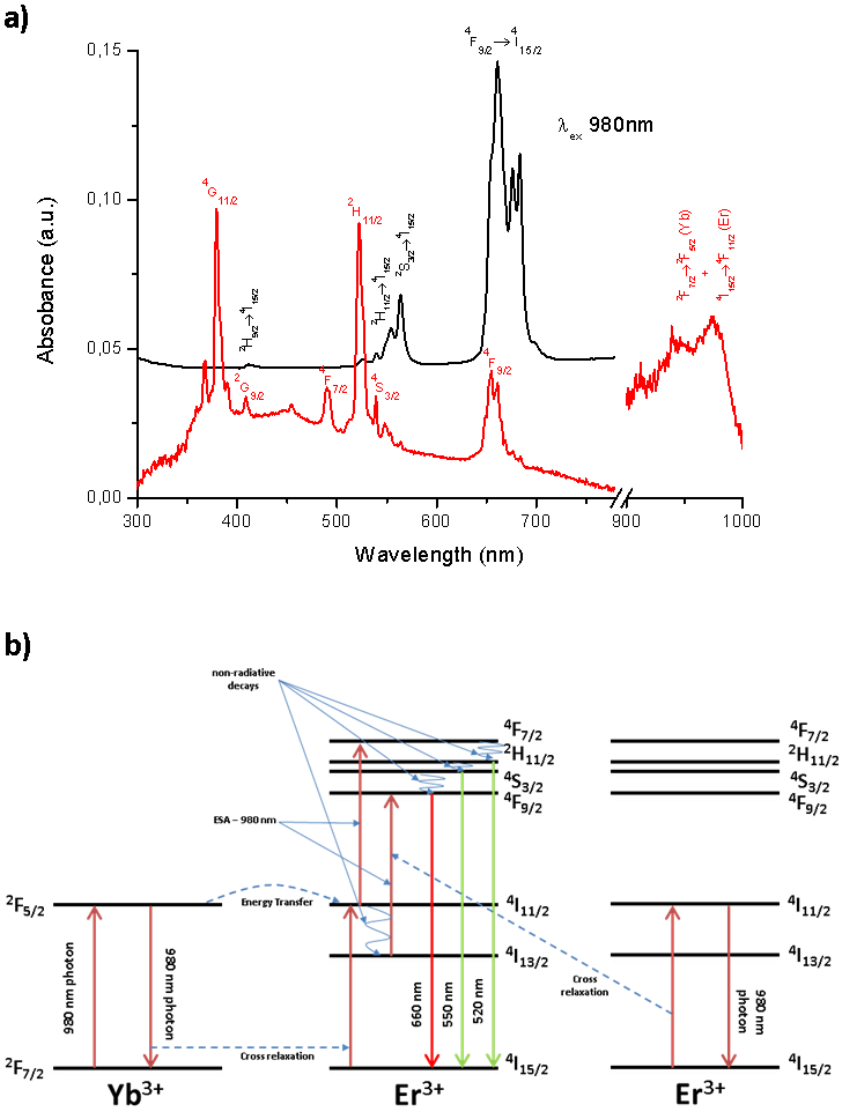

Figure 4. 17. a) UC spectrum upon excitation at 980nm (black line) and UV-VIS-NIR spectra (red line) of $Er_{0.04}Yb_{0.1}Y_{1.86}O_3$. Absorption bands correspond to transition from ground state $^4I_{15/2}$ of erbium to excited states listed in the figure, b) energy levels of the erbium and ytterbium ions.

4.2.2.2 Introduction of the Er,Yb-Y_2O_3NPs in TiO_2/CdSe photoanodes and evaluation of the final device

Having characterized the doped yttria sample, their ability to up-convert near infrared energy into visible light was tested for applications in solar hydrogen generation. So the doped yttria nanoparticles (UCNPs) were integrated into a photovoltaic device previously developed in Photovoltaic and Optoelectronic Devices Group from the Department of Physics at Universitat Jaume I (UJI).

The preparation of the device was done in several steps. First, the UCNPs were introduced into a heterostructured TiO_2/CdSe photoanode. For this purpose, a mesoporous TiO_2 paste was synthetized following a previously described method[44] and a 20 % wt of the UCNPs described above were incorporated into the paste. This mixture was screen printed into a FTO substrate previously coated with a TiO_2 compact layer, and further calcined at 450ºC for 30 minutes in order to remove all the organic moieties. A good dispersion of the UCNPs into the mesoporous titania film was observed along the cross-section of the film by SEM (Figure 4. 18). This multilayered system will constitute the electrode or photoanode of the final device.

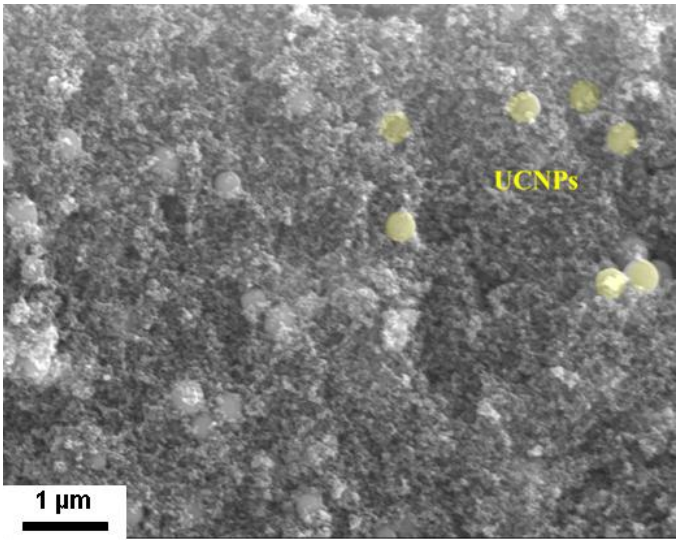

Figure 4. 18. . SEM image of a cross section of $Er_{0.04}Yb_{0.1}Y_{1.86}O_3/TiO_2$ mesoporous film. Some UCNPs have been colored in yellow for a better visualization.

The electrode was then sensitized with CdSe quantum dots (QDs) by a successive ionic layer adsorption and reaction (SILAR) method.[45,46] In brief, the electrode was immersed successively in two ethanolic solutions of Cd^{2+} and Se^{2-}. This process was conducted in a glovebox under N_2 atmosphere. Then, it was rinsed with ethanol and dried with N_2 flow. This cycle constitutes a SILAR cycle. Four SILAR cycles were carried out in order to sensitize the photoanode.

After that, a ZnS layer was grown over the sensitized electrode, following the same procedure as described above. The deposition of the ZnS layer in this kind of photovoltaic devices improves the photocurrent of the system by reducing the carrier recombination process at the TiO_2/electrolyte interface. Furthermore, it increases the stability of the device by avoiding the photocorrosion of the CdSe QDs.

Two reference samples (without UCNPs and without sensitizer) was also prepared in order to be sure that the structural features of the heterostructured electrode were not affected by the presence of the UCNPs. These samples were also used to evaluate their effect on the optical and photophysical behavior.

In Figure 4. 19a the absorbance of the films with different compositions is shown. Pure TiO_2 film only absorbs until 400 nm while when CdSe QDs are present the absorption goes up to 670 nm. The introduction of the doped yttria sample in the heterostructure introduces some scattering which increases the absorption capacity of the photoanode in the whole visible range. No *f-f* absorption bands are observed in the electrode, probably due to the low amount of Er^{3+} deposited in the photoanode.

In Figure 4. 19a, the UC emission spectrum of the yttria doped NPs has been included to underline that the absorption of the sensitized photoanode overlaps only with the green emission (around 550 nm) while the red one is not affected by this absorption. Thus, the red emission will be used to normalize the spectra of different electrodes.

The normalized up-conversion spectra of the sensitized and non-sensitized photoanode are given in Figure 4. 19b. The red emission still dominates the curve, as in pure UCNPs, but the presence of the QDs induces a decrease of the green emission probably caused by the absorption of the CdSe.

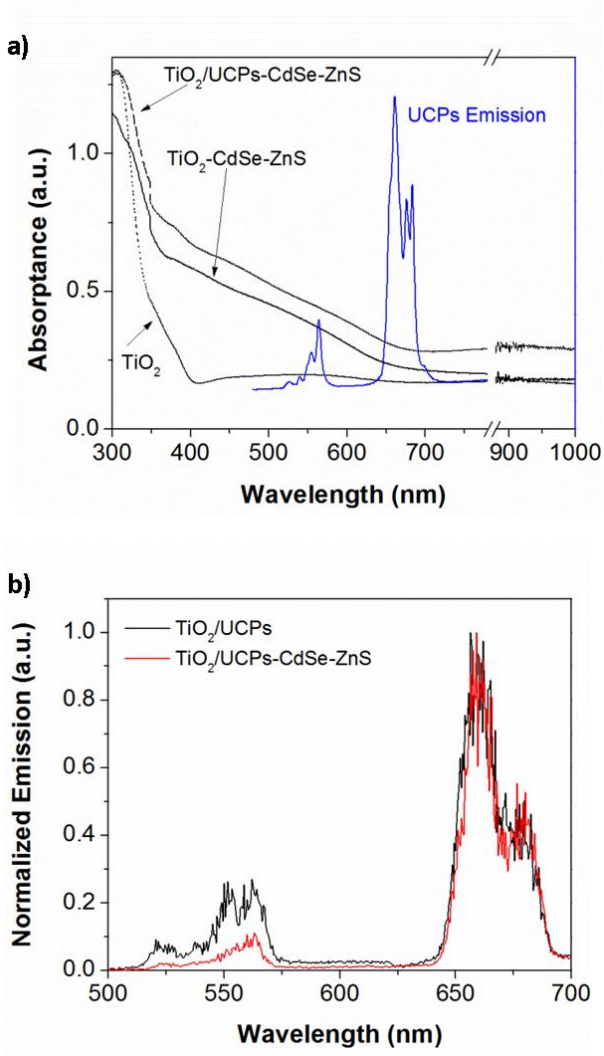

Figure 4. 19. a) Absorption spectra of different films (black), up-conversion emission spectrum of the UCNPs upon excitation at 980nm (blue), b) Normalized up-conversion spectra of non- and sensitized photoanode including the UCNPs.

In order to gain insight in this phenomenon, time resolved measurements were carried out monitoring the experiments at $^4F_{9/2} \rightarrow {}^4I_{15/2}$ (660 nm, red) and $^2S_{3/2} \rightarrow {}^4I_{15/2}$ (560 nm green) transitions upon 980 nm excitation. The relaxation curves for those transitions did not fit to a single-exponential function; as a consequence, a second-exponential function was used, obtaining two lifetimes values (Table 4. 5). The τ_2 values are longer than those reported for this phosphor in previous reports (11μs and 21 μs for green and red emissions, respectively)[41]

Table 4. 5. Lifetimes values at $^2S_{3/2} \rightarrow {}^4I_{15/2}$ (560 nm, green emission) and $^4F_{9/2} \rightarrow {}^4I_{15/2}$ (660 nm, red emission)

Sample	τ_1 [µs] [a] green emission	τ_2 [µs] [a] green emission	τ_1 [µs] [a] red emission	τ_2 [µs] [a] red emission
Er,Yb-Y_2O_3 NPs	1.8 ± 0.2	25.1 ± 1.6	19.8 ± 1.4	76.0 ± 6.4
TiO_2/UCNPs	1.4 ± 0.2	28.2 ± 1.6	18.7 ± 1.4	70.3 ± 6.4
TiO_2/UCPs-CdSe	1.4 ± 0.2	25.8 ± 1.6	17.2 ± 1.4	63.2 ± 6.4

Both contributions could be due to the existence of different coordination environments for the lanthanide ions in the yttria framework. The short lifetime component could be attributed to the ions located on the surface of the particles (with unsaturated coordination and shorter lanthanide-lanthanide distances) while the long one could be caused by the ions from the core of the nanoparticle (with a regular and saturated coordination). The short component and non-single exponential behavior has been previously associated with $Er^{3+} \rightarrow Yb^{3+}$ back-transfer processes occurring in other upconverter Er-Yb@Y_2O_3 systems.[47]

The lifetime values are almost the same if we compare the ErYb:Y_2O_3, and the non-sensitized and sensitized photoanode. From these data we can conclude that the optical interaction between the up-conversion emission and the CdSe absorption occurs via radiative emission-reabsorption process while a non-radiative energy transfer can be discarded. In other systems combining QDs and UC Er,Yb-$NaYF_4$ nanocrystals, an efficient energy transfer through a Forster resonance (FRET) mechanism was detected.[48,49] In our work, we have used a more stable but less efficient metal oxide as up-converting material, it is well known that the phonon energy is higher in oxides compared to fluorides, so in order to have similar optical efficiencies bigger crystal sizes are required. This fact could preclude a FRET mechanism in the photoanodes.

Time-resolved measurements were also registered at different power intensities (from 5 to 45 mV) without significant changes in the lifetime values, thus suggesting that the optical mechanism remains constant in this range of power densities.

4.2.2.3 H_2 generation from infrared radiation

The next step was to evaluate the photocurrent of the final device upon NIR excitation. When the reference photoanode (without UCNPs) is irradiated at 980 nm,

marginal photocurrent for H_2 generation is obtained (~0.1 μA·cm^{-2}), probably caused by the absorption of CdSe traps at the band gap or the sample heating effects. On the other hand, when this experiment is carried out in the photoanode with ErYb:Y_2O_3 particles, the photocurrent was one order of magnitude higher than the aforementioned reference (Figure 4. 20).

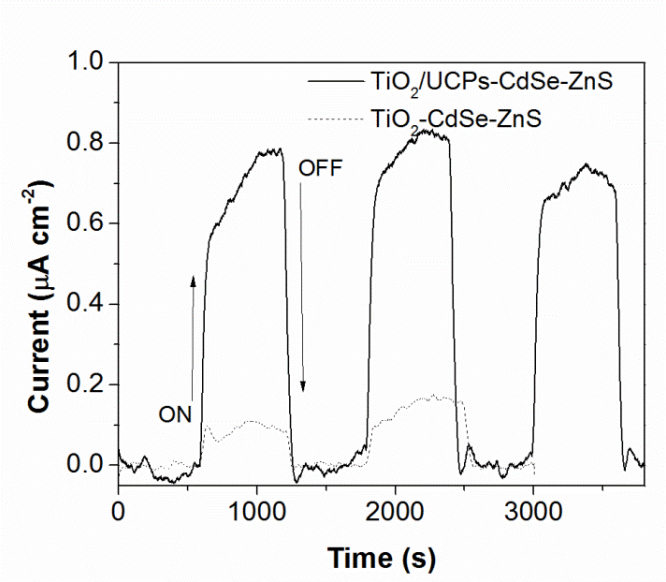

Figure 4. 20. Photocurrent at 0 V vs Ag/AgCl (0.946 vs RHE) for TiO_2 and TiO_2/ErYb:Y_2O_3 sensitized with CdSe irradiated at 980nm (power density 1500 mW/cm^2).

From these results, we can propose the following mechanism for the effective harvesting of the IR photons for H_2 generation with this photoanode (Figure 4. 21). The ErYb:Y_2O_3 particles absorbs the infrared light, emitting the up-converted green and red photons at shorter wavelengths. These photons are re-absorbed by the QDs via a radiative emission-reabsorption process that finally excites an electron from the valence band to the conduction band of the CdSe. These electrons are injected to the conduction band of TiO_2 and transported to the contact to generate H_2. On the other side, the holes generated are scavenged by the reduced species of the electrolyte closing the circuit.

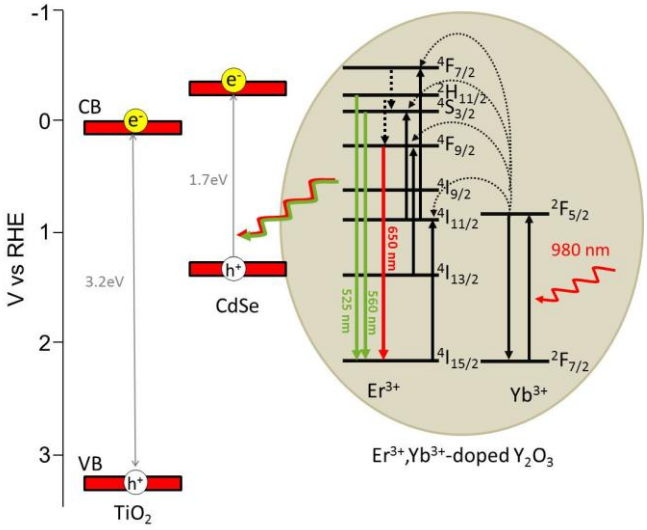

Figure 4. 21. Energy diagram mechanism proposed for the TiO_2/ErYb:Y_2O_3/CdSe photoanode

The external quantum efficiency (EQE) estimated at 980nm-irradiation was 3.75×10^{-4}%. This value is quite low, but three times higher if we compare it with an up-converting photoanode based on fluoride materials (150nA·cm^{-2} and 1.24×10^{-4}%) previously reported for water photooxidation.[25] Furthermore, our EQE value is very high since the UC response of metal oxide nanomaterials is around 10-times less efficient than the reported fluorides. Another advantage of our device is the excellent stability. No significant performance loss after 1 hour of chronoamperometric measurements was detected (Figure 4. 20).

4.3 Conclusions

This section has been devoted to the development and evaluation of different metal oxides with interest in photocatalytic applications.

The first part of this section deals with the synthesis of copper-doped titania nanomaterials as photocatalysts for CO_2 reduction. The samples have been synthetized by solvothermal methodology using metalorganic precursors dissolved in ethanol in the presence of water, for promoting the hydrolysis and condensation of the reagents and acetylacetone for controlling these processes.

This methodology provides nanocrystalline materials (7nm) that grow up to 12-15 nm with annealing at 500ºC. Different instrumental techniques have been employed to analyze the spatial distribution and oxidation state of the copper ions. The XRD, Raman, SEM, HRTEM and XPS measurements indicate that a solid solution was formed, where copper ions are substituting the titanium sites in the framework. The introduction of copper ions into titania matrix promotes a decrease in the band-gap absorption of the material.

The different copper doped materials were tested for the photocatalytic reduction of CO_2 in aqueous media in the presence of different sacrificial electron donors. The most active material was found to be 3.0CTH500, producing formic acid, CO, and significant amounts of H_2 from the reduction of CO_2 and sodium sulfide as electron donor. The copper content in titania has important effects mostly on the hydrogen generation.

This study has allowed preparing active Cu-TiO_2 materials with some advantages compared to current photocatalysts for CO_2 reduction. This strategy allows combining both, the sulfide removal from water, where is a noxious and toxic pollutant in wastewaters, and the production of fuels from the reduction of H_2O and CO_2 through an efficient light-activated process.

The second part has been focused on the development of a photocatalytic device for hydrogen generation via near-infrared excitation. For that, erbium and ytterbium codoped Y_2O_3 NPs were synthesized, which exhibited high crystallinity, sharp particle size distribution, good lanthanide dispersion, and good up-converting properties.

This material was then introduced in TiO_2/CdSe photoanodes producing photocurrent for the H_2 production under irradiation at 980nm. The optical mechanism involved in

the process was further studied by time resolved measurements, indicating that it occurs via radiative emission-reabsorption process.

4.4 References

(1) Centi, G.; Perathoner, S. *Catal. Today* **2009**, *148* (3–4), 191–205.

(2) Aresta, M.; Dibenedetto, A.; Angelini, A. *Chem. Rev.* **2014**, *114* (3), 1709–1742.

(3) Graciani, J.; Mudiyanselage, K.; Xu, F.; Baber, a. E.; Evans, J.; Senanayake, S. D.; Stacchiola, D. J.; Liu, P.; Hrbek, J.; Sanz, J. F.; Rodriguez, J. A. *Science (80-.).* **2014**, *345*, 546–550.

(4) Mikkelsen, M.; Jørgensen, M.; Krebs, F. C. *Energy Environ. Sci.* **2010**, *3* (1), 43–80.

(5) Darensbourg, D. J. *Chem. Rev.* **2007**, *107* (6), 2388–2410.

(6) Sastre, F.; Puga, A. V; Liu, L.; Corma, A.; García, H. *J. Am. Chem. Soc.* **2014**, *136* (19), 6798–67801.

(7) Meng, X.; Wang, T.; Liu, L.; Ouyang, S.; Li, P.; Hu, H.; Kako, T.; Iwai, H.; Tanaka, A.; Ye, J. *Angew. Chemie - Int. Ed.* **2014**, *53*, 11478–11482.

(8) Ma, Y.; Wang, X.; Jia, Y.; Chen, X.; Han, H.; Li, C. *Chem. Rev.* **2014**, *114*, 9987–10043.

(9) Dhakshinamoorthy, A.; Navalon, S.; Corma, A.; Garcia, H. *Energy Environ. Sci.* **2012**, *5* (11), 9217–9233.

(10) Indrakanti, V. P.; Kubicki, J. D.; Schobert, H. H. *Energy Environ. Sci.* **2009**, *2* (7), 745–758.

(11) Izumi, Y. *Coord. Chem. Rev.* **2013**, *257* (1), 171–186.

(12) Salmet; Nasution, W. H.; Purnama, E.; Kosela, S.; Gunlazuardi, J. *Catal. Commun.* **2005**, *6* (5), 313–319.

(13) Tseng, I.-H.; Chang, W.-C.; Wu, J. C. S. *Appl. Catal. B Environ.* **2002**, *37* (1), 37–48.

(14) Tseng, I.-H.; Wu, J. C.-S. *Catal. Today* **2004**, *97* (2–3), 113–119.

(15) Richardson, P. L.; Perdigoto, M. L. N.; Wang, W.; Lopes, R. J. G. *Appl. Catal. B Environ.* **2013**, *132–133*, 408–415.

(16) Yang, C.-C.; Yu, Y.-H.; van der Linden, B.; Wu, J. C. S.; Mul, G. *J. Am. Chem. Soc.* **2010**, *132* (24), 8398–8406.

(17) Zhang, L.; De Schryver, P.; De Gusseme, B.; De Muynck, W.; Boon, N.; Verstraete, W. *Water Res.* **2008**, *42* (1–2), 1–12.

(18) Zhang, K.; Guo, L. *Catal. Sci. Technol.* **2013**, *3* (7), 1672–1690.

(19) Chen, X.; Shen, S.; Guo, L.; Mao, S. S. *Chem. Rev.* **2010**, *110*, 6503–6570.

(20) Zayat, M.; Garcia-Parejo, P.; Levy, D. *Chem. Soc. Rev.* **2007**, *36* (8), 1270–1281.

(21) Auzel, F. *Chem. Rev.* **2004**, *104* (1), 139–173.

(22) Huang, X.; Han, S.; Huang, W.; Liu, X. *Chem. Soc. Rev.* **2013**, *42* (1), 173–201.

(23) Qin, W.; Zhang, D.; Zhao, D.; Wang, L.; Zheng, K. *Chem. Commun.* **2010**, *46* (13), 2304–2306.

(24) Wang, W.; Ding, M.; Lu, C.; Ni, Y.; Xu, Z. *Appl. Catal. B Environ.* **2014**, *144*, 379–385.

(25) Zhang, M.; Lin, Y.; Mullen, T. J.; Lin, W.; Sun, L.; Yan, C.; Patten, T. E.; Wang, D.; Liu, G. *J. Phys. Chem. Lett.* **2012**, No. 3, 3188–3192.

(26) de Camargo, A. S. S.; Possatto, J. F.; Nunes, L. A. D. O.; Botero, É. R.; Andreeta, É. R. M.; Garcia, D.; Eiras, J. A. *Solid State Commun.* **2006**, *137* (1–2), 1–5.

(27) Wang, F.; Liu, X. *Chem. Soc. Rev.* **2009**, *38* (4), 976–989.

(28) Haase, M.; Schäfer, H. *Angew. Chemie Int. Ed.* **2011**, *50* (26), 5808–5829.

(29) Patra, A.; Friend, C. S.; Kapoor, R.; Prasad, P. N. *J. Phys. Chem. B* **2002**, *106*, 1909–1912.

(30) Korzenski, M. B.; Lecoeur, P.; Mercey, B.; Camy, P.; Doualan, J.-L. *Appl. Phys. Lett.* **2001**, *78* (9), 1210.

(31) Julián-López, B.; Martos, M.; Ulldemolins, N.; Odriozola, J. a; Cordoncillo, E.; Escribano, P. *Chem. - A Eur. J.* **2009**, *15* (45), 12426–12434.

(32) Soler-illia, G. J. D. A. A.; Sanchez, C.; Lebeau, B.; Patarin, J. *Chem. Rev.* **2002**, *102* (11), 4093–4138.

(33) Shannon, R. D. *Acta. Cryst.* **1976**, *A32*, 751.

(34) Nagaveni, K.; Hegde, M. S.; Madras, G. *J. Phys. Chem. B* **2004**, *108* (52), 20204–20212.

(35) Xu, J. F.; Ji, W.; Shen, X.; Tang, H.; Ye, X. R.; Jia, D. Z.; Xin, Q. *J. Solid State Chem.* **1999**, *147*, 516–519.

(36) Chen, L.; Horiuchi, T.; Osaki, T.; Mori, T. *Appl. Catal. B Environ.* **1999**, *23*, 259–269.

(37) Velu, S.; Suzuki, K.; Okazaki, M.; Kapoor, M. P.; Osaki, T.; Ohashi, F. *J. Catal.* **2000**, *194* (2), 373–384.

(38) Praliaud, H.; Mikhailenko, S.; Chajar, Z.; Primet, M. *Appl. Catal. B Environ.* **1998**, *16*, 359–374.

(39) Kisch, H.; Lutz, P. *Photochem. Photobiol. Sci.* **2002**, *1* (4), 240–245.

(40) Kanemoto, M.; Shiragami, T.; Pac, C.; Yanagida, S. *J. Phys. Chem.* **1992**, *96* (8), 3521–3526.

(41) Vetrone, F.; Boyer, J.-C.; Capobianco, J. A.; Speghini, A.; Bettinelli, M. *J. Appl. Phys.* **2004**, *96* (1), 661.

(42) Kawashita, M.; Takayama, Y.; Kokubo, T.; Takaoka, G. H.; Araki, N.; Hiraoka, M. *J. Am. Ceram. Soc.* **2006**, *89* (4), 1347–1351.

(43) Tang, Y.; Yang, X.; Xu, Y. *J. Mater. Sci. Mater. Electron.* **2015**, *26*, 2311–2315.

(44) Ito, S.; Chen, P.; Comte, P.; Nazeeruddin, M. K.; Liska, P.; Péchy, P.; Grätzel, M. *Prog. Photovoltaics Res. Appl.* **2007**, *15*, 603–612.

(45) Giménez, S.; Lana-Villarreal, T.; Gómez, R.; Agouram, S.; Muñoz-Sanjosé, V.; Mora-Seró, I. *J. Appl. Phys.* **2010**, *108*, 64310.

(46) Braga, A.; Gimmenez, S.; Concina, I.; Vomiero, A.; Mora-Seró, I. *J. Phys. Chem. Lett.* **2011**, *2*, 454–460.

(47) Auzel, F.; Baldacchini, G.; Laversenne, L.; Boulon, G. *Opt. Mater. (Amst).* **2003**, *24* (1–2), 103–109.

(48) Bednarkiewicz, A.; Nyk, M.; Samoc, M.; Strek, W. *J. Phys. Chem. C* **2010**, *114* (41), 17535–17541.

(49) Yan, C.; Dadvand, A.; Rosei, F.; Perepichka, D. F. *J. Am. Chem. Soc.* **2010**, *132*, 8868–8869.

Chapter 5

Nanocomposites for photonics

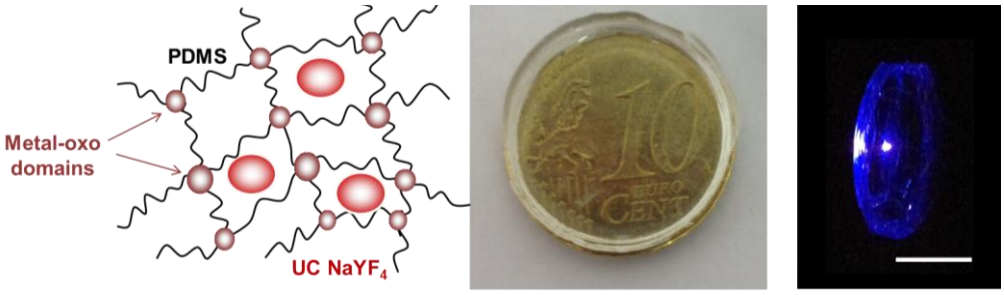

5.1 Introduction

The possibility to combine the properties of organic and inorganic compounds in only one material is an ancient challenge. Indeed, examples of mixed organic and inorganic components at the nanoscale can be found in Egyptian inks, green bodies of china ceramics, prehistoric frescos, maya blue pigment, etc. Most of these examples are paints and polymers which take profit from the properties of inorganic pigments or fillers which are dispersed in an organic media such as solvents, surfactants, polymers, etc.

The hybrid organic-inorganic materials are not a simple physical mixture. As the particle size get reduced at the nanometer scale, the importance of the interface interactions increases, leading to nanocomposites, where the different components interact at molecular level in a synergetic way. Nowadays, the development of new synthetic approaches, using soft chemistry processes ("*Chimie Douce*"), has opened new opportunities for designing new hybrid organic-inorganic materials. Thus, new materials have been developed combining the properties of both counterparts and leading to new functionalities with potential applications in optics, electronics, ionics, mechanics, membranes, protective coatings, catalysis, sensors, biology, etc.[1]

Depending on the possible interactions connecting the organic and inorganic parts of the hybrid composite, the following classification is established: *Class I hybrids*, those that show weak interactions such as hydrogen bonding, van der Waals or electrostatic forces; and *Class II hybrids*, those where the organic and inorganic components are linked at least by one strong chemical bond (covalent, iono-covalent, or Lewis acid-base bonds).[1,2]

The development and study of the photoluminescence of lanthanide-doped organosilicas has become more relevant in the last two decades. A growing interest in this class of materials has emerged because of the tunable properties of organic residues and siloxane skeleton (hydrophilicity, flexibility, transparency, low refractive index…) as well as possibility of shaping and surface modification (miniaturization, integration and funtionalization) for practical technologies.[3] Furthermore, the optical properties from the organo-siloxane constituent and the metal-Ln^{3+} centers offers great possibilities for the worldwide telecommunications, nanobiotechnology and other technological areas.[4,5]

Indeed, several reviews have been reported on these issues[6–9]. However, there are still unexplored fields that will emerge in the next years. One of them is the research on upconverting hybrid materials (UCHy) able to absorb low energy photons (typically

800-1000nm, NIR) and transform into visible emissions (300-750 nm, VIS). These NIR-to-VIS hybrid converters can find breakthrough applications in solar energy production, solar concentrators, and telecommunications, as well as in bioimaging and bioassays.

As already mentioned in Chapter 4, the photon up-conversion (UC) process is usually found in lanthanide-doped inorganic materials with low phonon energy, i.e. fluorides such as $NaYF_4$ and metal oxides like ZrO_2 or Y_2O_3.

One of the main drawbacks for a commercial implementation of UC nanocrystals is that they are usually presented as powders (from micro- to nano- scale), which limits the processability for their use (optical fibers, sensors, biolabels, solar concentrators, etc). Therefore, the introduction of the UC nanoparticles in hybrid organic-inorganic matrices will allow to produce new nanocomposites whose properties such as flexibility, low density, permeability, colour, hydrophobia, etc. combined with the luminescent properties in a unique material, will offer a wide range of possibilities to elaborate tailor-made materials in terms of processing and physicochemical properties.[10]

In this chapter, we present the synthesis of two families of UC hybrid materials with outstanding properties. The first one is made of red emitting UC ZrO_2 NPs integrated in an organic-inorganic hybrid siloxane material enriched with di-ureasil groups. The incorporation of these groups aims to enhance the chemical compatibility of both organic and inorganic counterparts and avoid phase-separations and heterogeneities in the hybrid material. The idea was to include di-ureasil groups in order to help the dispersion of the emitting nanoparticles via weak interactions between the carbonil groups from the di-ureasil functions and the hydroxylated surface of zirconia nanoparticles.

The second family of materials is based on polydimethylsiloxane derivatives (PDMS) including UC $NaYF_4$ NPs and, further, processed as thin films. PDMS (Figure 5. 1a) is the most widely used silicon-based organic polymer, and is particularly known for

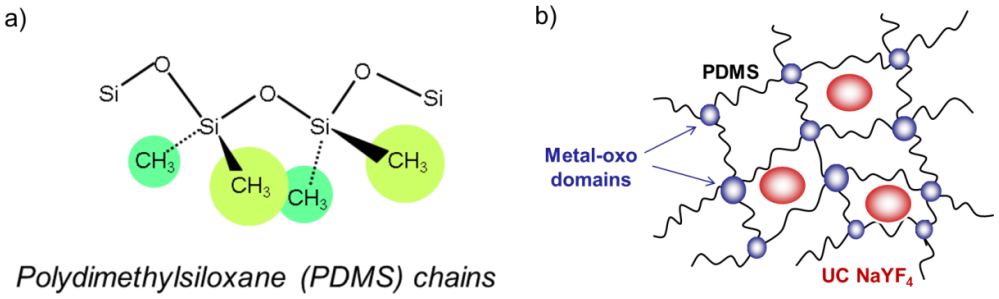

Figure 5. 1. a) Polydimethylsiloxane (PDMS) chain and b) schematic representation of $NaYF_4$-PDMS nanocomposite.

its non-toxicicty, optically clear and unusual rheological and lubricant properties. In its pure state, it is used in contact lenses and other medical devices, in heat-resistant tiles or shampoos. Organically-modified PDMS hybrids (ORMOCERs) allow their mechanical properties to be tuned between those of polymers and glasses. Furthermore, other properties such as porosity, hydrophilic character, refractive index, etc. can be modified affording new materials with applications in automotive, membranes, functional coating, micro-optics, and so on.[2] In this work, the hybrid material is constituted by PDMS chains cross-linked with amorphous metal-oxo nanodomains (M_xO_y, with M: Ti, Zr, Nb, Ta…)[11], and includes small crystalline Yb^{3+}-, Er^{3+}- or Tm^{3+}- doped $NaYF_4$ nanoparticles (Figure 5. 1b). In this case, the oxo-domains would facilitate the integration of the UC NPs. Thus, besides the properties of the hybrid matrix, this material is able to absorb near infrared light at 980 nm and to emit visible photons in the blue, green and red region.

5.2 Results and discussion

5.2.1 ZrO_2 up-converting NPs embedded in di-ureasil hybrids

In this section the synthesis ZrO_2 up-converting NPs and their integration in the organic inorganic di-ureasil hybrid will be presented. Firstly the synthesis and characterization of zirconia Er and Yb doped NPs will be discussed. Next, the introduction of these NPs in the di-ureasyl hybrid, as well as their structural and optical properties will be disclosed.

5.2.1.1 ZrO_2 doped NPs: synthesis and characterization

The synthesis of zirconia doped with Er^{3+} and codoped with Er^{3+}/Yb^{3+} ions was carried out following a previously reported sol-gel procedure.[12] Briefly, the proper amount of $Zr(OPr^n)_4$ was mixed with acetylacetone (acac) in the parent alcohol, once mixed, an aqueous solution of $Er(NO_3)_3xH_2O$, $Yb(NO_3)_35H_2O$ and p-toluenesulfonic acid (PTSH) was added dropwise under magnetic stirring, the molar ratio followed was Zr / acac / PTSH / H_2O : 1/1/0.2/10.

The solution was refluxed during 3 days at 60ºC in order to induce nanocrystallization. After that the solvent was evaporated and the remaining solid was dryed under IR lamp. The materials were annealed at 800ºC in order to increase the crystallinity and to remove the remaining organic moieties. The different materials synthetized were represented as ZE_x and ZE_xY_y were x and y denotes the molar percentage of Er and Yb respectively (Table 5. 1).

Table 5. 1. Composition and crystal sizes of the Er^{3+} and Er^{3+}/Yb^{3+} doped zirconias.

Sample	Crystallite Size (nm)	Sample	Crystallite Size (nm)
Z	16.8	-	-
$ZE_{0.5}$	17.3	$ZE_{0.5}Y_{5.0}$	12.5
$ZE_{1.0}$	16.5	$ZE_{1.0}Y_{5.0}$	11.9
$ZE_{1.5}$	17.2	$ZE_{1.5}Y_{5.0}$	11.8
$ZE_{2.0}$	16.9	$ZE_{2.0}Y_{5.0}$	11.1
$ZE_{5.0}$	15.5	$ZE_{5.0}Y_{5.0}$	9.7

XRD analysis was performed in order to identify the crystal phase obtained and to calculate the crystal size (using the Scherrer equation) of the different materials. The main crystalline phase observed for the non-doped zirconia was the tetragonal (JCPDS card no. 17-0923) or cubic one (JCPDS card no. 7-0337) with small amounts of monoclinic zirconia (JCPDS card no. 37-1484). At this temperature, only the monoclinic phase would be present according to the phase diagram of the ZrO_2 compound. However, the metastable *t*-/*c*-ZrO_2 phases are also developed in this case.

This fact could be related with the effect of the sulfonates reagents which are adsorbed at zirconia surface, promoting the formation of oxygen vacancies and stabilizing these phases[13] (Figure 5. 2). All doped materials present exclusively the tetragonal or cubic phases. This effect is certainly related with the introduction of the luminescent ions in the zirconia structure. In many reports, scientists reveal that the substitution of tetravalent zirconia by trivalent ions (yttrium, lanthanides, etc.) induce the stabilization of the metastable tetragonal lattice[14] (Figure 5. 2 and 5.3).

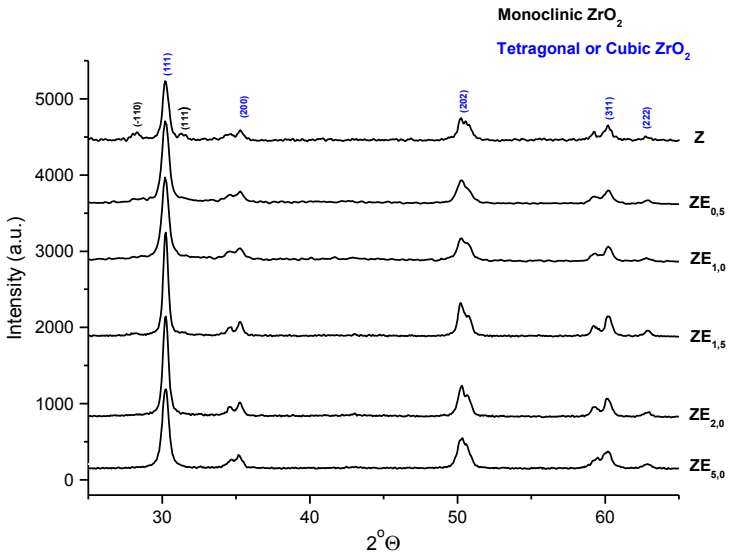

Figure 5. 2. XRD patterns of pure ZrO_2 and ZE_x nanocrystals.

Furthermore, the crystal sizes calculated by Scherrer equation (Table 5. 1) show a decrease in the crystal size upon increasing the content of lanthanide ions from 17.3 to 9.7 nm. The increasing introduction of lanthanide ions in the reaction media has a tendency in the crystal size[15] which could be explained as the ability of these ions to promote the nucleation of crystals in wet synthetic routes, thus leading to more nuclei and smaller crystal sizes as the content of the lanthanide ions increases.

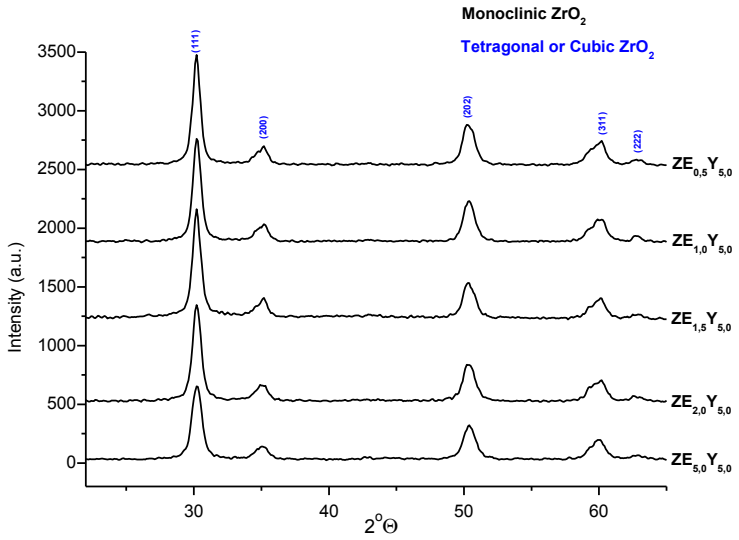

Figure 5. 3. XRD patterns of ZE_xY_y nanocrystals.

Cubic and tetragonal phases are quite similar structures, the only difference between them is an elongation of the crystallographic *c* axis, thus an oxygen displacement is observed in the tetragonal phase compared to the cubic.[16] The only way to differentiate these phases by XRD is to observe a split in the XRD peaks of the tetragonal pattern at high 2Θ, even that, the presence of this fact in the XRD patterns does not exclude the presence of cubic zirconia. Moreover, in nanocrystalline materials, as is our case, the large peak widths make this differentiation impossible.

A powerful tool to differentiate between tetragonal or cubic zirconias is Raman spectroscopy because it is a highly sensitive technique towards oxygen-cation vibrations, thus the active modes for these phases are quite different. The Raman spectra of ZE_xY_y is shown in Figure 5. 4. The bands at 154, 270, 445, 640 and the shoulders at 313 and 608 cm^{-1} can be assigned to the six active modes $A_{1g}(R)$, $2B_{1g}(R)$ and $3E_g(R)$ of the tetragonal polymorph.[17,18] Moreover it is also observed a band at 520 cm^{-1}, that can be attributed to the cubic polymorph with only one active mode (F_{2g}).[16,18] The intensity of this band increases as the amount of lanthanide ions increases, thus it is possible to say that these ions partially stabilize the cubic phase in good agreement with previous works.[14]

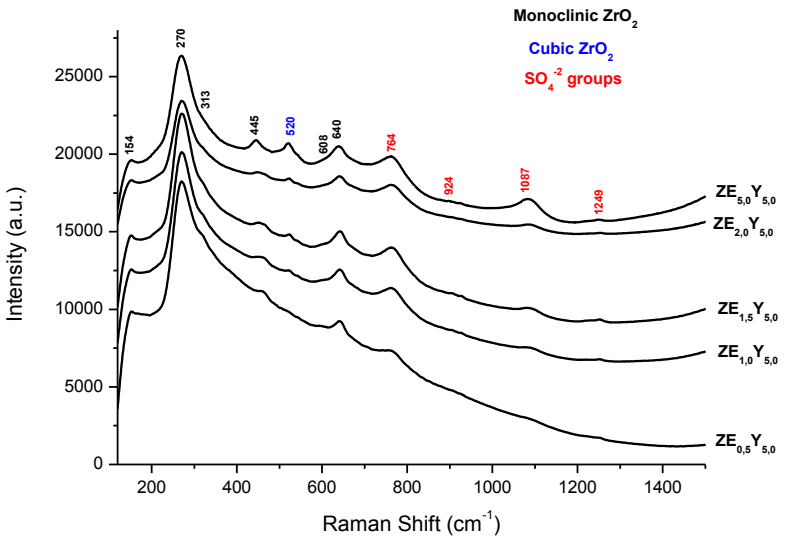

Figure 5. 4. Raman spectra of ZE_xY_y.

Finally, at higher wavelength we find other peaks, at 764, 924, 1087 and 1249 cm^{-1}, which don't correspond to the zirconia structure and can be assigned to symmetric and asymmetric vibrations of surface sulfated groups (SO_4^{2-})[19–22] which probably comes from the partially non-decomposed p-toluensulfonic acid used in the synthesis.

Taking all these results into account, it is possible to say that the non-doped zirconia is composed by a mixture of monoclinic and tetragonal phases, being the last one the majority, while when zirconias are doped with Er^{3+} or Er^{3+}+Yb^{3+} we find a mixtures tetragonal and cubic polymorphs whose amount of cubic polymorph increases as the content of lanthanide ions increases.

The materials were also characterized by electron microscopy. The FE-SEM images show that the zirconia materials are composed by small nanoparticles of around 20-30 nm (Figure 5. 5a). To further study these materials HR-TEM was performed, showing that the as prepared materials are composed of small crystalline particles with a size around 20 nm (Figure 5. 5b) in good agreement with the FE-SEM micrographies and the XRD analysis. After the thermal treatment at high temperature the particles agglomerate a little bit but the crystal size remain almost unaltered (Figure 5. 5c).

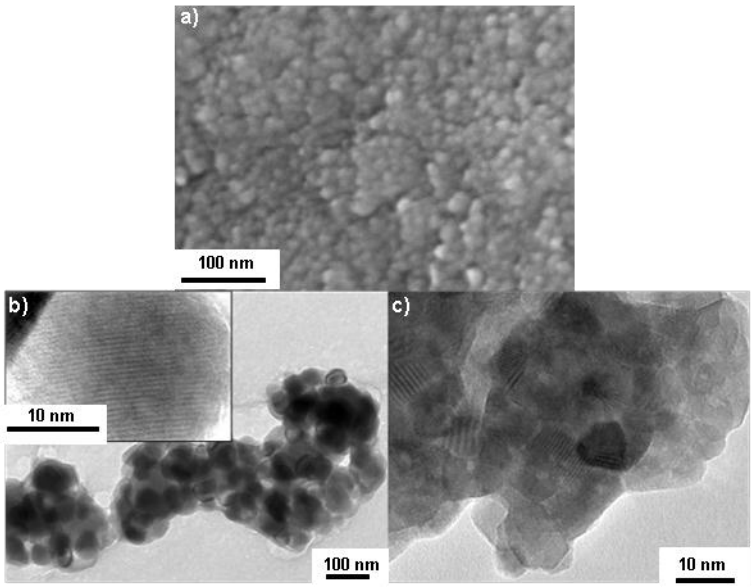

Figure 5. 5. a) FE-SEM micrograph of ZE_5Y_5 treated at 800ºC, HR-TEM of ZE_5Y_5 b) as prepared and c) after the treatment at 800ºC.

5.2.1.2 Synthesis and characterization of ZrO_2-di-ureasil hybrid materials

In a first step, the hybrid precursor, di-ureapropyl-triethoxysilane (d-UPTES(600)), was synthesized as previously described.[23] Briefly, 3-isocyanatepropyltriethoxysylane (ICPTES) and Jeffamine ED-600 were mixed in tetrahydrofurane (THF) in a molar ratio 2:1 respectively, this solution was stirred at room temperature for 24 hours. During this time the amine groups of Jeffamine ED-600 attacks the isocyanate group of the alkoxysilane providing the urea cross-linked organic-inorganic precursor. Finally the THF was removed in a rotatory evaporator.

After that, 0.41 mL of EtOH, 0.41 mL of a water suspension of the nanoparticles with a concentration 5mg/mL, previously sonicated for 1 hour, were mixed with 1.91g of d-UPTES(600). After stirring, 9.6 µL of HCl 0.5M was added in order to promote the sol-gel transition (Scheme 5. 1). This solution was used to produce monoliths (8×8×15 mm) by solvent cast and films by spin coating on glass substrates (SCHOTT®) varying the deposition conditions in order to obtain films with different thickness (Table 5. 2). The films and the monoliths were dried at 45ºC for 7 days in order to remove any residual solvent and to consolidate the sol-gel process. Hybrids

embedding $ZE_{0.5}$, $ZE_{5.0}$, $ZE_{0.5}Y_{5.0}$ and $ZE_{5.0}Y_{5.0}$ were named d-U(600)- $ZE_{0.5}$, d-U(600)- $ZE_{5.0}$, d-U(600)- $ZE_{0.5}Y_{5.0}$, d-U(600)- $ZE_{5.0}Y_{5.0}$ respectively.

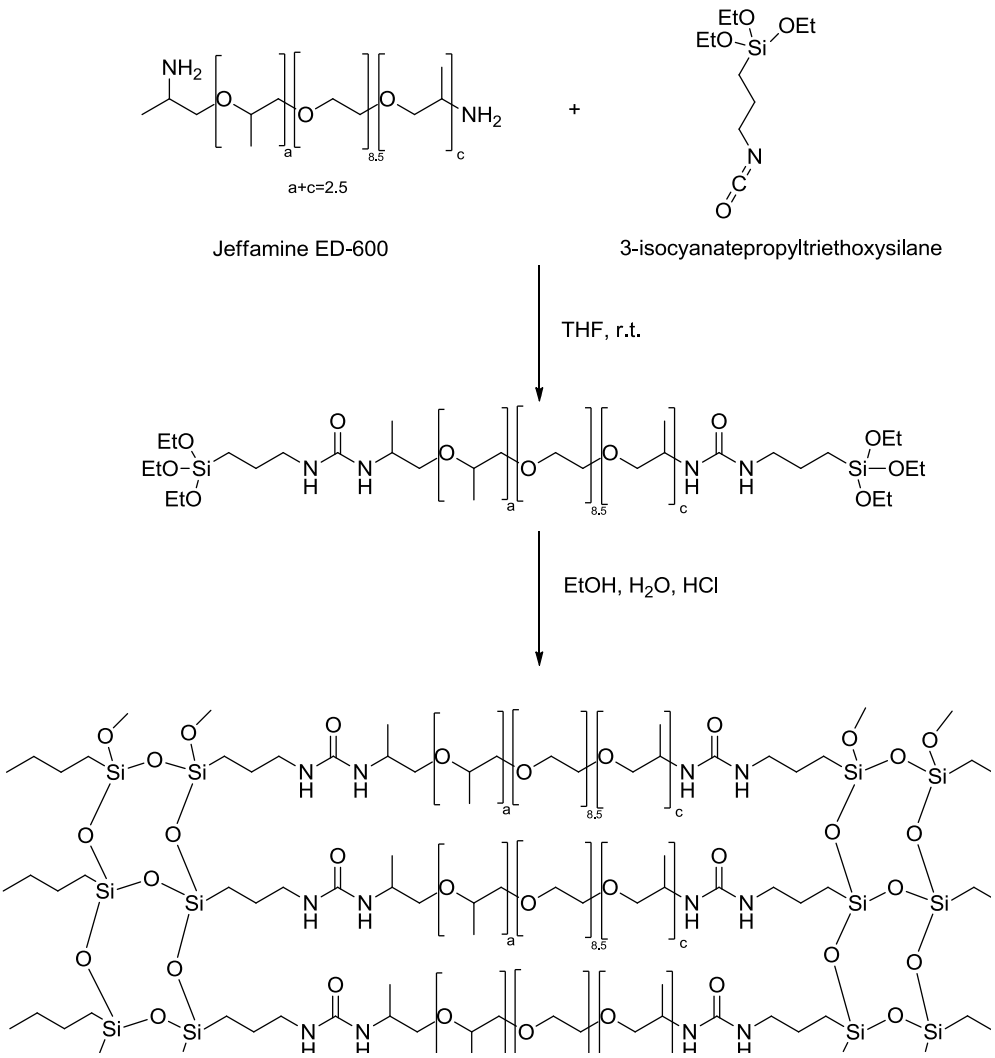

Scheme 5. 1. Scheme of the main steps in the **s**ynthesis of pure di-ureasils hybrids. In the doped systems, the UCNPs are introduced as aqueous suspension, instead of pure water.

Table 5. 2. Spin-coating conditions for the preparation of hybrid films.

Reference	Conditions
Film 1	d-U(600)–$ZE_{5.0}Y_{5.0}$ – 1 layer 1000 rpm/ 25mg of UCNPs
Film 2	d-U(600)–$ZE_{5.0}Y_{5.0}$– 2 layers 1000 rpm/ 25mg of UCNPs
Film 3	d-U(600)–$ZE_{5.0}Y_{5.0}$ – multilayer / 25mg of UCNPs 5 layers (300 rpm), RT
Film 4	d-U(600)–$ZE_{5.0}Y_{5.0}$ – multilayer / 100 mg of UCNPs 4 layers (300 rpm), RT (the sol was more dense than in film 3)
Film 5	d-U(600)–$ZE_{0.5}Y_{5.0}$ – 1 layer 1000 rpm / 25mg of UCNPs
Film 6	d-U(600)–$ZE_{0.5}$ – 1 layer 1000 rpm / 25mg of UCNPs
Film 7	d-U(600)–$ZE_{5.0}$ – 1 layer 1000 rpm / 25mg of UCNPs

The integration of the ZrO_2 nanoparticles into the hybrid led to transparent monoliths and films (Figure 5. 6) as a consequence of the homogeneous distribution and the small particle size (below the visible wavelength range) of the zirconias.

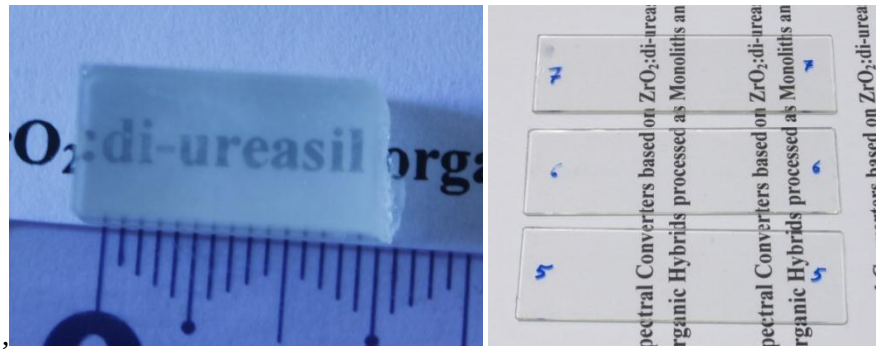

Figure 5. 6. (Left) photograph of d-U(600) $ZE_{5.0}Y_{5.0}$ monolith, (right) photograph of films 5, 6 and 7.

In order to check in what way the nanoparticles are dispersed into the hybrid, ultramicrotomed sections of d-U(600)-$ZE_{5.0}Y_{5.0}$ were analyzed by HR-TEM (Figure 5. 7) showing that the zirconia nanoparticles are embedded into the amorphous di-ureasil hybrid. Moreover it is also possible to calculate the interplanar distances of zirconia (2.9 Å) which fits with (1,0,1) plane corresponding to t-ZrO_2, indicating that UCNPs are stable after their introduction within the nanocomposite.

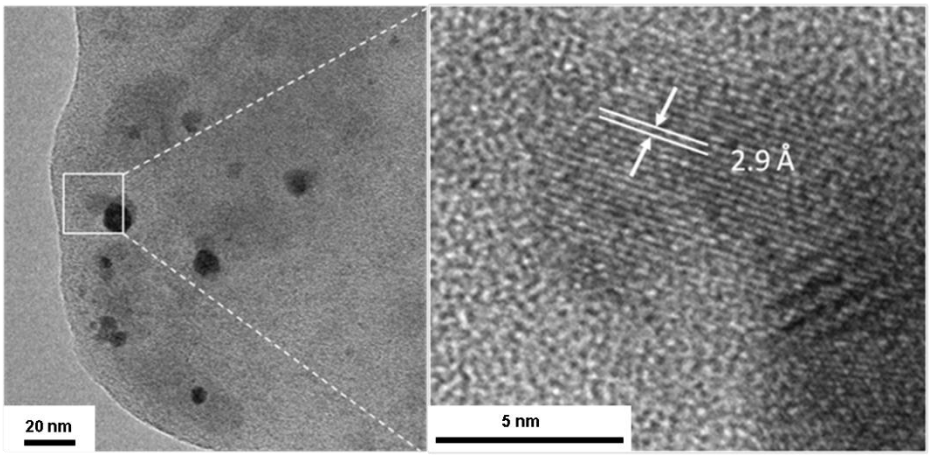

Figure 5. 7. HR-TEM micrographs of microtomed d-U(600) $ZE_{5.0}Y_{5.0}$.

Hybrid siloxane-based materials are able to present some periodicity in the local arrangement of the organic and inorganic counterparts. In order to study this issue, X-ray diffraction was performed on grinded monoliths. Representative XRD of d-U(600) and d-U(600) $ZE_{0.5}Y_{5.0}$ are given in Figure 5. 8. We can observe a broad band at 21.5º which corresponds to amorphous siliceous domains,[24] the second order of this peak is found around 42º. Two peak are observed around 4 and 13º which are assigned to interparticle scattering interference[25] and to an another intra-siloxane domains.[24] No peak corresponding to ZrO_2 was observed, because of the low content of this material in the nanocomposite and the masking effect of the siliceous band. Moreover the local structure was preserved after the incorporation of zirconia nanoparticles.

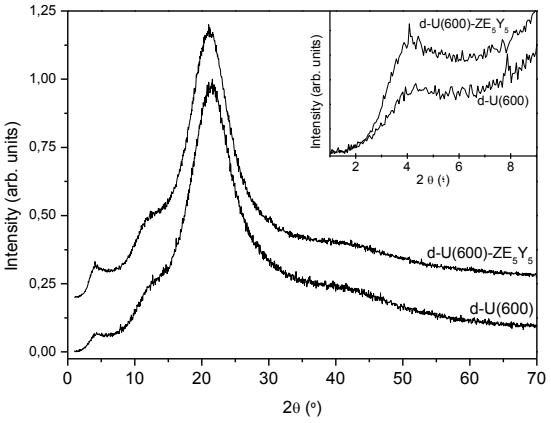

Figure 5. 8. XRD pattern of and d-U(600) $ZE_{5.0}Y_{5.0}$. Inset show a magnification of the XRD patterns al low 2ºΘ.

To study the extent of interaction between the di-ureasil component and the embedded zirconia nanoparticles, the bond vibrations on Fourier-Transform Infrared (FTIR) and Raman spectroscopy were analyzed. Figure 5. 9a shows the FTIR spectra of non-doped and different d-U(600)-ZrO_2, showing the typical bands corresponding to di-urea cross-linked poly(oxyethylene)(POE)/siloxane materials: the bands at 3350, 2950-2750, 1650, 1550 and 1110 cm^{-1} can be assigned to N-H (hydrogen bonded amide), C-H, C=O, C-N/C-C and C-O groups respectively.[24] No clear vibration was identified for the inorganic Zr-O modes or bridges "*Zr-O-Si*" (*Zr* from UCNPs and *Si-O* from the siloxane network). Since the vibrational modes of the inorganic networks falls close to the limit of the energy range of our FTIR apparatus (400 cm^{-1}), Raman measurements were also conducted.

The micro-raman spectra of d-U(600) $ZE_{0.5}Y_{5.0}$ and reference samples ($ZE_{0.5}Y_{5.0}$ and d-U(600)) are shown in Figure 5. 9b, showing the vibrational bands from the silane component and ZrO_2 (asterisks) in the nanocomposite. Unfortunately, again no signals corresponding to the organic-inorganic interface were detected. This point would be relevant because there is a poor understanding on the nature of chemical interaction between the constituents of the hybrid material, and we are not able to classify this hybrid as Class I or Class II according to the mentioned classification of hybrids. Our idea was to incorporate di-ureasil groups in order to enhance the dispersability of the inorganic nanoparticles through hydrogen bonding or Van der Waals interactions, but no evidence of that point has appeared.

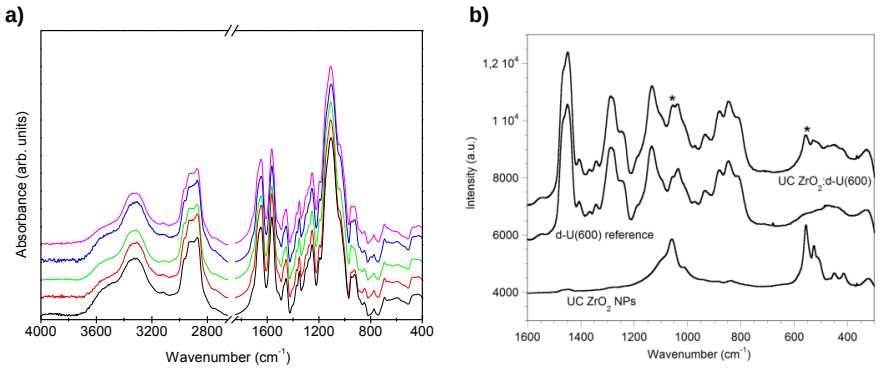

Figure 5. 9. a) FTIR spectra of d-U(600) (black line), d-U(600) $ZE_{0.5}$ (red line), d-U(600) $ZE_{5.0}$ (green line), d-U(600) $ZE_{0.5}Y_{5.0}$ (blue line) and d-U(600) $ZE_{5.0}Y_{5.0}$ (magenta line). b) Micro-raman spectra of d-U(600) $ZE_{5.0}Y_{5.0,}$ d-U(600) and $ZE_{5.0}Y_{5.0}$.

Another technique quite useful to study amorphous hybrid materials is solid-state nuclear magnetic resonance. In particular, siloxane materials are ideal for their study with ^{29}Si NMR. These studies have been performed at the University of Aveiro. ^{29}Si NMR of d-U(600), d-U(600) $ZE_{0.5}$ and d-U(600) $ZE_{5.0}Y_{5.0}$ were recorded (Figure 5. 10). It is possible to see three broad peaks at 50, 58 and 66 ppm which corresponds to T_1, T_2, T_3 respectively (T_n where n=1, 2 and 3, is the number of Si-bridging oxygen atoms $R'Si(OSi)_n(OR)_{3-n}$)[26] for d-U(600) sample. While in d-U(600)$ZE_{0.5}$ and d-U(600) $ZE_{5.0}Y_{5.0}$ only T_2 and T_3 peaks appear. From the integration of the peak areas, the condensation degree (defined as $c=1/3(\%T_1+2T_2+3T_3)$) for d-U(600), d-U(600)$ZE_{0.5}$ and d-U(600)$ZE_{5.0}Y_{5.0}$ was estimated to be 76.0, 89.5, and 95.4% respectively. These results suggest that both the introduction of zirconia NPs and the increasing content of lanthanides in the UCNPs increase the condensation degree of the hybrid.

From all this data it is possible to conclude that the hydrolysis and condensation levels increase as the content of zirconia nanoparticles and rare earth content increases, while the local structure of the hybrid remains almost unchanged.

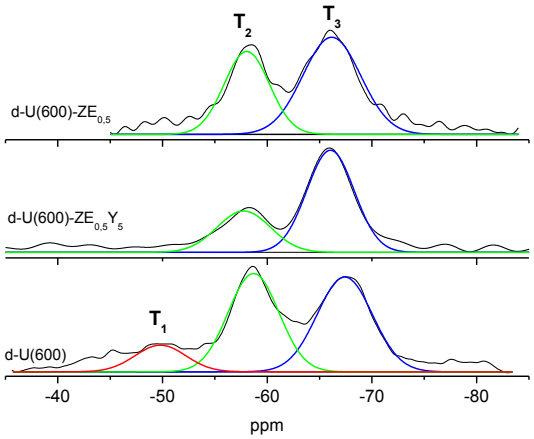

Figure 5. 10. ^{29}Si MAS NMR spectra of d-U(600), d-U(600)$ZE_{0.5}$ and d-U(600)$ZE_{5.0}Y_{5.0}$.

5.2.1.3 Optical characterization of the UC ZrO_2 and ZrO_2-di-ureasyl hybrids

Several transparent films (Figure 5. 6) were easily spin-coated with a suspension of zirconia doped nanoparticles and di-ureasil precursor using different conditions (Table 5. 2). Selected films (5, 6 and 7) synthesized under the same conditions were further characterized by spectroscopic ellipsometry. The thickness obtained by this technique was in the order of several microns, and fits well with the data extracted from SEM images (Table 5. 3 and Figure 5. 11). Also, the films obtained by one-by-one layer deposition provide quite similar thickness independently of the zirconia nanoparticles used.

Table 5. 3. Films thickness obtained by spectroscopic ellipsometry and SEM measurements.

Reference	Thickness (±0.1 μm) ellipsometry	Thickness (±0.1 μm) SEM
Film 5 – dU(600)-$ZE_{0.5}Y_{5.0}$	8.9	9.6
Film 6 – dU(600)-$ZE_{0.5}$	8.5	8.5
Film 7 – dU(600)-$ZE_{5.0}$	8.5	8.0

The refractive index dispersion at different wavelength was also obtained by spectroscopic ellipsometry for the selected films (Figure 5. 12). In these measurements we can observe that the refractive index is lower for film 5, while film 6 shows the maximum refractive index. This trend can be tentatively explained because of the different sizes in the zirconia nanoparticles (12.5, 15.5 and 17.3 nm for $ZE_{0.5}Y_{5.0}$ (film 5), $ZE_{5.0}$ (film 7) and $ZE_{0.5}$ (film 6)), thus as bigger are the nanoparticles bigger is the volume fraction induced and as a consequence higher is the refractive index. On the other hand, the refractive index of the films at 600 nm is 1.59 (Film 5) and ~1.68 (Films 6 and 7) which are lower than ZrO_2 bulk (2.3) but higher than di-ureasil host (1.49). This fact can also be explained on the basis of the relative decrease of the polymeric fraction relative to the zirconium content.[27]

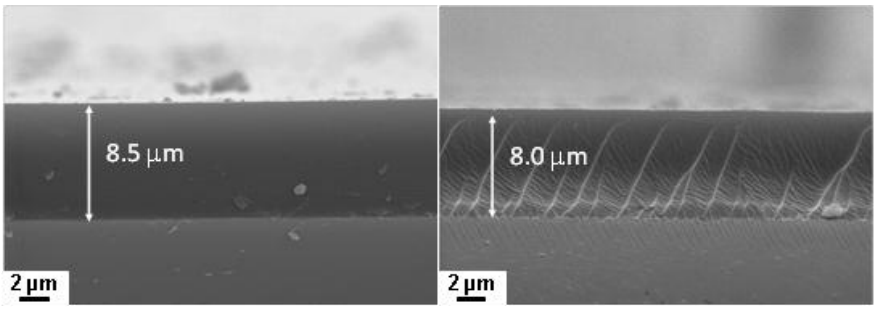

Figure 5. 11. SEM micrograph of film 5 (left) and 6 (right).

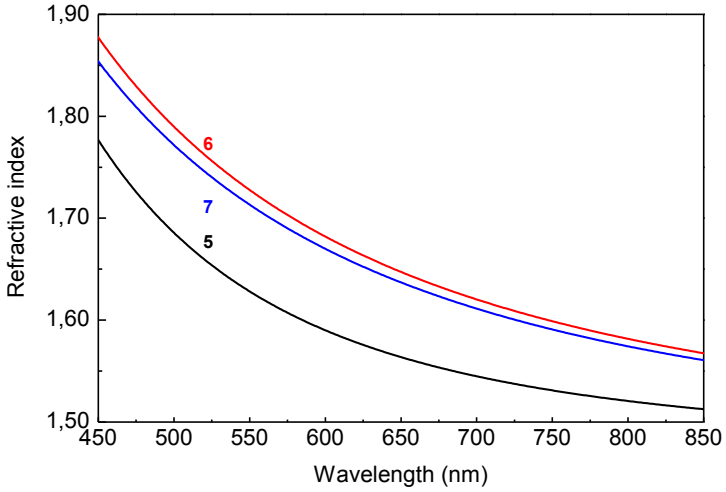

Figure 5. 12. Refractive index curves for Films 5, 6 and 7.

Exciting the nanocomposites in the range of 260-400 nm at room temperature, they provide emission from the visible range to the NIR. The emission in the visible region (Figure 5. 13) was composed by a broad band whose maximum changes, upon changing the excitation wavelength. This profile is originated by di-ureasil emission coming from the donor-acceptor pairs involved in the photoinduced proton transfer between NH_2^+ and NH groups (~2.5 eV) as well as the oxygen defects occurring in the siloxane clusters related to species such as •O–O–Si≡(CO_2) (~2.5 eV).[28,29] No relevant changes are detected in the emission spectra depending on the lanthanide content. Only in the case of samples with higher Er^{3+} content, self-absorption bands appear at the same wavelength that the $^4I_{9/2}\rightarrow{}^4F_{7/2}$, $^2K_{13/2}$, $^4H_{11/2}$ transitions (Figure 5. 13). This behavior has been previously reported in the literature and it is known as *inner filter* effect [30] which is caused by radiative energy transfer between the hybrid matrix excited states and the intra-$4f^{11}$ levels.

The emission lines in the near infrared region (Figure 5. 14) correspond to the Er^{3+} $^4I_{13/2}\rightarrow{}^4I_{15/2}$ transition and the Yb^{3+} $^2F_{5/2}\rightarrow{}^2F_{7/2}$ transition in the co-doped samples. This indicates that the lanthanide ions are well protected from non-radiative deactivation inside the hybrid matrix.

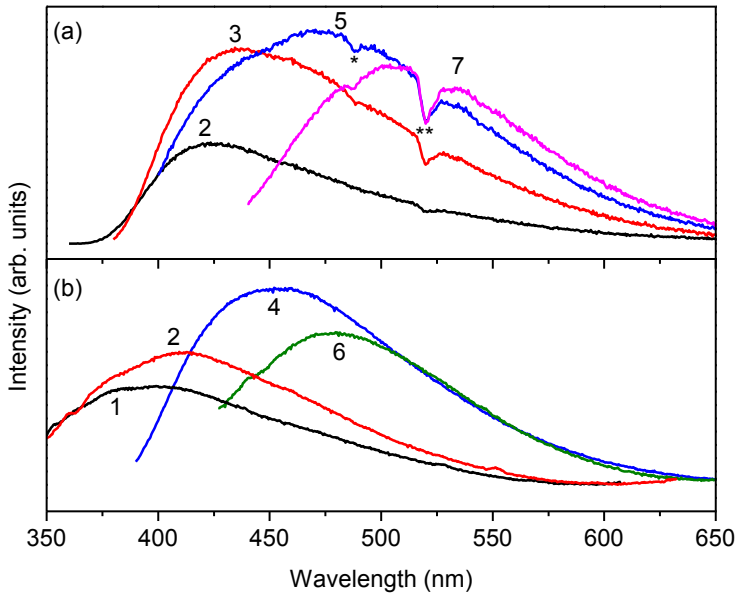

Figure 5. 13. Emission spectra of (a) d-U(600)-$ZE_{5.0}$ and (b) d-U(600)-$ZE_{0.5}Y_{5.0}$ excited at (1) 320 nm, (2) 335/340 nm, (3) 360 nm, (4) 370 nm, (5) 380 nm, (5) 400 nm and (7) 420 nm. The intra-$4f^{11}$ self-absorptions ascribed to transitions from the $^4I_{9/2}$ state to the (*) $^4F_{7/2}$ and (**) $^2K_{13/2}$, $^4H_{11/2}$ excited states, respectively, are also indicated.

The excitation spectra (Figure 5. 14) monitored at 1530 nm (Er^{3+} transition) shows a broad band in the UV region corresponding to the hybrid host excited states[28] and different narrow lines associated to transitions from $^4I_{15/2}$ to intra-$4f^{11}$ excited levels. This fact points out the efficient energy transfer between the hybrid matrix to the Er^{3+} ions, proving that there is an active visible-to-NIR energy conversion at room temperature. The excitation spectra recorded after monitoring at 1041 nm (Yb^{3+} level) is similar to that obtained monitoring at Er^{3+} levels (1.5 μm) suggesting that the hybrid matrix is also populating the Yb^{3+} $^2F_{5/2}$ level and that Er^{3+}-to- Yb^{3+}energy transfer is also present due to back-transfer mechanism.

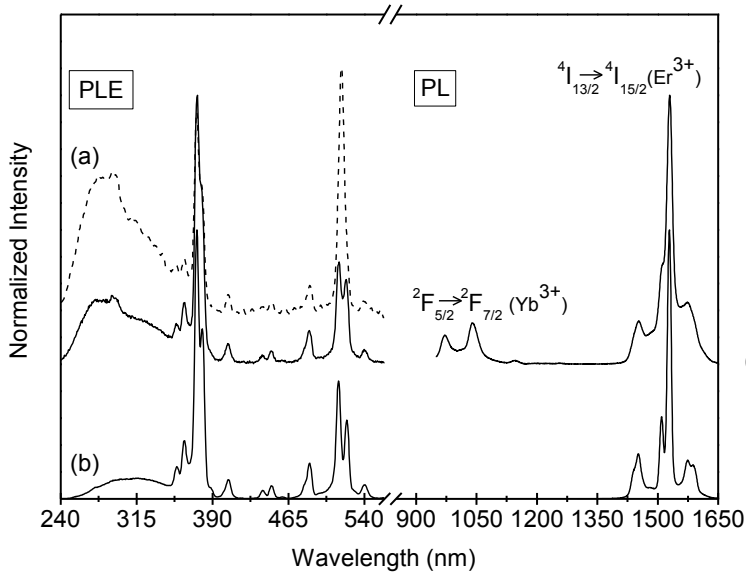

Figure 5. 14. Emission (PL) and excitation (PLE) spectra the (a) d-U(600)-ZE_5 and (b) d-U(600)-$ZE_{0.5}Y_5$ excited at 375 nm and monitored at 1041 (dashed line) and 1530 nm (solid line), respectively.

The up-converting emitting properties are presented in Figure 5. 15 and 5.16 for the single UCNPs and the UCNPs-diureasyl hybrid, respectively. In the case of the different zirconia nanoparticles synthetized, they exhibit high up-conversion intensities when these materials are excited at 980nm. The normalized up-converting spectra of the Er and Yb co-doped materials are shown in Figure 5. 15, where it is possible to see the Er^{3+} emission in the green ($^2H_{11/2} \rightarrow {}^4I_{15/2}$, 525 nm; $^4S_{3/2} \rightarrow {}^4I_{15/2}$, 562 nm) and the red ($^4F_{9/2} \rightarrow {}^4I_{15/2}$, 678 nm) spectral regions. Moreover as higher is the Er content higher is the red/green ratio. This fact can be explained due to a resonant cross-relaxation mechanism, in which $^4F_{7/2} \rightarrow {}^4F_{9/2}$ and $^4F_{9/2} \leftarrow {}^4I_{11/2}$ are taking place populating the $^4F_{9/2}$ red emitting state. Moreover this process is concentration-dependent, so increasing the Er^{3+} content increases its efficiency.[31,32]

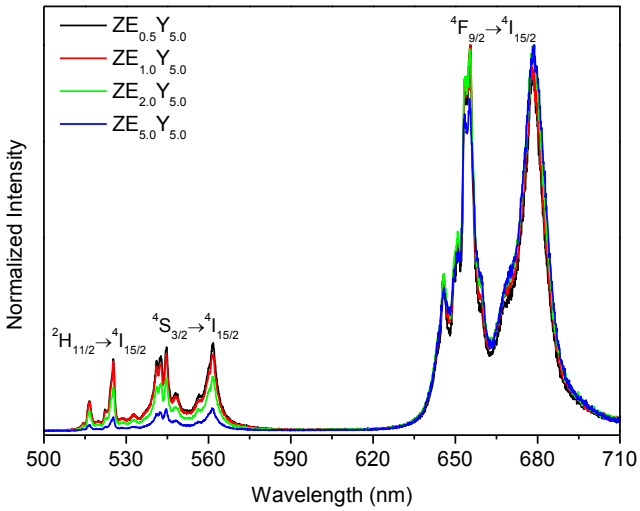

Figure 5. 15. UC emission spectra of $ZE_{0.5}Y_{5.0}$, $ZE_{1.0}Y_{5.0}$, $ZE_{2.0}Y_{5.0}$, $ZE_{5.0}Y_{5.0}$ NPs excited at 980 nm at 0.143 W.

The optical mechanism operating in the UC emission observed in these materials may take place via excited state absorption (ESA), energy transfer up conversion (ETU) mechanisms,[33] and two photon absorption (TFA) process[34] (Scheme 5. 2). In the first mechanism one Er^{3+} is excited by ground state absorption (GSA) to $^4I_{11/2}$, after that another photon, of the same energy, excites again the pre-excited Er^{3+} at $^4F_{7/2}$ level. Once at this level the ion is non-radiatively to $^2H_{11/2}$ and $^4S_{3/2}$.

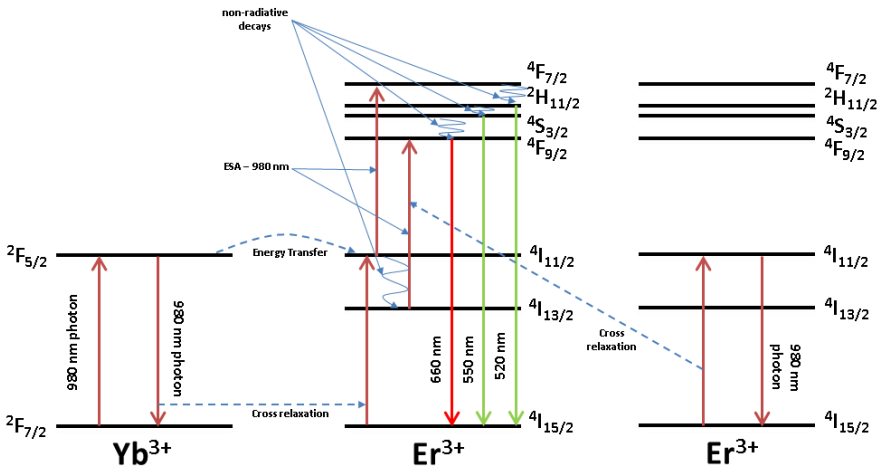

Scheme 5. 2. Energy level diagram of Er^{3+} and Yb^{3+} and UC mechanisms.

In the ETU mechanism, two Er^{3+} ions could be excited at $^4I_{11/2}$ level or one Er^{3+} and one Yb^{3+} are excited to $^4I_{11/2}$ and $^4F_{5/2}$ levels respectively (GSA). Once at these states, one of the ions (Er^{3+} or Yb^{3+}) transfer energy to the other pre-excited ion leading to Er^{3+} in $^4F_{7/2}$ state. After that, as before, this level decays non-radiatively to $^2H_{11/2}$ and $^4S_{3/2}$. In these two mechanisms the $^2H_{11/2}$ and $^4S_{3/2}$ levels are excited and decay radiatively via $^2H_{11/2}\rightarrow{}^4I_{15/2}$ and $^4S_{3/2}\rightarrow{}^4I_{15/2}$ leading to the green emission. Moreover these two levels can also decay non-radiatively to $^4F_{9/2}$ which de-excites radiatively ($^4F_{9/2}\rightarrow{}^4I_{15/2}$) giving the red emission.

Another possible mechanism is TFA, where two photons can be absorbed simultaneously through a real or virtual state. This mechanism is more relevant at higher pump powers. In the case of Er^{3+} a real state is involved in the TFA mechanism exciting at 980 nm, thus leading to a high efficient green emission.

The up-converting spectra of different zirconia co-doped Er^{3+} and Yb^{3+} nanoparticles at different laser power intensities are shown in Figure 5. 16. In general the number of photons (*N*) required to populate an emitting state, for unsaturated conditions (low excitation powers) can be determined plotting a log-log plot of the emitted integrated intensity (P_{emi}) *vs* excitation intensity (I_{exc}), whose slope is equal to the mean number of photons involved in the process (because of the power-like relation ($P_{emi}\alpha\, I_{exc}{}^N$).[35]

The slope of this adjustment is around 2 for all samples and for both, the green and red emission, which indicates that the number of photons involved in the up-conversion luminescence is 2 (Figure 5. 17a). The red and green ratio versus laser power is represented in Figure 5. 17b where it is possible to see that this ratio decreases as the pump power increases, which is of great interest because the color can be tuned as a function of the pump power.

In this way, in the UC luminescence of Er^{3+} the emitting states $^2H_{11/2}$and $^4S_{3/2}$ and $^4F_{9/2}$ are populated via both ESA and ETU mechanisms emitting in the green and red spectral regions. The rate constants of $^4S_{3/2}$ and $^4F_{9/2}$ are not equal, so the high power limit is not the same for both levels. In the low power regime the emission intensity increases with quadratic laser power dependence, but in an intermediate power regime the population of $^4S_{3/2}$ and $^4F_{9/2}$ will depend of different power intensities,[36,37] thus leading different color tunability as a function of the pump power.

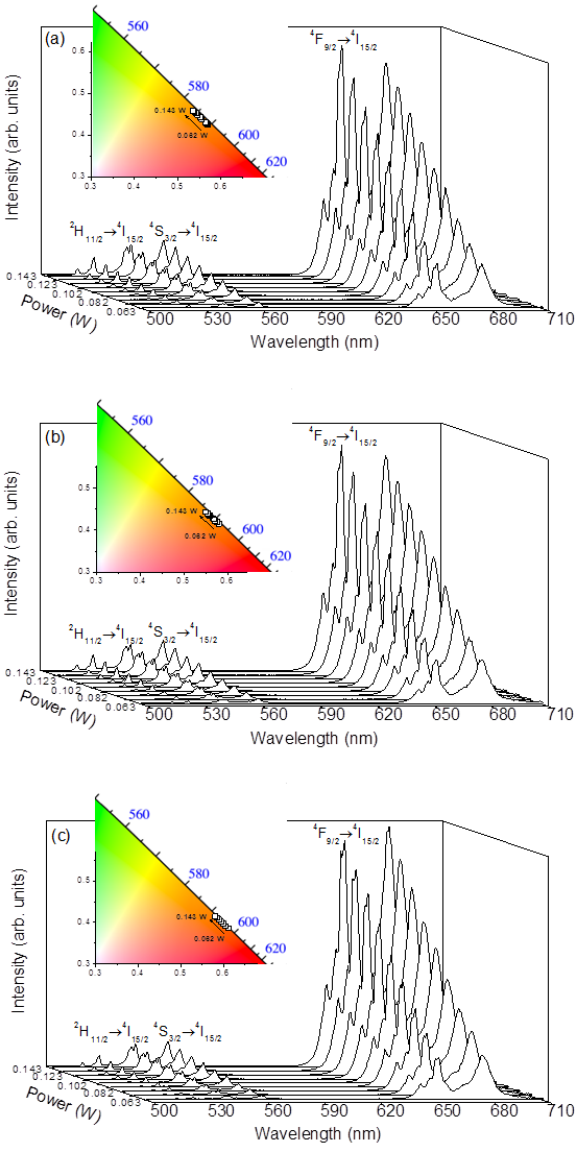

Figure 5. 16. Up-conversion RT emission spectra registered at different pump power intensities of (a) $ZE_{0.5}Y_5$, (b) ZE_1Y_5 and (c) ZE_2Y_5 NPs, upon excitation at 980 nm. The f–f transitions of Er^{3+} are attributed in the figure. The insets show the CIE (1931) UC emission colour coordinates as a function of the power excitation.

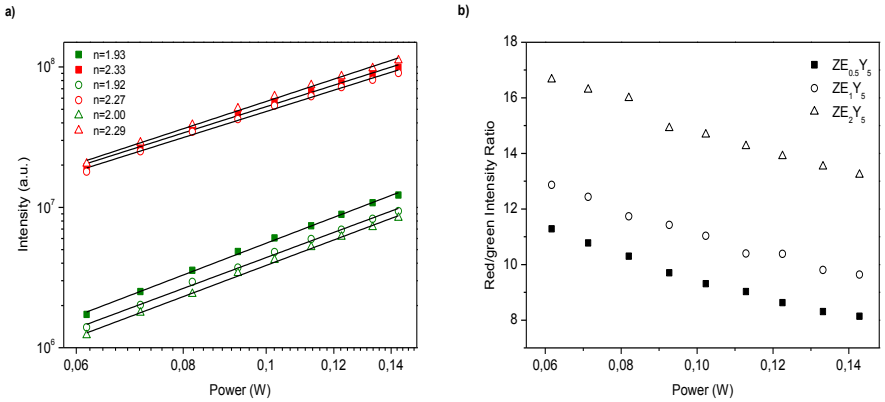

Figure 5. 17. a) Dependence of the emission UC intensities as a function of the excitation power at 980 nm of (closed squares) $ZE_{0.5}Y_5$, (open circles) ZE_1Y_5 and (open triangles) ZE_2Y_5 NPs. The green and red colors correspond to green and red integrated emission intensities, respectively. b) Red-green intensity ratio of $ZE_{0.5}Y_5$, ZE_1Y_5 and ZE_2Y_5 NPs as a function of the excitation power.

The different particles were introduced in the di-ureasil hybrid processing it as monoliths and films. Their up-converting properties were further studied. For brevity only dU(600)-$ZE_{5.0}Y_{5.0}$ is shown (Figure 5. 18). These spectra show the up-conversion emission different pump powers, as before, the emission appears in same green ($^2H_{11/2}\rightarrow{}^4I_{15/2}$, 525 nm; $^4S_{3/2}\rightarrow{}^4I_{15/2}$, 562 nm) and red ($^4F_{9/2}\rightarrow{}^4I_{15/2}$, 678 nm) spectral regions. The peaks observed in the film and the monoliths present the same energy peak position and FWHM, suggesting that in both cases the Er^{3+} ions are in the same symmetry site, independently of the processing.

If we compare the profiles of the ZE_xY_y nanoparticles (Figure 5. 16) with the nanoparticles embedded in the hybrid (Figure 5. 19) we can observe that the emission of the hybrid nanocomposite gives larger FWHM due to an inhomogeneous broading and Stark splitting of the Er^{3+} ions.

As before, the plot of log of the band intensity versus log of the laser power gives a slope around 2 (Figure 5. 19a), pointing out that the optical mechanism in the UC hybrid and in the pure UCNPs is the same.

Moreover, as in the UCNPs, the red/green ratio decreases as the power pump increases in the monolith, being more intense the green emission than the red one at this intermediate power regime. This effect is related, as explained above, to the

different rate constant in the up-converting emitting level at intermediate power pumps. Furthermore, there are no significant variations in the optical behavior with the different processing (monoliths or films).

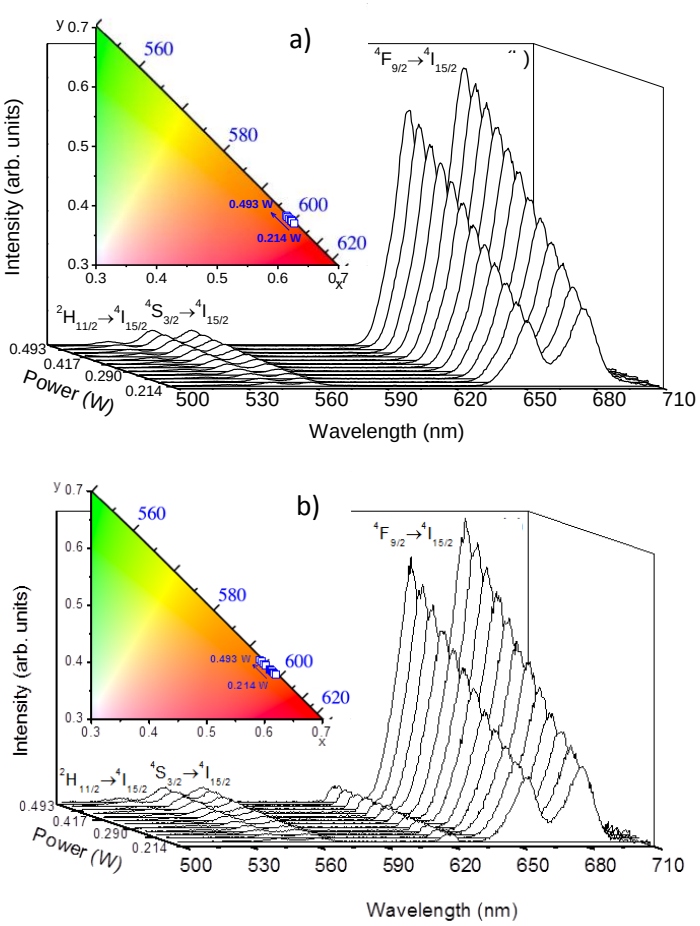

Figure 5. 18. Up-conversion emission spectra (300 K) of (a) d-U(600)-ZE_5Y_5 monolith and (b) Film 4 upon excitation at 980 nm. The insets show the CIE (1931) UC emission colour coordinates as a function of the power excitation.

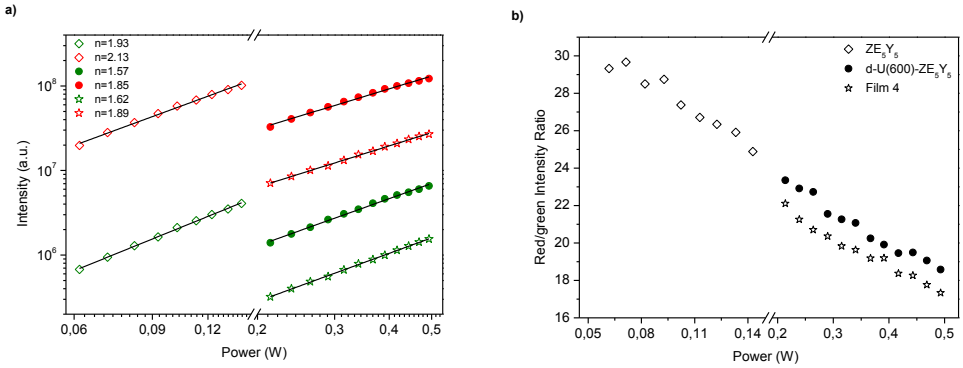

Figure 5. 19. a) Dependence of the emission UC intensities as a function of the excitation power at 980 nm of (open rhombus) ZE_5Y_5, (closed circles) d-U(600)-ZE_5Y_5 and (open stars) Film 4. The green and red colours correspond to green and red integrated emission intensities, respectively. The solid lines correspond to the data best fit using a linear function (R>0.99). b) Red-green intensity ratio of ZE_5Y_5 NPs, d-U(600)- ZE_5Y_5 monolith and Film 4 as a function of the excitation power.

The Comission Internacionale d'Éclairage, CIE (x,y) colour coordinates were also studied as a function of the pump power in the zirconia nanoparticles (insets Figure 5. 16) and for the d-U(600)- ZE_5Y_5 monolith and Film 4 (insets Figure 5. 18). As previously discussed, the change in the red/green ratio leads to a change in the CIE colour coordinates. For the ZE_5Y_5 NPs the coordinates change in the red region from (0.647,0.350) to (0.632,0.364). After the introduction of this nanoparticles in the di-ureasyl hybrid the emission colour coordinates change within the red-orange regions, from (0.629, 0.368) to (0.614, 0.383) for the monolith and from (0.620, 0.378) to (0.591, 0.404) for the Film 4. If we compare the colour coordinates in the zirconia nanoparticles, for the $ZE_{5.0}Y_{5.0}$ the coordinates change within the red region, while for the low Er^{3+} content zirconia the coordinates change within the dark to light orange regions, from (0.570, 0.425) to (0.535, 0.458).

As a conclusion, up converting zirconia NPs with different sizes and Er^{3+}/Yb^{3+} doping levels have been successfully synthetized and introduced in the di-ureasyl hybrid. The zirconia small size has allowed an excellent distribution of these NPs in the hybrid providing transparent films and monoliths. The optical properties of the NPs and the nanocomposites were further studied showing that the upconverting emission color can be adjusted upon excitation power density.

5.2.2 $NaYF_4$ up-converting NPs embedded in PDMS hybrids

In this part of this chapter the synthesis and characterization of $NaYF_4$ doped NPs will be discussed. After that the introduction of these particles in PDMS matrices with different cross linkers (Nb, Ta, Ti and Zr) will be exposed and their structural and optical properties deeply discussed.

5.2.2.1 Synthesis and characterization of doped $NaYF_4$ NPs

The doped $NaYF_4$ nanoparticles (Er:Yb 2:20 and Tm:Yb 2:20) were synthetized through thermal decomposition as previously reported by G. S. Yi et.al. Briefly, the porper amount of $RE(CH_3COO)_3$ were dissolved in oleylamine and CF_3COOH (See Experimental Section for further details). The mixture purged three times with Argon at 100ºC and the reaction temperature was increased to 340ºC for two hours. Finally the nanoparticles were precipitated with ethanol and centrifugated several times.

The NPs synthetized were further characterized by XRD and HR-TEM. In both samples (Er and Tm doped) the phase obtained correspond to the most optically efficient phase (hexagonal $NaYF_4$, JCPDS 28-1192) as Figure 5. 20 shows.

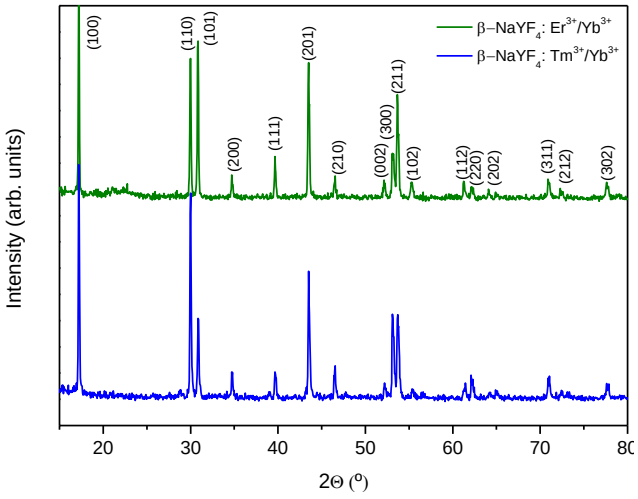

Figure 5. 20. XRD of the as-synthetized $NaYF_4$ UCNPs.

In order to gain insight in the morphology of the synthetized nanoparticles, the samples were further studied by HR-TEM. Figure 5. 21 shows a representative HR-TEM micrograph of the materials synthetized where is possible to see that are composed of quasi spherical nanoparticles with an average particle size around 20 nm.

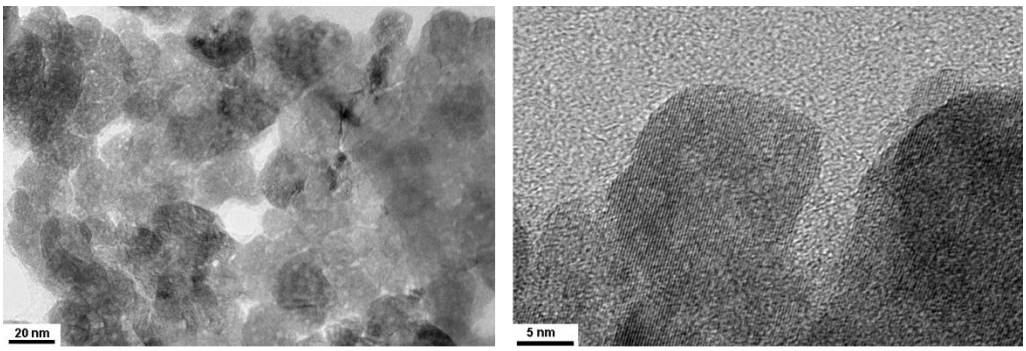

Figure 5. 21. HR-TEM miccrograph of $NaYF_4$:Er^{3+}/Yb^{3+} UCNPs.

These NPs were dispersed in cyclohexane with a concentration of 1mg/mL, obtaining clear solution, as a consequence of their hydrophobic character, thus their surface is coated by oleylamine.

5.2.2.2 Synthesis and structural characterization of $NaYF_4$-PDMS hybrid nanocomposites

The synthesis of $NaYF_4$-PDMS nanocomposites were carried out following the procedure previously developed by our gruoup[11] using Ta, Nb, Ti and Zr as linkers (HyTa, HyNb, HyTi and HyZr respectively), but introducing in each synthesis 0.25 mL of the NPs suspension previously prepared (see Experimental Section for further details). Following this procedure, even introducing an apolar solvent in the synthesis and the UCNPs, transparent monoliths are obtained (Figure 5. 22a), this fact would indicate that the hydrolysis and condensation of the metaloorganic precursors seems not to be affected by this modification. In order to gain insight about this issue and about the stability of the UCNPs inside the organic-inorganic matrix, HR-TEM study of the ultramicrotomed hybrids was performed. Figure 5. 22 b and c, show representative HR-TEM images of HyTa-Er^{3+}/Yb^{3+}, where is possible to see that the UCNPs are well dispersed in the hybrid nanocomposite into small aggregates (< 200nm), not observing any agglomerated which could be assigned to Ta_2O_5. The interplanar distance calculated from the HR-TEM image (Figure 5. 22c) is 2.99 Å

which corresponds to (110) plane distance of the hexagonal phase of $NaYF_4$, pointing out that the crystalline structure is preserved after the gelification of the nanocomposite. Thus it can be said that the introduction of the UCNPs suspension in the gelation media does not affect the hydrolysis and condensation steps, because no segregation of undesired metal oxide domains has been detected, leading to homogeneous and transparent nanocomposites. Moreover the structural integrity of the UCNPs is conserved after the gelation process, which is of high importance in order to keep the luminescence properties of the starting material in the final nanocomposite.

Finally, the different hybrids were also processed as thin films by spin coating, leading films with a thickness around 450 nm.

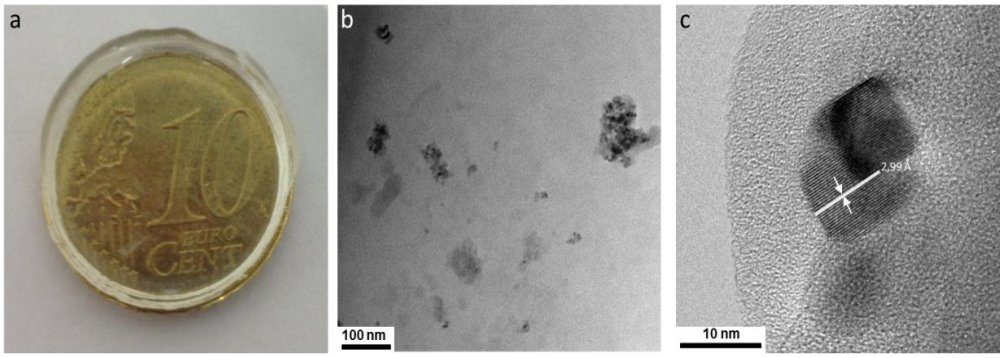

Figure 5. 22. a) Digital photograph of HyTa-Er^{3+}/Yb^{3+}. b- c) HR-TEM micrograph of ultramicrotomed HyTa-Er^{3+}/Yb^{3+}.

5.2.2.3 Optical characterization of $NaYF_4$-PDMS hybrid nanocomposites

The UV-Vis-NIR spectra of the starting NPs and the monoliths are shown in Figure 5. 23. For $NaYF_4$ NPs we can observe the typical bands corresponding to *f-f* transitions of the lanthanide ions characteristic of Er^{3+} and Tm^{3+}. In both samples (Er^{3+} and Tm^{3+} doped) a band around 980 nm characteristic of the $^2F_{7/2} \rightarrow {}^2F_{5/2}$ transition of Yb^{3+} ion is observed. This transition overlaps with $^4I_{15/2} \rightarrow {}^4I_{11/2}$ Er^{3+} transition and is near of $^3H_5$ level which corresponds to Tm^{3+}, this facts promotes the up-conversion process when this level is pumped.

The different monoliths no show any absorption band in the near infrared and visible region, caused by the small amount of UCNPs that contain and as a consequence of its transparency. In the UV region we can observe a strong band (around 200nm, not

shown) which corresponds to the O→M charge transfer in the amorphous metal oxo domains in good agreement with previous works.[38] Moreover HyTa, HyNb and HyZr show a band centered at 280nm and at 376 for HyTi, this difference in the position of this band can be explained on the basis of the higher refractive index of titanium oxide.[39,40]

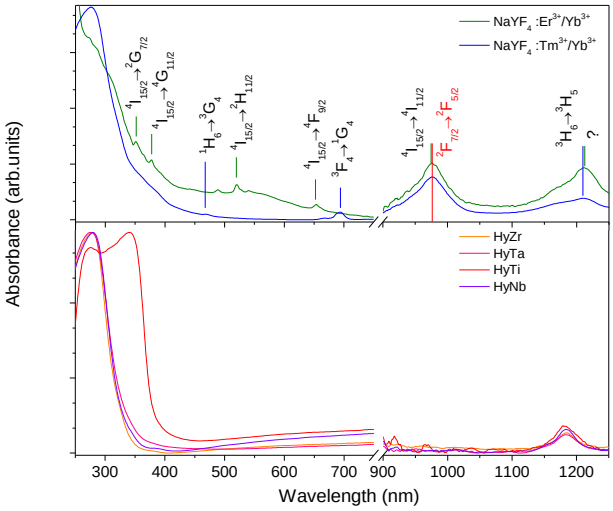

Figure 5. 23. UV-VIS-NIR absorption spectra of $NaYF_4$: Er^{3+}/Yb^{3+} and $NaYF_4$: Tm^{3+}/Yb^{3+} (top) and of the hybrid monoliths embeding $NaYF_4$: Er^{3+}/Yb^{3+} nanoparticles.

The suspension of the UCNPs in cyclohexane and the hybrid monoliths show bright green and blue emission for the Er^{3+} and Tm^{3+} respectively, upon exciting at 980nm (Figure 5. 24). These emissions are possible to observe by naked eye and correspond to $^2H_{11/2}\rightarrow{}^4I_{15/2}$ and $^4S_{3/2}\rightarrow{}^4I_{15/2}$ transitions for the Er^{3+} doped sample and to the $^1G_4\rightarrow{}^3H_6$ for the Tm^{3+} doped one.

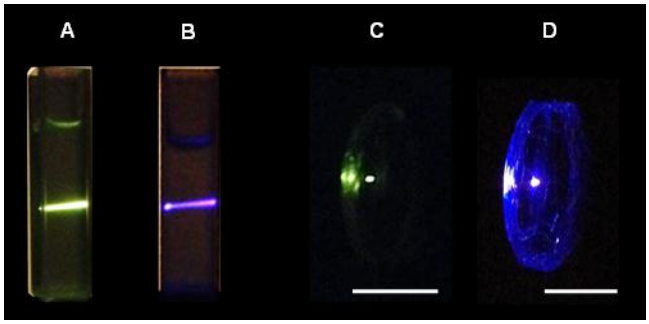

Figure 5. 24. Digital photograph of cyclohexane suspensión of A) $NaYF_4$: Er^{3+}/Yb^{3+}, B) $NaYF_4$: Tm^{3+}/Yb^{3+}, and HyTa monoliths embedding C) $NaYF_4$: Er^{3+}/Yb^{3+}, B) $NaYF_4$: Tm^{3+}/Yb^{3+}. Under excitation at 980nm. The cuvettes length is 10 mm and the scale bars in C) and D) correspond to 20 mm.

Hyperspectral Imaging consist into obtain the electromagnetic spectrum for every single pixel which compose a given image, in such a way a picture with selective and specific information about the distribution of the measured property is obtained.[41]

This technique has been further developed in the last years due to the introduction of better optical devices and the improvement of algorithms for data processing. Allowing its implementation in pharmaceutical industry, agriculture, food industry, physics, astronomy, biomedicine, etc.[41]

Figure 5. 25a shows the optical image of HybTa embedding $NaYF_4$:Er,Yb under 980 nm laser irradiation, where different spherical bright spots, between 1.0 to 6.0 µm, are observed, which may correspond to $NaYF_4$ agglomerates observed in HRTEM analysis. The emission of the surface of the monoliths was evaluated by hyperspectral microscopy (Figure 5. 25b, c and e) which provide an image of the dispersion of the NPs within the hybrid. In dark regions (area 1 and 4 in Figure 5. 25c and e) no up converting emission is detected while in bright regions in a single pixel area (area 2 and 3 Figure 5. 25c and e) the corresponding emission is observed (Figure 5. 25d and f).

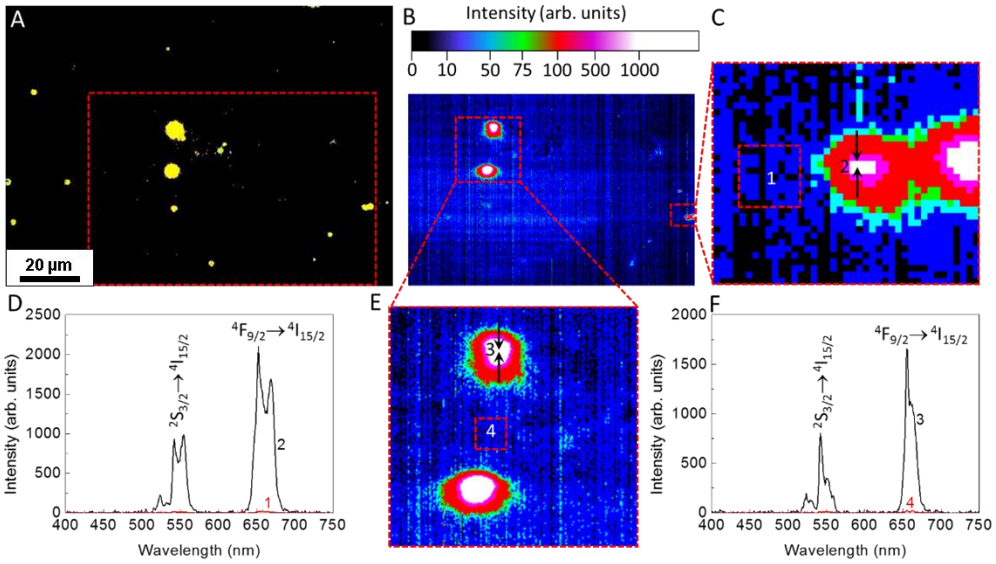

Figure 5. 25. (A) Optical and (B) hyperspectral micrsocopy image of the área marked in A with a red dashed rectangle of HyTa: $NaYF_4$:Er,Yb under 980 nm CW laser irradiation at room temperature. The color of each pixel is based on the intensity emission spectrum at 656 nm. (C) and (E) amplifications of dashed red rectangles in (B). (D) Emission spectra of region 1 (10x10 pixels, 1280x1280 nm^2) and region 2 (single pixel area, 128x128 nm^2) in (C). (F) Emission spectra of region 3 (single pixel area, 128x128 nm^2) and region 4 (10x10 pixels, 128x128 nm^2) in (D).

Moreover, Figure 5. 26 also shows the upconversion spectra of the different nanocomposites processed as monolith, film and the grinded monolith. If we compare these spectra with the NPs one, we can observe that they show the same profile and almost the same relative band intensity. Indeed, the NPs, monolith and film spectra have almost the same relative band intensity, thus it seems that the introduction the the NPs in the hybrid matrix does not affect its emission properties. Nevertheless if we carefully check the grinded monolith spectra, an augmentation in $^2H_{11/2}\rightarrow{}^4I_{15/2}$ band and a diminution in $^4S_{3/2}\rightarrow{}^4I_{15/2}$ transition is observed, in the green region, relatively to the red ($^4F_{9/2}\rightarrow{}^4I_{15/2}$) transition. This trend is shown by the four systems independently of the cosslinker used. This fact could be explained on the basis of the different sensitivity of the electronic transitions to the scattered radiation (incident and emitted light), thus in the monolith and in the films, the nanocompasite are transparent, yielding almost the same peak intensity spectra than the NPs. While in

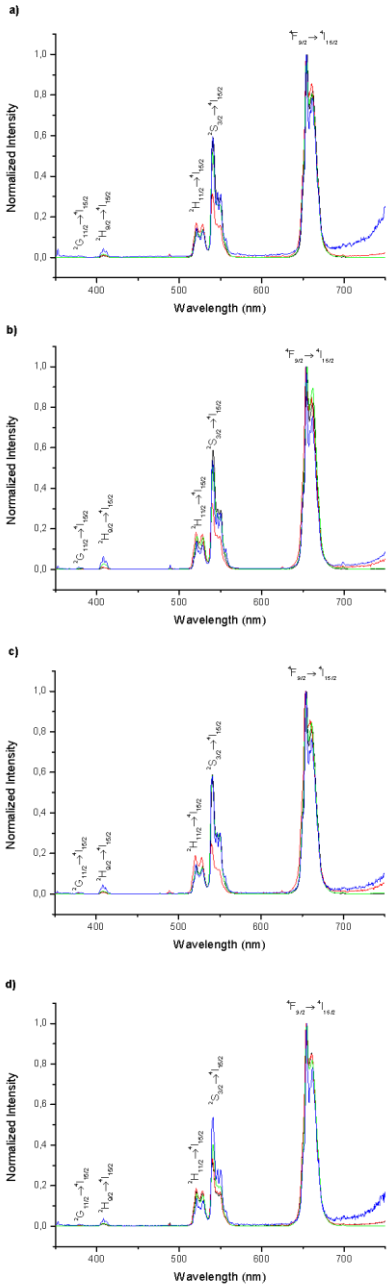

Figure 5. 26. Room temperatura upconversion emission spectra (980 nm excitation) of $NaYF_4:Er^{3+}/Yb^{3+}$ NPs using 29.5 $W \cdot cm^{-2}$ excitation power density (black) of monolith (green), film (blue) and grinded monolith (red) using 128.5 $W \cdot cm^{-2}$ power density of a) HyNb, b) HyTa, c)HyZr and d) HyTi embedding $NaYF_4:Er^{3+}/Yb^{3+}$ NPs.

the grinded samples, the incident and the emitted light is scattered providing difference in the relative band intensity in the upconversion spectra.

Figure 5. 27 shows the upconversion spectra of the different films (a), grinded monoliths (b) and monoliths (c), using the different crosslinkers at the same exciting power density. In the case of the grinded monoliths and films the relative peak intensity between the different hybrids is almost the same, thus implying that indepently of the metal used as a crosslinker in the hybrid, the upconversion

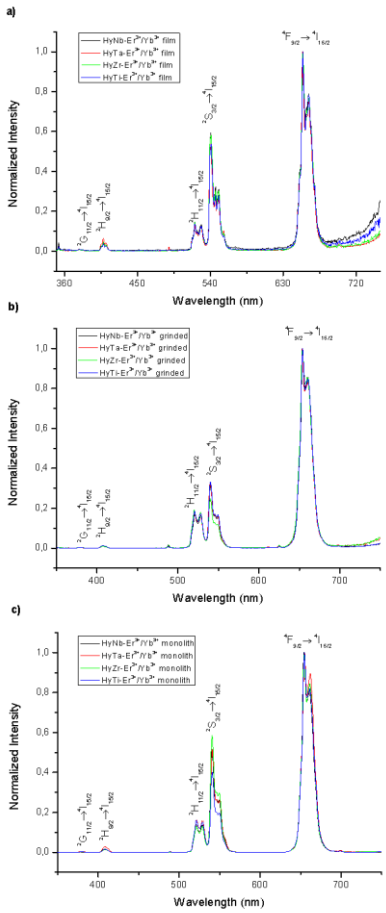

Figure 5. 27. Room temperatura upconversion emission spectra (980 nm excitation) of HyNb, HyTa, HyZr and HyTi embedding $NaYF_4:Er^{3+}/Yb^{3+}$ NPs processes as a) film, b)grinded monolith and c) monolith using 128.5W·cm^{-2} excitation power density.

properties remain unaltered. On the other hand, in the case of monoliths (Figure 5. 27) small differences in green ($^2H_{11/2}\rightarrow{}^4I_{15/2}$ and $^4S_{3/2}\rightarrow{}^4I_{15/2}$) emission relatively to the $^4F_{9/2}\rightarrow{}^4I_{15/2}$ red transition are observed, probably caused by small differences in the local distribution of the UCNPs in the monolith during the slow drying process.

The number of photons involved in the green ($^2H_{11/2}\rightarrow{}^4I_{15/2}$ and $^4S_{3/2}\rightarrow{}^4I_{15/2}$) and ($^4F_{9/2}\rightarrow{}^4I_{15/2}$) red emission for the $NaYF_4$:Er^{3+}/Yb^{3+} NPs and in the hybrids embedding it were calculated by plotting the log of the integrated intensity versus the excitation power density. Figure 5. 28 shows a representative example (HyTa:Er^{3+}/Yb^{3+}) of the upconversion spectra at different power densities and its *log-log* plot of the emitted integrated intensity vs excitation power density for green and red emissions.

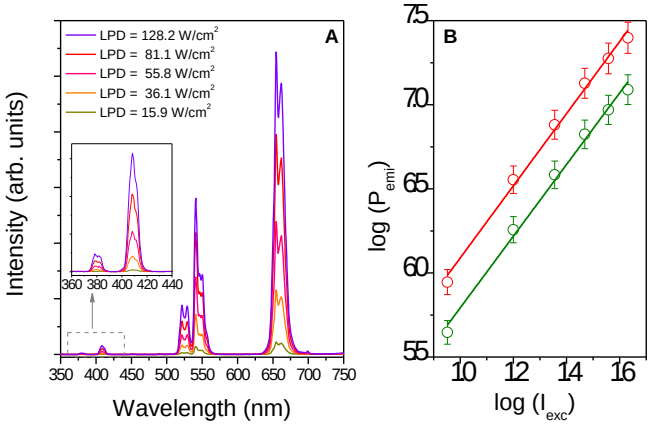

Figure 5. 28. (A) Spectral power of HyTa-Er^{3+}/Yb^{3+} upong different excitation power densities. The inset shows the magnification of the 360-440nm wavelength region (B) log-log plot of the integrated emitted power of the green and red transitions with the laser intensity resulting from the integration of the spectral power in the ranges 500-580 nm and 620-710 nm respectively.

Table 5. 4 compiles the number of photons calculated for green and red upconverting emission for $NaYF_4$:Er^{3+}/Yb^{3+} and the hybrids embedding it. In all cases the slope is close to 2 as it correspond for Er^{3+} doped upconverting materials and indicating a two-photon emission process. Moreover the red/green integrated intensity ratio is almost constant in the excitation power density for all the hybrids (Figure 5. 29) in good agreement with previous works regarding $NaYF_4$:$Er^{3+}Yb^{3+}$ materials.[42]

Table 5. 4. Slopes from the dependence of the integrated emitted power (P_{emi}) with the excitation laser intensity (I_{exc}) for the $NaYF_4:Er^{3+}/Yb^{3+}$ NPs and HyM-Er^{3+}/Yb^{3+} systems.

Sample	Green transitions $^2H_{11/2}$, $^4S_{3/2}\rightarrow{}^4I_{15/2}$	Red transition $^4F_{9/2}\rightarrow{}^4I_{15/2}$
$NaYF_4:Er^{3+}/Yb^{3+}$	1.8	1.8
HyNb- Er^{3+}/Yb^{3+}	1.6	1.6
HyTa- Er^{3+}/Yb^{3+}	1.8	1.9
HyTi- Er^{3+}/Yb^{3+}	2.0	2.0
HyZr- Er^{3+}/Yb^{3+}	1.7	1.7

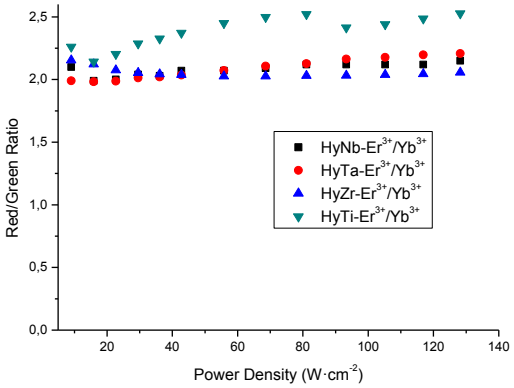

Figure 5. 29. Red to Green intensity ratio of the upconversion emission for the HyM-Er^{3+}/Yb^{3+} as a function of the power density.

For the UCNPs doped with thulium, upon exciting at 980nm the upconversion spectra show blue ($^1G_4\rightarrow{}^3H_6$) and red ($^1G_4\rightarrow{}^7F_4$ and $^3F_3\rightarrow{}^3H_6$) emission. The different hybrid nanocomposites embedding the $NaYF_4:Tm^{3+}/Yb^{3+}$ NPs show small differences in the red ($^1G_4\rightarrow{}^7F_4$ and $^3F_3\rightarrow{}^3H_6$) emission relatively to the $^1G_4\rightarrow{}^3H_6$ blue transition,

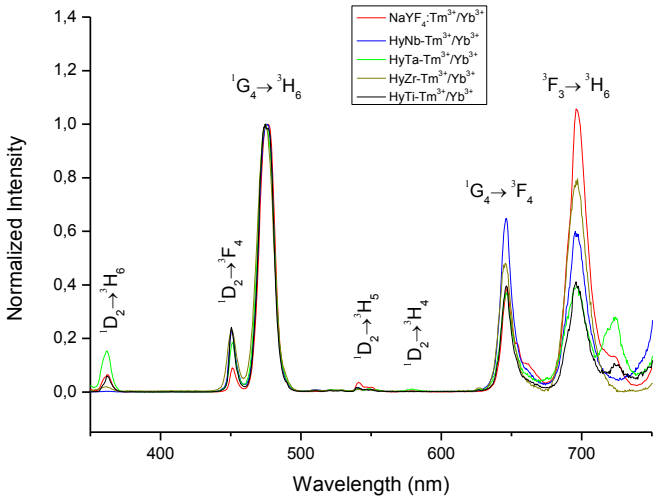

Figure 5. 30. Room temperatura upconversion emission spectra (980 nm excitation) of $NaYF_4:Tm^{3+}/Yb^{3+}$ NPs using 15.9 $W \cdot cm^{-2}$ excitation power density and HyM- Tm^{3+}/Yb^{3+} processed as monolith using 295.5 $W \cdot cm^{-2}$ power density.

probably caused by small differences in the local distribution of the UCNPs in the monolith during the slow drying process, as discussed above (Figure 5. 30).

The optical mechanism for this upconversion emission consist in the excitation of the Yb^{3+} ions from $^2F_{7/2}$ to $^2F_{5/2}$, thus the Tm^{3+} have no energy level above the ground state (Figure 5. 31). After that Yb^{3+} excites a Tm^{3+} ion form $^3H_6$ to $^3H_5$ state via energy transfer. After that Tm^{3+} relaxes non radiatively to $^3F_4$ state and then another energy transfer from Yb^{3+} to Tm^{3+} populates the $^3F_{23}$ state. The red emission centered at 695 nm is ascribed to the radiative transition between $^3F_{2,3}$ and $^3H_6$. Additionally, the $^3F_{2/3}$ state can non-radiatively decay to $^3H_4$ and then this state decay rediatively to $^3H_6$ state providing the band centered at 802 nm (not shown in the spectra). Finally a third energy transfer from Yb^{3+} to Tm^{3+} promotes the excitation from $^3H_4$ to $^1G_4$ state, whose radiative transitions to $^3F_4$ and $^3H_6$ states leads to the red (647 nm) and blue (476 nm) emissions.

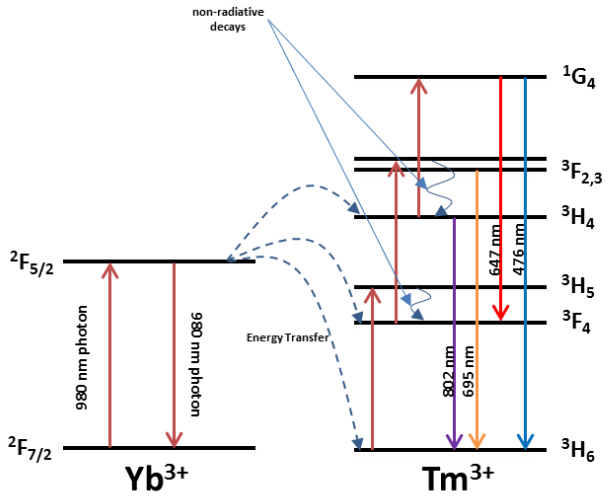

Figure 5. 31. Energy level diagrams of the Yb^{3+} and Tm^{3+} ions and the proposed upconversion mechanism following diode laser excitation at 980 nm.

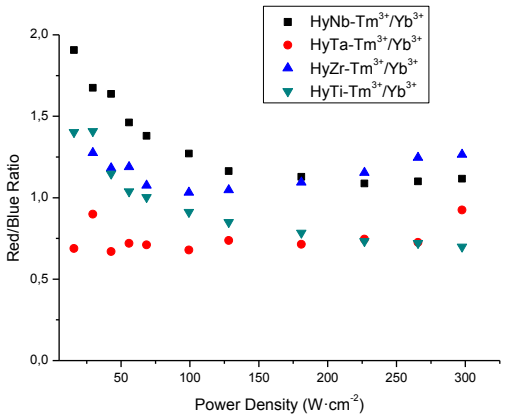

Figure 5. 32. Red to Green intensity ratio of the upconversion emission for the HyM-Tm^{3+}/Yb^{3+} as a function of the power density.

Figure 5. 32 shows the red-blue ratio for each hybrid nanocomposite as a function of the excitation power density. In the case of HyTa-Tm^{3+}/Yb^{3+} this ratio remains almost constant in all power regime. While in the case of the three other nanocomposites, in the low power regime the red-blue ratio decreases until 100 W·cm^2, then at higher power exciting densities this ratio remains almost constant as in HyTa. This fact implies that at lower power excitation densities, upon increasing it, the blue emission

increases in a higher rate compared to the red one. Once at higher excitation power densities, the system becomes saturated and this ratio remains constant.

Table 5. 5. Slopes from the dependence of the integrated emitted power (P_{emi}) with the excitation laser intensity (I_{exc}) for the $NaYF_4:Tm^{3+}/Yb^{3+}$ and HyM-Tm^{3+}/Yb^{3+}.

Sample	Blue transitions $^1G_4 \rightarrow {}^3H_6$	Red transition $^3F_3 \rightarrow {}^3H_6$
$NaYF_4:Tm^{3+}/Yb^{3+}$	3.1	2.6
HyNb- Tm^{3+}/Yb^{3+}	1.8	1.6
HyTa- Tm^{3+}/Yb^{3+}	1.6	1.7
HyTi- Tm^{3+}/Yb^{3+}	1.2	1.2
HyZr- Tm^{3+}/Yb^{3+}	1.7	1.5

The numbers of photons involved in the upconversion emission of the Tm^{3+} doped materials were calculated by calculating the slope in the *log-log* plot of the integrated emitted power of the blue and red transitions with the laser intensity (Table 5. 5). For the $NaYF_4:Tm^{3+}/Yb^{3+}$ NPs the slopes for the blue and red emissions are close to 3 which means that the number of photons involved in these emissions is 3, in good agreement with the mechanism commented above. On the other side for HyM-Tm^{3+}/Yb^{3+} composites the slopes for both emissions in all materials are close to 2. This fact could be related because of Tm^{3+} up conversion emission is a 3 photon assisted process, which is less efficient compared to Er^{3+}, that implies 2 photons. As consequence the power density required for obtaining a good emission signal is higher for Tm^{3+} samples and probably we are on saturated conditions, which provide a slope lower than 3.

5.3 Conclusions

In this section we have performed the synthesis and characterization of up conversion NPs which were introduced in organic-inorganic hybrids processed as transparent monolith and films. Moreover their physical and optical properties were further characterized.

In the first part, transparent and easy-to-shape organic-inorganic hybrid materials based on Er^{3+}:Yb^{3+}:ZrO_2:di-ureasil were synthesized and characterized. For this purpose, Er^{3+} and Er^{3+}:Yb^{3+} doped ZrO_2 NPs with different doping levels and with less than 20 nm were obtained. These NPs were successfully introduced and dispersed in the di-ureasil hybrid and processed as transparent monolith and films. The introduction of ZrO_2 NPs in the hybrid does not affect the local structure of the hybrid while the refraction index is increased upon introduction of zirconia NPs.

The optical characterization shows that these hybrids behave as multimodal spectral converters, thus upon UV and visible excitation white emission is obtained from di-ureasil component and an efficient hybrid-Er^{3+} energy transfer is also observed, in addition of green and red up converting emission when the nanocomposites are pumped at 980 nm. The emission can also be tuned thus, white emission shifts upon changing the UV-visible excitation wavelength and the green/red upconverting ratio can be tunned upon changing the Er^{3+}content and the pumping intensity.

On the other side transparent $NaYF_4$-PDMS-(M_xO_y) nanocomposites with green and blue upconverting properties where synthesized. The properties of these nanocomposites, such as refractive index, mechanics, hydrophobic character, etc, can be tuned upon varying the nature of the crosslinker (M_xO_y, M: Nb, Ta, Ti, Zr). The nanocomposites are synthesized through an easy two-step sol-gel procedure and provide hybrids with good UCNPs dispersion. The up converting emission properties are retained after the introduction of the NPs in the hybrid organic-inorganic with minor modification upong changing the crosslinker metal or the processing sample (monolith, film or grinded sample).

5.4 References

(1) Sanchez, C.; Soler-Illia, G. J. de A. A.; Ribot, F.; Lalot, T.; Mayer, C. R.; Cabuil, V. *Chem. Mater.* **2001**, *13* (10), 3061–3083.

(2) Sanchez, C.; Julián, B.; Belleville, P.; Popall, M. *J. Mater. Chem.* **2005**, *15* (35–36), 3559–3592.

(3) Ungureanu, S.; Birot, M.; Laurent, G.; Deleuze, H.; Babot, O.; Julián-López, B.; Achard, M.-F.; Popa, M. I.; Sanchez, C.; Backov, R. *Chem. Mater.* **2007**, No. 19, 5786–5796.

(4) Haders, D. J.; Burukhin, A.; Zlotnikov, E.; Riman, R. E. *Chem. Mater.* **2008**, No. 6, 7177–7187.

(5) Carlos, L. D.; Ferreira, R. A. S.; de Zea Bermudez, V.; Ribeiro, S. J. L. *Adv. Mater.* **2009**, *21* (5), 509–534.

(6) Binnemans, K. *Chem. Rev* **2009**, *109*, 4283–4374.

(7) Feng, J.; Zhang, H. *Chem. Soc. Rev.* **2013**, *42* (1), 387–410.

(8) Escribano, P.; Julián-López, B.; Planelles-Aragó, J.; Cordoncillo, E.; Viana, B.; Sanchez, C. *J. Mater. Chem.* **2008**, *18* (1), 23–40.

(9) Carlos, L. D.; Ferreira, R. A. S.; de Zea Bermudez, V.; Julián-López, B.; Escribano, P. *Chem. Soc. Rev.* **2011**, *40* (2), 536–549.

(10) Gómez-Romero, P.; Sanchez, C. *Functional Hybrid Materials*; WILEY-VCH: Germany, 2004.

(11) Julián, B.; Gervais, C.; Cordoncillo, E.; Escribano, P.; Babonneau, F.; Sanchez, C. *Chem. Mater.* **2003**, No. 15, 3026–3034.

(12) Julián, B.; Corberán, R.; Cordoncillo, E.; Escribano, P.; Viana, B.; Sanchez, C. *Nanotechnology* **2005**, *16* (11), 2707–2713.

(13) Corma, A. *Chem. Rev.* **1995**, *95* (3), 559–614.

(14) Julián-López, B.; De La Luz, V.; Gonell, F.; Cordoncillo, E.; López-Haro, M.; Calvino, J. J.; Escribano, P. *J. Alloys Compd.* **2012**, *519*, 29–36.

(15) Qiu, H.; Chen, G.; Fan, R.; Cheng, C.; Hao, S.; Chen, D.; Yang, C. *Chem. Commun. (Camb).* **2011**, *47* (34), 9648–9650.

(16) Tahir, M. N.; Gorgishvili, L.; Li, J.; Gorelik, T.; Kolb, U.; Nasdala, L.; Tremel, W. *Solid State Sci.* **2007**, *9* (12), 1105–1109.

(17) Li, W.; Huang, H.; Li, H.; Zhang, W.; Liu, H. *Langmuir* **2008**, *24* (15), 8358–8366.

(18) Fernández López, E.; Sánchez Escribano, V.; Panizza, M.; Carnasciali, M. M.; Busca, G. *J. Mater. Chem.* **2001**, *11* (7), 1891–1897.

(19) Li, C.; Li, M. *J. Raman Spectrosc.* **2002**, *33*, 301–308.

(20) Noda, L. K.; Gonçalves, N. S.; de Borba, S. M.; Silveira, J. A. *Vib. Spectrosc.* **2007**, *44* (1), 101–107.

(21) Zalewski, D. J.; Alerasool, S.; Doolin, P. K. *Catal. Today* **1999**, *53* (3), 419–432.

(22) Riemer, T.; Spielbauer, D.; Hunger, M.; Mekhemer, G. a. H.; Knözinger, H. *Chem. Commun.* **1994**, No. 10, 1181–1182.

(23) Bermudez, V. D. Z.; Carlos, L. D.; Alcácer, L. *Chem. Mater.* **1999**, *11*, 569–580.

(24) Fu, L.; Sá Ferreira, R. A.; Silva, N. J. O.; Carlos, L. D.; De Zea Bermudez, V.; Rocha, J. *Chem. Mater.* **2004**, *16* (8), 1507–1516.

(25) Fu, L.; Sá Ferreira, R. a.; Fernandes, M.; Nunes, S. C.; de Zea Bermudez, V.; Hungerford, G.; Rocha, J.; Carlos, L. D. *Opt. Mater. (Amst).* **2008**, *30* (7), 1058–1064.

(26) Lima, P. P.; Ferreira, R. A. S.; Júnior, S. A.; Malta, O. L.; Carlos, L. D. *J. Photochem. Photobiol. A Chem.* **2009**, *201* (2–3), 214–221.

(27) Molina, C.; Moreira, P. J.; Gonçalves, R. R.; Sá Ferreira, R. a.; Messaddeq, Y.; Ribeiro, S. J. L.; Soppera, O.; Leite, A. P.; Marques, P. V. S.; de Zea Bermudez, V.; Carlos, L. D. *J. Mater. Chem.* **2005**, *15* (35–36), 3937.

(28) Carlos, L. D.; Sá Ferreira, R. A.; De Zea Bermudez, V.; Ribeiro, S. J. L. *Adv. Funtional Mater.* **2001**, *11* (2), 111–115.

(29) Carlos, L. D.; Sá Ferreira, R. A.; Pereira, R. N.; Assunçao, M.; Bermudez, V. D. Z. *J. Phys Chem. B* **2004**, *108*, 14924–14932.

(30) Thomson, L. C.; Marvin, J. R.; Bettenberg, N. C. *J. Alloys Compd.* **1992**, *180*, 229–234.

(31) Vetrone, F.; Boyer, J. C.; Capobianco, J. A.; Speghini, A.; Bettinelli, M. *J. Phys. Chem. B* **2003**, *107* (5), 1107–1112.

(32) Vetrone, F.; Boyer, J.; Capobianco, J. A.; Speghini, A.; Bettinelli, M. *Chem. Mater.* **2003**, No. 14, 2737–2743.

(33) Auzel, F. *Chem. Rev.* **2004**, *104* (1), 139–173.

(34) Kumar, G. A.; Pokhrel, M.; Martinez, A.; Dennis, R. C.; Villegas, I. L.; Sardar, D. K. *J. Alloys Compd.* **2012**, *513*, 559–565.

(35) Chen, G.; Ohulchanskyy, T. Y.; Kumar, R.; Ågren, H.; Prasad, P. N. *ACS Nano* **2010**, *4* (6), 3163–3168.

(36) Pollnau, M.; Gamelin, D. R.; Lüthi, S. R.; Güdel, H.; Hehlen, M. P. *Phys. Rev. B Condens. Mater.* **2000**, *61* (5), 3337–3346.

(37) Ferrari, J. L.; de Oliveira Lima, K.; Pecoraro, E.; Ferreira, R. a. S.; Carlos, L. D.; Gonçalves, R. R. *J. Mater. Chem.* **2012**, *22* (19), 9901.

(38) Graubner, V. M.; Jordan, R.; Nuyken, O.; Lippert, T.; Hauer, M.; Schnyder, B.; Wokaun, A. *Appl. Surf. Sci.* **2002**, *197–198*, 786–790.

(39) Julián, B.; Corbera, R.; Cordoncillo, E.; Escribano, P.; Viana, B.; Sanchez, C. *J. Mater. Chem.* **2004**, No. 14, 3337–3343.

(40) Ravindra, N. M.; Ganapathy, P.; Choi, J. *Infrared Phys. Technol.* **2007**, *50* (1), 21–29.

(41) Amigo, J. M.; Babamoradi, H.; Elcoroaristizabal, S. *Anal. Chim. Acta* **2015**, *896*, 34–51.

(42) Mai, H.-X.; Zhang, Y.-W.; Sun, L.-D.; Yan, C.-H. *J. Phys. Chem. C* **2007**, *111* (37), 13721–13729.

Chapter 6

Experimental Section

6.1 Materials Synthesis

6.1.1 Synthesis of materials of Chapter 2

Synthesis of ZA-y and y-WZA-x NPs

The proper amount of $ZrOCl_2 \cdot 8H_2O$ and $Na2WO_4 \cdot 2H_2O$ precursors (47 mmol in total) were dissolved in 80 mL of milliQ water. The solution was transferred into two Teflon cups of 100 mL each and introduced in a microwave oven Synthos 3000 from Anton Paar. Thus, the temperature was increased at 20^oC/min until 220^OC, with a dwell time of 10 minutes. Then, the vials were allowed to cool to room temperature and the precipitates were washed and centrifuged several times. The material was dispersed in water and dialyzed until no chloride ions were detected. Finally, the suspension was dried under air flow and annealed at 500 and 800^OC for 2 hours in a muffle furnace. These samples were denoted as ZA-x for the pure zirconia and y-WZA-x for the tungsten-doped samples, where x denotes the annealing temperature of the sample and y the molar percentage of tungsten.

Synthesis of ZU-y and y-WZU-x NPs

The proper amount of $ZrOCl_2 \cdot 8H_2O$ and $Na2WO_4 \cdot 2H_2O$ precursors (47 mmol in total) were dissolved in 80 mL of milliQ water with 54 mmol of urea. The solution was transferred into two Teflon cups of 100 mL each and introduced in a microwave oven Synthos 3000 from Anton Paar. Thus, the temperature was increased at 20^oC/min until 220^OC, with a dwell time of 10 minutes. Then, the vials were allowed to cool to room temperature and the precipitates were washed and centrifuged several times. The material was dispersed in water and dialyzed until no chloride ions were detected. Finally, the suspension was dried under air flow and annealed at 500 and 800^OC for 2 hours in a muffle furnace. These samples were denoted as ZU-x for the pure zirconia and y-WZU-x for the tungsten-doped samples, where x denotes the annealing temperature of the sample and y the molar percentage of tungsten

Synthesis of pure monoclinic and tetragonal ZrO_2 NPs

Pure tetragonal (T) and monoclinic (M) zirconias were synthetized as previously described.[1] Briefly, 0.6 mols of $ZrO(NO_3)_2xH_2O$ were dissolved in the 150 mL of the corresponding solvent, once dissolved 6 mols of urea were solubilized in the mixture and transferred to teflon-lined autoclave and heated to 150 °C for 18 h. The solvent used was water for obtaining the monoclinic phase and methanol for the tetragonal polymorph. The precipitated products were further washed and centrifuged in the mother solvent and dried at 100ºC overnight. Finally the materials were annealed at 400ºC in a muffle furnace in air atmosphere.

Synthesis of 10WZM800 and 10WZT800

Pure crystalline zirconia polymorph synthesized as explained above and they were wet impregnated with an aqueous solution of $(NH_4)_6H_2W_{12}O_{40}H_2O$ at 80ºC, dried overnight at 110ºC and finally treated at 800ºC for obtaining 10WZM800 and 10WZT800.

Synthesis of Sn:W 2:1

The tungsten-tin oxide was synthetized as previously described.[2–4]Briefly, Sn-W hydroxide with a Sn/W molar ratio of 2 was prepared by dissolving 2.47 g (7.5 mmol) of $Na_2WO_4 \cdot 2H_2O$ in 15 mL of milliQ water, and adding 5.26 g of $SnCl_4 \cdot 5H_2O$.(15 mmol) This solution was stirred for 1 hour, then 60 mL of milliQ water was added and stirred during 24h. The white precipitate was thoroughly filtered and washed with water and dried under vacuum. This material was annealed at 500 and 800ºC for 2 hours and denoted as SnW 2:1 followed by the annealing temperature.

Synthesis of 10WZDis

The coprecipitated W/ZrO_2 catalyst was synthetized following a procedure previously reported.[5,6] Briefly 1.6 mmol of $(NH_4)_6H_2W_{12}O_{40}H_2O$ was dissolved in 50 mL of

milliQ water and pH was increased to 10 with NH_4OH (25% weight), then a solution of 16.2 mmol of $ZrOCl_2 \cdot 8H_2O$ in 20 mL of milliQ water was introduced drop by drop keeping the pH at 10 with the ammonia solution. The white slurry was aged during 24 hours at room temperature, filtered, and washed with water until no chloride was detected. Finally it was dried overnight at 100ºC and annealed at 500 and 800ºC for two hours. These samples were denoted as 10WZDis followed by the annealing temperature.

Synthesis of 10WZDep

The impregnated W/ZrO_2 catalyst was synthetized using the same amount of reagents than before, but in this case, firstly zirconium hydroxide was precipitated and after that a tungsten salt was wet impregnated. Briefly, 16.2 mmol of $ZrOCl_2 \cdot 8H_2O$ was dissolved in 20 mL of milliQ water. The zirconium hydroxide was precipitated with NH_3 at pH 10. The precipitate was filtrated, repeatedly washed with water until no chloride was detected, and dried overnight at 100ºC. Then, the solid was wet-impregnated at 80ºC with 1.6 mmol of $(NH_4)_6H_2W_{12}O_{40}H_2O$ dissolved in 10 mL of milliQ water. The final material was dried at 100ºC overnight and annealed at 500 and 800ºC for 2 hours. This material was denoted as 10WZDep followed by the temperature of treatment.

6.1.2 Synthesis of materials of Chapter 4

Synthesis of Cu-TiO_2

The synthesis of Cu-TiO_2 was carried out following a solvothermal methodology previously reported by our group[7] with some modifications. Briefly, the proper amounts of $Cu(Ac)_2$ (Sigma Aldrich 98%) and $Ti(iOPr)_4$ (Sigma Aldrich 97%) (12.5 mmol as a sum of both) were dissolved in 50mL of EtOH. Once dissolved, acetylacetonate (acac) was added in a molar ratio (Cu+Ti):acac 1:2 in order to afford the corresponding complex and to avoid the un-controlled hydrolysis and condensation[8] of the reagents. The mixture was stirred for 0.5 hours and transferred into a 125 teflon-lined autoclave and heated to 180ºC for 24h. The solid products

were washed with EtOH, isolated by centrifugation several times and dried at 100ºC overnight. Finally the material was annealed at 500ºC.

Synthesis of $Er_{0.04}Yb_{0.1}Y_{1.86}O_3$ NPs

The proper amount of Y, Er and Yb nitrates (Alfa Aesar 99.9%), in order to obtain a total concentration of 0.015 M (6.975 mmol of $Y(NO_3)_3 \cdot 6H_2O$, 0.15 mmol of $Er(NO_3)_3 \cdot 5H_2O$ and 0.375 mmol of $Yb(NO_3)_3 \cdot 5H_2O$), were dissolved in 0.5L of distilled water, the temperature of this solution was increased to 80ºC and then 0.25 mols of urea (Alfa Aesar 98%) were added, the suspension was stirred at this temperature during 6 hours. At this temperature urea is slowly hydrolyzed to CO_2 and NH_3 and it induces the precipitation of yttrium hydroxycarbonate $Y(OH)CO_3$ [9] because of the basicity of the yttrium ion. Finally the precipatates were thoroughly filtered and washed, dried at 100ºC overnight and calcined at 800ºC for two hours in a muffle furnace.

Preparation of TiO_2/UCs Electrodes

The preparation of the device was done in several steps. First, the $Er_{0.04}Yb_{0.1}Y_{1.86}O_3$ NPs were introduced into a heterostructured TiO_2/CdSe photoanode. For this purpose, a mesoporous TiO_2 paste was synthetized following a previously described method[10] and a 20 % wt of the UCNPs were incorporated into the paste. This mixture was screen printed into a FTO substrate previously coated with a TiO_2 compact layer, and further calcined at 450ºC for 30 minutes in order to remove all the organic moieties.

The electrode was then sensitized with CdSe quantum dots (QDs) by a successive ionic layer adsorption and reaction (SILAR) method.[11,12] In brief, the electrode was immersed successively in two ethanolic solutions of Cd^{2+} and Se^{2-}. This process was conducted in a glovebox under N_2 atmosphere. Then, it was rinsed with ethanol and dried with N_2 flow. This cycle constitutes a SILAR cycle. Four SILAR cycles were carried out in order to sensitize the photoanode.

After that, a ZnS layer was grown over the sensitized electrode, following the same procedure as described above. The deposition of the ZnS layer in this kind of photovoltaic devices improves the photocurrent of the system by reducing the carrier

recombination process at the TiO_2/electrolyte interface. Furthermore, it increases the stability of the device by avoiding the photocorrosion of the CdSe QDs.

6.1.3 Synthesis of materials of Chapter 5

Synthesis of $UPZrO_2$ NPs

The proper amount of $Zr(OPr^n)_4$ (70% in isopropanol (Sigma Aldrich)) was added to acetylacetone (acac) dissolved in isopropanol (IPA). Then, an aqueous solution composed of of p-toluensulfonic (PTSH) acid and the proper amount of $Er(NO_3)_3{\cdot}5H_2O$ and $Yb(NO_3)_3{\cdot}5H_2O$) was added drop wise to the previous solution. The molar ratio of the precursors are: $Zr(OPr^n)_4$: H_2O: acac: PTSH: IPA= 1: 10: 1: 0.2: 2.34.

The solution was refluxed at 60ºC for 3 days. After that the suspension was dried at 35ºC and the final powder was moltured in a Agate mortar and calcined at 800ºC in order to increase the NPs size and to remove the organic matter. Fiinally the powders were sieved trhough a 60µm mesh screen.

Synthesis of ZrO_2-di-ureasil hybrid materials

In a first step, the hybrid precursor, di-ureapropi-triethoxysilane (d-UPTES(600)), was synthetized as previously described.[13] Breifly, 3-isocyanatepropyltriethoxysylane (ICPTES) and Jeffamine ED-600 were mixed in tetrahydrofurane (THF) in a molar ratio 2:1 respectively, this solution was stirred at room temperature for 24 hours. During this time the amine groups of Jeffamine ED-600 attacks the isocyanate group of the alkoxysilane providing the urea cross-linked organic-inorganic precursor. Finally the THF was remover in a rotatory evaporator.

After that, 0.41 mL of EtOH, 0.41 mL of a water suspension of the ZrO_2 lanthanide doped NPs with a concentration 5mg/mL, previously sonicated for 1 hour, were mixed with 1.91g of d-UPTES(600) after stirring, 9.6 µL of HCl 0.5M was added in order to promote the sol-gel transition. This solution was used to produce monolith (8×8×15 mm) by solvent cast and films by spin coating on glass substrates

(SCHOTT®) varying the deposition conditions in order to obtain films with different thickness. The films and the monoliths were dried at 45ºC for 7 days in order to remove any residual solvent and to consolidate the sol-gel process.

Synthesis of $NaYF_4$ NPs

The doped $NaYF_4$ NPs (Er:Yb 2:20 and Tm:Yb 2:20) were synthetized through thermal decomposition as previously reported by G. S. Yi et.al[14]. Thus, 10 mmol of of $NaCF_3COO$ and 5 mmol of $RE(CH_3COO)_3$ were mixed together with 50 mL of oleylamine and was added to a three-necked flask. Then the temperature solution was increased to 100ºC and subjedted to three cycles of vacuum pump and argon aeration. Finally the temperature was increased to 340ºC for two hours under argon atmosphere. Finally the nanoparticles were precipitated with ethanol and centrifugated several times. The UCNPs were redispersed in cyclohexane with a nanocrystal concentration of 1mg/mL.

Synthesis of PDMS-M_xO_y- $NaYF_4$ NPs hybrid nanocomposites

Dimethyldiethoxysilane (DEDMS, 98%), Zirconium isopropoxide ($Zr(OPr^i)_4$), Titanium isopropoxide ($Ti(OPr^i)_4$), Tantalum ethoxide ($Ta(OEt)_5$) and Niobium ethoxide ($Nb(OEt)_5$)) were purchased from Sigma-Aldrich. Ethanol and cyclohexane were obtained from Scharlab. All reactants and solvents were used as received without further purification.

In a typical synthesis, 0.250 mL of the suspension of $NaYF_4$ NPs (1mg/mL in cyclohexane) was added to a prehydrolized Dimethyldiethoxysilane (DEDMS) solution (DEDMS ($6.95\cdot10^{-3}$) :H_2O:EtOH in a 1:1:1 molar ratio, acidified with HCl at pH=1, and 30 minutes of hydrolysis time. Then, the proper amount of the metal alcoxide ($Zr(OPr^i)_4$, $Ti(OPr^i)_4$, $Ta(OEt)_5$ and $Nb(OEt)_5$) was added in a 0.2 molar ratio to DEDMS. After 30 minutes of stirring, the sol was sonicated for 5 minutes and processed as monolith or film. For the preparation of the monoliths, 2.2 mL of sol were poured into PE round vials (from Kartell) and left drying at 35ºC for one week. The final monoliths were cylinders with about 20mm diameter by 1.5 mm high. Thin films of around 450 nm thickness were prepared by spin coating on a glass substrate. The nanocomposite made of PDMS-M_xO_y (with M: Ta, Nb, Ti, Zr) containing the

UCNPs (with Er/Yb or Tm/Yb as active ions) are referenced as HyTa, HyNb, HyTi and HyZr, followed by the active ions (-Er/Yb or -Tm/Yb).

6.2 Characterization techniques

X-ray powder diffraction (XRD)

XRD measurements of $Er_{0.04}Yb_{0.1}Y_{1.86}O_3$ NPs, $NaYF_4$ NPs and $UPZrO_2$ NPs samples were recorded on a D4 Endeavor, Bruker-AXS diffractometer with a Cu-Kα radiation with a wavelength of 0.1542 nm.

These measurements for Cu-TiO_2, W-ZrO_2 and Sn:W 2:1 materials were performed with a PANalytical Cubix'Pro diffractometer equipped with an X'Celerator detector and automatic divergence and reception slits using Cu-Kα radiation (0.154056 nm). The mean size of the ordered (crystalline) domains (d) was estimated using the Scherrer equation. The equation can be written as $d = \frac{0.9\,\lambda}{\beta\, cos\theta}$, where λ is the X-ray wavelength, β is the line broadening at half the maximum intensity (FWHM), after subtracting the instrumental line broadening, in radians, and θ is the Bragg angle.

The volume fractions of the tetragonal (v_t) and monoclinic (v_m) were calculated as previously reported,[15] by integrating the (111) peak of *t*-ZrO_2 and (111) and (-111) peaks of *m*-ZrO_2 and using the following equations:

$v_m = \frac{1.311x}{1+0.311x}$ and $v_t = 1 - v_m$, where $x = \frac{I_m(\bar{1}11)+I_m(111)}{I_m(\bar{1}11)+I_m(111)+I_t(111)}$

Raman spectroscopy

Raman spectra were recorded with a spectral window of 100–1600 cm^{-1} on a Jasco NRS-3100 laser Raman spectrophotometer (exc = 785 nm).

N_2 adsorption-desorption experiments

N_2 Adsorption–desorption isotherms were collected on a Micromeritics Gemini V gas adsorption analyzer at 77 K, after degassing the samples at 150°C overnight in a Micromeritics Flow prep 060 system with nitrogen flux gas. The surface areas were calculated from the adsorption branch of the isotherm according to the BET method.[16]

Transmission electron microscopy (TEM)

The characterization by TEM for the as prepared W-ZrO_2 was carried out on a Tecnaï Spirit G2 apparatus, at an accelerating voltage of 120 kV, and for the annealed samples the high resolution electron microscopy (HRTEM) was carried out in a JEOL JEM 2100F at an accelerating voltage of 200 kV coupled with an Inca Energy TEM 200(Oxford) energy dispersive X-ray (EDX) spectroscopy and a high-angle annular dark field (HAADF) detector.

For the other samples, HRTEM measurements were carried out in a JEM-2100 LaB_6 (Jeol) microscope, coupled with an Inca Energy TEM 200 (Oxford) energy dispersive X-ray spectroscopy (XEDS).

For the sample preparation, the materials were suspended in a convenient solvent, one droplet of this suspension was allowed to dry on a carbon-coated copper or nickel grid.

The UP-monoliths were sectioned by a Leica Ultracut UCT microtome, equipped with a diamond knife. The microtome sections were between 100 and 200 nm thick, judged by the light reflection of each cut when floating in fluid

Scanning Electron Microscopy (SEM)

Scanning electron micrographs of the samples were taken with a field emission gun scanning electron microscope (FEG-SEM) model JEOL 7001F, equipped with a spectrometer of energy dispersion of X-ray (EDX) from Oxford instruments by using the following operational parameters: acceleration voltage 20 KV, measuring time 305 s, working distance 10 mm, counting rate 1.2 kcps. The samples for microstructural and microanalysis determinations were covered with a Pt film.

Thermogravimetric analysis (TGA)

TGA was performed using a Mettler Toledo TGA/SDATA851e thermo-balance under air from room temperature to 800 °C.

Inductively Coupled Plasma Emission Spectroscopy

The chemical analyses were carried out in a Varian 715-ES ICP-Optical Emission spectrometer, after solid dissolution in HNO_3/HCl/HF aqueous solution.

X-ray photoelectron spectroscopy (XPS)

(XPS) data were collected on a SPECS spectrometer equipped with a 150-MCD-9 detector and using a non-monochromatic Al Kα (1486.6 eV) X-ray source. Spectra were recorded at 175°C, using an analyzer pass energy of 30 eV, an X-ray power of 50 W and under an operating pressure of 10^{-9}mbar. During data processing of the XPS spectra, binding energy (BE) values were referenced to the C1s signal (284.6 eV). Spectra treatment has been performed using the CASA software

Fourier Transform Infrared (FTIR) spectroscopy

Materials surface can present acidity, which can be Lewis of Brönsted acid centers. A Brönsted acid center is able to donate, or at least partially transfer a proton. While a Lewis acid center is able to accept an electron pair forming a bond, which is different from oxidation-reduction reactions where a complete electron transfer is going on.[17]

In order to identify the type of acid sites, their strength and density in a solid, adsorption of pyridine and desorption at different temperatures coupled with FT-IR spectroscopy is usually employed.

Pyridine is a basic molecule able to interact with Brönsted and Lewis acid centers of a solid, thus pyridine protonated by Brönsted acid sites (pyridinium ions) appear at ~1540 cm^{-1} while pyridine coordinated to Lewis acid centers appears at ~1450 cm^{-1}.

Thus by taking into account the intensity of these bands, the number and type of acid sites of a solid which can retain pyridine at a certain temperature (strength)can be calculated.[17]

The Fourier Transform Infrared (FTIR) spectra were recorded on a Jasco FT/IR-6200 model spectrometer. For these measurements, samples were prepared as self-supported pellets.

Solid State Nuclear Magnetic Resonance (NMR)

^{29}Si magic-angle spinning (MAS) nuclear magnetic resonance (NMR) spectra were recorded on a Bruker Avance 400 (9.4T) spectrometer at 79.49 MHz, with 2 μs (equivalent to 30°) rf pulses, a recycle delay of 60 s and at 5.0 kHz spinning rate.

Photoluminescence spectroscopy

The photoluminescence spectra the UV/visible and NIR spectral ranges were recorded at room temperature with a modular double grating excitation spectrofluorimeter with a TRIAX 320 emission monochromator (Fluorolog-3, Horiba Scientific) coupled to a R928 and H9170 Hamamatsu photomultipliers, respectively, using a front face acquisition mode. The excitation source was a 450W Xe arc lamp.

For up-conversion emission, the excitation source was a Thorlabs semiconducting diode laser (LDM2) emitting at 980 nm with power between 0.050 and 2.000 W. The laser power was quantified using a power meter (Coherent, Field MaxII-TOP) coupled to a high-sensitivity silicon photodiode optical sensor (diameter of $7 \cdot 10^{-3}$ m, Coherent, OP-2 VIS). During the measurements the laser spot was focused with a spot diameter of $5 \cdot 10^{-4}$ m, which means that the excitation optical density varied between $2.5 \cdot 10^{5}$ and $2.5 \cdot 10^{6}$ W.m^{-2}.

The emission spectra were corrected for detection and optical spectral response of the spectrofluorimeter, and the excitation spectra were corrected for the spectral distribution of the lamp intensity using a photodiode reference detector.

The steady state and time-resolved photoluminescence measurements were carried out using a Nd:YAG pulsed laser (pulse duration 4−6 ns, pulse frequency 10 Hz), model Brilliant (Quantel), coupled to an optical parametric oscillator (OPO), model

Vibrant (Opotek), as excitation light source (980 nm, 2 mJ/pulse). The output signal was collected into an electronically tunable monochromator, model SpectraPro-2300i (Acton Research Corporation), coupled to a photodiode with a photomultiplier tube, model H7732−10 (Hamamatsu), and the signal was monitored using a digital oscilloscope, model TDS5000B (Tektronix). The transient PL decays were fitted to a biexponential ($y = y0 + A1e^{-x/\tau 1} + A2e^{-x/\tau 2}$) function. The error intervals for the measured lifetimes were obtained from testing at least three identical samples.

Photoelectrochemical measurements

Photoelectrochemical measurements were performed in a three-electrode configuration using a graphite bar as counter electrode (Sigma-Aldrich, 100 mesh) and 0.25:0.35 M NaS2:NaSO3 aqueous solution as electrolyte to prevent photocorrosion of the CdSe QDs (pH 12.7). Electrochemical measurements were referred to the reversible hydrogen electrode (RHE) by the equation VRHE = VAg/AgCl + 0.197 + 0.059·pH. The electrodes were illuminated by a monochromatic 980 nm laser with 1500 mW/cm^2 power. The electrode illuminated area was 0.026 cm^2.

Spectroscopic ellipsometry

The spectroscopic ellipsometry measurements were made using an AutoSE ellipsometer (HORIBA Scientific) with a total of 218 points in the wavelength interval 450–850 nm, an incidence angle of 70°, an acquisition time of 50 ms per point and an average of 20 measurements per point. The refractive index values of the film were calculated using the Cauchy absorbing empirical model, which expresses the complex refractive index as function of the wavelength (λ) described: by

$$n(\lambda) = \left\{A + \frac{B}{\lambda^2} + \frac{C}{\lambda^4}\right\} + i\left\{D + \frac{E}{\lambda^2} + \frac{F}{\lambda^4}\right\}$$

where A, B, C, D, E and F parameters and a three-layered structure model (substrate, hybrid layer and air as an ambient medium, with a refractive index value of 1.00) was used. The thickness of the substrate was considered infinite and the refractive index was obtained by direct inversion of the ellipsometric data (not shown). The fit method has been described elsewhere.[18] The reported values for the thickness and refractive

index are the average of three measurements performed for each sample with a maximum standard deviation of 5%.

Difuse reflectance spsectroscopy

Diffuse reflectance UV–VIS (DRUV–vis) absorption spectra were carried out on a CARY 500SCAN VARIAN spectrophotometer in the 300–1000 nm range. For the calculation of the ban gap the following expression was taken into account:

$$\alpha_b = \frac{B(h\upsilon - E_g)^n}{h\upsilon}$$

Where α_b is the absorption coefiecient, *hv* is the absorbed energy where *h* is the Planck's constant and *v* is the frequency of vibration, *B* is a constant, E_g is the Band Gap energy and n is 1/2 for direct transition, 3/2 for forbidden transition, 2 for an indirect transition or 3 for indirect forbidden transition. In our case, TiO_2 shows direct allowed transition thus n=1/2 will be used.

When α value is 0, taking into account the previous expression, the absorbed energy value is the same as the Band Gap energy.

Thus the acquired diffuse reflectance spectrum is converted to Kubelka-Munk function:

$$F(R\infty) = \frac{(1-R)^2}{2R}$$

Where R is reflectancy (%) and *F(R∞)* is the reflectance transformed according to Kubelka Munk which is proportional to the absorption coefficient.

Substituting F(R∞) for α_b in Tauc equation we obtain:

$$\left(h\upsilon F(R\infty)\right)^2 = B(h\upsilon - E_g)$$

After that we Plot $(hv\ F(R\infty))^2$ against *hv* (in electron volts) and we draw the tangent line to the inflection on the curve. The *hv* value at the point of intersection of the tangent line and the horizontal axis is the Band Gap (*Eg)* energy value.

Gas Chromatography (GC)

GC analysis were carried out in an Agilent 7890A equipped with a Flame Ionization Detector (FID) and with a HP-5MS (30m x 0.25mm x 0.25µm) column with an stationary phase made of 5% alternated phenylsilicone.

Taking into account that the ionization detectors give a signal proportional to the mass product analyzed trough the chromatographic area, the use of corrected areas using response factors of each analyte, allows the concentration calculation of each component in the mixture.

$$n_i = \frac{A_i \cdot n_{S_i}}{A_{S_i} \cdot R_i}$$

Where n_i is the mols of the i compound

$A_i$is the chromatographic area of the i compound

n_{S_i} is the mols of the internal standard

A_{S_i} is the chromatographic area of the internal standard

R_i is the response factor of the i compound

Thus, knowing the number of initial mols of your reagent ($n_{r,0}$) and the mols of this substrate at a determined time t ($n_{r,t}$), the conversion at this time is determined by the following equation

$$Conv_t(\%) = \frac{n_{r,0} - n_{r,t}}{n_{r,0}} \cdot 100$$

$Yield_{i,t}$ and selectivity $Selec_{i,t}$ for a determined time is defined as:

$$Yield_{i,t}(\%) = \frac{n_{sit}}{n_{r,0}} \cdot 100 \qquad Selec_{i,t}(\%) = \frac{n_{sit}}{n_{r,0} - n_{r,t}} \cdot 100$$

Where n_{sit} is the number of moles a compound in a time t.

Gas Chromatography coupled with Mass Spectromety (GC-MS)

GC-MS were carried out in an Agilent 6890N equipped with a Flame Ionization Detector (FID) and with a HP-5MS (30m x 0.25mm x 0.25µm) and a 5973N selective mass detector.

6.3 Experimental procedures

Catalytic Tests

The catalytic and kinetic studies where performed in a reinforced glass reactor made in the Instituto de Tecnología Química. This reactor is composed by a conic vial made of reinforced glass. Its cover is modified by introducing a system to read the pressure inside the reactor (manometer) and a system prepared to the introduction of gases and the extraction of samples during the catalytic experiments, which is a canula with a valve that can be acopled to a gas jeringe. This reactor can be hotted in a silicon bath and strirred upon introducing a triangular magnetic stirrer and can work up to 15 bars.

Aldoxime dehydration reaction: 50 mg of the catalyst, 0.50 mmol Benzaldoxime, 1.5 mL o-xylene and nitrobencene as standard were added to a reinforced glass reactor equipped with pressure controllers, under argon atmosphere, and the temperature was increased to 150ºC with a silicon bath. During the experiment the reactors were stirred (magnetic stirring) at a rate of 1200 rpm.

Alkyne hydration reaction: 50 mg of the catalyst, 0.50 mmol Phenyl acetylene, 2.5 mmol water, 1.5 mL cyclooctane and dodecane as standard were added to a reinforced glass reactor equipped with pressure controllers and the temperature was increased to 95ºC with a silicon bath. During the experiment the reactors were stirred (magnetic stirring) at a rate of 1200 rpm.

MPV reaction: 25 mg of the catalyst, 0.50 mmol cyclohexanone, 1 mL isopropanol and dodecane as standard were added to a reinforced glass reactor equipped with pressure controllers and the temperature was increased to the desired temperature with a silicon bath. During the experiment the reactors were stirred (magnetic stirring) at a rate of 1200 rpm.

For each reaction, aliquots were taken periodically at different reaction times and analyzed by GC/MS and GC equipped with HP-5 column (30m×0.32×0.25µm) and a FID as detector.

Theorethical Calculations

Periodic density functional theory (DFT) calculations were performed using the Perdew−Wang (PW91) exchange-correlation functional within the generalized gradient approach (GGA)[19,20] as implemented in the VASP code.[21] The valence density was expanded in a plane wave basis set with a kinetic energy cutoff of 450 eV, and the effect of the core electrons in the valence density was taken into account by means of the projected augmented wave (PAW) formalism.[22] All calculations are spin polarized. Integration in the reciprocal space was carried out at the Γ k-point of the Brillouin zone. Transition states were located using either the DIMER algorithm[23,24] or the nudged elastic band NEB method.[25,26] Dispersion interactions were evaluated using the D3 Grimme's method.[27]

The (-111) facet of monoclinic zirconia and the (101) facet of tetragonal zirconia were represented by means of (2x2) and (2x3) supercell slabs, with dimensions 13,72 x 13,27 $Å^2$ and 12,85 x 11,09 $Å^2$, respectively. Both slab models contain 48 Zr and 96 O atoms arranged in three layers in the case of *m*-ZrO_2 and four layers in the case of *t*-ZrO_2, and with an empty region of ~20 Å between repeated slabs. During the geometry optimizations, the coordinates of the adsorbates and of the Zr and O atoms in the two uppermost layers of the ZrO_2 models were allowed to relax without any restriction until forces were below 0.02 eV $Å^{-1}$.

Relative energies E_{rel} of adsorbed reactant, intermediate, transition state and product structures were calculated by substracting the total energy of the relaxed ZrO_2 model $E(ZrO_2)$ and of optimized 2-propanol $E(C_3H_7OH)$ and cyclohexanone $E(C_6H_{10}O)$ from the total energy of the corresponding reactant, intermediate, transition state or product complex $E(ZrO_2\text{-complex})$, according to:

$$E_{rel} = E(ZrO_2\text{-complex}) - E(ZrO_2) - E(C_3H_7OH) - E(C_6H_{10}O)$$

Activation Eact and reaction DE energies were calculated as the difference between the total energy of the transition state TS or the product P for a given process and the corresponding reactant complex, according to the equations:

$$E_{act} = E(TS) - E(R)$$

$$\Delta E = E(P) - E(R)$$

6.4 References

(1) Li, W.; Huang, H.; Li, H.; Zhang, W.; Liu, H. *Langmuir* **2008**, *24* (15), 8358–8366.

(2) Yamaguchi, K.; Fujiwara, H.; Ogasawara, Y.; Kotani, M.; Mizuno, N. *Angew. Chem. Int. Ed. Engl.* **2007**, *46*, 3922–3925.

(3) Ogasawara, Y.; Uchida, S.; Yamaguchi, K.; Mizuno, N. *Chem. Eur. J.* **2009**, *15*, 4343–4349.

(4) Jin, X.; Oishi, T.; Yamaguchi, K.; Mizuno, N. *Chem. Eur. J.* **2011**, *17* (4), 1261–1267.

(5) Cortés-Jácome, M. A.; Angeles-Chavez, C.; López-Salinas, E.; Navarrete, J.; Toribio, P.; Toledo, J. A. *Appl. Catal. A Gen.* **2007**, *318*, 178–189.

(6) Cortés-Jácome, M. A.; Toledo, J. A.; Angeles-Chavez, C.; Aguilar, M.; Wang, J. A. *J. Phys. Chem. B* **2005**, *109*, 22730–22739.

(7) Julián-López, B.; Martos, M.; Ulldemolins, N.; Odriozola, J. a; Cordoncillo, E.; Escribano, P. *Chem. - A Eur. J.* **2009**, *15* (45), 12426–12434.

(8) Soler-illia, G. J. D. A. A.; Sanchez, C.; Lebeau, B.; Patarin, J. *Chem. Rev.* **2002**, *102* (11), 4093–4138.

(9) Kawashita, M.; Takayama, Y.; Kokubo, T.; Takaoka, G. H.; Araki, N.; Hiraoka, M. *J. Am. Ceram. Soc.* **2006**, *89* (4), 1347–1351.

(10) Ito, S.; Chen, P.; Comte, P.; Nazeeruddin, M. K.; Liska, P.; Péchy, P.; Grätzel, M. *Prog. Photovoltaics Res. Appl.* **2007**, *15*, 603–612.

(11) Giménez, S.; Lana-Villarreal, T.; Gómez, R.; Agouram, S.; Muñoz-Sanjosé, V.; Mora-Seró, I. *J. Appl. Phys.* **2010**, *108*, 64310.

(12) Braga, A.; Gimmenez, S.; Concina, I.; Vomiero, A.; Mora-Seró, I. *J. Phys. Chem. Lett.* **2011**, *2*, 454–460.

(13) Bermudez, V. D. Z.; Carlos, L. D.; Alcácer, L. *Chem. Mater.* **1999**, *11*, 569–580.

(14) Yi, G. S.; Chow, G. M. *Adv. Funct. Mater.* **2006**, *16* (18), 2324–2329.

(15) Toraya, H.; Yoshimura, M.; Somiya, S. *J. Am. Ceram. Soc.* **1984**, *67*, C119–C121.

(16) Brinauer, S.; Emmett, P. H.; Teller, E. *J. Am. Chem. Soc.* **1938**, *60* (2), 309–319.

(17) Corma, A. *Chem. Rev.* **1995**, *95* (3), 559–614.

(18) Fernandes, V. R.; Vicente, C. M. S.; Wada, N.; André, P. S.; Ferreira, R. A. S. *Opt. Express* **2010**, *18* (16), 16580–16586.

(19) Perdew, J. P.; Chevary, J. A.; Vosko, S. H.; Jackson, K. A.; Pederson, M. R.; Singh, D. J.; Fiolhais, C. *Phys. Rev. B* **1992**, *46*, 6671.

(20) Perdew, J. P.; Wang, Y. *Phys. Rev. B* **1992**, *45*, 13244.

(21) Kresse, G.; Furthmüller, J. *Phys. Rev. B* **1996**, *54*, 11169.

(22) Blöchl, P. E. *Phys. Rev. B* **1994**, *50*, 17953.

(23) Henkelman, G.; Jonsson, H. *J. Chem. Phys.* **1999**, *111*, 7010.

(24) Heyden, A.; Bell, A. T.; Keil, F. J. *J. Chem. Phys.* **2005**, *123*, 224101.

(25) Henkelman, G.; Uberuaga, B. P.; Jonsson, H. *J. Chem. Phys.* **2000**, *113*, 9901.

(26) Henkelman, G.; Jonsson, H. *J. Chem. Phys.* **2000**, *113*, 9978.

(27) Grimme, S.; Antony, J.; Ehrlich, S.; Krieg, H. *J. Chem. Phys.* **2010**, *132*, 154104.

Chapter 7

Diseño de nuevos nanomateriales para su uso en catálisis y fotoquímica

En aplicación de la normativa de estudios de doctorado sobre la elaboración de Tesis Doctorales según el programa RD 99/2011, por la que se establece que: *la Tesis Doctoral escrita en una lengua diferente del valenciano o del castellano, en el momento de ser depositada, debe contener un apartado lo suficientemente amplio en una de estas dos lenguas, y debe formar parte de la encuadernación de la tesis;* el siguiente capítulo contiene un resumen en castellano del trabajo recogido en la presente Tesis Doctoral.

7.1 Introducción

El término nanomateriales se refiere a aquellos materiales cuyo tamaño se encuentra por debajo de la micra, más concretamente entre 1 y 100 nm. Estos conceptos fueron en primer lugar introducidos por Richard Feynman al final de la década de los 50 y desarrollados en los años posteriores.

La naturaleza se ha servido de los nanomateriales para desarrollar propiedades asombrosas como la superhidrofibidad mostrada por las hojas de muchas plantas, colores impresionantes u órganos con grandes tamaños y bajas densidades como los picos de muchos animales. El ser humano también ha hecho uso de ellos, sin realmente conocer muy bien su naturaleza. Un claro ejemplo es la copa de vidrio Lycurgus que muestra un efecto dicroico debido a las nanopartículas (NPs) de oro y plata que contiene el vidrio.

Pero no fue hasta la década de los 90, con el desarrollo de nuevas rutas sintéticas, que permitieron el control de la materia en el tamaño nanométrico. Los métodos de síntesis de nanomateriales se pueden clasificar en dos: rutas sínteticas “top-down” y “bottom-up”.

En los métodos de síntesis “top-down” se parte de materiales de escala micro y tu tamaño es reducido mediante métodos físicos como la trituración y molienda. A pesar de ser el preferido desde un punto de vista industrial, debido a su bajo coste, produce nanomateriales con elevada polidispersidad de partícula.

Por otro lado, los métodos de síntesis “bottom-up” se basan en rutas químicas que utilizan moléculas o átomos como bloques de construcción. Estos métodos son los más utilizados ya que permiten la obtención de nanomateriales con formas y distribuciones de tamaños de partículas más controladas. De entre ellos cabe destacar

el método sol-gel, hidrotermal/solvotermal, síntesis por microondas, síntesis por descomposición térmica o reducción de NPs metálicas.

El gran interés que han suscitado los nanomateriales en los últimos años se debe a muchas propiedades de la materia cambian cuando se encuentran en esta escala comparados con los materiales de tamaño macroscópico. La aparición de nuevas propiedades se debe al aumento de la relación superficie/volumen lo que hace que aumente el número de átomos superficiales coordinativamente no saturados, los cuales tienen una mayor reactividad, o los efectos de confinamiento cuántico que tienen lugar cuando los tamaños se disminuyen a la nanoescala, proporcionando nuevas propiedades ópticas, electrónicas o magnéticas.

La catálisis es uno de los campos en los que se ha hecho un uso mayor de los nanomateriales. El aumento del número de átomos superficiales con la disminución del tamaño da acceso a un mayor número de átomos coordinativamente insaturados que les confiere una mayor reactividad. Este hecho está claramente ilustrado con los catalizadores de oro. Clásicamente se pensaba que dicho metal era catalíticamente inactivo, pero con la preparación de catalizadores con tamaños nanométricos se han podido desarrollar catalizadores de oro muy activos en diversas reacciones.[1–4]

La fotocatálisis permite promover reacciones catalíticas con la ayuda de la luz. Debido a la gran abundancia de la luz procedente del sol, se han realizado un gran número de estudios para el aprovechamiento de esta luz mediante fotocatalizdores para convertir CO_2 en combustibles, transformar agua en H_2 y O_2 o simplemente generar fotocorriente. En este sentido, la nanotecnología permite diseñar materiales más eficientes que permiten un mejor aprovechamiento de la luz y mejorar el rendimiento de estos procesos fotoquímicos.

Finalmente, en el campo de la fotónica, la introducción de los nanomateriales ha supuesto una auténtica revolución debido a producción de óxidos, calcogenuros, haluros, fluoruros y nanopartículas metálicas con extraordinarias propiedades en este campo. Uno de los procesos ópticos con mayor interés es la conversión de energía, que permite la absorción de dos o más fotones y la emisión de uno de mayor energía. La introducción de este fenómeno en los nanomateriales ha permitido el desarrollo de nanomateriales con gran interés en fotónica,[5], fotocatálisis[6, 7], fotovoltaica[8], sensores[9], biotecnología[10],etc

7.2 Objetivos

El objetivo general de la presente Tesis Doctoral es el estudio de nuevos nanomateriales y nanocompuestos híbridos obtenidos a partir de métodos de síntesis simples y de bajo coste, basados en rutas de química suave, que presenten propiedades mejoradas en el campo de la catálisis, fotocatálisis y fotónica.

El objetivo general puede ser desglosado en 5 objetivos más específicos que juntos abarcan el objetivo de la presente Tesis Doctoral:

- CATALISIS #1: Síntesis y caracterización de nanopartículas de ZrO_2 como nanocatalizadores. El trabajo incluye la estabilización de diferentes fases cristalinas además de su modificación con diferentes especies de WO_x, y la evaluación de sus propiedades catalíticas en reacciones de interés.
- CATALISIS #2: Síntesis de nuevos nanomateriales para la hidrogenación selectiva de compuestos orgánicos con interés industrial (Este capítulo contiene información confidencial por lo que su contenido no se mostrará).
- FOTOCATALISIS #1: Desarrollo de nuevos fotocatalizadores basados en TiO_2 nanocristalino, dopados con Cu. Las propiedades estructurales más importantes incluyendo la fase cristalina, tamaño y morfología, distribución de las especies de cobre y las propiedades superficiales serán analizadas y relacionadas con sus propiedades fotocatalíticas en reacciones con implicaciones medioambientales como son la reducción de CO_2 y el tratamiento de aguas.
- FOTOCATALISIS #2: Preparación de partículas conversoras de energía basadas en Y_2O_3 mediante el método de precipitación homogénea y la evaluación de sus propiedades fotocatalíticas en un dispositivo fotovoltaico para la generación de hidrógeno a partir de agua. El dispositivo fotovoltaico será sintetizado con nanopartículas de Y_2O_3 y puntos cuánticos para la absorción de radiación infrarroja para mejorar la eficiencia fotocatalítica.
- FOTONICA #2: Desarrollo de dos sistemas híbridos nanocompuestos preparados mediante el método sol-gel con propiedades conversoras de energía. Las propiedades estructurales y ópticas serán analizadas en detalle y su potencial aplicación en fotónica será examinado.

7.3 Discusión de resultados

7.3.1 ZrO_2 y WO_x-ZrO_2 nanocristalino obtenido mediante síntesis microondas.

El óxido de circonio presenta diferentes fases cristalinas que son estables en función de la presión y la temperatura.[11] La termodinámicamente estable a temperatura ambiente es la monoclínica. Pero otras fases metaestables, como la cúbica o tetragonal, pueden ser estabilizadas a temperatura ambiente a través de diversos métodos de síntesis o dopando la matriz con iones divalentes o trivalentes.[12–16] Dichas fases presentan diferente acidez y basicidad en función de su estructura cristalina, lo que les confiere diferente actividad y selectividad en diversas reacciones catalíticas.[17–21]

Las propiedades ácidas del ZrO_2 se pueden incrementar con la introducción de molibdeno, tunsgeno o iones sulfato. De entre ellos el tungsteno es el preferido ya que los materiales con molibdeno no presentan tanta acidez y los que contienen sulfatos se desactivan por la pérdida de éstos en los procesos catalíticos.[11] De este modo, debido a su alta acidez las circonas modificadas con tungsteno han presentado una excelente actividad catalítica en infinidad de reacciones.[22–28]

Para la síntesis de estos materiales se han empleado diferentes metodologías como la deposición de sales de tungsteno en circona amorfa,[22,29] intecambio iónico,[30,31]coprecipitación,[32,33] síntesis hidrotermal,[34] sol-gel,[35] etc. Uno de los métodos de síntesis que no se han descrito en la bibliografía para la obtención de ZrO_2 o WO_x-ZrO_2 es la síntesis por microondas. Este método presenta varias ventajas frente a los métodos convencionales como son los cortos tiempos de reacción para la obtención de materiales ya cristalinos, temperatura homogénea dentro del matraz de reacción, que evita los gradientes de temperatura y heterogeneidades y que permite un control de la morfología y del tamaño de las partículas con el control de las condiciones sintéticas.

Así se han sintetizado por síntesis por microondas NPs de ZrO_2 o WO_x-ZrO_2 con diferentes fases cristalinas y especies de wolframio. La actividad catalítica de estos materiales fue evaluada en la deshidratación de aldoximas, hidratación de alquinos y la reducción Meerwein-Pondorf-Verley con excelentes resultados y su actividad se ha analizado en función de las propiedades estructurales.

7.3.1.1 Síntesis y caracterización de ZrO_2 y WO_x-ZrO_2

La síntesis de los diferentes materiales se realizó mediante síntesis microondas con y sin la adición de urea (síntesis básica y ácida respectivamente). En general, los materiales obtenidos mediante la síntesis básica presentaban fase tetragonal mientras que los obtenidos en medio ácido presentaban la monoclínica.

Las síntesis se detuvieron a diferentes tiempos y temperaturas de reacción y los materiales obtenidos se analizaron en profundidad mediante DRX, espectroscopía Raman y microscopía de transmisión. Los resultados nos indican que, en medio ácido, los tetrámeros de $[Zr(OH)_2 \cdot 4H_2O]_4^{8+}$ polimerizan mediante unión y olación de los hidroxilos[21,36] proporcionando circona amorfa que con el aumento de la temperatura proporciona circona monoclínica a través de un mecanismo de disolución-cristalización[37,38] ya que en este medio las especies de circonio son solubles. En cambio, en presencia de urea, dada su descomposición a 80ºC en CO_2 y NH_3, el pH del medio aumenta progresivamente. Los OH^- desplazan el agua de los tetrámeros que condensan vía olación dando lugar a circona amorfa cuya estructura a corta distancia es muy similar a la circona tetragonal,[39] pero seguidamente aumentando la temperatura de reacción se obtiene la estructura tetragonal. A pH básico las especies de circonio no son muy solubles lo que desemboca en un desplazamiento mínimo de los iones, dando lugar a la circona tetragonal.

Estos materiales se calcinaron a 500 y 800ºC conservando en la mayoría de los casos la fase obtenida en la síntesis. Además se observó que los materiales que contenían tungsteno presentaban unos menores tamaños de cristal tras los tratamientos térmicos y por ende unas superficies mayores que los no dopados.

Las distintas especies de tungsteno se caracterizaron por espesctroscopía Raman. Los materiales obtenidos por ambas metodologías y calcinados a 500ºC, presentaron especies de W(VI) en coordinación tetraédrica. Los obtenidos mediante la síntesis ácida y calcinados a 800ºC presentaron WO_3 microcristalino sobre circona monoclínica mientras que los obtenidos en medio básico y calcinados a esta temperatura presentaron clústeres de polioxowolframato interconectados e hidratados sobre circona tetragonal. De este modo, en función de la acidez en el medio de síntesis y de la temperatura de calcinación se pudieron aislar diferentes fases cristalinas del ZrO_2 y especies de tungteno. (Esquema 7. 1).

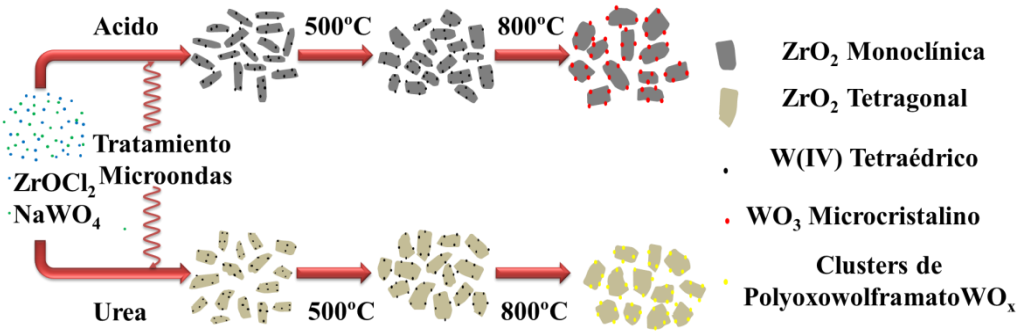

Esquema 7. 1. Síntesis por microondas de WO_x-ZrO_2 que permite modular la fase de cirona y las epecies de tungsteno en función del medio de síntesis y la temperatura de calcinación.

Las distintas especies anteriormente mencionadas fueron observadas en microscopia electrónica de alta resolución como puntos negros en campo claro o puntos blancos en campo oscuro (Figura 7. 1).

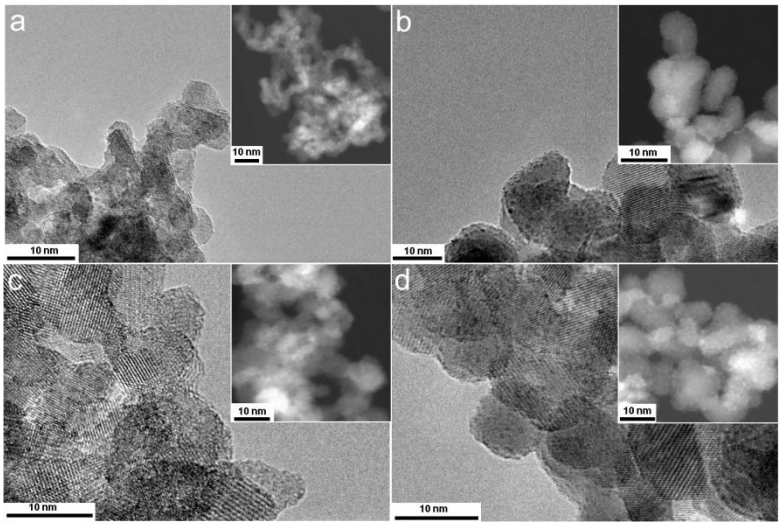

Figura 7. 1. Micrografías de microscopía de alta resolución en campo claro y campo oscuro (recuadros) de las circonas obtenidas en medio ácido (calcinadas a a) 500ºC y b) 800ºC) y en medio básico ((calcinadas a c) 500ºC y d) 800ºC).

Los distintos tipos de centros ácidos, su densidad y fuerza se determinaron por adsorción de piridina y desorción a distintas temperaturas. Las muestras calcinadas a 500ºC mostraron sólo acidez Lewis de comparable densidad y fuerza. Para las muestras calcinadas a 800ºC el número de centros Lewis es similar a baja temperatura de desorción, pero a mayor temperatura la muestra obtenida en medio básico es la que

presenta mayor fuerza en estos centros. Ambas muestras calcinadas a 800^{o}C presentaron centros Bønsted pero su densidad y fuerza eran mayores en la muestra sintetizada en medio básico.

7.3.1.2 Resultados catalíticos

Los distintos materiales se probaron en la deshidratación de aldoximas (Esquema 7. 2). De entre ellos, los mejores resultados catalíticos se obtuvieron con los materiales dopados con wolframio y calcinados a 500^{o}C. Por lo tanto las especies con mayor actividad catalítica son el tungsteno en coordinación tetraédrica independientemente de la fase cristalina que presente la circona, debido a que presentan la acidez Lewis adecuada para esta reacción.

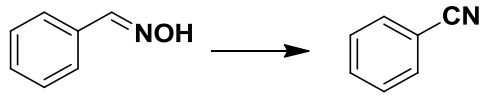

Esquema 7. 2. Deshidratación de benzaloximas.

La actividad catalítica de los distintos materiales también se evaluó en la hidratación de alquinos (Esquema 7. 3). Los únicos materiales que mostraron actividad en esta reacción fueron los calcinados a 800^{o}C. De entre ellos, los que se obtuvieron en medio básico, fueron los que mejores resultados proporcionaron, de los que se desprende que los clústeres de polioxowolframato interconectados e hidratados sobre circona tetragonal son las especies más activas en esta reacción debido a su acidez Bønsted.

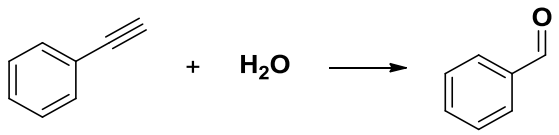

Esquema 7. 3. Hidratación de alquinos.

Las diferentes circonas también se probaron como catalizadores en la reducción de Meerwein-Pondorf-Verley (Esquema 7. 4). Los materiales sin calcinar fueron los que mejores actividades catalíticas mostraron debido a su mayor superficie específica. De entre estos resultados cabe destacar la gran diferencia de actividad que se observa

entre las circonas monoclínica y tetragonal, siendo la primera mucho más activa. Para tener un mayor conocimiento a nivel molecular sobre dicho comportamiento se llevó a cabo un estudio cinético junto a cálculos teóricos.

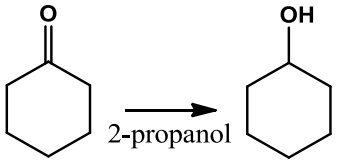

Esquema 7. 4. Reducción de Meerwein-Pondorf-Verley.

Las energías de activación se calcularon a partir de las constantes cinéticas a distintas temperaturas, obteniendo valores muy similares (43-52 $kJ \cdot mol^{-1}$). Lo que indica que las diferencias en la actividad catalítica vienen determinadas por el factor de frecuencia que está relacionado con los efectos entrópicos que vienen determinados por la probabilidad de encontrar las moléculas de reactivo adsorbidas de la manera correcta. Efectivamente, los cálculos teóricos mostraron cómo sobre *m*-ZrO_2 sólo existe un posible camino de reacción, mientras que en *t*-ZrO_2 existen varios posibles caminos, siendo el menos energético, no el más estable, lo que da lugar a una menor actividad de esta polimorfo en esta reacción.

7.3.2 Nanomateriales para fotocatálisis

En los últimos años una mayor conciencia social sobre la utilización de los recursos naturales y la minimización de la huella humana sobre la tierra ha surgido en la sociedad. Como consecuencia, se han desarrollado nuevas tecnologías basadas en nuevas energías renovables, como la hidráulica, eólica, biomasa, etc. Entre ellas, cabe destacar la energía solar, por su abundancia y facilidad de obtención.

Uno de los campos más importantes para el aprovechamiento de la energía solar es la fotocatálisis, que se define como la aceleración de una reacción con la presencia de un fotocatalizador activado por fotones.

El CO_2 es uno de los gases con efecto invernadero que se produce en la combustión de los combustibles fósiles. Debido a su alta estabilidad es difícil convertirlo en otras moléculas que tengan valor añadido. Una posible vía para su conversión es el uso de catalizadores que contengan metales para activar los enlaces C-O y la ayuda de la luz para poder convertir dicha molécula. Por ello, en este apartado se explicará la síntesis

de nanomateriales basados Cu-TiO_2 sintetizado mediante síntesis solvotermal y su uso como fotocatlizador en la reducción de CO_2 en fase acuosa.

Otro de los temas importantes en relación a la fotocatálisis es el aprovechamiento del espectro solar. La radiación solar que llega al nivel del mar está compuesta por un 5% de radiación ultravioleta, un 40% de visible y un 55% de infraroja. En la actualidad los fotocatalizadores y los dispositivo sólo aprovechan la parte más energética del espectro del sol (UV-VIS), siendo la parte infraroja desaprovechada. Se han desarrollado, varias estrategias para poder aprovechar dicha radiación. Por ejemplo, la introducción de NPs conversoras de energía en dispositivos fotovoltaicos es una de las más prometedoras.

La conversión de energía es un proceso mediante el cual se absorben dos o más fotones y se emite uno de mayor energía. Normalmente, para obtener este efecto, iones lantánidos como Er^{3+}, Tm^{3+}, Ho^{3+} e Yb^{3+} se introducen en matrices inorgánicas cómo los óxidos (ZrO_2, Y_2O_3, etc.) o fluoruros ($NaYF_4$, LaF_3, etc.). En este apartado se discutirá la introducción de nanopartículas de Y_2O_3 conversores de energía en celdas fotovoltaicas sensibilizadas con CdSe, produciendo fotocorriente a partir de luz infraroja.

7.3.2.1 Fotocatalizadores basados en Cu-TiO_2 para la conversión de CO_2 y purificación de agua

La síntesis seguida para la obtención de NPs de Cu-TiO_2 se basó en un protocolo previamente desarrollado en nuestro grupo de investigación[40] con alguna modificación. Con dicha metodología se obtuvieron materiales con una incipiente cristalinidad que fueron calcinados a 500^{o}C para eliminar cualquier resto de materia orgánica que pudiera interferir en la cuantificación de los productos durante los ensayos catalíticos y también aumentar la cristalinidad.

Los materiales obtenidos presentaron tamaños de cristal de alrededor de 20 nm y áreas BET de menos de 3 m^2/g siendo poco útiles para su uso en catálisis debido a su baja área superficial. Se observó que debido a la falta de agua en el sistema de síntesis, parte de los precursores no habían condensado lo que llevó a la introducción de una pequeña cantidad de agua en la síntesis.

Los materiales obtenidos de esta manera presentaron tamaños de cristal de alrededor de 7 nm. Una vez calcinados los tamaños de cristal fueron de 13-15 nm y las áreas de

30-50 m^2/g. De este modo la introducción de agua en el medio de síntesis promueve la hidrólisis y condensación de los precursores metalorgánicos, proporcionando materiales crudos con mayor cristalinidad y que presentan mayor resistencia a la sinterización durante el tratamiento térmico, y a su vez una mayor área BET.

El análisis difracción de rayos X de las muestras sintetizadas con agua y calcinadas a 500ºC mostraron un pequeño desplazamiento del pico más intenso, de lo que se desprende que los iones Cu^{2+} han sustituido a los átomos de Ti(IV) en la matriz de anatasa (Figura 7. 2).

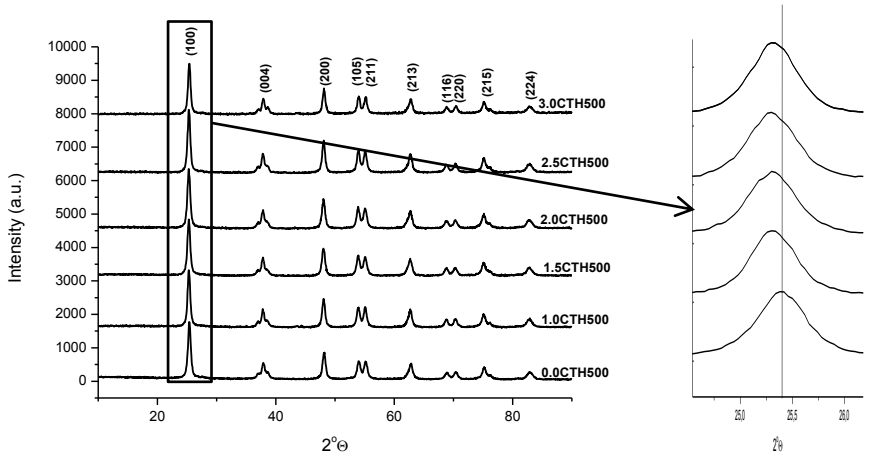

Figura 7. 2. DRX de XCTH500, el recuadro muestra el desplazamiento en el plano (101).

Los espectros Raman de los diferentes materiales mostraron que la fase obtenida era anatasa y no se detectó ningún pico correspondiente a alguna especie de Cu. Los espectros de absorbancia mostraron que a medida que se aumentaba el contenido en cobre el material tenía mayor absorción en el visible.

La actividad fotocatalítca de los materiales se evaluó en la reducción de CO_2 con agua como disolvente. En primer lugar se probaron diferentes solutos siendo el Na_2S el que dio mejores resultados produciendo ácido fórmico, H_2 y CO. Además se detectó un sobrenadante blanco que pudo ser separado del medio de reacción por simple decantación y se identificó cómo azufre elemental. Experimentos en blanco y con ^{13}C descartaron que el origen de dichos productos fuera la posible materia orgánica remanente en el catalizador o residuos carbonos adsorbidos en la superficie. Por otro lado, muestras preparadas por impregnación de una sal de cobre sobre TiO_2 P25 dieron peores resultados en dicha reacción, poniendo de manifiesto la importancia

que la alta dispersión del cobre en la muestras sintetizadas mediante la metodología solvotermal tiene sobre los resultados catalíticos.

Los distintos materiales con diferentes contenidos en cobre fueron evaluados en las condiciones catalíticas óptimas, obteniendo diferentes distribuciones de fotoproductos, siendo los materiales con un 2 y 3% del metal de transición los que dieron mejores resultados. La cinética de reacción mostró que a tiempos cortos el producto mayoritario era el ácido fórmico, que era consumido a lo largo de la reacción, mientras que la producción de H_2 aumentaba con el tiempo. Con estos resultados se pudo proponer el siguiente esquema de reacción, en que las ecuaciones 1-3 corresponden a las reacciones de reducción mientras que la 4 la oxidación.

$$2\ H^+(ac) + 2\ e^-(Cu\text{-}TiO_2)(s) \rightarrow H_2(g) \quad (1)$$

$$CO_2(g) + 2\ e^-(Cu\text{-}TiO_2)(s) + 2\ H^+(aq) \rightarrow HCO_2H(aq) \quad (2)$$

$$CO_2(aq) + 2\ e^-(Cu\text{-}TiO_2)(s) + 2\ H^+(aq) \rightarrow CO(g) + H_2O(aq) \quad (3)$$

$$S^{2-}(aq) + 2\ h^+(Cu\text{-}TiO_2)(s) \rightarrow {}^1\!/_n\ S_n(s) \quad (4)$$

7.3.2.2 Materiales fotocatalíticos para la producción de H_2 solar

Para la síntesis de Y_2O_3 dopado con Er^{3+} e Yb^{3+} se utilizó el método de precipitación homogénea con urea y posterior calcinación a 800^{o}C. La composición que se eligió para este estudio fue 2% molar de Er^{3+} y 5% Yb^{3+} de acuerdo con datos de la bibliografía. Con esta metodología se obtienen partículas esféricas de alrededor de 300 nm con distribución de tamaño muy homogénea. Mediante DRX se observó que dichas partículas estaban formadas por nanocristales de 40 nm y que los iones lantánidos sustituían al itrio en la matriz oxídica.

Estas partículas se introdujeron en una pasta comercial de TiO_2 y se conformaron en forma de film sobre sustratos de FTO siguiendo una metodología previamente descrita[41] obteniendo una buena dispersión de las partículas de Y_2O_3 en el film de TiO_2 (Figura 7. 3). Posteriormente siguiendo la metodología SILAR[42,43] el fotoánodo se sensibilizó con CdSe y ZnS.

El objetivo era que las NPs conversoras de energía, tras la excitación en la región infrarroja, emitieran a longitudes de onda del visible, y que a su vez, éstas emisiones

fueran absorbidas por los puntos cuánticos de CdSe/ZnS, para finalmente activar el TiO_2 semiconductor.

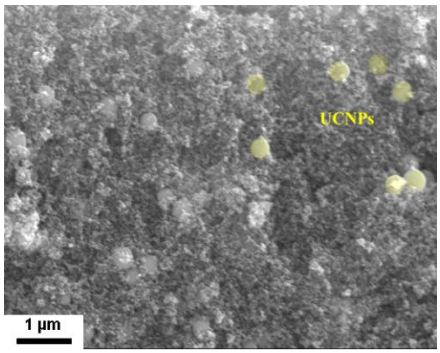

Figura 7. 3. Micrografía del microscopio electrónico de barrido del film mesoporoso de $Er_{0.04}Yb_{0.1}Y_{1.86}O_3/TiO_2$. Algunas partículas conversoras de energía están resaltadas en amarillo.

Las partículas de ErYb:Y_2O_3 bajo radiación laser de 980 nm emitieron en el verde ($^2H_{11/2}\rightarrow{}^4I_{15/2}$, 525 nm; $^4S_{3/2}\rightarrow{}^4I_{15/2}$, 562 nm) y en el rojo ($^4F_{9/2}\rightarrow{}^4I_{15/2}$, 678 nm), emisión característica del Er. Los films sensibilizados con las NPs conversoras mostraron una absorción por debajo de los 670 nm característica del CdSe (Figura 7. 4a) solapándose fundamentalmente con la banda verde de las NPs. La transferencia de energía entre las NPs de Y_2O_3 hacia los puntos cuánticos se demuestra con la disminución en la intensidad de la banda de emisión verde respecto a la roja cuando es comparada con el espectro del fotoánodo no sensibilizado (Figura 7. 4b).

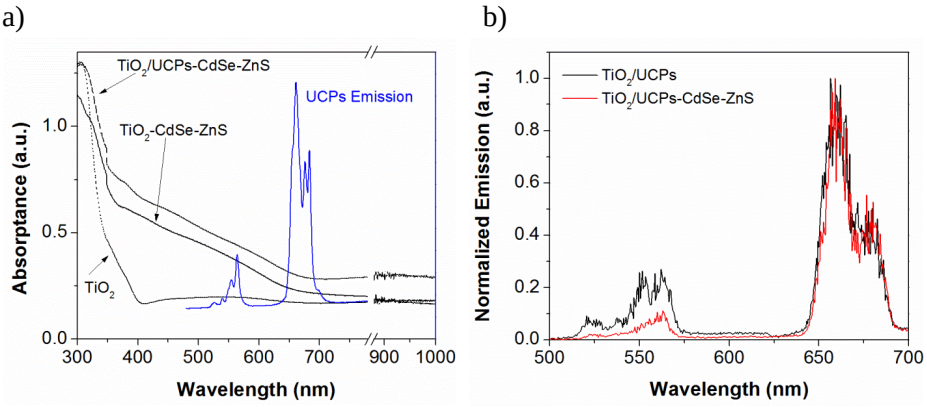

Figura 7. 4. a) Espectro de absorción de los diferentes films y espectro de conversión de energía normalizado del film sensibilizado y no sensibilizado.

Para tener un mayor conocimiento sobre el proceso que estaba ocurriendo se llevaron a cabo medidas dependientes con el tiempo. Los tiempos de vida para el fotoánodo sensibilizado y sin sensibilizar fueron muy similares en las diferentes emisiones, hecho que indica que no se produce un proceso de transferencia energética no radiativa sino que se está produciendo un proceso de emisión-absorción entre ErYb:Y_2O_3 y el CdSe.

Finalmente, el fotodispositivo se evaluó en la creación de fotocorriente para la formación de H_2. El dispositivo sin las partículas conversoras de energía bajo radiación de 980 nm produjo una corriente marginal, mientras que el dispositivo con las partículas de ErYb:Y_2O_3 bajo la misma radiación produjo una fotocorriente de un orden de magnitud mayor (Figura 7. 5a).

De este modo cuando las partículas partículas de ErYb:Y_2O_3 son irradiadas a 980nm se produce el fenómeno de conversión de energía emitiendo en el verde y rojo. Esta emisión es reabsorbida por el CdSe, excitando los electrones de la banda de valencia a la banda de conducción. Éstos, a su vez, son inyectados a la banda de conducción del TiO_2 y transportados al contacto para producir H_2. Finalmente, los huecos generados reaccionan con el electrolito cerrando el circuito (Figura 7. 5b).

a) b)

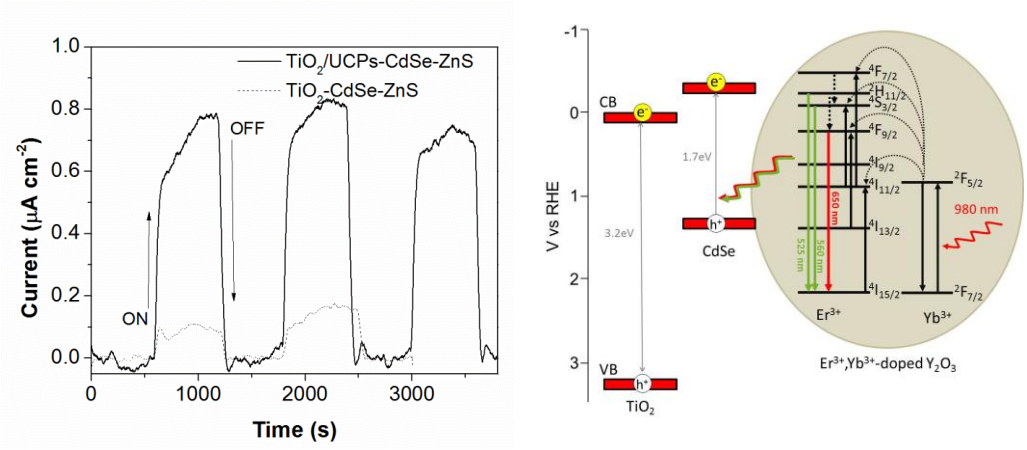

Figura 7. 5. a) Fotocorriente para el fotoánodo con y sin partículas ErYb:Y_2O_3 b) Diagrama energético para el mecanismo propuesto para el fotoánodo de TiO_2/ErYb:Y_2O_3/CdSe.

7.3.3 Híbridos orgánicos-inorgánicos con propiedades conversoras de energía

Los híbridos orgánicos-inorgánicos son materiales que combinan una parte orgánica y otra inorgánica. Gracias al desarrollo nuevas rutas sintéticas se han desarrollado nuevos materiales híbridos con nuevas propiedades, que no sólo combinan las propiedades orgánicas e inorgánicas de los componentes del material, sino que además desarrollan nuevas propiedades debido a que los diferentes componentes del material (en la nanoescala) interaccionan a nivel molecular. Como consecuencia, el desarrollo de nuevos materiales híbridos proporcionan materiales con nuevas funcionalidades para su aplicación en óptica, electrónica, membranas, catálisis, sensores, biología, recubrimientos protectores, etc.[44]

Uno de los temas que ha suscitado mayor interés en las últimas décadas es el desarrollo de materiales híbridos que incluyen iones lantánidos luminiscentes. Estos materiales proporcionan propiedades características de los híbridos (miniaturización, transparencia, fácil conformación en distintas formas (films, monolitos, etc), tuneabilidad de sus propiedades como la flexibilidad, hidrofilia, hidrofobia o índice de refracción) con las propiedades ópticas de los iones lantánidos.[45–49] Una de las áreas aún inexploradas en este campo es la integración de materiales conversores de energía en híbridos orgánicos-inorgánicos, los cuales pueden proporcionar nuevos nanocompuestos con aplicaciones en la producción de energía, concentradores solares, telecomunicaciones, bioimagen o bioensayos, etc.

En este apartado de la presente Tesis Doctoral se presentarán la síntesis de ZrO_2 y $NaYF_4$ con propiedades conversores de energía y su integración en híbridos di-ureasil y polidimetilsiloxano (PDMS) respectivamente. Su conformado en forma de film y monolito y el estudio de sus propiedades ópticas se discutirá en profundidad.

7.3.3.1 NPs de ZrO_2 conversoras de energía en híbridos de di-ureasil

ZrO_2 nanocristalino se sintetizó de acuerdo con un procedimiento experimental que había sido previamente publicado en nuestro grupo.[50] En este caso, el óxido se dopó con Er^{3+} o $Yb^{3+}Er^{3+}$ en diferentes proporciones. La difracción de rayos X de la matriz sin dopar calcinada a 800^{o}C muestra que dicho material está compuesto mayoritariamente por circona tetragonal. Por otro lado, los materiales dopados con iones lantánidos presentan en todos los casos la estructura tetragonal o cúbica. Para poder discernir entre ambas estructuras las muestras se analizaron por espectrocopía

Raman, mostrando que los materiales presentaban mezcla de fases tetragonal y cúbica, cuyo contenido en fase cúbica aumenta a medida que crece el contenido en tierras raras.

Los tamaños de cristal se determinaron con los espectros de DRX mediante la ecuación de Scherrer, obteniéndose tamaños entre 10 y 20 nm. Dicho tamaño disminuye a medida que se aumenta el contenido en lántanidos como consecuencia de su habilidad para promover la nucleación de los cristales, dando como consecuencia mayor número de núcleos y cristales más pequeños a medida que el contenido de tierras raras aumenta.[51]

La morfología de las nanopartículas fue estudiada por microscopía electrónica de transmisión. Las nanopartículas sin calcinar ya se muestran cristalinas con un tamaño de alrededor de 20 nm (Figura 7. 6a). Tras el tratamiento térmico las nanopartículas se aglomeran un poco pero conservan su tamaño (Figura 7. 6b) en consonancia con el tamaño calculado anteriormente por DRX.

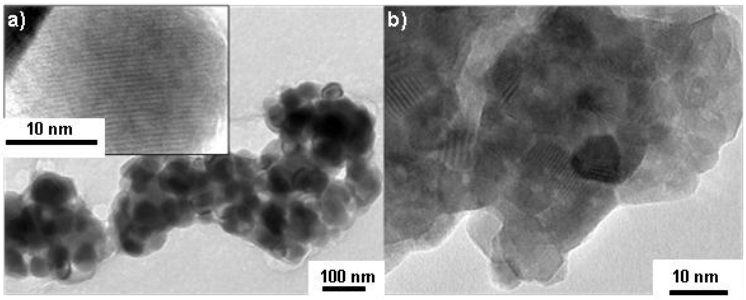

Figura 7. 6. ErYb:ZrO_2 a) sin calcinar y b) calcinada a 800ºC.

Las diferentes NPs se introdujeron en híbridos diureasiles y se conformaron como monolito y films, presentando en ambos casos alto grado de transparencia debido a la buena suspensión y dispersión de las NPs en el híbrido (Figura 7. 7).

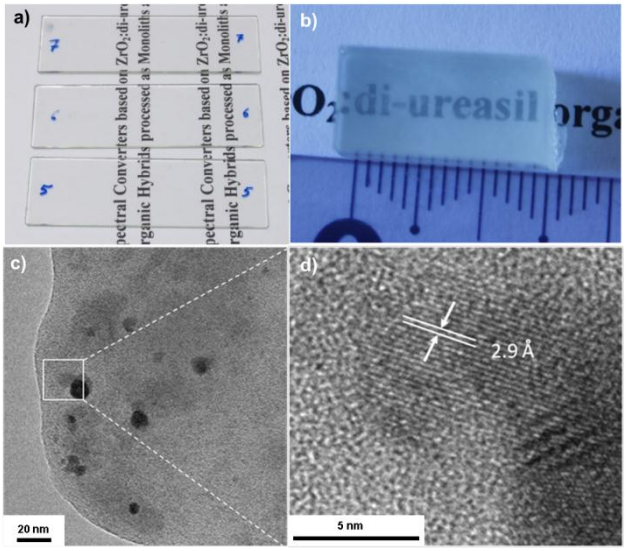

Figura 7. 7. a) films, b) monlitos y c) y d) micrografías HR-TEM de la muestra d-U(600) $ZE_{5.0}Y_{5.0}$.

Los diferentes híbridos se estudiaron por DRX, espectrocopía infraroja y raman, RMN de sólidos y elipsometría espectroscópica. Como conclusión de todas estas técnicas de caracterización se puede decir que la introducción de las NPs no afecta a la estructura local del híbrido, pero si aumenta su índice de refracción.

Las propiedades ópticas de los híbridos fueron profundamente estudiadas. Excitando el nanocompuesto a entre 260 y 400 nm se observó una banda ancha de emisión cuyo máximo cambia en función de la longitud de onda de excitación. Dicha emisión es característica de los híbridos di-ureasiles.[52,53]

Por otro lado las propiedades conversoras de energía de los distintos materiales fueron evaluadas excitando a 980 nm observando la emisión característica del Er^{3+} en el verde ($^2H_{11/2}\rightarrow{}^4I_{15/2}$, 525 nm; $^4S_{3/2}\rightarrow{}^4I_{15/2}$, 562 nm) y en el rojo ($^4F_{9/2}\rightarrow{}^4I_{15/2}$, 678 nm). El ratio entre la emisión roja y verde puede ser modificado en función de la concentración del ion Er^{3+} y de la densidad de potencia de excitación incidente obteniendo materiales cuyo color de emisión es modulable (Figura 7. 8).

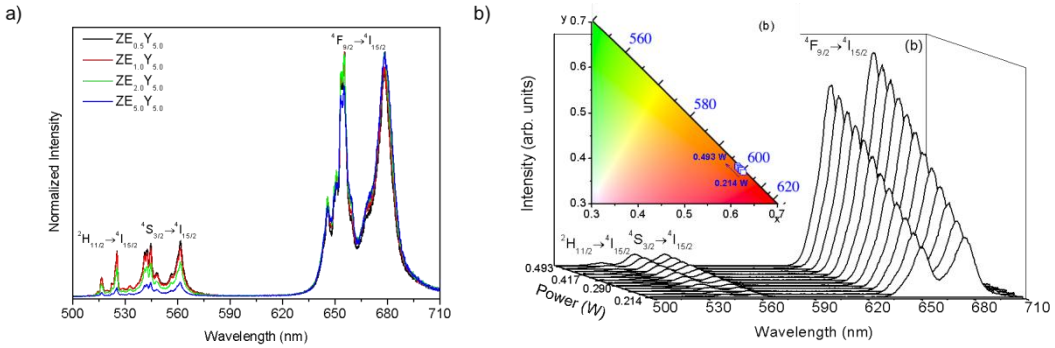

Figura 7. 8. Espectro de conversión de energía de a) $ZE_{0.5}Y_{5.0}$, $ZE_{1.0}Y_{5.0}$, $ZE_{2.0}Y_{5.0}$, $ZE_{5.0}Y_{5.0}$ NPs excitadas a 980 nm at 0.143 W y b) monolito de d-U(600)-ZE_5Y_5.

7.3.3.2 NPs de $NaYF_4$ conversoras de energía en híbridos de PDMS

NPs de $NaYF_4$ fueron sintetizadas siguiendo un protocolo previamente descrito mediante descomposición térmica de los precursores.[54] De esta manera se obtuvieron NPs de en torno a 20 nm de fase hexagonal y dopadas con Er^{3+}/Yb^{3+} y Tm^{3+}/Yb^{3+}. Dichas NPs se introdujeron en híbridos basados en PDMS entrecruzados por dominios oxometálicos M_xO_y (donde M:Nb, Ta, Ti, Zr) siguiendo la metodología desarrollada anteriomente en nuestro grupo[55] y se conformaron en forma de monolito y films. Los híbridos obtenidos mostraron alto grado de transparencia (Figura 7. 9a) como consecuencia de la buena dispersión de las NPs en el híbridos (Figura 7. 9b y c) hecho que junto a la posibilidad de modular su índice de refracción y su absorción en el infrarrojo les proporcionan un gran interés para su uso en dispositivos miniaturizados.

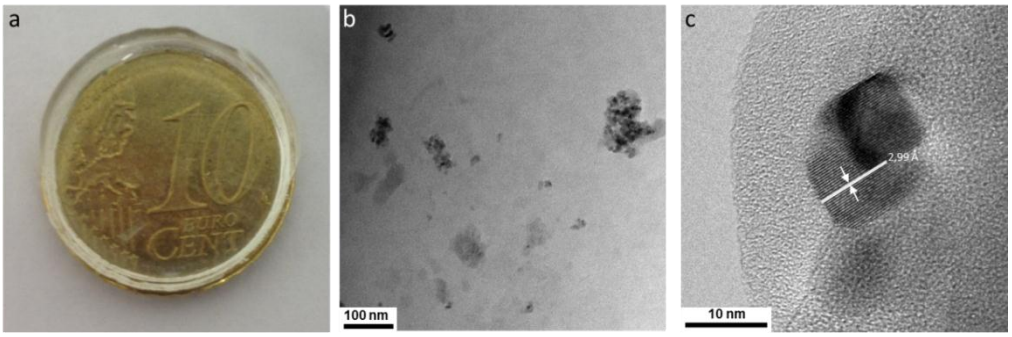

Figura 7. 9. Fotografía digital b) y c) fotografías HR-TEM de HyTa-Er^{3+}/Yb^{3+}.

Las propiedades conversoras de energía de los diferentes híbridos se estudiaron en profundidad. Los híbridos que contenían nanopartículas dopadas con Er^{3+} mostraron emisión en verde ($^2H_{11/2}\rightarrow{}^4I_{15/2}$, 525 nm; $^4S_{3/2}\rightarrow{}^4I_{15/2}$, 562 nm) y en el rojo ($^4F_{9/2}\rightarrow{}^4I_{15/2}$, 678 nm) mientras que las dopadas con Tm^{3+} emitieron en el azul ($^1G_4\rightarrow{}^3H_6$) y en el rojo ($^1G_4\rightarrow{}^7F_4$ and $^3F_3\rightarrow{}^3H_6$), emisión que podía verse a simple vista (Figura 7. 10). En ambos tipos de monolitos se observa diferente relación de intensidades entre las bandas de los espectros en función de los dominios oxometálicos. Este hecho puede ser causado por pequeñas diferencias en la distribución local de las NPs en el monolito durante el lento proceso de secado.

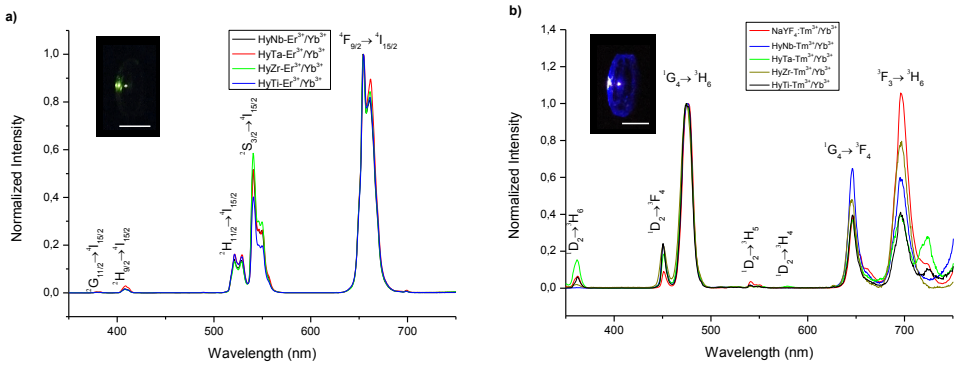

Figura 7. 10. Espectros conversores de energía (λ_{ex} 980nm) de los híbridos con NPs dopadas con a) Er^{3+} y b) $Tm^{3.}$ Los recuadros interiores muestran fotografía digitales de la emisión de los híbridos.

7.4 Conclusiones

Como conclusiones generales se puede decir que se han desarrolado nanomateriales que han sido aplicados cómo catalizadores, fotocatalizadores y en fotónica.

En primer lugar se sintetizaron NPs de ZrO_2 y WO_x-ZrO_2 mediante síntesis por microondas, controlando la fase cristalina y las especies de tungsteno a través del pH de la síntesis y del tratamiento térmico. Las propiedades catalíticas de los distintos materiales se evaluaron para la deshidratación de aldoximas, hidratación de alquinos y la reducción de Meerwein-Pondorf-Verley, obteniendo excelentes resultados en función de la fase cristalina y de las especies de tungsteno.

Seguidamente se sintetizaron nanomateriales de Cu-TiO_2 mediante la metodología solvotermal en los cuales el cobre se encontraba sustituyendo al titanio en la red de anatasa. Estos materiales se probaron en la fotoreduccón de CO_2 en agua y con Na_2S, que es un contaminate habitual en aguas residuales obteniendo como fotoproductos ácido fórmico, CO, H_2 y azufre elemental. De esta manera, los nanomateriales de Cu-TiO_2 sintetizados permiten convertir el CO_2 en ácido fórmico y CO, producir H_2 y transformar el sulfuro, que es un contaminante habitual en aguas residuales en azufre elemental que puede separarse del agua fácilmente.

Por otro lado, se sintetizaron partículas conversoras de energía basada en Y_2O_3 mediante el método de coprecipitación homogénea. Estas se introdujeron en un fotoánodo sensibilizado con CdSe el cual produjo fotocorriente para la producción de H_2 bajo radiación infrarroja.

Finalmente, se sintetizaron NPs conversoras de energía tanto de naturaleza oxídica como fluorada (ZrO_2 y $NaYF_4$) que se introdujeron en matrices híbridas orgánicas-inorgánicas de tipo di-ureasil y PDMS, respectivamente. Los distintos híbridos se conformaron en forma de monolito y films presentado una excelente transparencia debido a la buena dispersión de las NPs en la matriz híbrida. Sus propiedades ópticas y conversoras de energía se estudiaron en profundidad obteniendo diferente respuesta en función del dopado, procesado o de la intensidad de luz incidente.

7.5 Referencias

(1) Corma, A.; Serna, P. *Science* **2006**, *313*, 332–334.

(2) Grirrane, A.; Corma, A.; García, H. *Science* **2008**, *322* (5908), 1661–1664.

(3) Haruta, M. *CATTECH* **2002**, *6* (3), 102–115.

(4) Haruta, M. *Gold Bull.* **2004**, *37* (1–2), 27–36.

(5) Huang, X.; Han, S.; Huang, W.; Liu, X. *Chem. Soc. Rev.* **2013**, *42* (1), 173–201.

(6) Qin, W.; Zhang, D.; Zhao, D.; Wang, L.; Zheng, K. *Chem. Commun.* **2010**, *46* (13), 2304–2306.

(7) Wang, W.; Ding, M.; Lu, C.; Ni, Y.; Xu, Z. *Appl. Catal. B Environ.* **2014**, *144*, 379–385.

(8) Zhang, M.; Lin, Y.; Mullen, T. J.; Lin, W.; Sun, L.; Yan, C.; Patten, T. E.; Wang, D.; Liu, G. *J. Phys. Chem. Lett.* **2012**, No. 3, 3188–3192.

(9) de Camargo, A. S. S.; Possatto, J. F.; Nunes, L. A. D. O.; Botero, É. R.; Andreeta, É. R. M.; Garcia, D.; Eiras, J. A. *Solid State Commun.* **2006**, *137* (1–2), 1–5.

(10) Wang, F.; Liu, X. *Chem. Soc. Rev.* **2009**, *38* (4), 976–989.

(11) Shukla, S.; Seal, S. *Int. Mater. Rev.* **2005**, *50* (1), 1–20.

(12) Postole, G.; Chowdhury, B.; Karmakar, B.; Pinki, K.; Banerji, J.; Auroux, A. *J. Catal.* **2010**, *269*, 110–121.

(13) García, J.; Quintana, P.; Aguilar, D. H.; López, T.; Gómez, R. *J. Sol-Gel Sci. Technol.* **2006**, *37*, 185–188.

(14) Liu, S.; Ma, J.; Guan, L.; Li, J.; Wei, W.; Sun, Y. *Microporous Mesoporous Mater.* **2009**, *117* (1–2), 466–471.

(15) Thangadurai, P.; Chandra Bose, A.; Ramasamy, S. *J. Mater. Sci.* **2005**, *40*, 3963–3968.

(16) Ghosh, a.; Suri, a. K.; Pandey, M.; Thomas, S.; Rama Mohan, T. R.; Rao, B. T. *Mater. Lett.* **2006**, *60*, 1170–1173.

(17) Hertl, W. *Langmuir* **1989**, *5* (1), 96–100.

(18) Bachiller-Baeza, B.; Rodriguez-Ramos, I.; Guerrero-Ruiz, A. *Langmuir* **1998**, *14*, 3556–3564.

(19) Pokrovski, K.; Jung, K. T.; Bell, A. T. *Langmuir* **2001**, *17*, 4297–4303.

(20) He, D.; Ding, Y.; Luo, H.; Li, C. *J. Mol. Catal. A Chem.* **2004**, *208* (1–2), 267–271.

(21) Jung, K. T.; Bell, A. T. *J. Mol. Catal. A Chem.* **2000**, *163* (1–2), 27–42.

(22) Hino, M.; Arata, K. *J. Chem. Soc., Chem. Commun* **1988**, 1259.

(23) Arata, K.; Hino, M. *Proc. 9th Int. Congr. Catal. Calgary, Canada, 1988; Philips, M. J., Ternan, M., Eds.; Chem. Inst. Canada, Ottawa, Canada* **1988**, 1727.

(24) Hasan, Z.; Jeon, J.; Jhung, S. H. *J. Hazard. Mater.* **2012**, *205–206*, 216–221.

(25) Sarish, S.; Devassy, B. M.; Böhringer, W.; Fletcher, J.; Halligudi, S. B. *J. Mol. Catal. A Chem.* **2005**, *240*, 123–131.

(26) Barton, D. G.; Soled, S. L.; Meitzner, G. D.; Fuentes, G. A.; Iglesia, E. *J. Catal.* **1999**, *181*, 57–72.

(27) Wang, D.; Osmundsen, C. M.; Taarning, E.; Dumesic, J. a. *ChemCatChem* **2013**, *5*, 2044–2050.

(28) Baertsch, C. D.; Komala, K. T.; Chua, Y.; Iglesia, E. *J. Catal.* **2002**, *205*, 44–57.

(29) Corma, A. *Chem. Rev.* **1995**, *95* (3), 559–614.

(30) Figueras, F.; Palomeque, J.; Loridant, S.; Fèche, C.; Essayem, N.; Gelbard, G. *J. Catal.* **2004**, *226*, 25–31.

(31) Loridant, S.; Feche, C.; Essayem, N.; Figueras, F. *J. Phys. Chem. B* **2005**, *109*, 5631–5637.

(32) Cortés-Jácome, M. A.; Angeles-Chavez, C.; López-Salinas, E.; Navarrete, J.; Toribio, P.; Toledo, J. A. *Appl. Catal. A Gen.* **2007**, *318*, 178–189.

(33) Santiesteban, J. G.; Vartuli, J. C.; Han, S.; Bastian, R. D.; Chang, C. D. *J. Catal.* **1997**, *441*, 431–441.

(34) Cortés-Jácome, M. A.; Toledo, J. A.; Angeles-Chavez, C.; Aguilar, M.; Wang, J. A. *J. Phys. Chem. B* **2005**, *109*, 22730–22739.

(35) Boyse, R. A.; Ko, E. I. *J. Catal.* **1997**, *171*, 191–207.

(36) Clearfield, A.; Serrette, G. P. D.; Khazi-Syed, A. H. *Catal. Today* **1994**, *20* (2), 295–312.

(37) Denkewicz, R. P.; TenHuisen, K. S.; Adair, J. H. *J. Mater. Res.* **1990**, *5* (11), 2698–2705.

(38) Jolivet, J.-P. *De la solution à l'oxyde*; EP Sciences-CNRS Editions: Paris, 2015.

(39) Livage, J.; Mazieres, C. *J. Am. Ceram. Soc.* **1968**, *51* (6), 349–353.

(40) Julián-López, B.; Martos, M.; Ulldemolins, N.; Odriozola, J. a; Cordoncillo, E.; Escribano, P. *Chem. - A Eur. J.* **2009**, *15* (45), 12426–12434.

(41) Ito, S.; Chen, P.; Comte, P.; Nazeeruddin, M. K.; Liska, P.; Péchy, P.; Grätzel, M. *Prog. Photovoltaics Res. Appl.* **2007**, *15*, 603–612.

(42) Giménez, S.; Lana-Villarreal, T.; Gómez, R.; Agouram, S.; Muñoz-Sanjosé, V.; Mora-Seró, I. *J. Appl. Phys.* **2010**, *108*, 64310.

(43) Braga, A.; Gimmenez, S.; Concina, I.; Vomiero, A.; Mora-Seró, I. *J. Phys. Chem. Lett.* **2011**, *2*, 454–460.

(44) Sanchez, C.; Soler-Illia, G. J. de A. A.; Ribot, F.; Lalot, T.; Mayer, C. R.; Cabuil, V. *Chem. Mater.* **2001**, *13* (10), 3061–3083.

(45) Carlos, L. D.; Ferreira, R. A. S.; de Zea Bermudez, V.; Ribeiro, S. J. L. *Adv. Mater.* **2009**, *21* (5), 509–534.

(46) Binnemans, K. *Chem. Rev* **2009**, *109*, 4283–4374.

(47) Feng, J.; Zhang, H. *Chem. Soc. Rev.* **2013**, *42* (1), 387–410.

(48) Escribano, P.; Julián-López, B.; Planelles-Aragó, J.; Cordoncillo, E.; Viana, B.; Sanchez, C. *J. Mater. Chem.* **2008**, *18* (1), 23–40.

(49) Carlos, L. D.; Ferreira, R. A. S.; de Zea Bermudez, V.; Julián-López, B.; Escribano, P. *Chem. Soc. Rev.* **2011**, *40* (2), 536–549.

(50) Julián, B.; Corberán, R.; Cordoncillo, E.; Escribano, P.; Viana, B.; Sanchez, C. *Nanotechnology* **2005**, *16* (11), 2707–2713.

(51) Qiu, H.; Chen, G.; Fan, R.; Cheng, C.; Hao, S.; Chen, D.; Yang, C. *Chem. Commun. (Camb).* **2011**, *47* (34), 9648–9650.

(52) Carlos, L. D.; Sá Ferreira, R. A.; De Zea Bermudez, V.; Ribeiro, S. J. L. *Adv. Funtional Mater.* **2001**, *11* (2), 111–115.

(53) Carlos, L. D.; Sá Ferreira, R. A.; Pereira, R. N.; Assunçao, M.; Bermudez, V. D. Z. *J. Phys Chem. B* **2004**, *108*, 14924–14932.

(54) Yi, G. S.; Chow, G. M. *Adv. Funct. Mater.* **2006**, *16* (18), 2324–2329.

(55) Julián, B.; Gervais, C.; Cordoncillo, E.; Escribano, P.; Babonneau, F.; Sanchez, C. *Chem. Mater.* **2003**, No. 15, 3026–3034.